

# **Advanced light management concepts for perovskite photovoltaics**

Zur Erlangung des akademischen Grades eines

**Doktor-Ingenieurs**

von der KIT-Fakultät für  
Elektrotechnik und Informationstechnik  
des Karlsruher Instituts für Technologie (KIT)

genehmigte

**Dissertation**

von

**Raphael Schmager (M.Sc.)**

geb. in Kehl

Tag der mündlichen Prüfung: 12. Mai 2020

Hauptreferent: Dr. Ulrich W. Paetzold

Korreferenten: Prof. Dr. Bryce S. Richards

Prof. Dr. Carsten Rockstuhl





This document is licensed under a Creative Commons  
Attribution-ShareAlike 4.0 International License (CC BY-SA 4.0):  
<https://creativecommons.org/licenses/by-sa/4.0/deed.en>



## Kurzfassung

Um die rasante Zunahme der Treibhausgasemission zu bremsen und damit die globale Erderwärmung, ist ein schneller Umstieg von fossilen Brennstoffen auf erneuerbare Energien unabdingbar. In dieser Hinsicht spielt die Photovoltaik (PV) eine entscheidende Rolle, um eine effiziente Dekarbonisierung der globalen Stromerzeugung voranzutreiben. Dafür wird gegenwärtig sowohl an bestehender Silizium-PV, als auch an neuen PV-Technologien geforscht.

Der prominenteste Kandidat unter den neuen Technologien sind die Perowskit-Solarzellen. Diese haben in den letzten 10 Jahren eine beispiellose Effizienzsteigerung durchlaufen und erzielen heute Rekordwirkungsgrade über 25%. Die rasche Entwicklung der Perowskit-basierten PV ist vor allem durch das Versprechen einer kostengünstigen, effizienten und skalierbaren Technologie motiviert. Sie gilt zum einen als Konkurrenz zur bestehenden Silizium-PV und zum anderen als Partner für die Anwendung in Perowskit/Silizium Tandem-PV. In dieser Hinsicht bietet die Perowskit-basierte Tandem-PV die Aussicht, den derzeitigen Rekordwirkungsgrad von Silizium (c-Si) Solarzellen ( $\approx 27\%$ ) und sogar die Shockley-Queisser-Grenze für Einfachsolarzellen ( $\approx 34\%$ ) zu übertreffen.

Eine verbleibende Herausforderung, sowie ein aktuell stark untersuchtes Forschungsthema von Perowskit/c-Si-Tandemsolarzellen, ist ihre geringere Lichtausbeute im Vergleich zu konventionellen c-Si Solarzellen. Dies ist insbesondere auf zusätzlich erforderliche Funktionsschichten, wie die transparenten Elektroden, Ladungstransport-schichten und Passivierungsschichten zurückzuführen, die gemeinsam zu Reflexionsverlusten und Verlusten durch parasitäre Absorption beitragen. Dies reduziert sowohl den Wirkungsgrad (PCE) als auch den Energieertrag (EY) der Tandem-Solarzelle. Um Reflexions- und Absorptionsverluste zu minimieren, ist ein fortschrittliches Lichtmanagement unerlässlich. Da sich die realistischen Einstrahlungsbedingungen stark von typischen Standardtestbedingungen unterscheiden (z.B. spektrale Variation und variabler Einfallswinkel des Sonnenlichts), ist es zwingend notwendig, PV-Module nicht nur für den PCE, sondern auch für den EY zu optimieren. Daher ist ein ausgeklügeltes Lichtmanagement nicht nur auf Tandem-Solarmodule beschränkt, sondern für jede Art von Solarmodul wichtig.

In dieser Arbeit werden verschiedene Lichtmanagementkonzepte für die Perowskit-basierte-PV diskutiert und in Bezug auf den PCE und den jährlichen EY bewertet. In diesem Zusammenhang werden Mikrot Texturen für eine verbesserte Lichteinkopplung an der Luft/Glas-Grenzfläche untersucht, was für alle PV-Technologien relevant ist. Die Mikrot Texturen an der Vorderseite des Solarmoduls bieten die Möglichkeit, die Luft/Glas-Reflexion fast vollständig zu eliminieren und bei schrägen Einfallswinkeln (z.B.  $80^\circ$ ) um ca.  $80\%_{\text{rel}}$  zu reduzieren. Die experimentelle Realisierung zeigt die Erhöhung des PCE um  $12\%_{\text{rel}}$  bzw.  $5\%_{\text{rel}}$  für planare und texturierte Siliziumsolarzellen. Darüber hinaus werden Mikrot Texturen auf Perowskit/c-Si-Tandem-Minimodulen realisiert, die den PCE um  $10\%_{\text{rel}}$

verbessern. Aufgrund der ausgezeichneten Winkelstabilität der Mikrostrukturen spiegelt sich die Verbesserung des PCE auch im EY wider, was durch Simulationen gezeigt wird, bei denen die Verbesserungen im EY die des PCE um 2%<sub>rel</sub> übertreffen.

Zusätzlich zur ersten Grenzfläche jedes Solarmoduls werden die Reflexionsverluste an den vorderen halbtransparenten Indiumzinnoxid (ITO) Elektroden der Perowskit-Solarzellen untersucht. Mit Hilfe von nanotexturierten Glas/ITO-Grenzflächen können diese Verluste minimiert werden, was zu einem verbesserten Strom in der oberen Perowskit- und unteren c-Si-Solarzelle führt. Dies verbessert den Tandem-PCE um 2%<sub>rel</sub>. Darüber hinaus sind die nanotexturierten Elektroden winkelstabil und versprechen in den Simulationen eine Erhöhung des EY um 10%<sub>rel</sub>, was höher ist als die simulierte Verbesserung des PCE um 9%<sub>rel</sub>.

Weitere nanophotonische Modifikationen der Absorberschicht der Perowskit-Solarzelle führen zu einer verbesserten Absorption in der Nähe der Bandlücke, indem das einfallende Licht in quasi-geführte Moden eingekoppelt wird. Simulationen zeigen, dass dies die Stromerzeugung in den Perowskit-Solarzellen um bis zu 6%<sub>rel</sub> verbessert. Erste experimentelle Ergebnisse demonstrieren eine Verbesserung um 2%<sub>rel</sub>. Darüber hinaus bieten die nanophotonischen Perowskit-Solarzellen eine einfache Möglichkeit, den umweltschädlichen Bleigehalt in den Perowskit-Solarzellen bei gleichbleibendem Wirkungsgrad, um 30%<sub>rel</sub> zu verringern. Darüber hinaus verändert die nanophotonische Modifikation des Absorbers die Winkelabhängigkeit der Perowskit-Solarzellen nicht und führt zu den äquivalenten Verbesserungen des EY.

Schließlich wird ein neuartiges Herstellungsverfahren für Perowskit-Solarzellen vorgestellt, das eine einfache Laminierung der Perowskit-Solarzellen ermöglicht. Damit umgeht die Laminierung Inkompatibilitäten bei konventionellen Schichtabscheidungstechniken und bietet somit mehr Flexibilität und Freiheit bei der Wahl der Ladungstransportmaterialien für die Perowskit-Solarzellenherstellung. Erste Prototypen zeigen eine ausgezeichnete Langzeit- und Temperaturstabilität der laminierten Perowskit-Solarzellen mit einem PCE über 14%. Das vorgestellte Laminierungskonzept bahnt damit den Weg für eine direkte Laminierung von Perowskit-Solarzellen auf die bestehende Siliziumtechnologie und hat so ein großes Potential für die aktuelle Perowskit-basierte Tandemforschung.

## Abstract

To slow the rapid increase in greenhouse gas emissions, and thus slow down global warming, a rapid transition from fossil fuels to renewable energies is crucial. In this respect, photovoltaics (PV) plays a decisive role in driving forward the efficient decarbonization of global electricity generation. Currently, research is being conducted on existing technologies such as silicon PV as well as on new PV technologies. The most prominent candidate among the new technologies are the perovskite solar cells, which have experienced an unprecedented increase in performance over the last 10 years, with current record power conversion efficiencies (PCEs) exceeding 25%. The rapid development of perovskite-based PV is mostly motivated by the promise of a cost-effective, efficient and scalable technology, which is seen as a competitor to silicon-based PV and partner for the existing silicon technology for tandem applications. In this respect, perovskite-based tandem PV offers the prospect of exceeding the current record PCE of crystalline silicon (c-Si) solar cells ( $\approx 27\%$ ) and even the single junction Shockley-Queisser limit ( $\approx 34\%$ ).

A remaining challenge and currently strongly investigated research topic of perovskite/c-Si tandem solar cells is their reduced light-harvesting compared to conventional c-Si solar cells. In particular, this is due to additional required functional layers such as the transparent electrodes, charge transport layers and passivation layers, which all contribute to reflection losses as well as losses due to parasitic absorption. This reduces the overall PCE and EY of the tandem solar cell. Therefore, advanced light management is essential to minimize reflection and absorption losses. Since realistic irradiation conditions differ greatly from typical standard test conditions (e.g. spectral variation and variable angle of incidence of sunlight), it is essential to optimize PV modules not only for PCE but also for EY. Thus, sophisticated light management is not limited to tandem solar modules, but is important for any type of solar module.

In this thesis, various light management concepts for perovskite-based PV are discussed and evaluated with respect to the PCE and the annual EY. In this context, microtextures for improved light-incoupling at the air/glass interface are investigated, which is relevant for all PV technologies. The microtextures at the front of the solar module provide the ability to eliminate the air/glass reflection almost completely and reduce it by around  $80\%_{\text{rel}}$  for oblique incidence angles (e.g.  $80^\circ$ ). Experimental realization demonstrates the increase of the PCE by  $12\%_{\text{rel}}$  and  $5\%_{\text{rel}}$  for planar and textured silicon solar cells, respectively. Moreover, microtextures on top of perovskite/c-Si tandem minimodules are realized, which improve the PCE by  $10\%_{\text{rel}}$ . Due to the excellent angular stability of the microtextures, this improvement in the PCE is reflected in the EY as well, which is shown by simulations, where the enhancements in the EY exceed those of the PCE by  $2\%_{\text{rel}}$ .

In addition to the first interface of each solar cell architecture, the reflection losses at the front semitransparent indium tin oxide (ITO) electrodes of the perovskite solar cells are investigated. By means of nanotextured glass/ITO interfaces, these losses can be minimized, resulting in an improved current in the top perovskite and bottom c-Si solar cell. This improves the tandem PCE by 2%<sub>rel.</sub> Furthermore, the nanotextured electrodes are angular stable and promise an increase in EY of 10%<sub>rel.</sub> in simulations, which is higher than the simulated improvement in PCE of 9%<sub>rel.</sub>

Further nanophotonic modifications of the absorber layer of the perovskite solar cell itself leads to an improved absorption near the band gap by coupling the incident light to quasi-guided modes. Simulations show that this improves the current in the perovskite solar cells by up to 6%<sub>rel.</sub> First experimental results demonstrate an improvement of 2%<sub>rel.</sub> Moreover, the nanophotonic perovskite solar cells provide a simple way to mitigate the environmentally harmful lead content in perovskite solar cells by about 30%<sub>rel.</sub> while maintaining the same efficiency. Furthermore, the nanophotonic modification of the absorber does not change the angular dependence of the perovskite solar cells and leads to similar improvements in EY.

Finally, a novel manufacturing method for perovskite solar cells is presented, which enables a facile lamination of the perovskite solar cells. With this, the lamination evades layer incompatibilities in conventional layer depositions techniques, and thus offers flexibility and brings freedom in the choice of charge transport materials to the perovskite solar cell fabrication. First prototypes show excellent long-term and thermal stability of the perovskite solar cells with PCEs above 14%. The presented concept of lamination paves the way for the direct lamination of perovskite solar cells onto the existing silicon technology, and thus has great potential for current perovskite-based tandem research.





# Table of Contents

Kurzfassung .....	i
Abstract .....	iii
<b>1 Introduction .....</b>	<b>1</b>
<b>2 Fundamentals .....</b>	<b>7</b>
2.1 Working principle of a solar cell .....	7
2.2 Light-matter interaction .....	13
2.3 Limits of light management .....	14
<b>3 Methods .....</b>	<b>17</b>
3.1 Optical simulations .....	17
3.2 Fabrication methods .....	22
3.3 Characterization of solar cells .....	27
<b>4 Methodology of energy yield modelling .....</b>	<b>31</b>
4.1 Introduction .....	32
4.2 The framework for energy yield modelling .....	33
4.3 Irradiance module for realistic irradiation conditions .....	35
4.4 Optics module: modelling of multi-junction solar cells .....	37
4.5 Electrics module: the current – voltage characteristics .....	40
4.6 Energy yield calculation .....	42
4.7 Demonstration of the energy yield framework .....	44
4.8 Summary and discussion .....	49
<b>5 Microtextures for improved light incoupling and light harvesting by retro- reflection .....</b>	<b>51</b>
5.1 Introduction .....	52
5.2 Light-incoupling via microtextures .....	53
5.3 Concept of retro-reflection .....	57
5.4 Light harvesting by retro-reflection in solar cells .....	59
5.5 Biomimetic retro-reflection .....	71
5.6 Energy yield of microtextured perovskite/c-Si tandem solar cells .....	76
5.7 Summary .....	80
<b>6 Nanophotonic textures for enhanced light incoupling in perovskite/c-Si tandem solar cells .....</b>	<b>83</b>
6.1 Introduction .....	84
6.2 Optimization of nanophotonic ITO electrodes using optical simulations .....	85
6.3 Disordered nanophotonic front electrodes for perovskite-based multi-junction PV ..	94
6.4 Energy yield estimation of nano-patterned ITO electrode-based perovskite/c-Si tandem PV .....	100
6.5 Summary .....	102
<b>7 Nanophotonic perovskite solar cells with improved light trapping .....</b>	<b>105</b>
7.1 Introduction .....	106

7.2 Nanophotonic perovskite solar cells.....	107
7.3 Nano-patterning of the perovskite absorber layer.....	115
7.4 Nanoimprinted perovskite solar cells.....	123
7.5 Energy yield estimation of nanophotonic perovskite solar cells.....	129
7.6 Summary.....	131
<b>8 Laminated perovskite solar cells.....</b>	<b>133</b>
8.1 Introduction.....	134
8.2 Hot pressing of perovskite solar cells.....	136
8.3 Contact design.....	137
8.4 Influence of hot-pressing parameters.....	139
8.5 Laminated perovskite solar cells.....	143
8.6 Flexible and semitransparent laminated devices.....	146
8.7 Summary.....	147
<b>9 Conclusion and Outlook.....</b>	<b>149</b>
<b>Appendix.....</b>	<b>155</b>
<b>References.....</b>	<b>163</b>
<b>List of publications and contributions to conferences.....</b>	<b>177</b>
<b>Acknowledgements.....</b>	<b>181</b>

# 1 Introduction

Although human life on planet Earth becomes increasingly energy efficient, carbon dioxide emissions will continue to rise unless there is a fundamental change in current policies and technological trends. Under the Paris Agreement, the countries of the world committed themselves to reducing these emissions and, in particular, to keeping the rise in the global average temperature well below 2°C above pre-industrial levels [1]. This is a difficult but inevitable target to achieve, since the global energy consumption is projected to grow up to 30% through 2040, which is largely led by fossil fuels [2]. This growth is driven by further increase of the world population and economic growth in the global “East,” while the energy consumption in the “West” remains more or less constant. However, the exponentially increasing consumption of fossil fuels cannot continue in its present form. On the one hand, the availability of fossil fuels will simply and inevitably come to an end; on the other hand, global warming is advancing steadily, which – if not prevented – will have serious consequences for human life on earth. Therefore, particularly renewable energy sources, such as solar and wind, are key to a sustainable future on planet Earth. Since solar energy is abundantly available and a very versatile energy source, it can play a crucial role on this important path.

The growth of the market for photovoltaic (PV) technologies brings economies of scales [3]. Over the past two decades, a remarkable reduction in the manufacturing costs of solar modules, mainly due to automated mass production, has made PV one of the most important driving forces towards changing the global electricity mix [4,5]. Moreover, the renewable power generation capacity is set to expand by up to 50% until 2024 [4]. Especially, among renewable energy sources, electricity generation from PV is predicted to dominate the growth until 2040 (see **Figure 1.1**). Therefore, the rapid increase in solar capacity is expected to significantly contribute to the share of renewable energy electricity generation and is even projected to account for around 40% of global energy production by 2050 [6]. Moreover, the growth of energy generation from solar PV together with wind energy supports the renewables to overtake coal in the power generation mix (see Figure 1.1), so that by 2040 more than half of the total electricity generation is expected to stem from low-carbon sources [4].

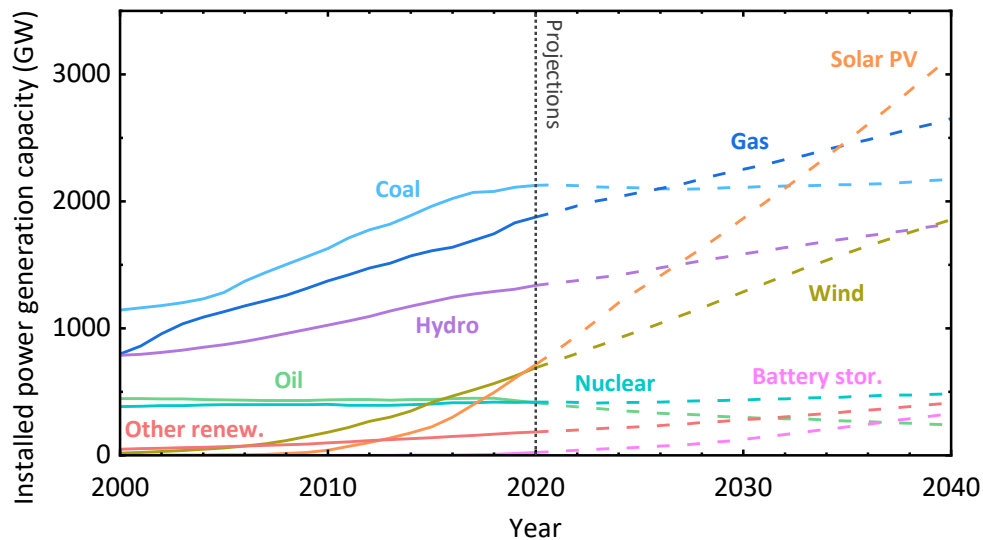


**Figure 1.1.** Installed power generation capacity by source in the Stated Policies Scenario from 2000 - 2040. The expansion of solar PV effectuates that renewables overtake coal in the global power generation mix. Based on data from the IEA World Energy Outlook 2019 [4], [www.iea.org/statistics](http://www.iea.org/statistics). All rights reserved.

Looking at commercially available PV technologies, the learning curve shows that with every doubling of cumulative module production over the last 40 years, prices fall by 24% [5]. To uphold this trend and to meet the predicted steeply increasing demand of installed electricity generation capacity in the future, the power conversion efficiency (PCE) of solar modules must be further increased. The steep increase in predicted PV capacity already manifests in the ‘International Technology Roadmap for Photovoltaic 2019’, which identifies a growing share of high-efficiency PV modules, and the appearance of bifacial and tandem modules in the next couple of years [7]. Bifacial PV utilizes incident light from both sides and tandem PV combines two absorbers of different optical band gaps that each harvest a different share of the solar spectrum, both resulting in an increased PCE compared to conventional single-junction monofacial architectures.

In addition, a number of new PV technologies have emerged in recent years, which are intensively researched worldwide, such as various thin-film technologies. The most prominent candidate in thin-film PV nowadays is the perovskite solar cells. The comprehensive research on perovskite-based PV over the past decade led to rapid advances with PCEs exceeding 25% nowadays [8]. The recent developments in perovskite PV has been largely underpinned by progress in material composition [9,10] and morphology of the perovskite absorber layer [11] as well as in device architectures [12] by employing passivation layers [13,14] or optimizing hole- and electron-transport layers [15,16].

Perovskite semiconductors continue to attract enormous attention due to their outstanding optoelectronic properties, such as high absorption coefficients, high carrier mobilities and low recombination rates [17,18]. Besides, their widely tunable band gap (1.5 - 2.5 eV), possible by compositional variations of the halide anion in the perovskite

crystal structure [19], allows strong light absorption in a broad spectral range [20]. These properties as well as low material costs and a wide range of possible – potentially scalable – deposition techniques [21], qualify perovskite semiconductors as promising candidates for two possible applications: Firstly, it might become an alternative to silicon-based PV, which currently dominates with a market share of  $\approx 95\%$  [5], especially for applications where rigid silicon substrates cannot be employed. Secondly, it could be used as the wide band gap top solar cell in next generation tandem PV in combination with existing low band gap bottom solar cells such as crystalline silicon (c-Si) or copper indium gallium selenide (CIGS) [22,23]. In this regard, particularly perovskite/c-Si tandem solar cells offer the prospect of exceeding the current record PCE of c-Si solar cells ( $\approx 27\%$ ) and even the single junction Shockley-Queisser limit ( $\approx 34\%$ ) [24,25].

However, one key challenge of perovskite/c-Si tandem solar cells to date is their inferior light-harvesting ability compared to single-junction c-Si solar cells [26]. Aside from the two photoactive materials, additional transparent electrodes, charge transport layers, and passivation layers are necessary. This results in reflection losses at the various interfaces as well as parasitic absorption. Especially, loss of the near infrared (NIR) radiation in the perovskite top solar cell reduces the available energy for the bottom c-Si solar cell, limiting the overall tandem PCE. Therefore, it is vital to employ light management concepts in order to reduce these reflection and transmission losses.

Sophisticated light management is not limited to tandem solar modules, but is important for any type of solar module. Moreover, the energy harvesting of PV modules needs to be optimized under realistic irradiation conditions, which must consider the varying angles of incident sunlight as well as the spectral composition of the solar irradiance. Accounting for these effects, the energy yield (EY) of solar modules is by far the superior measure than the PCE, which is determined under standard test conditions. In order to minimize the optical losses for a large range of incident angles and a broad spectrum, optimized light management concepts are paramount in PV modules to achieve highest PCEs and EYs. In this regard, the fundamental strategies encompass to: (i) improve light-incoupling at the front surface [27–30], (ii) enhance light absorption in weakly absorbing spectral regions by light trapping [31,32], and (iii) reduce reflection and parasitic losses in contacts, passivation's and charge transport layers [33–35].

In order to implement these concepts, textures of different dimensions can be utilized. Firstly, textures much smaller than the wavelength of the visible light – so called nanotextures – can be implemented to reduce reflection losses at material interfaces of solar modules. The nanotextures act as an effective medium for the incident light and the gradual change in refractive index through this interface drastically reduces reflection losses. Prominent examples are the subwavelength structures of the moth eye [36–38] and butterfly wing [39], as well as black silicon [40,41] and nano-porous coatings [42,43].

Secondly, light trapping and nanophotonic effects are achieved by mesoscopic textures with dimensions in the order of the wavelength. Here, plasmonic nanotextures [44,45] and photonic crystals [46–50] have been developed to guide and localize light within the photovoltaic devices to enhance the absorption. Moreover, diffraction gratings [51–54], randomly textured scattering surfaces [55,56], nanowire networks [57], and metamaterials [58] have evolved as important concepts for improved light harvesting in photovoltaic devices.

Thirdly, microtextures with dimensions on the order of multiple wavelengths can be employed to reduce surface reflection and enhance light trapping by increasing the path length of light inside the absorber layer. Here, the most prominent representative are the random pyramids on mono-crystalline silicon solar cells. In case of thin-film solar cells, for which layer thicknesses are limited to a few 100 nm, micro-texturing of the absorber is typically not applicable. Here, microtextures are usually applied in the form of a transparent polymer [59], and first work by our group already demonstrated the integration in a module front glass cover [30]. These non-invasive implementations at the front surface of the modules are of high significance, since they leave the absorber layer unaffected and makes the employment independent on the architecture and technology. Moreover, carefully designed micro-scaled textures can be applied on the front glass encapsulation of all kinds of solar modules to reduce the air/glass reflection.

Similar to thin-film anti-reflection coatings (quarter wavelength films), mesoscopic textures are usually optimized for a specific wavelengths and angular range, whereas nanotextures and microtextures do not show any spectral and only a low angular dependency on their light-incoupling properties. In addition to the efficient broadband incoupling of light up to high angles of incidence, the microtextures, provide retro-reflection properties. The retro-reflection redirects light, reflected by the solar cell, back to the solar cell, and thus causes an increase in the probability of absorption.

Each of these mechanisms can lead to significant enhancements in the total EY of a specific architecture and PV technology. The scope of this thesis is the development and evaluation of advanced light management concepts for perovskite PV. In this regard, the thesis focusses on improved light-incoupling and harvesting by microtextures. These microtextures are applied on silicon-, perovskite and perovskite/c-Si tandem solar cells and show enhanced PCEs as well as enhanced EYs. Moreover, nanotextures are employed to reduce the reflectance losses at the front semitransparent electrodes of the perovskite solar cells by introducing an effective refractive index gradient for the incident light. In addition, the intrinsic absorption properties of the perovskite absorber are tailored by imprinting mesoscopic textures inside, creating nanophotonic coupling of the incident light to the absorber layer itself. Finally, a novel method is demonstrated that enables facile lamination of the perovskite solar cells, thus providing flexibility and more freedom in the

choice of materials, paving the way for potential new manufacturing processes for perovskite-based tandem PV.

### **Outline of the thesis**

Chapter 2 provides the reader with the fundamental knowledge to understand the content of this thesis. Therefore, the chapter discusses the working principle of solar cells and the characteristic parameters to describe its performance. Next, the fundamentals on light and matter interaction are described briefly. Finally, the basics and limits of light management are discussed.

Chapter 3 introduces the optical simulation methods, the fabrication methods and the characterization tools. In Chapter 4, the methodology of energy yield modelling is discussed and the in-house developed framework is demonstrated. In each of the following chapters, this framework is used to test the influence of the presented light management concepts in relation to the EY.

Chapter 5 presents the work on improved light-incoupling by employing microtextures. Different artificial microtextures as well as biomimetic textures are utilized to enhance the current generation, and thus the power conversion efficiency of planar and textured crystalline silicon as well as perovskite/silicon tandem solar cells.

In chapter 6, nanophotonic front electrodes are demonstrated, which improve the light incoupling into the perovskite and perovskite/silicon tandem solar cells by reducing the reflection losses at the front transparent electrode.

Chapter 7 summarizes the results on nanophotonic perovskite solar cells, in which the perovskite absorber layer itself is patterned by thermal nanoimprint lithography. The nanoimprinted perovskite solar cells demonstrate improved current generation due to the coupling of incident light to quasi-guided modes in the perovskite absorber layer, increasing the absorption close to the band gap of the perovskite.

In chapter 8, the lamination of perovskite solar cells via two separately processed half-stacks is presented. This enables more freedom in the choice of charge transport materials, since it eliminates process related issues in the layer-by-layer deposition. In addition, two-terminal perovskite-based tandem solar cells might benefit from this facile lamination technique, since the perovskite layer stack could be laminated directly on top of the bottom solar cell.

Chapter 9 summarizes the key results of the thesis and aligns the achievements with their current state of research. Moreover, it provides an outlook for each of the presented topic.



## 2 Fundamentals

This section describes the fundamentals of photovoltaics by deriving the working principle of solar cells, followed by a brief description of the interaction between light and matter. Finally, the fundamental limits of light management are discussed.

### 2.1 Working principle of a solar cell

A solar cell is an electrical device that converts light directly into electrical energy. The physical basis of the conversion relies on the photovoltaic effect, which is a special case of the internal photoelectric effect. The fundamental steps involve: (1) absorption of an incident photon in the absorber material, (2) the generation of a bound electron-hole pair (exciton), (3) the separation of the photo-generated charge carriers, and (4) finally the collection of the photo-generated charge carriers at the terminals of the junction (see **Figure 2.1a**).

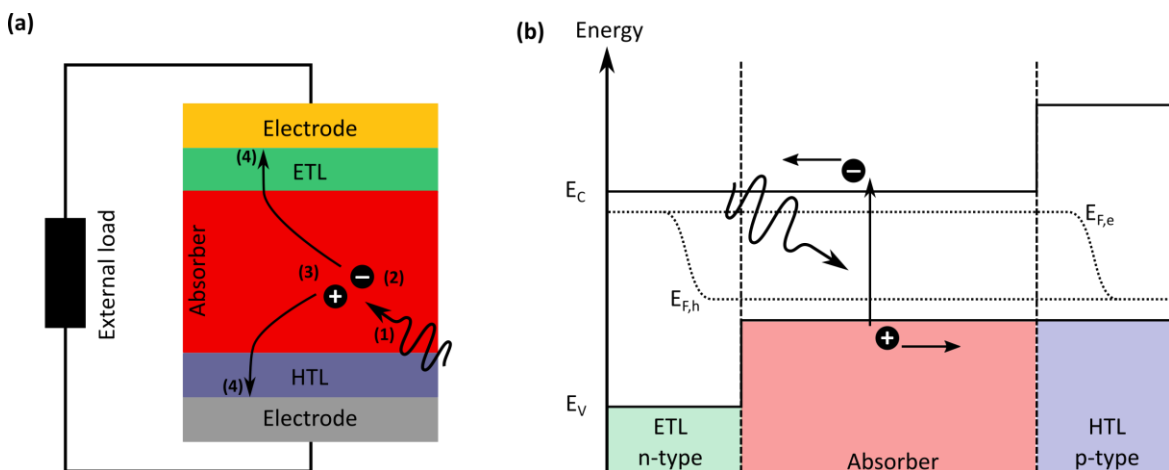


**Figure 2.1.** (a) Schematic of the main physical processes taking place inside a solar cell. (b) Schematic band diagram of a *p-i-n* solar cell under illumination close to open-circuit conditions.

In this regard, only photons with energy above that of the band gap  $E_G$  of the absorber material can be absorbed. Photons with lower energy will pass through the material or will be reflected at its interface. The surplus of energy of the photons with higher energy is converted to heat (thermalization loss). The generated electron-hole pairs are meta-stable and will only exist, on average, for a time equal to the minority carrier lifetime before they recombine. If the carriers recombine, the light-generated electron-hole pair is lost and no current or power can be generated. Therefore, efficient collection of these carriers is needed.

In general, a  $p$ - $n$  homojunction or  $p$ - $i$ - $n$  heterojunction is used to spatially separate electrons and holes. Typically, the silicon solar cell forms a  $p$ - $n$  junction by doping the intrinsic silicon and forming a junction of the  $n$  and  $p$  doped materials. In this regard, the difference of the quasi Fermi energies of the valence band holes ( $p$ -doped) and the conduction band electrons ( $n$ -doped) are the driving mechanism for the separation of the charges [60]. The principle of a heterojunction is to form a similar junction by sandwiching an intrinsic absorber between a  $n$ -type and  $p$ -type conductor, namely the electron and hole transport layers. Their band gaps differ from the absorber band gap, so that the contacts between them and the absorber act as  $p$ - $n$ -like membranes. The  $p$ - $i$ - $n$  structure therefore links to perovskite solar cells, where charge transport (also: charge extraction) layers surround the perovskite absorber material (see Figure 2.1a).

Within the  $p$ - $i$ - $n$ -junction, the (generated) free charge carriers are separated by a gradient in the electrochemical potential [61]. The electrochemical potential is the sum of the chemical and electrical potential. A gradient in the chemical potential (inhomogeneous charge distribution) leads to diffusion of the charge carriers. A gradient in the electric potential leads to a drift of the charge carriers. The electrochemical potential is tantamount with the quasi-Fermi energies  $E_{F,e}$  and  $E_{F,h}$  of the electrons and holes in the non-equilibrium state of the illuminated absorber (see Figure 2.1b). In the dark, the Fermi-levels are in equilibrium. Under illumination, the concentration of minority carriers (electrons in the  $p$ -type region and holes in the  $n$ -type region) strongly increases. Therefore, the Fermi energies split up into quasi-Fermi energies of the electrons and holes.

Under open-circuit conditions (no connection between the  $n$ -type and the  $p$ -type regions), no net current can flow inside the  $p$ - $n$  junction. The open-circuit voltage  $V_{OC}$  measured is equal to the difference in the quasi-Fermi levels of the majority carriers.

Under short-circuit conditions ( $n$ -type and  $p$ -type region is connected), the electrostatic potential barrier is not changed. However, due to a strong variation of the quasi-Fermi levels inside the depletion region, a net current is flowing inside the semiconductor. This photo-generated current  $I_{ph}$  is also called the short-circuit current  $I_{SC}$ .

When an external load  $V$  is applied between the electrodes of the illuminated junction, only a fraction of the photo-generated current will flow through this external circuit. The difference of the electrochemical potential between the  $n$ -type and  $p$ -type regions will be

lowered by the voltage drop due to the external load. This lowers the electric potential over the depletion region and results in an increase of the recombination current  $I_{\text{rec}}$ . The relation between the net current  $I$  under an applied voltage  $V$  is then given by:

$$\begin{aligned} I(V) &= I_{\text{rec}}(V) - I_{\text{gen}}(V) - I_{\text{ph}} \\ &= I_0 \left( \exp\left(\frac{qV}{k_B T}\right) - 1 \right) - I_{\text{ph}}, \end{aligned} \quad 2.1.$$

where  $I_0$  is the dark saturation current,  $q$  the charge of an electron,  $k_B$  the Boltzmann constant and  $T$  the temperature.

To describe the performance of a solar cell, characteristic parameters are derived from the current-voltage characteristics (see Equation 2.1), which is illustrated in **Figure 2.2a**. Firstly, the short-circuit current density  $I_{\text{SC}}$ , which gives the maximum current and is obtained at  $V=0$ . Secondly, the open-circuit voltage  $V_{\text{OC}}$ , which is measured when the output terminal is opened and  $I$  is therefore zero. Thirdly, the maximum output power  $P_{\text{MPP}}$ , which is defined by the maximum power point of the solar cell. The maximum power point is defined as the point where the product of  $V_{\text{MP}}$  and  $I_{\text{MP}}$  maximizes and one therefore finds the largest possible rectangle below the  $I$ - $V$  characteristic. The ratio of the  $P_{\text{MPP}}$  to the product of  $I_{\text{SC}}$  and  $V_{\text{OC}}$  is called fill factor:

$$\text{FF} = \frac{P_{\text{MPP}}}{I_{\text{SC}} \cdot V_{\text{OC}}} = \frac{V_{\text{MP}} \cdot I_{\text{MP}}}{I_{\text{SC}} \cdot V_{\text{OC}}}. \quad 2.2.$$

Finally, the power conversion efficiency of the solar cell is given by the ratio of maximum output power  $P_{\text{MPP}}$  and input power  $P_{\text{in}}$ .

$$\text{PCE} = \frac{P_{\text{MPP}}}{P_{\text{in}}} = \frac{V_{\text{OC}} \cdot I_{\text{SC}} \cdot \text{FF}}{P_{\text{in}}}. \quad 2.3.$$

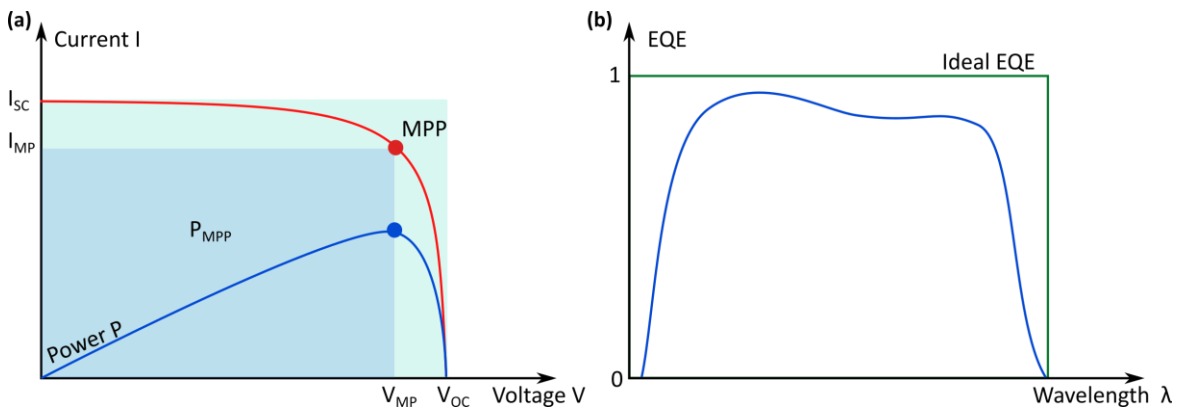


**Figure 2.2.** (a) Schematic current-voltage characteristics. The current at zero voltage  $V$  is defined as the short-circuit current  $I_{\text{SC}}$ . The voltage at zero current is defined as open-circuit voltage  $V_{\text{OC}}$ . The maximum power point (MPP) defines the current  $I_{\text{MP}}$  and voltage  $V_{\text{MP}}$ , where the maximum power  $P_{\text{MPP}}$  is obtained. The square  $P_{\text{MPP}}$  to the product of  $I_{\text{SC}}$  and  $V_{\text{OC}}$  is the FF. (b) Illustration of an ideal external quantum efficiency (EQE) and of a more realistic one (blue). The difference is due to surface recombination at short-wavelengths, overall reflection losses, and weak absorption or surface recombination close to the band gap.

Besides the  $I$ - $V$  characteristic, also the external quantum efficiency (EQE) is commonly used to describe the performance of a solar cell. The EQE is defined as the ratio of collected charge carriers to the number of incident photons and is therefore dependent on the energy of the photons.

$$\text{EQE} = \frac{N_e}{N_\nu} \quad 2.4.$$

Below the band gap of the solar cell, the EQE is zero (see Figure 2.2b). From the EQE, the spectrally dependent behavior of a solar cell can be analyzed by its product with the spectral irradiance  $\Phi$ .

$$J_{\text{sc}} = \frac{q}{hc} \int \text{EQE}(\lambda) \Phi(\lambda) d\lambda \quad 2.5.$$

### Maximum efficiency of a solar cell:

In order to derive the maximum obtainable efficiency of a photovoltaic device, various derivations have been published. The upper most limit is the thermodynamic limit, which simply derives from the Carnot heat engine:

$$\eta = 1 - \frac{T_{\text{cell}}}{T_{\text{sun}}}, \quad 2.6.$$

which leads to an efficiency limit of 95% when taking a solar cell at 300 K and the sun's temperature of 6000 K. Obviously, more realistic considerations have to account for the intrinsic properties of energy conversion in a solar cell. In this regard, Shockley and Queisser where the first in 1961, examining the amount of electrical energy that is extracted per photon of incoming sunlight [62]. Here, the maximum efficiency, which can be obtained by a photovoltaic device is derived with the principle of detailed balance and rely on the most basic physics only.

In their original form, the Shockley-Queisser (SQ) limit makes several fundamental assumptions. Similar to above, the sun and the solar cell are treated with their temperature and considered as black bodies, radiating at their specific temperature. It is assumed that all incident photons with an energy  $E=h\nu$  above the band gap  $E_g$  of the absorber will be (completely) absorbed. Moreover, the mobility of the charges is infinite, allowing to collect of carriers irrespective of their position of generation. Two scenarios are considered (see **Figure 2.3**): An absorber temperature of 0 K, which leads to the so called 'ultimate efficiency'; and an absorber temperature of 300 K, which gives the SQ limit. In the latter, radiation through the black-body radiation effect is considered via radiative recombination of electron-hole pairs. Considering the recombination of electron hole pairs, the maximum achievable efficiency recedes from  $\approx 44\%$  to  $\approx 34\%$ . In Figure 2.3, the ultimate efficiency is derived for the sun treated as a black-body radiating at 6000 K – for the SQ-limit, a more realistic spectrum (AM1.5G) is used. The AM1.5G spectrum is defined as the irradiance of the sun at  $41^\circ$  above the horizon, which corresponds to an air

mass of 1.5 atmospheres, onto a solar cell that is tilted by  $37^\circ$  from the horizontal. The total irradiance sums up to  $1000 \text{ Wm}^{-2}$ . In the original derivation, the SQ-limit accounted for a blackbody radiation of the sun at 6000 K instead of the AM1.5G spectrum – and is therefore slightly lower. This is due to the atmosphere absorption of photons with energies  $<1 \text{ eV}$ , simply reducing the overall heating of the solar cell.

In the SQ limit, due to the principle of detailed balancing and allowing for the recombination of electron-hole pairs, the efficiency is reduced compared to the ultimate efficiency. It is assumed that the recombination rate depends on the voltage  $V$  across the cell, but is constant irrespective of the illumination conditions. Thus, the rate, is proportional to  $\exp(V/V_c)$  times the blackbody radiation above the band-gap energy. In this regard,  $V_c$  is the thermal voltage. The efficiency defined by the SQ limit then depends on the ratio of open-circuit voltage  $V_{oc}$  to band-gap voltage  $V_g$ :

$$v = \frac{V_{oc}}{V_g}, \quad 2.7.$$

on the ultimate efficiency factor  $u$  as well as on the impedance matching factor  $m$ :

$$m = \frac{z_m^2/z_{oc}}{1 + z_m - \exp(-z_m)}, \quad z_m = \frac{V_{max}}{V_c}, \quad z_{oc} = z_m + \ln(1 + z_m), \quad 2.8.$$

whereas the  $m$  gives the ratio of power extracted and is therefore linked to the FF of the solar cell. In total, the SQ efficiency limit is simply the product of those quantities [62]

$$\eta_{SQ} = t_s \cdot u \cdot v \cdot m, \quad 2.9.$$

with  $t_s$  being the fraction of generated electron-hole pairs. It should be noted that  $u$ ,  $v$  and  $m$  depend particularly on the band gap of the absorber and on the above discussed quantities.

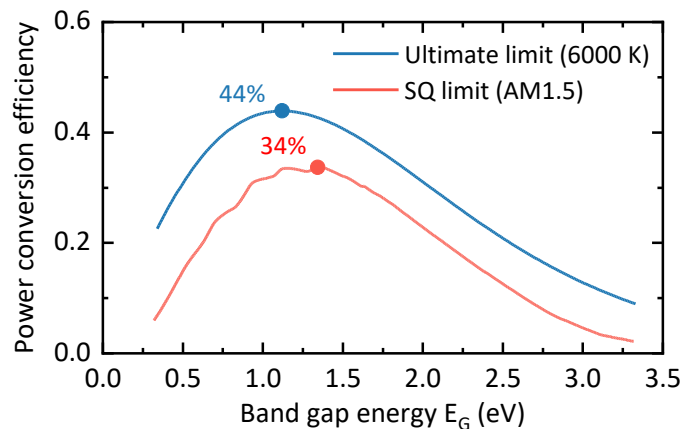


**Figure 2.3.** The Shockle-Queisser (SQ) limit for the maximum efficiency of a single-junction solar cell under unconcentrated sunlight at 300 K. The ultimate limit assumes the sun as black body with a temperature of 6000 K and the cell at 0 K. For the SQ limit, the more realistic AM1.5G spectrum is chosen and the solar cell temperature is 300 K.

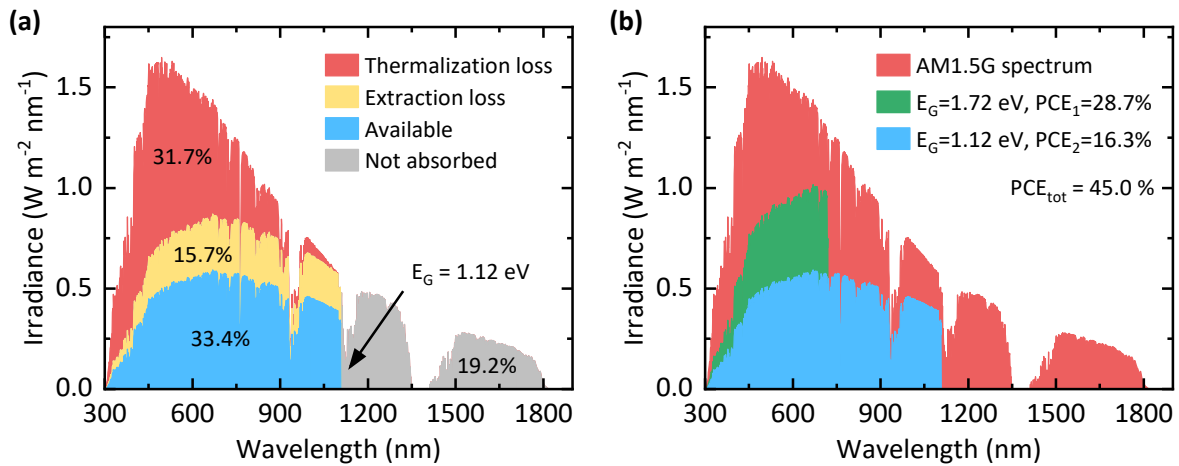


**Figure 2.4.** (a) AM1.5G irradiance spectrum with corresponding thermalization and extraction loss for a silicon solar cell (band gap  $E_G=1.12$  eV) within the principle of detailed balance by Shockley-Queisser. (b) Illustration of a perovskite ( $E_G = 1.72$  eV) and silicon ( $E_G=1.12$  eV) tandem solar cell. The model assumes an incident AM1.5G irradiation and is performed according to ref. [63].

The unavoidable extraction loss related to the detail balancing between the collection of carriers at a high electrical potential and collecting those carriers before they recombine is also illustrated as extraction loss in (Figure 2.4a). Here, the share of utilizable photons for an idealized silicon solar cell is depicted compared to the AM1.5G spectrum. Besides the fundamental radiative recombination, there are a number of other factors, which further reduce the theoretical power of a solar cell. In this regard, finite mobilities and non-radiative recombination will be the most dominant effects.

However, it is also possible to substantially exceed the proposed efficiency limit by Shockley and Queisser by various scenarios. The most interesting examples are the multi-junction or tandem solar cells, allowing the absorption of the sunlight by multiple absorbers. Therefore, the thermalization losses will reduce proportional to the number of absorbers and efficiencies of up to 42% (for two absorbers), 49% (for three absorbers), and 68% (for infinite absorbers) are theoretically examined [64]. For a tandem solar cell with a band gap of 1.12 eV (silicon) and 1.72 eV (perovskite), the share of useful spectrum is illustrated in Figure 2.4b. It should be noted that the illustrated data in Figure 2.4 is higher, since it is derived with the AM1.5G spectrum and not, as was done in ref. [64] with a blackbody radiation spectrum (see explanation above).

In addition to multi-junction PV, the concentration of sunlight – and therefore the intensity – makes it also possible to exceed the SQ limit. This increases the theoretical limit to  $\approx 40\%$  for only one absorber and to  $\approx 86\%$  for a multi-junction consisting of an infinite number of absorbers. Moreover, it is possible to upconvert low energy photons and re-emit them at higher energies (up-conversion), which theoretically leads to  $\approx 73\%$  [65]. Similar, the down-conversion of high energy photons could be used to reach  $\approx 40\%$  [66].

## 2.2 Light-matter interaction

Light propagation in matter can be described by the theory of electromagnetic fields [67,68], which is based on Maxwell's equations [69]. In this regard, the Maxwell equations describe how electric  $\mathbf{E}$  and magnetic fields  $\mathbf{H}$  interact with each other and with electric charges and electric current under given boundary conditions.

$$\nabla \cdot \mathbf{B}(\mathbf{r}, t) = 0 \quad 2.10.$$

$$\nabla \cdot \mathbf{D}(\mathbf{r}, t) = \rho(\mathbf{r}, t) \quad 2.11.$$

$$\nabla \times \mathbf{E}(\mathbf{r}, t) = -\frac{\partial \mathbf{B}(\mathbf{r}, t)}{\partial t} \quad 2.12.$$

$$\nabla \times \mathbf{H}(\mathbf{r}, t) = \mathbf{J}(\mathbf{r}, t) + \frac{\partial \mathbf{D}(\mathbf{r}, t)}{\partial t} \quad 2.13.$$

In this regard,  $\mathbf{D}$  is the dielectric displacement,  $\mathbf{B}$  the magnetic field flux density,  $\mathbf{J}$  the free electric current density and  $\rho$  the free charge density. Here,  $\mathbf{D}$  and  $\mathbf{B}$  include the material response on time-varying electric and magnetic fields, respectively. Since, the material response is described by a convolution in time domain, a transformation to frequency domain simplifies the relationship between  $\mathbf{D}$  and  $\mathbf{E}$ , as well as between  $\mathbf{H}$  and  $\mathbf{B}$ , which are then given by the constitutive relations:

$$\mathbf{D}(\mathbf{r}, \omega) = \epsilon_0 \mathbf{E}(\mathbf{r}, \omega) + \mathbf{P}(\mathbf{r}, \omega) = \epsilon_0 \epsilon_r(\mathbf{r}, \omega) \mathbf{E}(\mathbf{r}, \omega), \quad 2.14.$$

$$\mathbf{B}(\mathbf{r}, \omega) = \mu_0 \mathbf{H}(\mathbf{r}, \omega) + \mathbf{M}(\mathbf{r}, \omega) = \mu_0 \mu_r(\mathbf{r}, \omega) \mathbf{H}(\mathbf{r}, \omega), \quad 2.15.$$

where  $\mathbf{P}$  is the polarization,  $\mathbf{M}$  the magnetization,  $\epsilon_0$  is the vacuum permittivity,  $\epsilon_r$  is the dielectric function,  $\mu_0$  the vacuum permeability and  $\mu_r$  the relative permeability. For homogeneous, non-magnetic, isotropic materials with linear response to external fields, and no free charges, the Helmholtz wave equation(s) can be derived by the Maxwell equations:

$$\Delta \{\mathbf{E}, \mathbf{H}\}(\mathbf{r}, \omega) = -\frac{\omega^2}{c^2} \epsilon(\omega) \{\mathbf{E}, \mathbf{H}\}(\mathbf{r}, \omega). \quad 2.16.$$

The general solution of these wave equations are linear superpositions of plane waves:

$$\{\mathbf{E}, \mathbf{H}\}(\mathbf{r}, \omega) = \{\mathbf{E}_0, \mathbf{H}_0\}(\mathbf{k}, \omega) e^{i\mathbf{k} \cdot \mathbf{r}}, \quad 2.17.$$

where  $\mathbf{E}_0$  and  $\mathbf{H}_0$  are the corresponding amplitudes and  $\mathbf{k}$  denotes the wave vector, which is linked to the complex refractive index  $\tilde{n}$ .

$$k^2 = \frac{\omega^2}{c^2} \epsilon(\omega) \quad \rightarrow \quad k(\omega) = \frac{\omega}{c} \sqrt{\epsilon(\omega)} = \frac{\omega}{c} \tilde{n} \quad \text{with} \quad \tilde{n} = n(\omega) + ik(\omega), \quad 2.18.$$

where  $n$  indicates the phase velocity and  $\kappa$  denotes the extinction coefficient. For  $\kappa \neq 0$ , some part of the light when traveling through a medium will always be attenuated. The intensity  $I$  at a position  $z$  is described by the Lambert-Beer law:

$$I(z) = I_0 e^{-\alpha z} = I_0 e^{-\frac{2\kappa(\omega)\omega}{c}z}, \quad 2.19.$$

with  $\alpha$  defined as the absorption coefficient.

On incidence onto the interface between two media with complex refractive indices  $n_1$  and  $n_2$ , the plane wave can partially reflect, refract and transmit. Considering the plane wave propagating towards a planar interface with the wave vector  $\mathbf{k}_i$  under an angle  $\theta_i$  with respect to the face normal, the Snell's law is derived by considering that the parallel component of the wave vector  $\mathbf{k}_{||}$  is continuous.

$$\begin{aligned} k_{||,1} &= k_{||,2} \\ n_1 \sin \theta_i &= n_2 \sin \theta_t \end{aligned} \quad 2.20.$$

Since the reflected wave remains in the first medium with  $n_1$ , the reflected  $\theta_r$  and incident angle  $\theta_i$  are the same. Since the parallel component of the electric field  $E_{||}$  and the magnetic field  $H_{||}$  are continuous at the interface, as is the normal component of the dielectric displacement  $D_{\perp}$  and the magnetic field flux density  $B_{\perp}$ , the Fresnel equations can be derived:

$$\begin{aligned} r_s &= \frac{\tilde{n}_1 \cos \theta_i - \tilde{n}_2 \cos \theta_t}{\tilde{n}_1 \cos \theta_i + \tilde{n}_2 \cos \theta_t}, & t_s &= \frac{2\tilde{n}_1 \cos \theta_i}{\tilde{n}_1 \cos \theta_i + \tilde{n}_2 \cos \theta_t}, \\ r_p &= \frac{\tilde{n}_2 \cos \theta_i - \tilde{n}_1 \cos \theta_t}{\tilde{n}_2 \cos \theta_i + \tilde{n}_1 \cos \theta_t}, & t_p &= \frac{2\tilde{n}_1 \cos \theta_i}{\tilde{n}_2 \cos \theta_i + \tilde{n}_1 \cos \theta_t}, \end{aligned} \quad 2.21.$$

which describe the complex reflection and transmission coefficient of a perpendicular (s) and parallel (p) electromagnetic incident wave. The respective observable quantities – the reflectance  $R_{s,p}$  and transmittance  $T_{s,p}$  then given by:

$$\begin{aligned} R_{s,p} &= |r_{s,p}|^2, \\ T_{s,p} &= \Re \left( \frac{\tilde{n}_2 \cos \theta_t}{\tilde{n}_1 \cos \theta_i} \right) |t_{s,p}|^2. \end{aligned} \quad 2.22.$$

## 2.3 Limits of light management

The Yablonovitch limit is the thermodynamic limit of light trapping is expressed by the maximum path length enhancement inside an absorber [70]. This is reached by coupling light to all possible optical modes inside the absorber. In this regard, the entire phase space volume has to be filled by a scattering process (randomization) at the interface of the surrounding medium and the absorber. In case of vanishing absorption, a perfect randomization is achieved by Lambertian light trapping. For small absorptions,

deterministic light trapping has to be employed instead [34]. The maximum path length therefore derives to:

$$l_{\text{eff}} = 4n^2d \quad 2.23.$$

where  $n$  is the refractive index and  $d$  the thickness of the absorber. The factor  $n^2$  comes from the fact that the density of states in the absorber is  $n^2$  higher than in the surrounding air. In addition, detailed balancing of incident and escaping light brings a factor 2 due to the reduced outcoupling considering the escape cone. Another factor of 2 comes due to the assumption of one-sided illumination, where on the other side of the optical medium a white rear reflector is placed. By this, the number of escape channels for the light reduces by half and in turn increase the internal intensity by a factor of 2.

The equation was derived by Yablonovitch for a weakly absorbing material in the limit of geometrical (ray) optics when  $d \gg \lambda/2n$ , for an ergodic system and isotropic absorptance. Therefore, introducing angular selectivity by restricting the incident light within a light cone of half angle  $\theta_\Omega$ , the Yablonovitch limit adjusts according to Miñano [71] to:

$$l_{\text{eff}} = \frac{4n^2d}{\sin^2 \theta_{in}}. \quad 2.24.$$

This means that the light enhancement and therefore the light trapping can substantially exceed the  $4n^2$  limit. However, this comes along with the condition that the light trapping for other angles get worse. Even in the case of nanophotonic light trapping, the absorption enhancement factor remains valid for gratings with periods in the order of the wavelengths of the visible light [72]. Although, Yu *et al.* presented enhancements in the order of  $12 \times 4n^2$ , which is possible with a strong subwavelength-scale electric-field confinement, the thermodynamic limit reduces again to Equation 2.24 or 2.23 if the full phase-space (angles and wavelengths) are taken into account.



## **3 Methods**

This section describes the fundamentals on the optical simulations used in this work. In particular, raytracing, the finite element and the transfer matrix method are discussed. Moreover, the section provides details on the fabrication and replication of micro- and nanotextures as well as the characterization of solar cells.

### **3.1 Optical simulations**

Optical simulations are a powerful tool for advancing light management concepts in PV. Within this thesis, micro- and nanotextured layers have been numerically modelled to assess, predict and optimize their light management capabilities. Since, the adequate choice of methods depends mostly on the ratio of the wavelength of interest and dimension of the texture and simulation domain, different methods have been used. For large textures compared to the wavelength, the raytracing method describes the optical response accurately. In this regard, the light propagation is described by rays, which follow the Fermat's principle. For textures close or below the wavelength of the light, Maxwell's equations have to be solved rigorously by wave-optical methods. To simulate the propagation of light in three-dimensional domains with such small feature sizes, the finite difference time-domain method (FDTD) and the finite element method (FEM) have been used.

#### **3.1.1 Raytracing**

When light propagates through or inside objects whose dimensions are much larger than the wavelengths of the light, the wave nature of the light does appear and its behavior can be described by single rays. Those rays follow the Fermat's principle, which states that the optical lengths of the rays are minimum between two points of propagation. Therefore, the path of each ray through a homogenous media are straight lines. At an interface between two media of different refractive indices, rays can reflect and refract according to the Fresnel equations and Snell's Law. With raytracing, arbitrary geometrical shapes can be modeled by using a large number of rays impinging onto the texture of interest. The

rays therefore interact with the geometry and either reflect, refract, absorb and finally end up in a detector. The detector may either be a planar or spherical surface. The number of rays compared to the incident number of rays provides statistical information about the quantities like reflectance or transmittance. In addition, the angle of each ray can be tracked, which enables the description of the angular distribution of the reflected and transmitted light.

### 3.1.2 Finite difference time domain method

For textures with dimensions and features in the order or smaller than the wavelength of interest, the ray optics approximation is no longer valid. The problem must therefore be addressed with wave optics simulations. In this regard, the finite difference time domain (FDTD) method offers to solve the time-dependent Maxwell's equations for complex geometries. The idea of the FDTD method is to discretize the Maxwell's equations in a differential form, both, in time and space by the central difference approximation. This method was proposed by Yee [73]. The electric and magnetic fields are then calculated on the discrete values of the spacial grid and advanced in time.

The Yee method can be easily illustrated in one dimension. For this purpose, the propagation of a plane wave in the charge- and current-free space is assumed. Thus, the Ampère's law and Faraday's Law simplify to:

$$\begin{aligned}\partial_t E_x &= -\frac{1}{\epsilon_0} \partial_z H_y, \\ \partial_t H_y &= -\frac{1}{\mu_0} \partial_z E_x.\end{aligned}\tag{3.1}$$

Next, the derivatives are replaced by the central difference approximation:

$$\begin{aligned}\frac{E_x^{n+\frac{1}{2}}(k) - E_x^{n-\frac{1}{2}}(k)}{\Delta t} &= -\frac{1}{\epsilon_0} \cdot \frac{H_y^n(k + \frac{1}{2}) - H_y^n(k - \frac{1}{2})}{\Delta z}, \\ \frac{H_y^{n+\frac{1}{2}}(k + \frac{1}{2}) - H_y^{n-\frac{1}{2}}(k + \frac{1}{2})}{\Delta t} &= -\frac{1}{\mu_0} \cdot \frac{E_x^{n+\frac{1}{2}}(k + 1) - E_x^{n+\frac{1}{2}}(k)}{\Delta z}.\end{aligned}\tag{3.2}$$

To decouple the two equations, the electric and magnetic fields are shifted by half a Yee cell in space and time and updated by the leapfrog method [74]. Therefore, each field component is solved at a slightly different location within the Yee cell (see **Figure 3.1**). Firstly, the electric field at each location ( $k$ ) is calculated for the time step  $(n + \frac{1}{2})\Delta t$  from the electric field  $E_x^{n-\frac{1}{2}}(k)$  and the magnetic field at  $n\Delta t$ . Secondly, the magnetic fields  $H_y^{n+\frac{1}{2}}(k + \frac{1}{2})$  are calculated analogous. In this regard, all magnetic and therefore all electric fields are calculated for each time step.

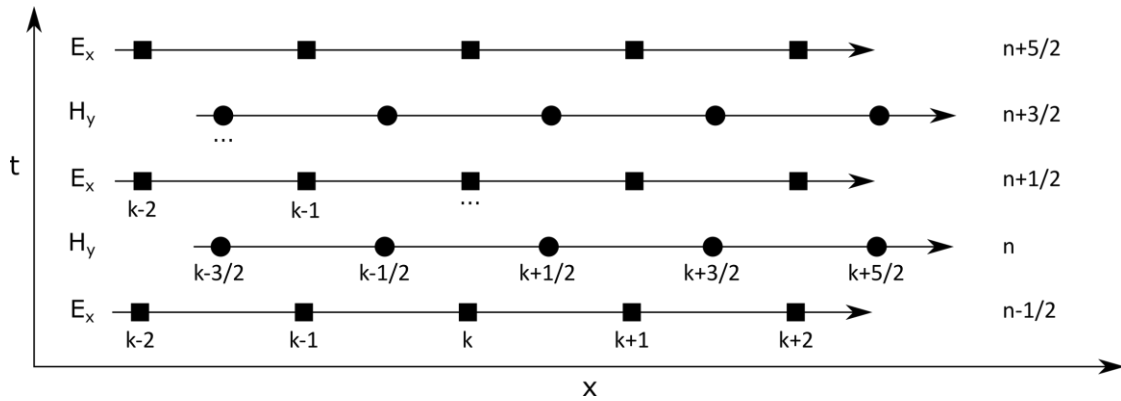


**Figure 3.1.** Illustration of the leapfrog method to calculate the E and H fields through both space (x) and time (t). Adapted from ref. [75].

Due to the time-marching nature of Yee's algorithm, electromagnetic waves physically propagate through the FDTD lattice in time steps of  $\Delta t$ . This iterative method is performed until a desired time step, when the change in the electric and magnetic fields are below a certain threshold.

### 3.1.3 Finite element method

Next to the FDTD method, the Maxwell's equations can be solved by the finite element method (FEM). The FEM provides a general approach to solve numerically a set of partial differential equations with certain boundary conditions. For electromagnetic problems, the FEM solves the Helmholtz equation either for the electric or magnetic field for arbitrary boundary conditions. A detailed description is beyond the scope of this thesis and can be found e.g. in ref. [76]. However, the basic structure of the FEM is outlined in the following.

The FEM is characterized by a variational formulation, a discretization strategy, a solution algorithm and a post processing procedure. First, the entire continuous domain is discretized by a finite number of small elements characterized by nodes and edges. In three dimensions, these small and finite elements are usually tetrahedrons or hexahedrons. This reduces the infinite number of degrees of freedom to a problem with a finite number of degrees of freedom. Subsequent, Ansatz functions with free parameters are defined to approximate the solution at each node. These functions also interpolate the solutions between the discrete values obtained at the mesh nodes. The physical problem therefore reduces to a finite set of functions and finite number of unknown parameters. Next, a system of algebraic equations is obtained by a variational formulation and a solution is obtained for the whole domain by solving this system of equations. From the field solution at the discrete nodes, all relevant quantities like the power flow or the absorbance are derived by a post-process.

It should be noted that this solution converges numerically towards the exact solution by either increasing the number of mesh points used for the discretization of the calculation domain or by increasing the polynomial order of the test function.

### 3.1.4 Transfer matrix method

The reflectance and transmittance at a single planar interface between two isotropic and homogenous dielectric materials is described by the Fresnel equations. However, for thin-film layer stacks with multiple parallel interfaces, the calculation elaborates, since partially reflected and transmitted light leads to interferences. The overall reflectance and transmittance are therefore an infinite sum of reflections and transmissions.

However, in such a multilayer dielectric stack with an infinite lateral extend and a finite extension in vertical (propagation) direction, the propagation of electromagnetic waves reduces to a one-dimensional problem. For this, the transfer matrix method (TMM) provides a simple formalism to calculate the light propagation [77]. According to the Maxwell's equations, there are continuity conditions for the electric field across the interfaces from one medium to the next. Therefore, if the field is known at the beginning of a layer, the field at the end of the layer can be derived from a simple matrix operation. A matrix  $\mathbf{T}$  can be assigned to the system, which relates the incident and reflected waves at one side of the multilayer stack to the incident and reflected wave at the other side of the stack.

Considering a multilayer stack with  $N$  layers with complex refractive indices  $\tilde{n}_i$  and  $N+1$  interfaces (see **Figure 3.2**), the transfer matrix  $\mathbf{T}$  can be derived as follows. For incoming waves from both sides of an interface  $m$ , the amplitudes of the outgoing waves  $E_{m+1}'^+$  and  $E_m^-$  are a superposition of the reflected wave in this medium and the transmitted wave from the next medium.

$$\begin{aligned} E_{m+1}'^+ &= E_m^+ t_{m,m+1} + E_{m+1}'^- r_{m+1,m} \\ E_m^- &= E_{m+1}'^- t_{m+1,m} + E_m^+ r_{m,m+1} \end{aligned} \quad 3.3.$$

The subscript defines the medium  $m$ , and the superscripts the direction + (left) and - (right) of the propagation. A prime indicates a wave at the right-hand side of an interface.

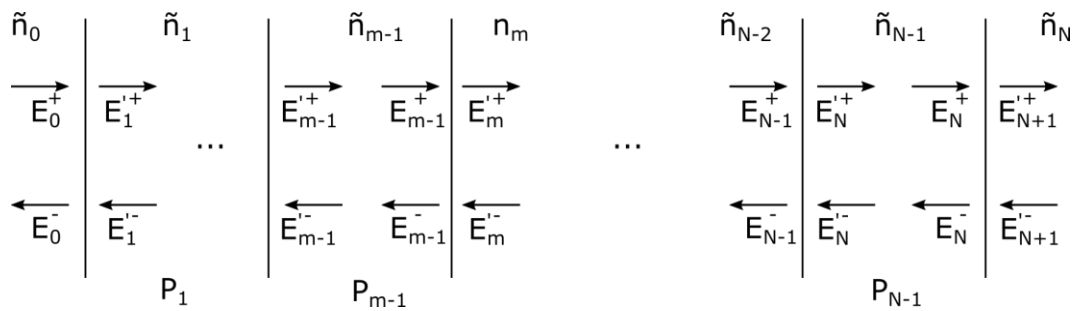


**Figure 3.2.** The schematic principle of the transfer matrix method for a multilayer system composed of  $N$  layers with complex refractive indices  $\tilde{n}_i$  with  $N+1$  interfaces. The electric field amplitudes  $E_i$  are defined before and after each interface. The subscript indicate the medium, the superscript the direction (+, right and -, left) of the wave, and the prime indicates waves on the right-hand side of an interface. The figure is adapted from ref. [77].

For the  $m$ -th interface, the field amplitudes on the left- and right-hand side of the interface are related by an interface matrix  $\mathbf{D}_{m-1,m}$ , which describes the reflection and transmission occurring at this interface.

$$\begin{pmatrix} E_{m-1}^+ \\ E_{m-1}^- \end{pmatrix} = \mathbf{D}_{m-1,m} \begin{pmatrix} E_m'^+ \\ E_m'^- \end{pmatrix} = \frac{1}{t_{m-1,m}} \begin{bmatrix} 1 & r_{m-1,m} \\ r_{m-1,m} & 1 \end{bmatrix} \begin{pmatrix} E_m'^+ \\ E_m'^- \end{pmatrix} \quad 3.4.$$

The  $t_{m-1,m}$  and  $r_{m-1,m}$  are the transmission and reflection Fresnel coefficients, respectively. Therefore, the interface matrix connects the amplitudes of the electric field directly before and after the interface  $m$ . The corresponding field amplitudes in the left- and the right-hand sides of the  $(m-1)$ -th layer are related by the propagation matrix  $\mathbf{P}_{m-1,m}$ .

$$\begin{pmatrix} E_{m-1}'^+ \\ E_{m-1}'^- \end{pmatrix} = \mathbf{P}_{m-1,m} \begin{pmatrix} E_{m-1}^+ \\ E_{m-1}^- \end{pmatrix} = \begin{bmatrix} \exp(i\delta_{m-1}) & 0 \\ 0 & \exp(-i\delta_{m-1}) \end{bmatrix} \begin{pmatrix} E_{m-1}^+ \\ E_{m-1}^- \end{pmatrix}, \quad 3.5.$$

Where  $\delta_m = 2\pi\tilde{n}_N d_N/\lambda$  is the phase accumulated by passing through the  $n$ -th layer. The above transformation for all  $N$  layers finally leads to a product of  $N+1$   $2 \times 2$  matrices. The iterative multiplication specifies the relationship between the amplitudes in the start and end media.

$$\begin{pmatrix} E_0^+ \\ E_0^- \end{pmatrix} = \mathbf{D}_{0,1} \left[ \prod_{m=1}^N \mathbf{P}_m \mathbf{D}_{m,m+1} \right] \begin{pmatrix} E_{N+1}^+ \\ E_{N+1}^- \end{pmatrix} = \mathbf{T} \begin{pmatrix} E_{N+1}^+ \\ E_{N+1}^- \end{pmatrix} \quad 3.6.$$

The product matrix  $\mathbf{T}$  refers to the system transfer matrix. Since there is no light source in the end medium, the backward running wave amplitude is zero ( $E_{N+1}^- = 0$ ). Assuming that the amplitude of the incoming wave is unity, the reflection and transmission coefficients of the entire stack can be expressed by the matrix elements of  $\mathbf{T}$ :

$$\begin{aligned} r &= \frac{E_0^-}{E_0^+} = \frac{T_{21}}{T_{11}}, \\ t &= \frac{E_{N+1}'^+}{E_0^+} = \frac{1}{T_{11}}. \end{aligned} \quad 3.7.$$

The overall reflectance  $R$  and transmittance  $T$  are then defined by the amplitude coefficients according to Fresnel's equations. Finally, the absorption  $A$  in the  $n$ -th layer is given by the subtraction of the time averaged Poynting vectors at the beginning and end of the two layers  $n$  and  $n+1$ .

$$A_n = \langle S_n \rangle_{\mathbf{T}} \mathbf{z} - \langle S_{n+1} \rangle_{\mathbf{T}} \mathbf{z} \quad 3.8.$$

## 3.2 Fabrication methods

In the following, different fabrication methods, which are used within this thesis are described. This includes mainly the transfer of textures via polydimethylsiloxane (PDMS) from a master template into a glass-like material. First, the fabrication of the different templates and the individual steps to replicate those are described. Next, the general approach to obtain those replicas of micro- and nanotextures is presented.

### 3.2.1 Master template fabrication and preparation

For this work, various micro- and nanotextures have been used as master mold. In terms of microtextures, micro-cones have been fabricated with direct laser writing (DLW). Moreover, biological surfaces from plant leaves and petals, which also show micron-scale textures have been used. In terms of nanotextures, different periodic gratings consisting of cylindrical pillars have been used. These nanotextures are processed by electron beam (e-beam) lithography. The corresponding method to fabricate the micro- and nanotextures is described in the following:

The **DLW** process enables to create freeform architectures on the nano- and micro-scale by a two-photon polymerization process. For the DLW process the commercial system Photonic Professional GT (Nanoscribe, Germany) is used. The micro-cones with 25  $\mu\text{m}$  diameter are written with the commercial resist IP-S (Nanoscribe). More details on the DLW process and how to fabricate micro-cones with different aspect ratios can be found in the work of Dottermusch *et al.* [78].

The **leaves and petals** are collected in nature and subsequently carefully cleaned with a nitrogen gun. The cleaned leaves are glued with double-sided tape on top of an aluminum plate. Then, a mold is fabricated (see below).

**E-beam lithography** is used to fabricate nanotextures (here: two-dimensional gratings of pillars). In the e-beam lithography, a focused beam of electrons is used for scanning and therefore writing a two-dimensional pattern in an electron-sensitive film. The electron beam locally changes the chemical composition of the resist, which enables the selective removal of either the exposed or non-exposed regions.

### 3.2.2 Replication of micro and nanotextures into substrates

In order to accurately transfer the microtextures and nanotextures down to 100 nm feature sizes, a mixture of 10:1 (weight ratio) Sylgard<sup>®</sup> Silicone Elastomer 184 and Sylgard<sup>®</sup> Curing Agent 184 was prepared. For the smaller nanotextures, a combination of a thin layer of hPDMS from GELEST<sup>®</sup> (PP2-RG07) and Sylgard<sup>®</sup> PDMS is used. In case of the larger textures, the PDMS is directly purred over the micro- and nanotextures (see **Figure 3.3b**).

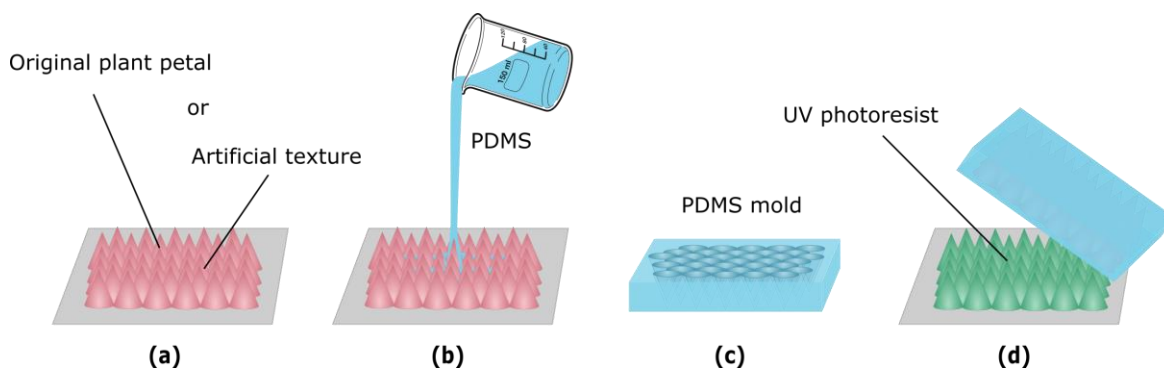


**Figure 3.3.** Replication of plant petal textures or artificially produced microtextures. (a) The original texture (plant petal, leaf or artificially fabricated texture) is glued on a rigid substrate. A box of aluminum foil is build around (not shown in the figure). (b) Then the PDMS is poured on the texture. (c) After demolding the cured PDMS from the original texture, a flexible PDMS mold is obtained. (d) The PDMS mold is used to replicate a UV photoresist on top of a substrate (e.g. glass or a solar cell).

For the replication of all textures (DLW microtextures and e-beam masters) as well as the biological surfaces (leaves and petals), the texture is carefully cleaned and fixed inside an edge-closed box consisting of aluminum foil with double-sided tape. The box of aluminum foil prevents the PDMS from flowing away, and enables the easy removal afterwards. Next, the PDMS is cured for  $\approx 1$  h at  $40^\circ\text{C}$  and subsequently for  $\approx 2$  h at  $60^\circ\text{C}$ . The hardened PDMS mold is separated from the original texture (see Figure 3.3c).

In case of the very small nanotextures, first, a thin hPDMS layer is spin coated (5000 rpm, 30s) on top of the nanotexture and subsequently prebaked at  $60^\circ\text{C}$  for 15 min. Finally, the PDMS from Sylgard<sup>®</sup> is poured on top, alike to the procedure above (see Figure 3.3b).

The obtained PDMS mold (see Figure 3.3c) is then used to replicate the texture onto a desired substrate (see Figure 3.3d). For the replication, the **photo nanoimprint lithography** is used. In the photo nanoimprint lithography, first, a photo (UV) curable liquid resist is applied onto a substrate (here: glass or solar cell). Secondly, the flexible PDMS mold is pressed on the substrate, enclosing the liquid resist. Thirdly, the resist is cured under UV exposure and becomes solid. After the mold separation, the (so obtained) inverse pattern is transferred into the resist onto the substrate material. This process is used for the glass-like photoresists: OrmoComp and OrmoStamp (microresist technology GmbH) as well as NOA88 (Norland Products Inc.). As UV source the Proma 140 017 UV exposure unit (60 W, 365 nm) is used. The OrmoComp and OrmoStamp cure within 5 min of exposure, the NOA88 needs  $\approx 8$  min.

### 3.2.3 Replication of nanotextures into the perovskite layer

For the replication of the nanotextures into the perovskite layer, a thermal nanoimprint lithography (TNIL) process is used. For the TNIL, robust stamps have to be fabricated. Therefore, two-dimensional gratings on top of glass substrates are fabricated with the process described above. In this regard, the PDMS is used to cast a flexible mold out of the

e-beam master templates (see **Figure 3.4a** and **b**). Further, an UV curable resist on top of a glass substrate is used. In this regard, a thin (1 – 10  $\mu\text{m}$  thin) OrmoStamp layer is spin coated on top of the glass substrate and subsequently patterned with a PDMS mold (see **Figure 3.4c**). In order to reduce the adhesion of the OrmoStamp mold in contact with the perovskite layer, a silanization with trichloro(1H,1H,2H,2H-perfluorooctyl)silane (PFOTS) is performed. The silanized stamps are then used to thermal nanoimprint the perovskite layers (see **Figure 3.4e** and **Figure 3.5a**).

The replication of nanotextured molds into the perovskite layers is performed with a vacuum hot embossing machine developed in-house in cooperation with Jenoptik Mikrotechnik [79]. The embossing machine consists of an upper fixed crossbar and the lower crossbar movable by a spindle drive (see **Figure 3.5a**). The lower and upper plates are heated and cooled via an oil heating and cooling unit. The operation window for samples up to 4-inch wafers, ranges from 0 kN to 290 kN and the maximum temperature is 190°C. The sample chamber is connected to a vacuum pump. For the imprinting, the glass substrate with the layers of the perovskite solar cell up to the perovskite, together with the mold is placed between the upper and lower planar plates. Perfect alignment of the plates is essential, to ensure a homogenous thermal nanoimprint. The periodic grating on the mold possess a height of  $\approx 200$  nm. The thermal nanoimprint is performed by hot pressing of the perovskite in contact with the textured mold (see **Figure 3.5a**). The process can be subdivided into three phases (see **Figure 3.5b**): (1) the heat up of the plates and sample, (2) the imprinting and (3) the cool down before the nanoimprinted perovskite layers can be released.

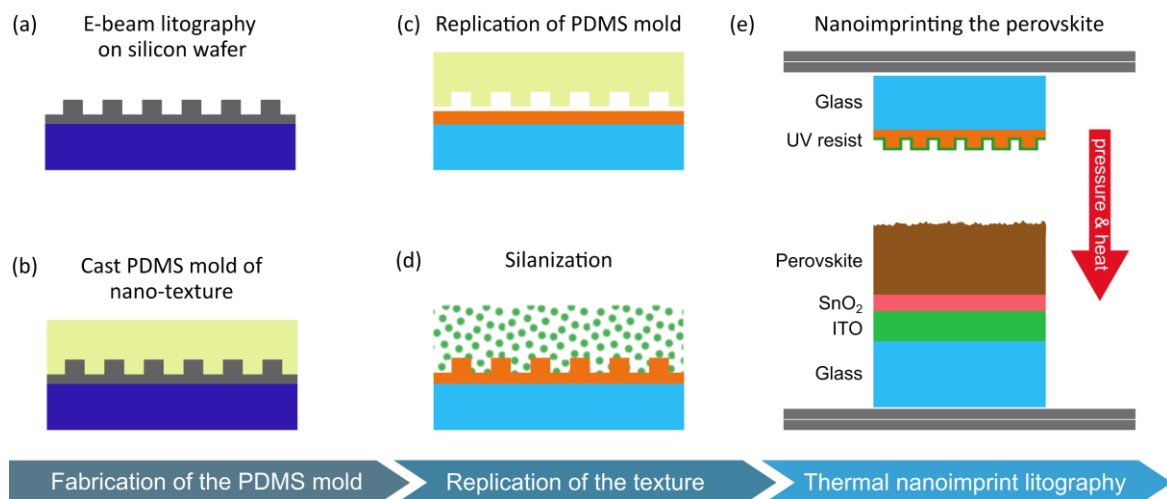


**Figure 3.4.** Schematic of the preparation of the mold for the thermal nanoimprint lithography (TNIL). (a) The periodic gratings are fabricated with electron-beam (e-beam) lithography. (b) PDMS is used to cast a flexible mold of the nanotextured silicon surface. (c) The nanotexture is replicated into a UV-curable resist. (d) To reduce the adhesion to the perovskite, a silanization with PFOTS is performed. (e) The OrmoStamp mold is used for the TNIL on the perovskite layer.

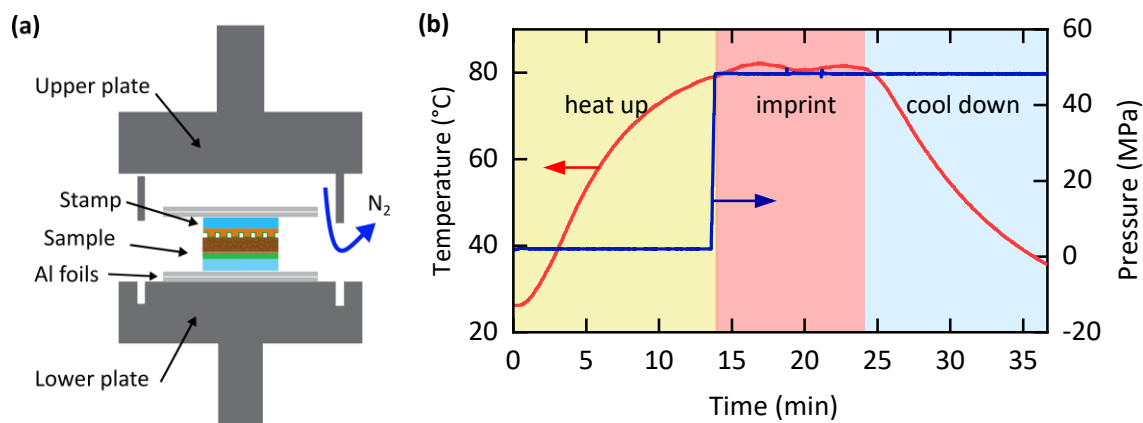


**Figure 3.5.** (a) Schematic illustration of the vacuum hot embossing process. The perovskite sample is placed on the lower plate. The stamp is in contact with the perovskite surface. Two sheets of aluminum foil are placed between the glass and the metal plates. (b) Process diagram of the hot pressing to nanoimprint the perovskite layers. During the heat up phase, the textured mold is in contact with the perovskite surface and the chamber is closed. The pressure is increased to  $\approx 50$  MPa once the two half-stacks reach the imprinting temperature of (here:  $\approx 80^\circ\text{C}$ ). After 5 min of applied pressure the cool down is initialized.

### 3.2.4 Perovskite solar cells

In this work, various silicon and perovskite solar cells as well as their combination in tandem solar cells are presented. Due to the rapid development in the field of perovskite PV and different collaborations, the perovskite solar cells presented in this thesis differ in their functional layers between the chapters. In the following, the preparation of the perovskite solar cell is described by its individual functional layers. However, the reader is kindly asked to refer to the respective - and at the given place also marked - coauthor publications for more details on the experimental fabrication parameters of the individual layers.

#### Electrodes

For the front electrodes pre-patterned indium tin oxide (ITO) substrates on glass (Luminescence Technology) were used. The **in-house front ITO** electrodes were sputtered (DC) using a Kurt J. Lesker PVD-75 thin film deposition system. The 4-inch target was purchased from Kurt J. Lesker. For the deposition of the 135 nm-thick ITO layers, the following parameters were used: base pressure =  $10^{-7}$  mTorr temperature =  $25^\circ\text{C}$ , deposition time = 2000 s, pressure = 0.8 mTorr, and O<sub>2</sub> partial flow = 2.5%. The samples were annealed for 30 min at  $200^\circ\text{C}$  in air on a hot plate that improved both the transmission and the conductivity. The 150 nm thick **in-house rear ITO** electrodes were sputtered with the following parameters: temperature =  $25^\circ\text{C}$ , deposition time = 2300 s, pressure = 0.8 mTorr, and O<sub>2</sub> partial flow = 2.5%. The substrates covered with ITO are finally cleaned in ultrasonic baths of deionized water, acetone and isopropyl alcohol for 10 min each. For the opaque devices a **gold** electrode is evaporated using a thermal evaporator (Vactec Coat 320).

### Electron transport layers

The tin oxide ( $\text{SnO}_2$ ) electron transport layer was spin-coated at a speed of 4000 rpm for 30 s. Therefore, a 15% aqueous colloidal dispersion of  $\text{SnO}_2$  (Alfa Aesar) is diluted to a final concentration of about 2%. The spin-coated  $\text{SnO}_2$  layer was then annealed in air at  $250^\circ\text{C}$  for 30 min.

### Hole transport layers

The hole transport layer **spiro-OMeTAD** (2,2',7,7'-tetrakis-(N,N-di-4-methoxyphenyl-amino)-9,9'-spirobifluorene) is spin-coated on top of the perovskite layers. Therefore, 80 mg/mL spiro-OMeTAD (Luminescence Technology) solution doped with 17.5  $\mu\text{L}$  of lithium bis-(trifluoromethanesulfonyl) imide (520 mg/mL in acetonitrile) and 28.5  $\mu\text{L}$  of 4-tert-butylpyridine was diluted in cyclohexanone (volume ratio 6:1) and spin-coated at 3000 rpm for 30 s in ambient atmosphere. Afterwards, the samples with the spiro-OMeTAD layer are oxidized in a drying cabinet at a relative humidity between 25% and 30% for about 12 h.

The nickel oxide ( $\text{NiO}_x$ ) hole-transport layers are sputtered using a Kurt J. Lesker PVD-75 thin film deposition system at 1 mTorr process pressure at 100 W under rf-conditions in combination with a NiO target (Kurt J. Lesker Company, 99,995% metallic purity). Argon is used as process gas. The base pressure in the chamber was  $<1 \cdot 10^{-7}$  mTorr before the deposition.

### Perovskite

The triple cation perovskite absorber solution  $\text{Cs}_{0.1}(\text{MA}_{0.17}\text{FA}_{0.83})_{0.9}\text{Pb}(\text{I}_{0.83}\text{Br}_{0.17})_3$  was prepared according to reference [80] with the precursors of methylammonium bromide (MABr, Greatcell Solar), formamidinium iodide (FAI, Dyesol), lead iodide ( $\text{PbI}_2$ , TCI), lead bromide ( $\text{PbBr}_2$ , TCI), and cesium iodide (CsI, Alfa Aesar). Two solutions were prepared: (1) CsI in DMSO (1.5M), and (2) FAI (1M),  $\text{PbI}_2$  (1.1M), MABr (0.2M), and  $\text{PbBr}_2$  (0.2M) in DMF:DMSO (volume ratio 4:1). An 88.9  $\mu\text{L}$  aliquot of solution 1 was transferred into solution 2 and then spin-coated by two following steps: (1) 1000 rpm for 10 s and (2) 6000 rpm for 20 s. 5-7s before the end of step (2) chlorobenzene (Sigma Aldrich), as anti-solvent, was released on the sample. The samples were annealed at  $100^\circ\text{C}$  for 1 h in nitrogen atmosphere.

### 3.3 Characterization of solar cells

This section provides an overview about different optical, electrical, surface and morphological characterization techniques of solar cells.

#### 3.3.1 Spectrophotometry

With the spectrophotometry a quantitative measurement of the reflectance and transmittance of a material (e.g. transparent thin film) as a function of the wavelengths is performed. In a spectrophotometer, light of a polychromatic light source is broken down into its spectral components by means of a monochromator. The diffracted light passes a mechanical slit and the remaining quasi-monochromatic light is then focused on the sample to be measured. Either the reflection at the sample surface or the transmission through the sample is determined by a suitable measuring arrangement. In this work, the spectrophotometry measurements are performed with the Lambda 1050 (PerkinElmer). Here, an integrating sphere is used to measure the total (or diffuse and specular) reflectance and transmittance of the sample. The interior of the integrating sphere is coated with a diffuse white reflective coating. As light source a deuterium and halogen lamp are used for the UV, visible and near-infrared spectrum. In order to detect the reflected or transmitted light a silicon and InGaAs photodiode are mounted at the bottom of the integrating sphere.

#### 3.3.2 Spectroscopic ellipsometry

The ellipsometry is an optical technique to investigate the dielectric properties of thin films. The method is non-invasive and non-destructive to the sample. The spectroscopic ellipsometry measures the relative change of the polarization of light reflected or transmitted by the thin film of interest for different wavelengths and angles. The exact change in polarization is related to the properties of the sample (thickness and refractive index). Usually, the sample is measured in reflectance, however the following explanation is true for transmission as well.

In principle, the ellipsometry uses the fact that linearly polarized light at an oblique angle of incidence to a surface changes its polarization when it is reflected. The light becomes elliptically polarized. The form of the ellipse is measured and related to the ellipsometric parameters  $\psi$  and  $\Delta$  for different wavelengths and angles of incidence. In this regard,  $\psi$  represents the amplitude ratio and  $\Delta$  the phase difference.

In order to derive the dielectric properties such as the complex refractive index of the thin-film sample, an optical model based on the Fresnel's equation (see TMM for multiple thin-film layers involved) is used to iteratively determine  $\psi$  and  $\Delta$ . Typically, the input for the Fresnel's equations is given by an oscillator-based modelling of the dielectric function.

In this regard, the parameters  $\psi$  and  $\Delta$  are linked to the ratio of the reflection coefficients of the parallel  $r_p$  and perpendicular  $r_s$  polarized light.

$$\rho = \frac{r_p}{r_s} = \tan(\Psi)e^{i\Delta} \quad 3.9.$$

The ellipsometry measurements are performed with the commercial system (VASE, from J. A. Woolam).

### 3.3.3 Scanning electron microscopy

The scanning electron microscopy is a technique to image the surface morphology of a sample by scanning the surface with a focused electron beam. In the scanning electron microscope (SEM), the focused ion beam generates secondary electrons emitted by the atoms of the first few atomic layers excited by the electron beam. The secondary ions are detected by the secondary ion detector. The brightness of the signal depends on the number of secondary electrons reaching the detector, which mainly depends on the texture of the sample. In addition, since heavy atoms typically backscatter electrons more strongly than lighter atoms, they appear also brighter in the image. The obtained image gives a three-dimensional impression; however, no height information is obtained. The SEM measurements are performed with a Supra 55P (Zeiss, Germany). The resolution is in the order of a few nanometers. In order to analyze microscopic samples, accelerating voltages of the electron gun are in the order of 10 kV, for the perovskite layers a voltage  $\approx 3$  kV is typically used to avoid degradation of the surface.

### 3.3.4 Atomic force microscopy

In order to analyze the surface roughness and topography of different substrates on a microscopy scale, the atomic force microscopy (AFM) is used. AFM is a common method and provides a wide range of different modes of operation [81]. As a scanning probe microscope, the AFM relies on a physical probe that is brought into the direct vicinity of the sample under investigation. By atomic forces between the atoms or molecules forming the sample surface and the probe, the deflection behavior of the probe can be observed. This is used to determine the structure of the sample at specific positions. By scanning a certain area of the sample, a three-dimensional image of the sample is obtained. The AFM measurements are performed with a JPK NanoWizard II (Bruker Nano GmbH), which operates in the intermittent mode [82]. Here, a cantilever, at the end of which a fine measuring tip, is set into oscillations close to its resonance frequency and scanned across the sample surface at a small distance. If the interaction between the measuring tip and the sample surface changes (e.g. due to material changes or height differences), this leads to a change in the resonance frequency, which can be measured optically via the reflection of a laser beam on the cantilever.

### 3.3.5 External quantum efficiency

The external quantum efficiency (EQE) gives the probability of an incident photon to be absorbed in the photoactive material and actually contribute to the extracted current. The EQE is typically measured wavelengths dependent for the relevant spectral range of absorption. From the EQE, the short-circuit current density ( $J_{sc}$ ) of a solar cell can be calculated by the multiplication with the air mass (AM) 1.5 global solar spectrum and the subsequent integration:

$$J_{sc} = \frac{q}{hc} \int \text{EQE}(\lambda) \cdot \text{AM1.5G}(\lambda) \cdot d\lambda, \quad 3.10.$$

where  $q$  is the elementary charge,  $h$  the Planck constant and  $c$  the speed of light. The reported EQE data is measured in a PVE300 EQE system (Bentham). The system consists of two lamps (xenon short arc and quartz halogen), which generate a broad spectrum. The light is passed through a monochromator and focused on the solar cell. The chopped light is detected with a lock-in amplifier. The EQE is a relative quantity that relates the measured current to the current of a reference cell with a known EQE. For the EQE of the perovskite solar cells, a silicon reference solar cell and for the perovskite/c-Si tandem measurements an additional germanium reference solar cell is used. The measurement of the wavelength-dependent EQE allows, in particular, precise information about the power generation of the solar cell as a function of the wavelength of the incident light.

### 3.3.6 Current density - voltage characteristics

The power conversion efficiency (PCE) of a solar cell is derived from the current density – voltage (J-V) characteristics. The J-V characteristics typically is measured under standard test conditions with a reference air mass (AM) 1.5 global solar spectrum and a temperature of 25°C. The J-V characteristics gives details about the multiple electrical properties of the solar cell. In this work, the measurement is performed in a single-lamp solar simulator of the company Newport (Oriel Sol3A) with a xenon lamp (Osram Licht AG). The intensity was calibrated with a KG5 filtered silicon reference solar cell to match the global standard AM1.5G spectrum. The solar cell sample temperature is controlled by an in-house sample holder, which is heated and cooled by a Peltier element. In order to consider the hysteresis effects in the perovskite solar cells, all perovskite solar cells are measured with the same scan rate of 600 mV·s<sup>-1</sup> in both backward and forward direction. To evaluate the long-term stability of the output power, the stabilized power output is additionally determined for at least 5 min using the maximum power point tracking method. The exact methodology is based on approaches from the literature [83].

### 3.3.7 Photoluminescence spectroscopy

The photoluminescence (PL) spectroscopy is a technique to characterize the optical and electronic properties of a sample, such as material imperfections and impurities. In PL spectroscopy, the material to be examined is brought into an electronically excited energy state by light absorption. Subsequently, the lower energy state is reached again by emitting light by spontaneous photon emission in the form of fluorescence or phosphorescence. The emitted light is detected and provides information about the electronic structure of the material. This is due to the reason that after the photo-excitation the excess energy leads to radiative and or nonradiative processes. Depending on the material, these free charge carriers recombine as electron-hole pairs, the so-called excitons, or fall into deeper states and recombine from there. Moreover, the recombination at defects show characteristic lifetimes, which are possible to measure in time-resolved photoluminescence (TRPL) measurements.

### 3.3.8 X-ray diffraction

In order to analyze the crystallographic properties of a thin-film, the X-ray diffraction (XRD) measurement is used. The principle of the XRD measurement relies on the fact that atoms (crystal planes) scatter X-ray waves. Therefore, crystals with a regular array of atoms lead to constructive and destructive interference according to Bragg's law:

$$2 d \sin \theta = n\lambda, \quad 3.11.$$

where  $d$  is the spacing between the diffracting planes of the crystal,  $\theta$  the incident angle,  $n$  is an integer giving the diffraction order, and  $\lambda$  the wavelengths of the X-rays. An unknown material can then be classified by the characteristic position of the resulting diffraction peaks. The XRD diffractogram is measured with a D2 PHASER (Bruker). In order to measure the distinct X-ray diffraction pattern of a sample, the position of the X-ray source (Cu  $K\alpha$  radiation) is fixed and the detector as well as the sample are tilted by  $\theta$  and  $2\theta$ , respectively. This has the advantage that the focus on the sample is always maintained.

## 4 Methodology of energy yield modelling

This section describes the methodology of energy yield modelling. The energy yield provides an accurate figure of merit for the realistic outdoor performance of solar modules. In the following, the developed energy yield simulation platform is presented. Furthermore, distinct aspects of the energy yield framework are discussed by exemplary studies.

### Acknowledgements and contributions

*This section covers the methodology of energy yield modelling, published in reference [84]. This publication was a joint project of the shared first authors Raphael Schmager, who wrote the section on the electrical modelling and composed the energy yield calculations and the demonstration of the simulation framework; and Malte Langenhorst, who compiled the parts on the realistic irradiation and optical modelling of the perovskite/c-Si tandem solar modules. The full methodology of energy yield modelling was developed by Ulrich W. Paetzold, Malte Langenhorst, Raphael Schmager and Jonathan Lehr and led to a close collaboration with the industrial partner OxfordPV. The code development of the energy yield platform was subdivided in individual modules: the irradiance module (developed by Ulrich W. Paetzold and improved by Malte Langenhorst and Raphael Schmager), the electric module (developed by Jonathan Lehr and improved by Raphael Schmager), the optics module (developed by Malte Langenhorst) and the energy yield core module (developed by Raphael Schmager). The present simulation platform on energy yield modelling have already led to multiple publications from our group in the field of perovskite-based tandem photovoltaic [85–88].*

## 4.1 Introduction

To describe and compare the device performance of photovoltaic modules, typically the power conversion efficiency (PCE) under standard test conditions (STC) is reported as the key figure of merit. However, the PCE determined under STC does not represent the realistic performance of solar modules well. This stems from the fact that the STCs define the solar cell performance for a standard global reference irradiance spectrum of  $1000 \text{ Wm}^{-2}$  with an air mass of 1.5 (AM1.5G), the light impinging the solar cell under normal incidence, and a constant solar cell temperature of  $25^\circ\text{C}$ . However, these conditions are never found in real world applications. Under realistic operating conditions, the temperature, spectral distribution – the share of specular and diffuse solar irradiation, absolute insolation, cloud cover and the normal movement of the sun usually change over the course of each day. To take all these effects into account, the energy yield (EY) of solar modules must be determined. The EY is by far the superior measure of comparison. The annual EY of a solar module provides the total energy per area obtained by a solar cell or module under consideration over the span of one year. Therefore, EY modeling offers a more accurate measure for comparing, evaluating and predicting the performance of solar modules under realistic outdoor conditions. In addition, the evaluation of a large number of influencing factors, such as the evaluation of different lighting management concepts, and the assessment of different architectures becomes possible. In this regard, EY modelling has already widely been used to optimize and predict improvements in single-junction PV [89–95], concentrator PV [96–101] and III-V/Si multi-junction PV [102–105].

In line with these studies, and to develop a common and comprehensive framework for EY modelling, this work enables the EY modelling framework for the newly emerging perovskite-based tandem architectures. In particular, textured perovskite/c-Si tandem modules should be mentioned here. Recently, numerous studies have been published discussing various correlations between outdoor conditions and optimum device parameters of perovskite/CIGS [88], perovskite/Si [23,86,106–110] and perovskite/perovskite tandem PV [111]. In particular, for multi-junction PV, the absorber thicknesses can differ significantly by up to 30%, when optimizing the architecture for annual EY rather than PCE under STC [86,88]. Moreover, a current focus is on the evaluation of bifacial perovskite-based tandem PV. [85,112]. In addition, the influence of the incident irradiation, which varies in intensity and spectral distribution over the day and year on different electrical interconnection schemes could be analyzed. Particularly, the current matching losses in two-terminal (2T) architecture compared to electrically more advanced three-terminal (3T) and optically lossier four-terminal (4T) architectures should be mentioned here.

In this chapter, the framework of EY modelling developed in the group of U. W. Paetzold is presented. This framework offers the possibility to simulate complex – textured and planar, monofacial and bifacial – architectures of single- and multi-junction PV

including all perovskite-based tandems and other tandem architectures. Especially, for the intensively investigated complex architectures of textured perovskite-based tandem solar modules, EY modelling is essential to predict realistic power outputs and annual yields. The EY modelling is able to predict the realistic performance from the above-mentioned variety of tandems with different architectures and electrical wiring concepts for various geographical locations. Besides, it offers the possibility to determine the EY for any module orientation and is able to evaluate various one- and two-axis tracking methods of the sun.

In the following, the framework is presented along the lines of the different modules. Due to the fact that the simulation framework is in constant further development, the fundamental functionalities are discussed here. For the latest developments, the reader is referred to the references provided at the appropriate place.

## 4.2 The framework for energy yield modelling

The most important figure-of-merit to evaluate and compare multi-junction solar modules is the annual EY, which gives the total accumulated energy produced by the solar module under realistic operation (and irradiation) conditions during one year. In the following, the framework for EY modelling is presented. The framework accounts for various realistic operation conditions: specular and diffusive irradiation, cloud cover, albedo, temperature variations, and the module orientation (see **Figure 4.1**).

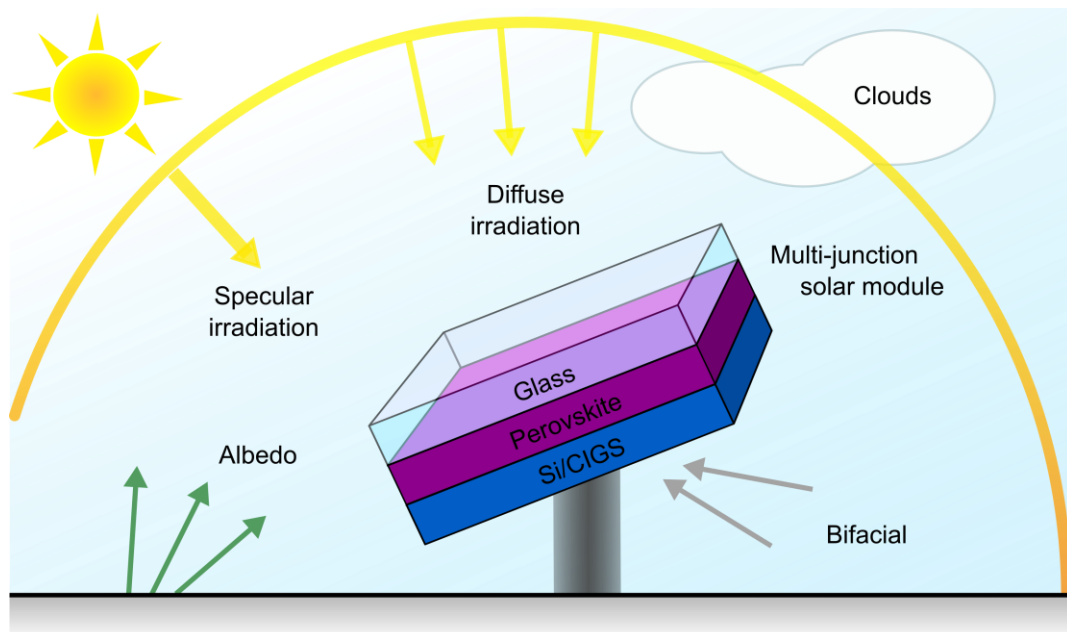


**Figure 4.1.** Schematic of energy yield modelling of multi-junction solar modules. The power generation of tilted multi-junction solar module varies with the sun's specular and diffuse irradiance, which depends to the location, time, orientation and the cloud cover. For different architectures (monofacial or bifacial), module installations angles, and ground reflectanceses (albedo), additional contributions of incident light to the generated current needs to be considered. Adapted with permission from ref. [84], © 2019 Optical Society of America.

The framework further is able to simulate complex – textured and planar, monofacial and bifacial – architectures of single- and multi-junction PV including all perovskite-based tandems and other tandem architectures in two-, three-, and four-terminal configuration.

The EY modelling is based on four independent – but interconnected – software modules (see below), which are linked by their in- and output parameters (see **Figure 4.2**). The main idea is to obtain the total power of a defined solar cell architecture by its optical and electrical response. The power is calculated on an hourly basis throughout the whole year accounting for (i) a realistic hourly and spectrally resolved irradiation of a broad range of locations in the USA, (ii) the optical and (iii) the electrical response of the absorber(s) in the (tandem) solar module.

In this regard, the irradiance module calculates the spectral and angular resolved irradiance over the course of one year with a temporal resolution of one hour. The irradiance data is calculated with the use of the atmospheric radiative transfer of sunshine (SMARTS) model [113], fed by the typical meteorological year (TMY3) data [114]. To account for the cloud cover provided by the TMY3 data, a simple cloud model is applied (see below). The optics module rapidly calculates the spectrally and angular resolved absorptance of the defined tandem architecture. Due to the different scales in textured perovskite/c-Si tandem modules, it is able to handle multiple interconnected planar and textured interfaces with coherent and incoherent light propagation by combining transfer matrix method (TMM), series expansion of Beer-Lambert law and geometrical raytracing.

The energy yield core module calculates the EY over the course of one year depending on the tandem orientation and location. The orientation can be either defined by a fixed tilt and rotation angle or by various one or two-axis tracking algorithms. Therefore, the core module calculates the power output on an hourly basis by combining the spectral and angular resolved solar irradiation (optionally accounting for various albedo or bifaciality), the spectral and angular resolved absorptance of the tandem solar module and the electrical properties provided by the electrical module.

The electric module calculates the temperature-dependent current density – voltage characteristics ( $J$ - $V$ ) for given short-circuit current densities. Hereby, the electrical calculations are based on the one-diode model, accounting for series and shunt resistance in the sub-cells, forming either a 2T or 4T tandem solar module. The electrical module determines for each hour of the year the maximum power (MPP) point of the tandem (or of each sub-) solar cell(s). In case of the 3T interconnection,  $J$ - $V$  characteristics is simulated numerically (see below).

This enables the EY framework to identify trends for specific architectures via the analysis of light-trapping concepts or the evaluation of the electric interconnection schemes, thus providing design rules for device properties (e.g. layer thicknesses, optimum band gaps) or the optimal tilt for various locations. In the following, the individual modules are described in more detail.

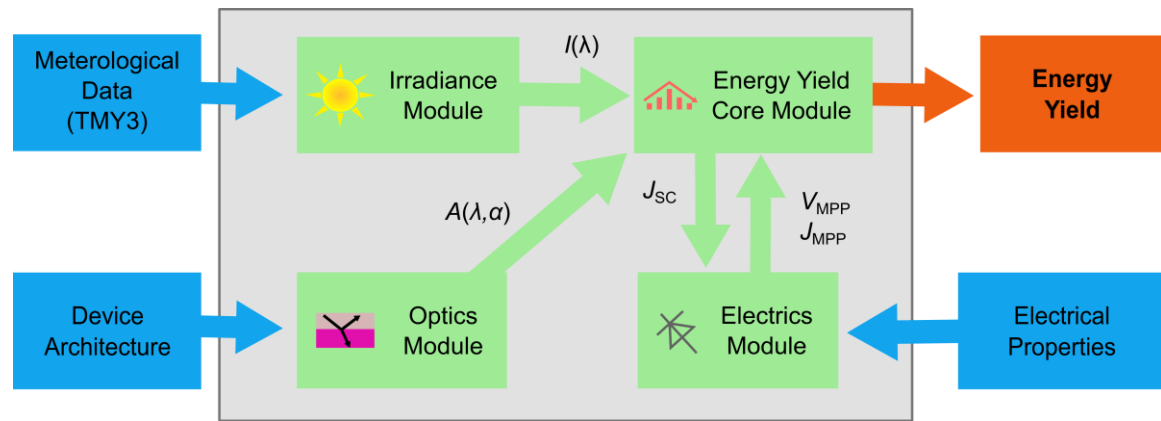


**Figure 4.2.** Schematic flow of the modular EY modelling. The irradiance module computes the spectral irradiance  $I$ , the optics module the absorptance  $A$ , and the energy yield module calculates the short-circuit current density  $J_{sc}$  and EY with the help of the electrics module. Adapted with permission from ref. [84], © 2019 Optical Society of America.

### 4.3 Irradiance module for realistic irradiation conditions

The irradiance module calculates the spectral and angular-resolved irradiance over the course of one year with a temporal resolution of one hour by applying SMARTS code [113] to TMY3 data [114] of locations in various climatic zones. The calculations are followed by the application of a simple cloud model to account for cloud cover such that realistic direct and diffuse irradiance are derived.

Realistic irradiation data is essential to determine the annual EY of any single or multi-junction PV device. For the assessment of different climatic regions, the TMY3 data sets are used, which are available from the National Renewable Energy Laboratory (NREL) [114]. The TMY3 data sets contain statistically representative hourly resolved meteorological and irradiation data of many ( $\approx 1000$ ) locations distributed over the USA. The different locations represent the four most relevant climatic zones according to the Köppen climate classification [115,116]: temperate, boreal, arid and tropical. Whereas hot and sunny regions belong to the tropical and arid - temperate and boreal account for cold and damp climatic regions.

The atmospheric data provide properties such as the pressure, precipitable water, optical depth of the aerosol, dry-bulb temperature, albedo, and the cloud cover of the sky. With this atmospheric information, the position of the sun and the irradiance, first the spectrally resolved (280 nm - 4000 nm) clear sky irradiance is calculated with the SMARTS code [113] for each hour of the representative year utilizing Shettle and Fenn's urban aerosol model and the US standard reference atmosphere [117].

Next, a simple cloud model accounts for the cloud cover  $CC$  as the ratio of covered sky. For this, it is assumed that the direct irradiation is not spectrally changed. Thereby, the direct irradiation is defined by the spectrally resolved clear sky irradiance, which is then scaled by the TMY3 measured absolute irradiance:

$$I_{\text{clouds,dir}}(\lambda) = \frac{I_{\text{clear,dir}}(\lambda)}{\int I_{\text{clear,dir}}(\lambda) d\lambda} I_{\text{meas,dir}} \quad 4.1.$$

In contrast to the direct irradiance, the spectral distribution changes for the diffuse irradiation depended on the amount of CC on the sky. Therefore, it is assumed that the light radiated by the clouds account for both spectral distribution of the diffuse and direct clear sky irradiance. However, the absolute intensity is scaled by the measured diffuse irradiance reported in the TMY3 data:

$$I_{\text{clouds,diff}}(\lambda) = \frac{I_{\text{clear,diff}}(\lambda) \cdot (1 - \text{CC}) + I_{\text{clear,dir}}(\lambda) \cdot \text{CC}}{\int (I_{\text{clear,diff}}(\lambda) \cdot (1 - \text{CC}) + I_{\text{clear,dir}}(\lambda) \cdot \text{CC}) d\lambda} I_{\text{meas,diff}} \quad 4.2.$$

The spectrally resolved direct and diffuse irradiation obtained with this simplified cloud model is illustrated in **Figure 4.3a** for a monthly average in Phoenix (Arizona, USA). For both, June and December, the direct irradiance exceeds the diffuse irradiance, which is a natural consequence of the meteorological conditions during those months of the year on the northern hemisphere. In addition, the diffuse part shows a strong blue shift compared to the direct irradiance, due to the strong wavelength dependence of Rayleigh scattering ( $\sim \lambda^{-4}$ ). This blue shift is well represented by the average photon energy (APE) of the irradiance spectrum. It is also visible on the timescale of one day (e.g. November 19<sup>th</sup>) as illustrated in Figure 4.3b.

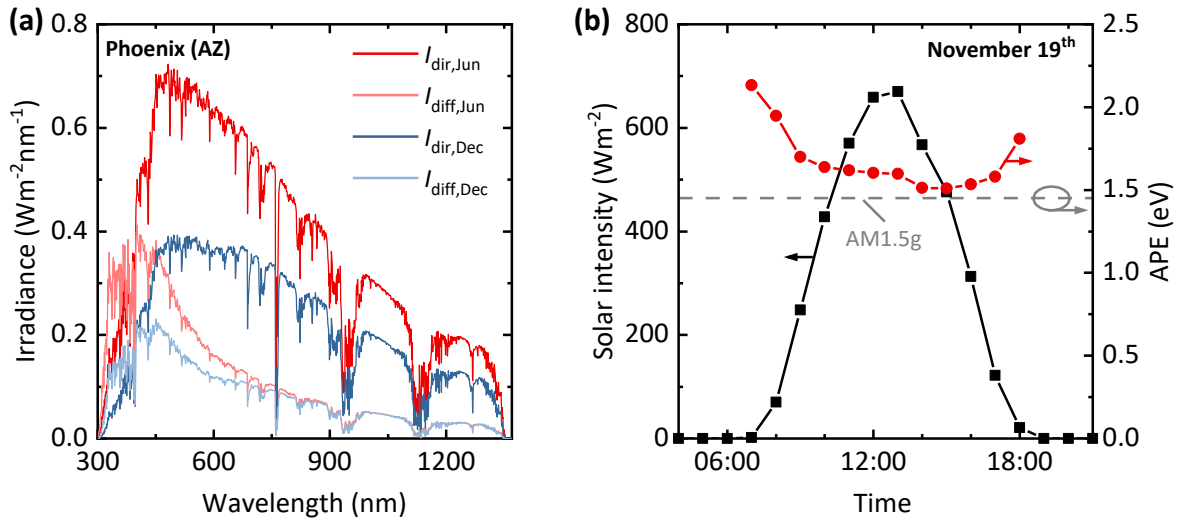


**Figure 4.3.** (a) Monthly average spectral irradiance of Phoenix (Arizona, USA) during June and December broken down into direct and diffuse portions. (b) Hourly resolved overall intensity of direct and diffuse irradiance and the average photon energy (APE) in November 19<sup>th</sup> in Phoenix (Arizona, USA). Adapted with permission from ref. [84], © 2019 Optical Society of America.

Compared to the APE of the global standard spectrum (AM1.5g), the APE of the modeled spectrum is blue shifted in the morning and evening when the total irradiance is mainly dominated by the diffuse share [88,108]. Moreover, as predicted by this simplified cloud model, the APE shifts blue for decreasing cloud cover (see Equation 4.2), which is in

accordance to Bartlett *et al.* [118]. Therefore, the APE of a realistic irradiation spectrum deviates almost for every hour of the day over the course of the year from the AM1.5g, which highlights the fact of the importance to consider realistic irradiation conditions to calculate the realistic performance of solar modules. It should be noted that the suggested cloud model is (still) very simplified. This is due to the fact that the modelling of radiative transfer of clouds is a complex subject [119] and there is yet no unified and comprehensive radiative transfer model for clouds [120], since optical properties of clouds strongly depend on their size, shape and composition [121]. Nevertheless, the variation of the incident irradiance mimics realistic operating conditions due to the constantly changing angle of incidence and cloud cover (fluctuating irradiances and spectral variations). Although the simple cloud model is very rudimentary, it provides realistic spectral irradiances.

#### 4.4 Optics module: modelling of multi-junction solar cells

The optics module calculates the spectrally and angular-resolved absorptance of the non-simplified architecture of tandem solar modules. The optical modelling of state-of-the-art single-junction and multi-junction solar modules has to account for various feature sizes: (i) multi-layer thin-film stacks, (ii) optically thick layers, and (iii) microtextured interfaces. Therefore, the optics module handles multiple planar and textured interfaces with coherent and incoherent light propagation by combining TMM, series expansion of Beer-Lambert law and geometrical raytracing.

To cope with the combination of the different scales and optical methods, the architecture is broken down to smaller domains (see **Figure 4.4a**), which are separately simulated using the adequate method (see below). Once, each domain is calculated, the optical response of the full architecture is calculated via redistribution matrices analogous to Eisenlohr *et al.* [122]. This formalism is extended by considering microtextures covered by thin-films, which are treated in the following as effective interfaces (see right part of Figure 4.4a). For a more detailed mathematical description the author is referred to the work of M. Langenhorst [123]. However, to give an insight into the working principle, the basic structure is outlined below and the three different methods are described briefly.

i. **Multi-layer thin-film stacks:** To treat thin-film PV technologies like III-V, CIGS, and perovskite, a coherent treatment of light propagation is needed. The coherent treatment of the absorption  $A_{\text{coh}}$  in the thin-films is calculated with the TMM. The TMM implemented in the EY framework is inspired by previous work of by S. J. Byrnes [124], the fundamental method is described in section 3.1.4).

ii. **Optically thick layers:** If the layer thickness is large compared to the coherence lengths of the incident light, the coherent assumption breaks down. For these optically

thick layers, light propagation needs to be treated incoherently. In this regard, the Beer-Lambert law described the incoherent absorption  $A_{\text{incoh}}$  of optically thick layers very well:

$$A_{\text{incoh}}(\lambda) = \begin{pmatrix} e^{-\alpha(\lambda) \cdot d/\cos(\theta_1)} & \dots & 0 \\ \vdots & \ddots & \vdots \\ 0 & \dots & e^{-\alpha(\lambda) \cdot d/\cos(\theta_n)} \end{pmatrix}. \quad 4.3.$$

Here,  $\alpha$  is the absorption coefficient,  $d$  the thickness of the incoherent layer, and  $\theta_n$  is the angle of light propagation inside the medium.

iii. **Microtextured interfaces:** For non-planar interfaces, geometrical raytracing as described by Baker-Finch and McIntosh [125] is used. The geometrical raytracing is an elegant method for rapid calculations of the impact of microtextures (e.g. pyramidal textures as found on alkaline-etched c-Si wafers) on an interface for all angles of incidence  $\theta_{\text{in}}$ . For pyramidal microtextures, the high symmetry allows only for a limited set of characteristic paths with specific intersection angles  $\theta_{\text{intersect}}$  at the facets of the pyramids (see Figure 4.4b) are possible. Compared to rigorous raytracing or wave-optical finite element methods (see section 3.1.2), the geometrical raytracing method provides a rapid calculation. However, for efficient modelling, the geometrical raytracing restricts the applicable textures to pre-calculated or pre-simulated textures of certain symmetry and limited characteristic paths.

For the energy yield framework, the characteristic paths of *regular upright*, *random upright* and *inverted* pyramids of typical etched c-Si surfaces have been extracted from the optical simulator OPAL 2 [126,127]. The optical response ( $R$ ,  $T$  and  $A$ ) of other non-pyramidal textures, textures with different aspect ratios (see Chapter 5), and any other effective interfaces must be calculated precisely by raytracing. In this regard, cones, inverted cones, pyramids and inverted pyramids have been simulated for a wide range of aspect ratios by raytracing. The pre-simulated optical response of those textures is available as input data in the simulation platform. Since the iterative summation of absorption follows a generic principle, more exotic textures can be implemented as well.

For textured c-Si solar cells covered with a thin-film layer stack, the total absorption  $A_{\text{path},i}$  along the path  $i$  is then given by:

$$A_{\text{path},i}(\lambda, \theta_{\text{in}}) = A_{\text{coh}}(\lambda, \theta_{\text{intersect},1}) + \sum_{j=2}^{j_{\text{max}}} \prod_{k=1}^{j-1} R_{\text{coh}}(\lambda, \theta_{\text{intersect},k}) \cdot A_{\text{coh}}(\lambda, \theta_{\text{intersect},j}). \quad 4.4.$$

Here,  $R_{\text{coh}}$  is the reflectance of the thin-film stack obtained from TMM calculations, and  $j$  is the index of facets hit by light along the path  $i$ . The total absorptance of this thin-film covered texture  $A_{\text{tex/coh}}$  is then determined by summation over the absorption of all characteristic paths and their individual probabilities  $P_{\text{path},i}$ :

$$A_{\text{tex/coh}}(\lambda, \theta_{\text{in}}) = \sum_i P_{\text{path},i}(\theta_{\text{in}}) \cdot A_{\text{path},i}(\lambda, \theta_{\text{in}}). \quad 4.5.$$

For the total reflectance  $R$  and transmittance  $T$ , similar equations can be derived. Moreover, for each wavelength,  $R$  and  $T$  can be expressed by redistribution matrices describing the interaction of light at an effective interface:

$$\{R, T\}(\lambda) = \begin{pmatrix} \{R, T\}(\lambda, \theta_1 \rightarrow \theta_1) & \cdots & \{R, T\}(\lambda, \theta_n \rightarrow \theta_1) \\ \vdots & \ddots & \vdots \\ \{R, T\}(\lambda, \theta_1 \rightarrow \theta_n) & \cdots & \{R, T\}(\lambda, \theta_n \rightarrow \theta_n) \end{pmatrix}. \quad 4.6.$$

At those effective interfaces, the incident light will be either reflected, transmitted or absorbed. Therefore, the following condition has to be fulfilled:

$$\sum_{\theta_{\text{ref}}} R(\lambda, \theta_{\text{in}} \rightarrow \theta_{\text{ref}}) + \sum_{\theta_{\text{trans}}} T(\lambda, \theta_{\text{in}} \rightarrow \theta_{\text{trans}}) + \sum_{\theta_{\text{ref}}} A_{\text{coh}}^{\text{tex}}(\lambda, \theta_{\text{in}}) = 1, \quad 4.7.$$

where  $\theta_{\text{in}}$  is the angle of incident,  $\theta_{\text{ref}}$  is the angle of back reflected light, and  $\theta_{\text{trans}}$  is the angle of transmitted light (see Figure 4.4a).

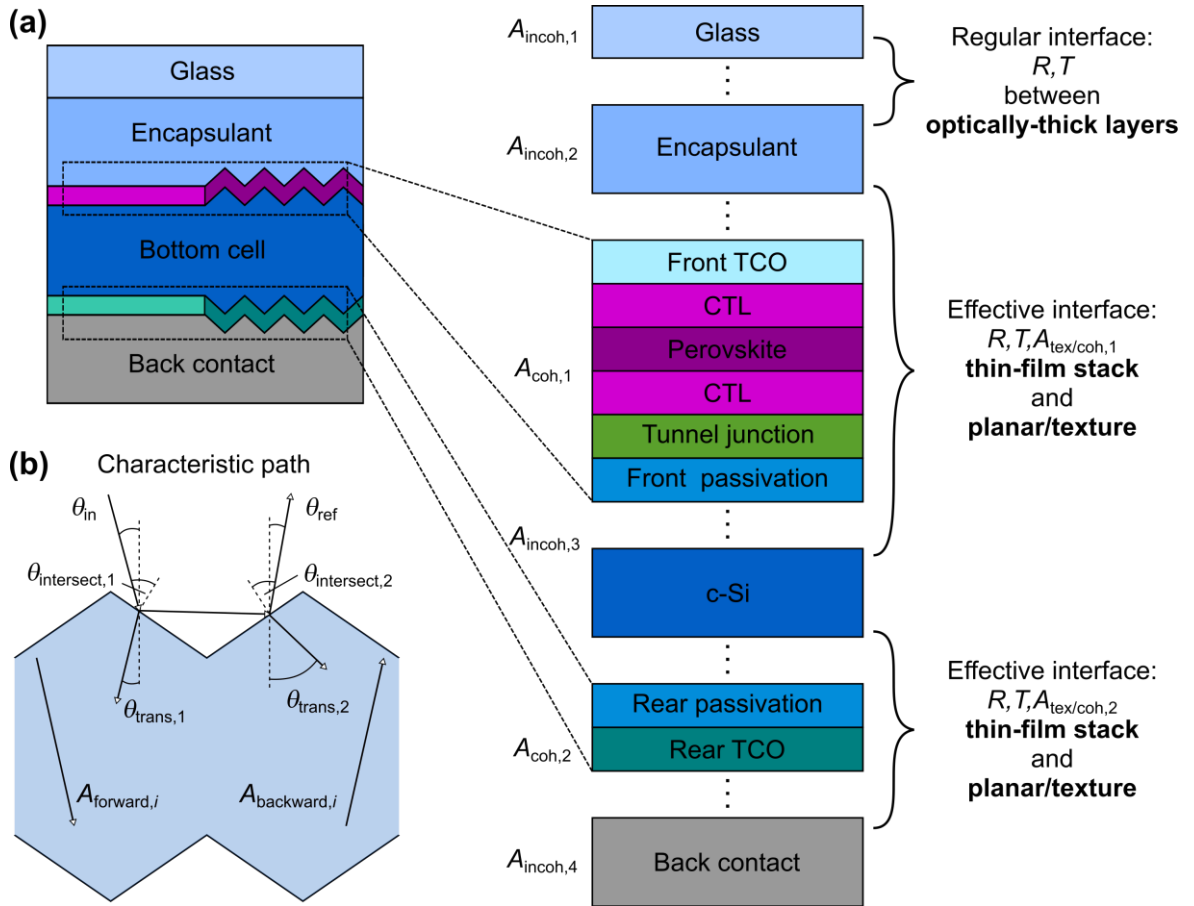


**Figure 4.4.** (a) Illustration of the abstraction levels of the complex architecture of multi-junction solar modules used for the optical simulation of their spectral response in dependence of the wavelength  $\lambda$  and the angle of incidence  $\theta_{\text{in}}$ . A perovskite/c-Si multi-junction solar module commonly exhibits three distinct features: optically-thick layers, multi-layer thin-film stacks and textures. (b) Textures are simulated using geometrical ray-tracing. The geometry of pyramidal textures only allows a specific set of characteristic light paths. Adapted with permission from ref. [84], © 2019 Optical Society of America.

With those quantities defined, the total absorption can be described by the iterative sum over all light paths in forward and backward direction through any material:

$$\begin{aligned} A(\lambda, \theta_{\text{in}}) &= A_{\text{forward}}(\lambda, \theta_{\text{in}}) + A_{\text{backward}}(\lambda, \theta_{\text{in}}) \\ &= \sum_i A_{\text{forward},i}(\lambda, \theta_{\text{in}}) + \sum_i A_{\text{backward},i}(\lambda, \theta_{\text{in}}), \end{aligned} \quad 4.8.$$

The obtained absorptance  $A$  is dependent on the angle of incidence  $\theta_{\text{in}}$  and the wavelength  $\lambda$ . In case of bifacial tandem modules, the absorptance  $A$  has to be calculated for front and rear illumination individually. In contrast to literature, where usually bifaciality factors are defined, the EY model explicitly accounts for the different front and rear spectral response.

Besides the architecture illustrated in Figure 4.4, where the perovskite thin film solar cell conformally covers the textured c-Si architecture, also a planar interface between the two sub cells – and at the rear of the c-Si solar cell is possible. Both designs are implemented as well. In case of a 4T interconnection, the two sub-cells are separated by an optically thick coupling layer. Therefore, a combination of the above-mentioned methods is typically used.

## 4.5 Electrics module: the current – voltage characteristics

The electrics module determines the temperature-dependent current density – voltage ( $J$ - $V$ ) characteristics accounting for series  $R_S$  and shunt resistances  $R_{SH}$  for a given  $J_{SC}$  of the sub-cells forming the tandem device in either a two-, three or four-terminal (2T-, 3T- or 4T) configuration. The electrics module then calculates the maximum power (MPP) point for each hour of the year. With this, the power output of the tandem module as well as the EY is determined. To derive the  $J$ - $V$  characteristics for a given  $J_{SC}$ , the Shockley diode equation is used (see section 2.1):

$$J(V) = J_{SC} - J_0 \left( e^{\frac{V+J \cdot R_S}{nV_{\text{th}}}} - 1 \right) - \frac{V + J \cdot R_S}{R_{SH}} \quad \text{with: } V_{\text{th}} = \frac{k_B T_{\text{module}}}{q}, \quad 4.9.$$

with the dark saturation current density  $J_0$ , the ideality factor  $n$ , the Boltzmann constant  $k_B$ , the elementary charge  $q$ , and the thermal voltage  $V_{\text{th}}$ . For realistic electrical modelling, the module temperature  $T_{\text{module}}$  has to be taken into account as well. However,  $T_{\text{module}}$  crucially depends on a wide range of parameters such as the meteorological conditions and the heat transfer inside the different components of the solar module. Since a rigorous thermal modelling of the absorbers in photovoltaics is a complex matter [128,129], an established empirical model based on the nominal operating cell temperature (NOCT) is used in the EY framework [130,131]. This model takes into account that the insolation  $S$  heats up the solar module above the ambient temperature  $T_{\text{ambient}}$  and can be described by:

$$T_{\text{module}} = T_{\text{ambient}} + \frac{\text{NOCT} - 20^{\circ}\text{C}}{800 \text{ Wm}^{-2}} \cdot S. \quad 4.10.$$

In this regard, the NOCT is defined as the temperature reached by a module under an insolation of  $800 \text{ Wm}^{-2}$ , a wind speed of  $1 \text{ ms}^{-1}$  and an ambient temperature of  $20^{\circ}\text{C}$ . For the calculations provided in this thesis a NOCT of  $48^{\circ}\text{C}$  is used, which represents a typical average module temperature [131].

The impact on the band gap due to a varying absorber temperature is modelled by temperature coefficients  $t_{V_{\text{OC}}}$  and  $t_{J_{\text{SC}}}$ , which scale the  $J_{\text{SC}}$  and  $V_{\text{OC}}$  accordingly.

$$V_{\text{OC}} = V_{\text{OC},0} \left( 1 + \frac{t_{V_{\text{OC}}}}{10^6} (T - T_0) \right) \quad 4.11.$$

$$J_{\text{SC}} = J_{\text{SC},0} \left( 1 + \frac{t_{J_{\text{SC}}}}{10^6} (T - T_0) \right) \quad 4.12.$$

The temperature coefficients for the  $V_{\text{OC}}$  and  $J_{\text{SC}}$  are defined at  $T_0 = 25^{\circ}\text{C}$  and expressed in  $\text{ppmK}^{-1}$  [132] and can be extracted from literature [133]. To solve the transcendental Equation 4.9. the Lambert-W-function is used, which allows the determination of a closed solution for the open-circuit voltage  $V_{\text{OC},0}$  at  $T_0$  and at any given temperature  $T$  [134,135].

$$V_{\text{OC},0} = (J_{\text{SC}} + J_0)R_{\text{SH}} - nV_{\text{th}} \cdot W \left( \frac{J_0 R_{\text{SH}}}{nV_{\text{th}}} e^{\frac{(J_{\text{SC}} + J_0)R_{\text{SH}}}{nV_{\text{th}}}} \right) \quad 4.13.$$

$$V(J) = -JR_{\text{S}} + (J_{\text{SC}} + J_0 - J)R_{\text{SH}} - nV_{\text{th}} \cdot W \left( \frac{J_0 R_{\text{SH}}}{nV_{\text{th}}} e^{\frac{(J_{\text{SC}} + J_0 - J)R_{\text{SH}}}{nV_{\text{th}}}} \right) - V_{\text{OC}}^{\text{RT}} + V_{\text{OC}} \quad 4.14.$$

This enables the electrical module to calculate the power output by deriving the MPP point of the  $J$ - $V$  characteristic curve for each hour of the year. The total power of the tandem module is then dependent on the actual electrical interconnection of the two sub solar cells. For a 2T configuration, the sub cells are connected in series and the current is limited by the lower current of both:

$$P_{2\text{T}} = V_{\text{MPP}} \cdot \min(J_{\text{MPP,top}}, J_{\text{MPP,bottom}}). \quad 4.15.$$

In a 4T configuration, both sub cells are operated individually at their distinct MPP points and the total power is derived by the sum of the power of each sub cell:

$$P_{4\text{T}} = V_{\text{MPP,top}} \cdot J_{\text{MPP,top}} + V_{\text{MPP,bottom}} \cdot J_{\text{MPP,bottom}} \quad 4.16.$$

In a 3T electrical interconnection, two interdependent electrical circuits are operated and no analytical solution to derive the  $J$ - $V$  characteristics is available. Therefore, the  $J$ - $V$  characteristics of the 3T is simulated numerically with the electronic circuit simulator LTspice (from Linear Technology). With LTspice, the electrical response of the equivalent electrical circuit modelling the module is simulated. Currently, this module is still under development by F. Gota [136].

## 4.6 Energy yield calculation

The energy yield core module manages the in- and outputs of the above described modules (see Figure 4.2) and calculates the EY over the course of one year of the sub-cells. In addition to that, the core module offers various additional features, such as the calculation of the EY for:

- (i) different locations,
- (ii) mono- or bifacial solar modules,
- (iii) 2T, 3T or 4T electrical interconnections,
- (iv) static tilt and/or rotation of the solar module,
- (v) dynamic/time-dependent tilt and/or rotation (1- and 2-axis sun tracking),
- (vi) and different albedo.

For this, the EY is calculated for each hour of the year by combining the spectral and angular resolved irradiance with the absorptance of each sub-cell and their electrical properties. Therefore, to derive the EY, the  $J_{SC}$  has to be determined first. The  $J_{SC}$  is dependent on the absorption of the sub-cells and on the insolation to the solar module. Since, the orientation of the solar module is a variable quantity in the EY framework, the polar  $\theta_{sun}$  and  $\varphi_{sun}$  azimuth angle of the sun coordinates  $\mathbf{S}$  need to be transformed into the local coordinate system of the solar module for each hour of the year:

$$\begin{aligned}\theta_{sun} &\rightarrow \theta'_{sun} \\ \varphi_{sun} &\rightarrow \varphi'_{sun}.\end{aligned}\quad 4.17.$$

The rotated sun coordinates  $\mathbf{S}'$  are obtained by a quaternion rotation  $\mathbf{q}$  about the corresponding Euler angle  $\theta_e$  about the Euler axis, given by:

$$\mathbf{S}' = \mathbf{q}\mathbf{S}\mathbf{q}^{-1} \quad \text{with} \quad \mathbf{q} = \cos \frac{\theta_e}{2} + (S_x\mathbf{x} + S_y\mathbf{y} + S_z\mathbf{z}) \sin \frac{\theta_e}{2}. \quad 4.18.$$

Compared to rotation matrices the quaternion rotation is numerically more stable and especially avoid the problem of gimbal lock [137]. The gimbal lock is the loss of one degree of freedom in a three-dimensional system, which occurs, when two axes of the three gimbals<sup>1</sup> are driven into a parallel configuration (e.g. by a rotation), "locking" the system into rotation.

To calculate the  $J_{SC}$ , the contribution of direct and diffuse sunlight is considered separately in the following. The direct irradiance from the sun is considered point-like at the position of the sun in the local coordinate system  $\mathbf{S}'$ . Therefore, the direct short-circuit current density  $J_{SC}^{dir}$  is derived by the integration over the product of the collection efficiency  $\chi$ , the absorptance  $A$  of the corresponding sub-cell, the direct irradiation  $I_{dir}$ , and the cosine of the angle between the sun and the normal of the solar module  $\theta'_{sun}$ .

<sup>1</sup> A gimbal is a pivoted support that allows the rotation of an object about a single axis.

$$J_{SC}^{dir} = \frac{q}{hc} \int \chi(\lambda) A(\lambda, \theta'_{sun}) I_{dir}(\lambda) \lambda \cos(\theta'_{sun}) d\lambda$$

with  $\theta'_{sun} < 90^\circ, \Gamma(\theta'_{sun}, \varphi'_{sun}) = 1$  4.19.

The elementary charge, the Planck constant and the speed of light are denoted by  $q$ ,  $h$  and  $c$ . It is important to note that the  $J_{SC}^{dir}$  is only calculated for accessible angles of the sun's position  $\theta'_{sun} < 90^\circ$  and  $\Gamma(\theta'_{sun}, \varphi'_{sun}) = 1$ . Where  $\theta'_{sun} < 90^\circ$  describes the possible maximum elevation of the sun, the function  $\Gamma(\theta', \varphi')$  defines all polar coordinates in the local coordinate system of the solar module from which light can ( $\Gamma = 1$ ) or cannot ( $\Gamma = 0$ ) impinge on the solar module. This is crucial for rotated or titled module orientations, where part of the direct (and diffuse – see below) irradiation reaches the rear side of the solar module (see **Figure 4.5**). In fact, for bifacial solar modules, this share is separately considered by the calculated absorption for rear side illumination.

For the diffuse irradiation  $I_{diff}$ , a Lambertian distribution of the light over the upper hemisphere is assumed. It should be noted that also measured data could be used. Analogous to the direct, the diffuse short-circuit current density  $J_{SC}^{diff}$  is derived by the additional integration over the polar and azimuth angles:

$$J_{SC}^{diff} = \frac{q}{hc} \iiint \chi(\lambda) A(\lambda, \theta'_{sun}) I_{diff}(\lambda) \cos(\theta') \lambda \Gamma(\theta', \varphi') \sin(\theta') d\varphi' d\theta' d\lambda. \quad 4.20.$$

For tilted solar modules, the additional contribution of ground-reflected light (albedo) is considered. In this regard, the EY model assumes a Lambertian distribution of the albedo. The spectral reflectivities of various grounds ( $\approx 3400$ ) are extracted from the ECOSTRESS spectral library [138,139] and the albedo is subsequently scaled by the level of direct and diffuse irradiance.

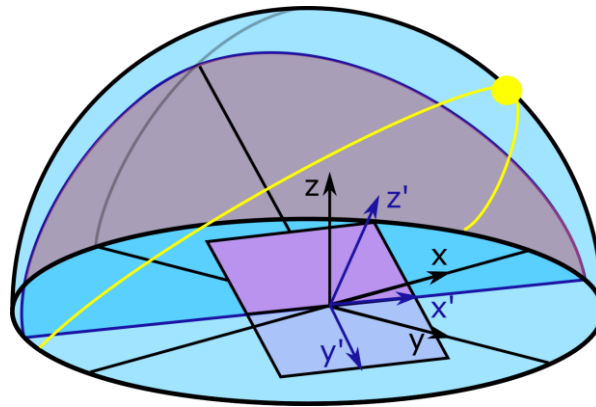


**Figure 4.5.** Schematic of a rotated solar module. From angles below the horizon in the pristine coordinate system  $S$  cannot access the solar module by the direct sunlight. This solid angle is only accessible by albedo. Further, a part of the solar module is shadowed in rotated coordinate system  $S'$  and only bifacial cells can benefit from light impinging on the solar cell from this solid angle.

The additional current generated by the albedo is added to the total short-circuit current density for the top and bottom solar cell individually.

$$J_{SC}^{tot} = J_{SC}^{dir} + J_{SC}^{diff} + J_{SC}^{diff,albedo-front} \quad 4.21.$$

When considering bifacial solar modules with albedo, three further contributions should be considered. Firstly, the albedo, which reaches the bifacial solar module from the rear side. Secondly, the direct and third the diffuse irradiance impinging on the rear side of the bifacial module. Therefore, the total short-circuit current density  $J_{SC}^{tot}$  has to be extended by those terms:

$$J_{SC}^{tot} = J_{SC}^{dir} + J_{SC}^{diff} + J_{SC}^{diff,albedo-front} + J_{SC}^{diff,albedo-rear} + J_{SC}^{dir,rear} + J_{SC}^{diff,rear}. \quad 4.22.$$

Due to self-shading effects by the module installation, the contribution of albedo has to be modified. The self-shading mainly scales with the module installation height and is implemented in the EY framework according to the light-collection model introduced by Sun *et al.* [140]. The implementation to the EY framework and the contribution of the albedo to the short-circuit current density of bifacial modules was studied in more detail by J. Lehr [85].

So far, only static tilts and rotations have been discussed. Since the above-mentioned calculation of the individual contributions to the total  $J_{SC}$  are performed for an hourly time-resolution, the evaluation of time-dependent tilts or rotations of the solar module are also possible. Therefore, various one- and two-axis tracking algorithms have been implemented [141]. In general, tracking the position of the sun is increasing the annual EY. The more sophisticated this tracking is, the higher the annual yield.

## 4.7 Demonstration of the energy yield framework

To demonstrate different aspects of the EY framework, exemplary studies are discussed in the following. Firstly, different tracking methods are showcased for a 2T perovskite/c-Si tandem module. Secondly, 2T, 3T and 4T solar module interconnection schemes are compared. Thirdly, the impact of albedo on mono- and bifacial 4T tandem modules is evaluated. For all studies a similar layer stack of a double sided-textured c-Si solar cell coated with a thin-film perovskite solar cell is used. The layers and corresponding thicknesses are illustrated in **Figure 4.6**. The electrical parameters are summarized in Table 1 and correspond to the ones used in a previous publication [86]. The refractive indices of the layers are summarized in the Appendix

To assess the potential of different tracking methods, the layer thicknesses are kept constant. It should be noted, that minor enhancements are expected by further optimizing the layers for each tracking method. For the one-axis tracking, two algorithms are analyzed: (i) a rotation around the zenith, where the tilted solar module moves only from

east to west, and (ii) a rotation about a fictitious axis on the tilted solar module from south to north, where the module can only toggle to west and east (see **Figure 4.7a**). For both one-axis tracking methods, the normal of the tilted solar module follows the azimuth angle of the sun  $\varphi_{\text{sun}}$ . In case of the two-axis tracking, the normal of the tandem solar module follows the sun's position every hour of the year.

The EY for different tracking methods is evaluated for a 2T perovskite/c-Si tandem solar module and compared with the EY for an installation under optimal tilt and with that of a module lying horizontally on the ground. Compared to the fixed optimal tilt, the one- and two-axis tracking of the sun demonstrate a strong increase in the annual EY (**Figure 4.7b**). The EY improves by up to 23% and 32% for the one- and two-axes tracking, respectively.

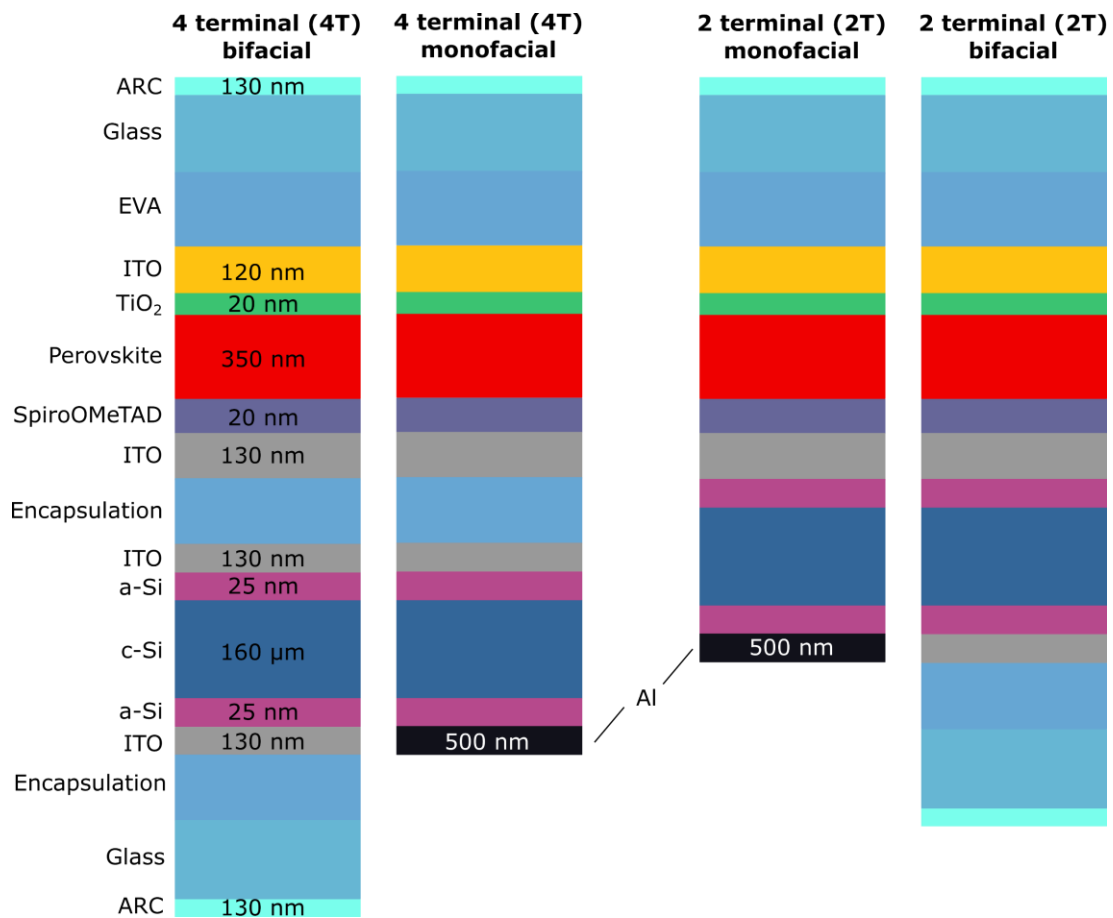


**Figure 4.6.** Layer stack of the perovskite/c-Si tandem solar cell(s) used for the demonstration of the EY framework. For simplicity, the layer thicknesses of the two-terminal (2T) and four-terminal (4T) architectures are assumed to be equal. Compared to the 2T, in the 4T an additional glass-like optical spacer (denoted as: “encapsulation”) is implemented.

**Table 1.** Electrical input parameters used for the demonstration of the EY framework.

	$R_{\text{SH}} (\Omega)$	$R_{\text{s}} (\Omega)$	$\chi$	$J_0 (\text{mAcm}^{-2})$	$n$	$t_{J_{\text{SC}}} (\text{ppmK}^{-1})$	$t_{V_{\text{OC}}} (\text{ppmK}^{-1})$
Tandem	850	15.9					
Top	1300	10.9	1	8E-15	1.43	0.0002	-0.002
Bottom	800	5	1	1E-14	0.82	0.00032	-0.0041

Especially around midday, the optimal tilt ( $28^\circ$  for Phoenix) is far superior compared to the solar module lying horizontally on the ground (see Figure 4.7c). This is due to the reduced angle of incidence of the sun during this time (see Figure 4.7d). The tilted solar module almost pointing towards the sun. In Figure 4.7c-d, an exemplary day (November 19<sup>th</sup>) is depicted for the location Phoenix (Arizona) to display the hourly change in power output. By following the sun with a one-axis tracking, the received power increases. With the one-axis tracking, the maximum power output is maintained at noon, but power generation is improved especially in the morning and evening when the sun rises and sets. In this regard, the east-west tilt makes better use of sunrise and sunset irradiation. In addition, when the solar module is tracked by two-axes, the maximum intensity is better projected on the solar cell and the overall EY is highest during the full day.

Tracking of the solar module changes not only the intensity, but also the spectrum of the light incident on the solar module. This is well described by the average usable photon energy (AUPE). The AUPE is the average photon energy (APE) that can potentially be used by the solar module (here: 300 nm - 1200 nm). For a second exemplary day (here June 14<sup>th</sup>) the AUPE is shown in Figure 4.7e. Due to the two-axes tracking, the APUE is significantly reduced in the early morning and late afternoon. This is due to the fact that the share of direct irradiation, which has a lower APE, is now higher. In contrast, at optimal tilt, the higher APE of diffuse radiation in the morning and afternoon dominates the AUPE.

Comparing the obtained  $J_{SC}$  of the two sub-cells for the selected day, it becomes clear that the perovskite solar cell always delivers a higher current than the c-Si cell for optimal inclination. However, in the two-axis tracking this trend is reversed (for sun rise and sun set) and the currents for bottom cell are slightly higher, and overall better matched. The improved matching is caused by the fact that the AUPE is closer to the band gap of perovskite. This reduces the annual energy loss due to mismatch from  $51.2 \text{ kWhm}^{-2}\text{a}^{-1}$  to only  $44.0 \text{ kWhm}^{-2}\text{a}^{-1}$ .

In summary, these observations show that tracking methods can reduce the relative energy loss due to current mismatch caused by spectral variations. Moreover, this also indicates that the architecture and particularly the layer thicknesses should be adapted to the respective operating scenario.

Besides the different tracking methods, also the actual electrical interconnection scheme affects the annual EY. Here, the 2T, 3T and 4T electrical interconnection is compared to each other. For this, the same 2T double-sided textured perovskite/c-Si solar module is used, as used for testing the tracking methods. For the 3T interconnection, the 2T monolithic layer stack is used. In case of the 4T architecture, the two sub-cells are stacked together with an encapsulation as optically spacer (see Figure 4.6). It should be noted that these assumptions are very rudimentary.

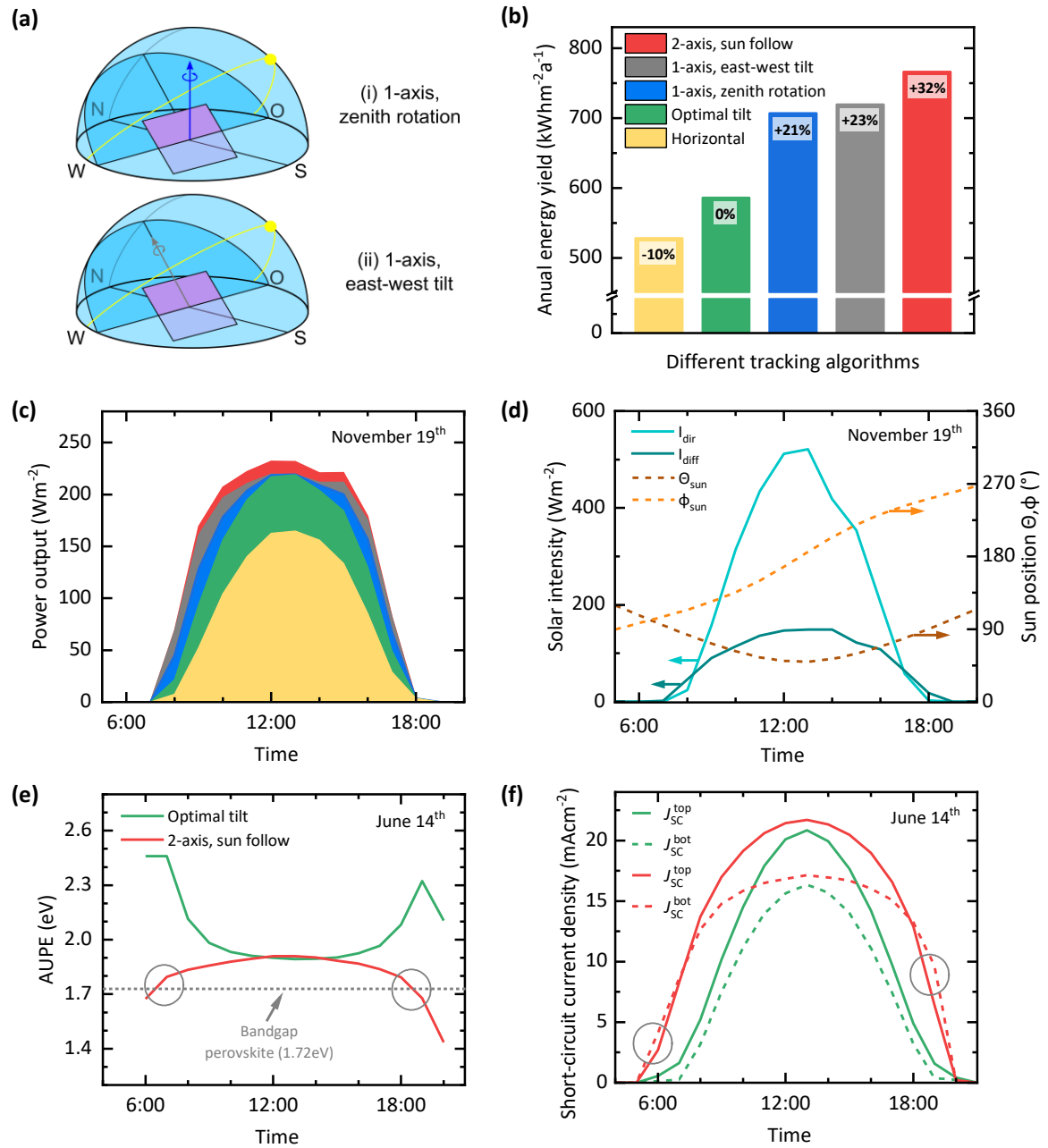


**Figure 4.7.** EY of a perovskite/c-Si multi-junction solar module for different tracking methods for a single day and the complete year in Phoenix (Arizona, USA). (a) Schematic of two different 1-axis tracking methods; (b) the angular EY; (c) the EY for a chosen day (November 19<sup>th</sup>); (d) the sun's polar  $\theta_{\text{sun}}$  and azimuth angle  $\phi_{\text{sun}}$  as well as the direct and diffuse irradiance for the same day; (e) the average usable photon energy (AUPE) for a chosen day (June 14<sup>th</sup>) and (f)  $J_{\text{sc}}$  of the top and bottom solar cell for optimal tilt (green) and 2-axis tracking (red) for the same chosen day (June 14<sup>th</sup>). Adapted with permission from ref. [84], © 2019 Optical Society of America.

Compared to the 2T architecture, the intermediate encapsulation and the front electrode of the bottom c-Si sub-cell increase the parasitic reflection in case of the 4T architecture (see **Figure 4.8a** and b). Moreover, for the same layer thicknesses, the absorption in the top perovskite solar cell is reduced. The overall EY for the three

configurations is highly dependent on the location (see Figure 4.8c). In the northern (temperate and boreal) regions the annual EY is lower, compared to the southern more tropical or arid locations (Miami and Phoenix). Employing the 3T or 4T electrical interconnection avoids the current mismatch characteristic of the 2T, and thus lead to an average increase in EY by 7%<sub>rel</sub> and 4%<sub>rel</sub> for all considered locations, respectively.

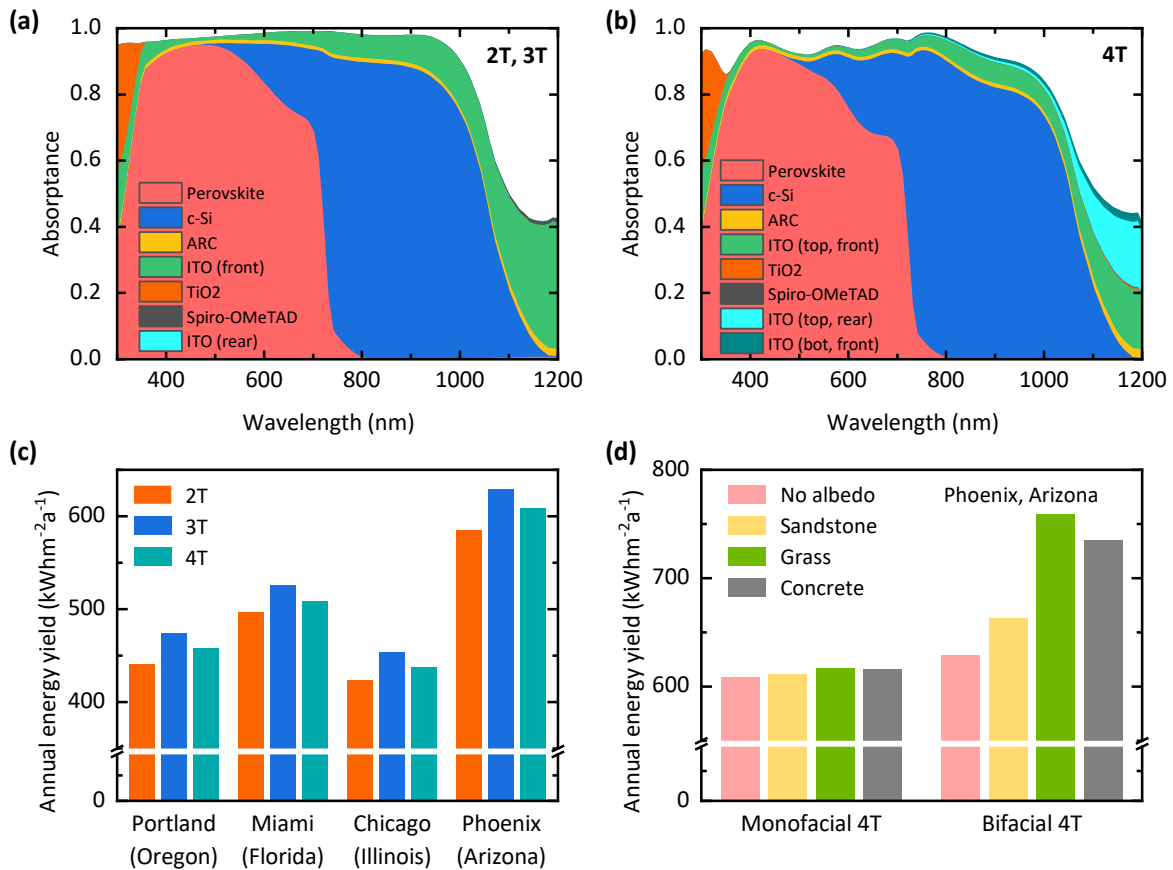


**Figure 4.8.** Absorbance of the individual layers in the (a) 2T and the (b) 4T multi-junction solar modules. (c) Annual EY for four locations with different climatic conditions: temperate (Portland, Oregon), tropical (Miami, Florida), boreal (Chicago, Illinois), and arid (Phoenix, Arizona) for a 2T, 3T and 4T monofacial perovskite/Si solar module. (d) Annual EY for a monofacial and bifacial 4T perovskite/Si solar module with three different ground surfaces (sandstone, grass and concrete) leading to different albedos. Adapted with permission from ref. [84], © 2019 Optical Society of America.

Another interesting aspect, is the possibility to assess the performance of bifacial double-sided textured perovskite/c-Si tandem solar modules within the developed framework (see Figure 4.8d). Compared to the monofacial 4T perovskite/c-Si tandem, the annual EY increases by 3%<sub>rel</sub> for the bifacial architecture. This is due to the additional direct and diffuse irradiation on the rear side of the solar module. In case of additional consideration of different grounds, reflecting the light back towards the tandem module (albedo), the strong impact on the bifacial modules becomes apparent. While the EY enhances by ≈1%<sub>rel</sub> for concrete and grass in the monofacial tandem in Phoenix for an

optimal tilt, the bifacial module improves the EY by up to 20%<sub>rel</sub>. Here the origin of the albedo plays a significant role. In particular, grass-covered ground contributes an additional 20%<sub>rel</sub> to the annual EY, while sandstone only 6%<sub>rel</sub> and concrete respectable 18%<sub>rel</sub>. These results highlight once more the strong impact of environmental conditions on the annual EY of bifacial tandem solar modules.

Overall, the EY framework provides stimulating insights to the performance of solar modules under realistic irradiation conditions. It becomes clear that conventional specifications derived under STC are not suitable for credible predictions of the outdoor performance of solar modules. Especially, for the recently heavily investigated perovskite/c-Si tandem solar modules design rules can be derived for various technological inquiries.

## 4.8 Summary and discussion

The present simulation platform, fast and accurately calculates the energy yield under realistic irradiation conditions including a broad range of locations distributed over the USA. It is able to account for planar single- and multi-junction solar modules as well as for complex optical geometries: e.g. microtextured interfaces between the individual sub cells or textured front glass covers. Furthermore, various one- and two axis tracking algorithms, fixed tilts, various albedo and bifaciality of the solar modules can be examined. Moreover, the multi-junction solar modules can be analyzed for 2T, 3T, and 4T interconnections.

However, it should be noted that the description of the electrical properties of the modelled solar cells is based on the one-diode model. In reality, however, recombination dominates in the *pn*-junction at lower voltages. Thus, the ideality factor also varies depending on the irradiance and a more complex two- or multi-diode model could be more accurate [142]. However, a two-diode model increases the complexity of the calculation and requires knowledge of the additional electrical properties of the second diode [143]. For 2T and 4T electrical interconnections, however, the single-diode model used is sufficiently accurate, as it deviates from the experimental data by less than 1% [144]. Independent thereof, for the 3T circuit, a more detailed approach based on a numerical modelling is currently being developed in our group (see ref. [136]).

For the temperature modelling, an established empirical model based on the nominal operating cell temperature (NOCT) is used [130]. This model is only a rough approximation, and strongly depends on the assumption of the NOCT value, giving the average module temperature [131]. Since the temperature of the absorbers has a significant impact on the current density – voltage characteristics of solar modules, a rigorous thermal modelling would lead to superior description of the absorber temperatures. Since, parameters like the ambient temperature, wind speed, total insolation are known for each hour of the year for every location, this seems possible, although it would be a complex matter [128,129]

and needs experimental validations. Furthermore, depending on the degree of complexity, this might slow down the overall simulation speed significantly.

Moreover, the suggested cloud model is very simple and therefore, the spectrally adjusted diffuse irradiance is distributed homogeneously over the full upper half sphere. To improve this – and to provide additional directional dependency, a unified and comprehensive radiative transfer model for clouds needs to be developed and employed within the energy yield framework. So far this has not been reported and should be one of the further concerns [119–121]. Nevertheless the simple cloud model already provides realistic diffuse spectral resolved irradiances [118]. In addition, the calculated annual energy yields match very well to others, which developed a similar simulation frameworks [107].

*In the further course of the work, the EY is estimated for single junction c-Si as well as for perovskite/c-Si tandem solar cells to review the proposed light management concepts and examine them under realistic irradiation conditions. This will provide detailed insights into mostly the angular and specular dependency of the employed concepts.*

## 5 Microtextures for improved light incoupling and light harvesting by retro-reflection

This section discusses the excellent light incoupling and moreover superior light harvesting properties by retro-reflection of microtextures. The investigated microtextures demonstrate a superior reduction of the reflection losses at the front planar air/glass interface of solar cells. Eliminating the front air/glass reflection, enables an absolute improvement of around 4% for normal incidence and up to 80% for oblique angles of incidence. This is of significant importance to almost any photovoltaic technology.

### Acknowledgements and contributions

*The majority of the following section on light incoupling and harvesting by retro-reflection is based on the first author publication on the “Texture of the viola flower for light harvesting in photovoltaics” [145] and the coauthor publications on microtextures for improved light incoupling and harvesting by retro-reflection [54,78,146,147]. The experimental values for reflectance of conical textures on different substrates are measured by Stephan Dottermusch. Moreover, he performed the electrical characterization of the planar crystalline silicon (c-Si) and textured c-Si solar cells equipped with cones of different aspect ratios (AR). The study on semitransparent perovskite solar cells resulted from a collaboration with Ihteaz M. Hossain. The conical textured foils for the application on the perovskite solar cells have been processed by Aiman Roslizar. The PDMS replica of the random upright pyramids was provided by The Duong from the Australian National University. The work on the retro-reflective foil, consisting of inverted pyramids, resulted from a collaboration with Manoj Jaysankar from imec, where Raphael Schmager supported the work with optical simulations.*

## 5.1 Introduction

In order to achieve high power conversion efficiencies (PCE) of any solar cell technology, it is key to guide as much light as possible to the photoactive layer(s) of the photovoltaic (PV) modules. Therefore, light management concepts are inevitable to ensure high absorption and minimize parasitic losses. The first loss of conventional PV modules occurs already at the very top interface of the modules. Typically, the modules are encapsulated with a glass cover to withstand realistic operation conditions [30]. This means that at normal light incidence, already  $\approx 4\%_{\text{abs}}$  of the light is reflected at the air/glass interface. In addition, at oblique angles of  $\approx 80^\circ$ , the Fresnel reflection even increase to  $\approx 40\%_{\text{abs}}$ . Since PV modules usually are operated under realistic irradiation conditions, which are suspect to variable angle of incidence, the energy harvesting of photovoltaic modules need to be optimized for all angles of incident.

In order to maximize the energy yield of PV modules, microtextures with dimensions in the order of multiple wavelengths are usually employed to reduce surface reflection and enhance light trapping by increasing the optical path length of the light inside the absorber layer<sup>1</sup>. In this regard, the most prominent representative are the random pyramids on the mono-crystalline silicon (c-Si) solar cells. In case of thin-film solar cells, where the layer thicknesses are limited to a few 100 nm, micro-texturing the absorber is typically not applicable. Here, microtextures are usually applied in transparent polymers [59], and first work already demonstrates the transfer and integration in the module front glass cover [30]. These non-invasive implementations are of high significance, since the implementation at the front surface of the solar modules, leaves the absorber layer unaffected and makes their employment independent on the architecture and technology.

In the following section, the light management of microtextures are studied for single junction c-Si solar cells and perovskite/c-Si tandem solar cells. For this purpose, cones, inverted cones, pyramids and inverted pyramids are analyzed. The key features of those microtextures are the ability to (1) strongly reduce the reflection loss for a broad spectral and angular range, as well as (2) recapture escaping light by the retro-reflection effect. The retro-reflection describes the property to redirect the light towards the solar cell via the back-reflection of the micro-texture, which causes an increase in the probability of absorption. Combining these excellent properties is very important and key for any good anti-reflection texture.

First, the anti-reflection and retro-reflection capability of the four different textures are analyzed by ray-tracing simulations (section 5.2 and 5.3). It is found that for increasing aspect ratio (AR) of the microtextures, the front reflectance tends towards zero. However, due to an angular redistribution of the transmitted light, the total reflection is strongly

---

<sup>1</sup> This is true for thick absorbers like crystalline silicon. Thin-film solar cells, will benefit mostly from the enhanced light incoupling.

---

influenced by the reflection properties of the underlying surface – e.g. the solar cell. Therefore, the light harvesting properties of the different textures by retro-reflection is analyzed for different reflectance properties.

Next, micro-cones are experimentally fabricated and implemented on top of planar and textured thin-film c-Si solar cells (section 5.4), leading to improved current densities of  $\approx 12\%_{\text{rel}}$  and  $\approx 5\%_{\text{rel}}$  compared to the planar (encapsulated) reference, respectively. In addition, the micro-cones as well as inverted pyramid textures are applied on top of semitransparent perovskite/c-Si tandem solar cells and lead to enhancements of up to  $10\%_{\text{rel}}$  in the PCE.

Besides the artificial produced microtextures, also biomimetic textures are analyzed in section 5.5. With regard to biomimetic textures, especially plant surfaces demonstrate similar conical microtextures as the ones simulated and designed in the beginning of this chapter. Moreover, the viola texture replicated on top of planar c-Si solar cells demonstrates enhancements of  $\approx 6\%_{\text{rel}}$  in the  $J_{\text{SC}}$ .

Finally, energy yield (EY) simulations are performed on the perovskite/c-Si tandem solar modules covered with the inverted pyramid microtextures. Due to the excellent angular stability of the microtextures, the enhancements in the EY exceeds those of the PCE by  $\approx 2\%_{\text{rel}}$ .

## 5.2 Light-incoupling via microtextures

In order to decrease reflection losses at the planar air/glass interface of solar cells, different microtextures are evaluated. The microtextures improve the light harvesting of the solar cell in three ways:

- i. they enhance the transmission at the air/glass interface by reducing the front surface reflection,
- ii. they improve light trapping by enlarging the angle of light propagation inside the absorber material, and
- iii. they redirect light reflected by the solar cell back to the solar cell (retro-reflection).

In the following, four different textures are analyzed: cones, inverted cones, pyramids and inverted pyramids (see **Figure 5.1**). All textures are defined in the following by their aspect ratio AR, which is defined by the ratio of their height  $h$  and base length  $d$ . The AR is linked to the inclination angle  $\beta$  by

$$\text{AR} = \frac{h}{d} = \frac{\tan(\beta)}{2}. \quad 5.1.$$

Due to rays impinging multiple times on the texture elements, the overall probability to incouple light increases compared to the planar reference. For sufficiently high textures

(large AR), the light is trapped between the texture elements (e.g. cones or pyramids) and the total front surface reflectance is therefore strongly reduced (see **Figure 5.2a**). For all four textures, the front surface reflectance decreases abruptly from  $\approx 4.8\%$ , which represents the planar reference (AR = 0) with a refractive index of  $n = 1.56$ , to values below 1% for  $AR \geq 0.5$ . For very high aspect ratios ( $AR > 1$ ), the front reflectance is further decreased and tends towards zero.

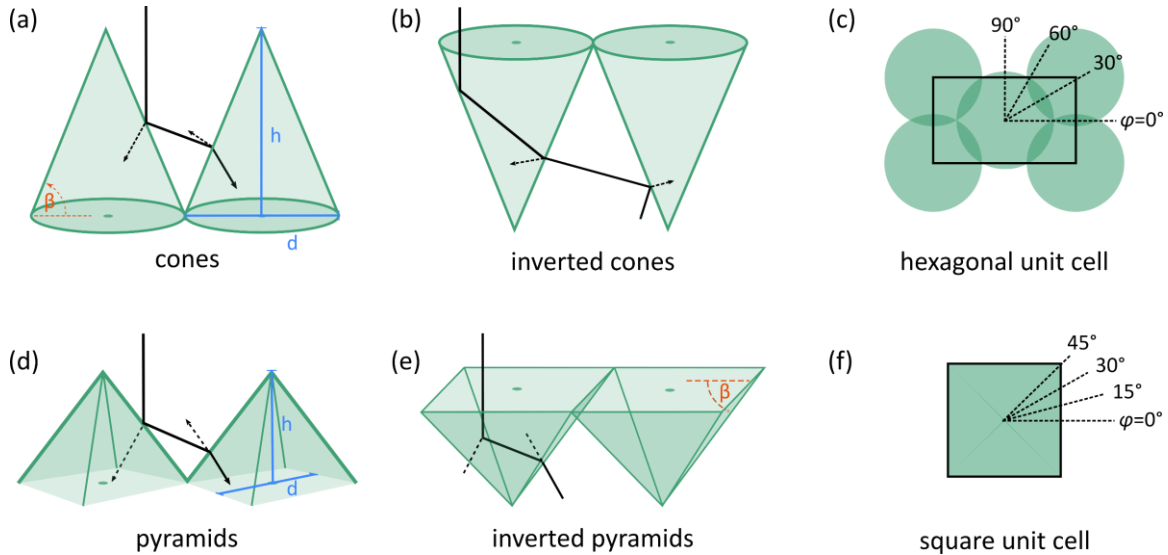


**Figure 5.1.** Illustration of the four different textures simulated. The (a) cones and (b) inverted cones are simulated in a (c) hexagonal unit cell with reflecting boundary conditions. The (d) pyramids and (e) inverted pyramids are simulated in a (f) square unit cell. For all textures, the inclination angle  $\beta$  is defined as the angle between the base and the sidewall and the aspect ratio AR is given by the quotient of height  $h$  and width  $d$ .

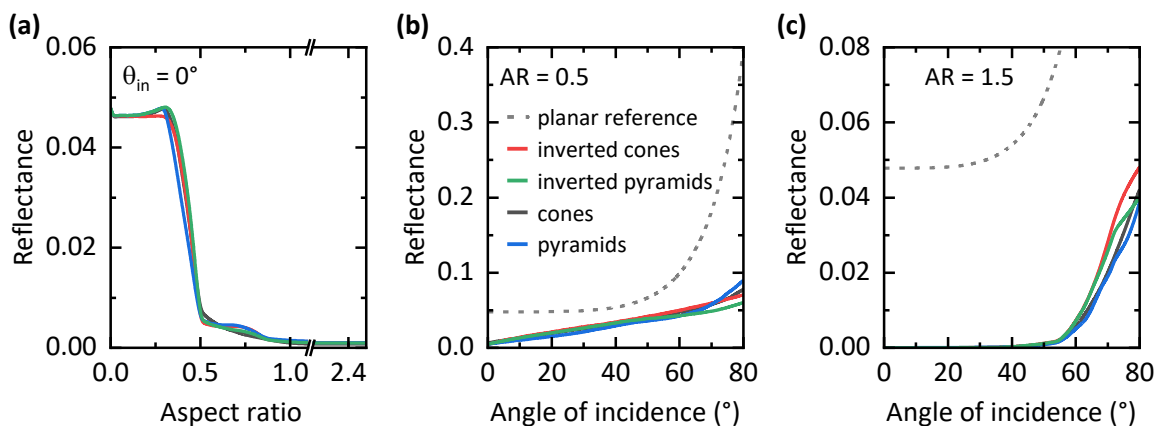


**Figure 5.2.** Front surface reflectance of different textures with (a) different aspect ratios and (b-c) for different angle of incidence. The cones, inverted cones, pyramids and inverted pyramids demonstrate a steep decrease in reflectance at normal incidence for aspect ratios above 0.5. Moreover, at large angle of incidence, the reflectance is drastically reduced compared to a planar air/glass interface.

Another strength of the microtextures is their ability to reduce the front surface reflectance efficiently for non-normal incidence. In Figure 5.2b and c, the reflectance for textures with an AR of 0.5 and 1.5 is illustrated for angles of incidence up to 80°. All four textures demonstrate extremely low reflectance and very low angular dependence. For an AR of 0.5, the front surface reflectance at 80° decreases to only  $\approx 8\%_{\text{abs}}$  and  $\approx 6\%_{\text{abs}}$  for pyramids and inverted pyramids, respectively. For higher ARs, the front reflectance only contributes for angles of incident above 50° and increases to values around  $4\%_{\text{abs}}$  only.

The textures do not only strongly reduce the front surface reflection, but also change the angular distribution of the transmitted (and reflected) light. In case of a planar interface, the angle of light propagation is given by Snell's law. For arbitrary textures, deriving an analytical formulation is not straightforwardly possible. To cope the full nature of the presented textures (cones, inverted cones, pyramids and inverted pyramids) and to study the influence of the aspect ratio on the ability to improve the light harvesting in photovoltaics, ray-tracing simulations are performed. For details on the ray-tracing method see chapter 3.1.1.

For the ray-tracing simulations, the commercially available software LightTools from Synopsys is used. To simulate the cones and inverted cones, a hexagonal unit cell of 3D overlapping cones is simulated (see Figure 5.1c). For the pyramids and inverted pyramids, a square lattice is used (see Figure 5.1f). The unit cell is illuminated with  $10^8$  parallel rays, which were sufficient for convergence of all the models. At the backside of the model, a perfect absorber is defined. Therefore, the attained reflectance and transmittance accounts only for the reflectance and transmittance at the front surface (the air/texture interface). To investigate the optical performance of the textures, different aspect ratios AR are modelled and simulated. Moreover, the polar  $\theta$  and azimuthal  $\varphi$  angle of incidence are varied. For each set of incident angles, the reflected and transmitted light is obtained dependent on their polar and azimuth angle of emergence. For the azimuth angle the symmetry of the texture is exploited. For cones, 0°, 15°, 30°, 45°, 60°, 75°, and for pyramids only 0°, 15°, 30° and 45° are simulated.

Moreover, the simulations are performed for top illumination as well as for bottom illumination. For top illumination, the light source is placed in air and the rays are directed towards the texture. For bottom illumination, the source resides inside the bulk with refractive index of the textures pointing upwards. The material of the textures is modelled as glass with a dispersion-less refractive index of  $n = 1.56$  without any absorption. For both sides of illumination, incident angles and aspect ratios, the simulations provide the angular resolved reflectance and transmittance. The reflectance and transmittance can be described by the following expression:  $\{R, T\}_{\{top, bottom\}}(\theta_{in}, \varphi_{in}, \theta_{out}, \varphi_{out}, AR)$ .

As an exemplary case, cones with an AR = 0.8 are considered in the following. For normal incidence ( $\theta_{in} = 0^\circ$ ), the reflectance for top and bottom illumination ( $R_{top}$ ,  $T_{top}$ ,  $R_{bottom}$  and  $T_{bottom}$ ) at the cones with an AR = 0.8 are illustrated in **Figure 5.3**. The color bar

provides the probability for rays to be either reflected (a and b) or transmitted (c and d) in distinct set of angles  $\theta_{\text{out}}$  and  $\varphi_{\text{out}}$ . The integration over both angles, gives the total reflectance and transmittance (see number below the color bar). Compared to the transmittance at a planar air/glass interface, the total transmittance is increased from 95.2% to  $\approx 99.8\%$ .

Similarly, the total reflectance at the front surface for illumination from the top is decreased to  $\approx 0.2\%$ . In addition to the change of total reflectance and transmittance, the distribution of the light strongly deviates from the planar reference. In the planar configuration the angle of light propagation is not changed (for normal incidence) and this would be represented by only a single spot at  $\{\theta_{\text{out}}, \varphi_{\text{out}}\} = \{0^\circ, 0^\circ\}$ . The transmittance for top illumination shows an increased probability of transmittance towards an angle of  $\theta_{\text{out}} = 25^\circ$  (see Figure 5.3c). Moreover, the hexagonal nature of the unit cell becomes visible by the hexagonal symmetry in the reflectance and transmittance (see especially Figure 5.3b).

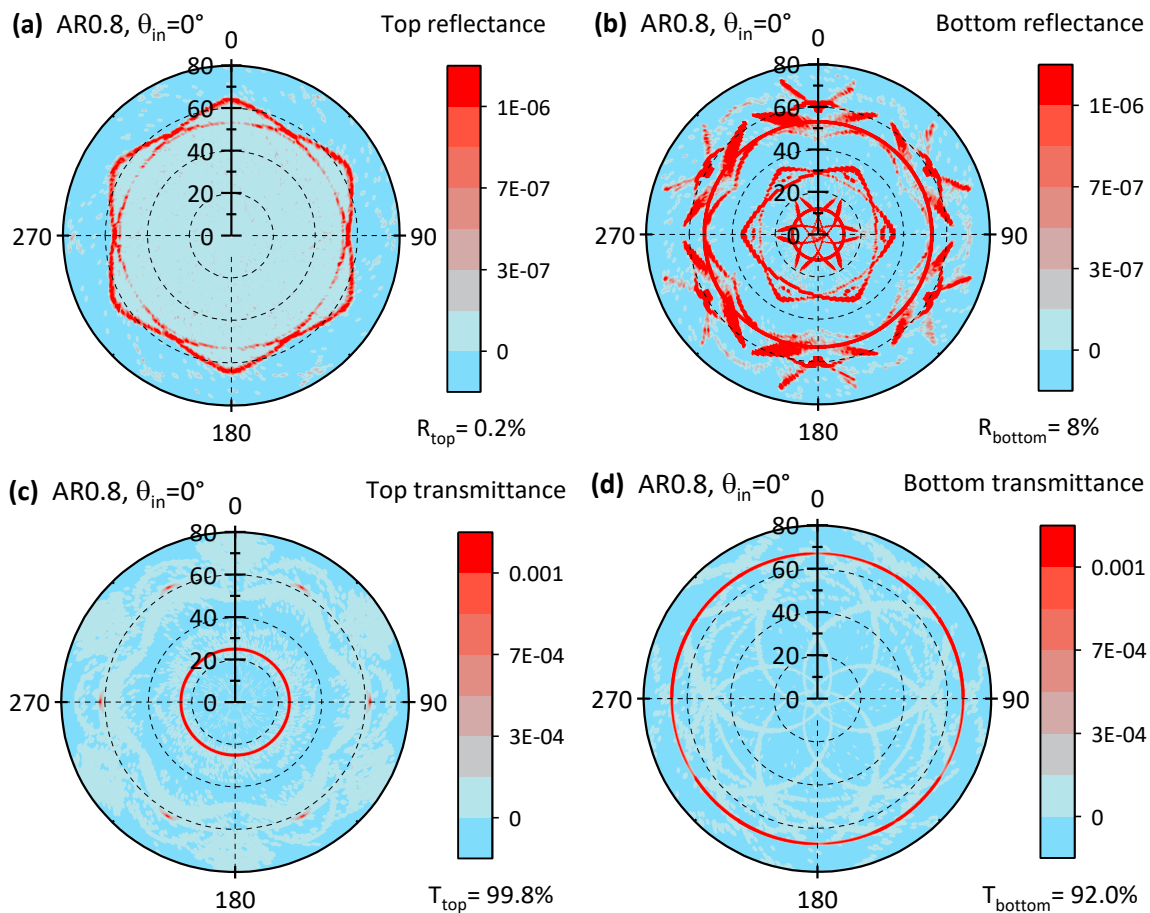


**Figure 5.3.** Angular resolved reflectance and transmittance probability for cones with an aspect ratio  $AR = 0.8$  for light incident under normal incidence. The angular distribution of reflected and transmitted light is displayed for: (a) reflected and (c) transmitted light for top illumination and (b) reflected and (d) transmitted light for bottom illumination.

For the illumination from inside the texture in direction of the air, the reflected light is strongly redistributed as well (see Figure 5.3b) – and the total reflectance increases to  $\approx 8.0\%$  – compared to the planar reflectance of  $\approx 4.8\%$ . This ability to increase reflection and redirect the light back to the solar cell is referred to as retro-reflection. Depending on the actual angle of incidence from bottom, the retro-reflection changes in absolute and angular distribution. For distinct configurations, it can strongly contribute to the light-harvesting properties.

### 5.3 Concept of retro-reflection

As seen by the increased reflectance ( $R_{\text{bottom}}$ ) for light travelling upwards, towards the textured glass/air interface (see previous section), the textures provide excellent properties for retro-reflection. Exploiting this retro-reflection can be beneficial for improved light harvesting inside a photovoltaic (PV) module.

The light harvesting properties of the cones, as well as of the inverted cones, pyramids, and inverted pyramids follows the same concept. First, the angular distribution of light incident at a textured interface is changed. **Figure 5.4** illustrates the redistribution of the incident light by the micro-texture (see green arrows). Assuming a specular reflection (black arrows in c) of the transmitted light at a solar cell, the redistributed light reaches the texture from below under certain angles, which are depended on the texture itself, on the aspect ratio AR and on the angle of incidence. Depending on the geometry of the micro-texture and the angles  $\theta_s$  of the light traveling upwards, retro-reflection occurs at the texture/air interface, which redirects the light back to the solar cell (red arrows).

For an AR of 0.8, the distribution is displayed in **Figure 5.5a**. Typically, for one angle of incidence, multiple propagation angles  $\theta_s$  of the transmitted light are apparent. Compared to the planar interface they are increased for normal and near normal incidence. For oblique angle of incidence, the angular distribution of transmitted light broadens. Similarly,  $R_{\text{bottom}}$  for different angle of incidence  $\theta_{\text{in}}$  broadens and the amount of light being reflected increases with increasing angle of incidence (see Figure 5.5b).

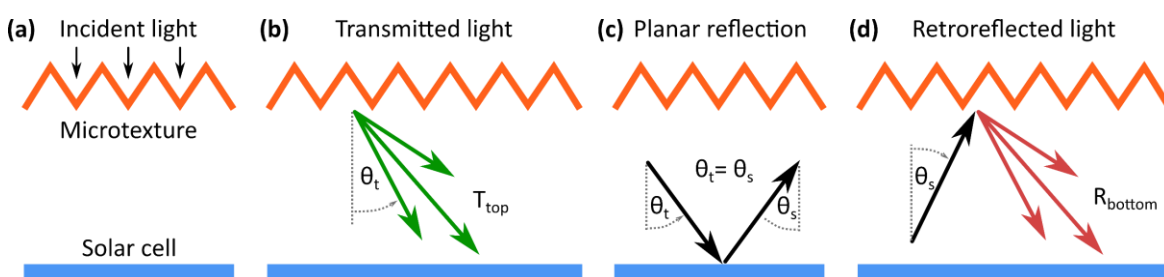


**Figure 5.4.** (a) The incident light is efficiently incoupled and transmitted inside the texture. (b) The transmitted light changes its angular distribution to larger angles. (c) Light, reflected by the solar cell is propagating towards the micro-texture/air interface. (d) Retro-reflection of the light towards the solar cell. Adapted reprinted with permission from ACS Photonics 2017, [145]. © American Chemical Society.

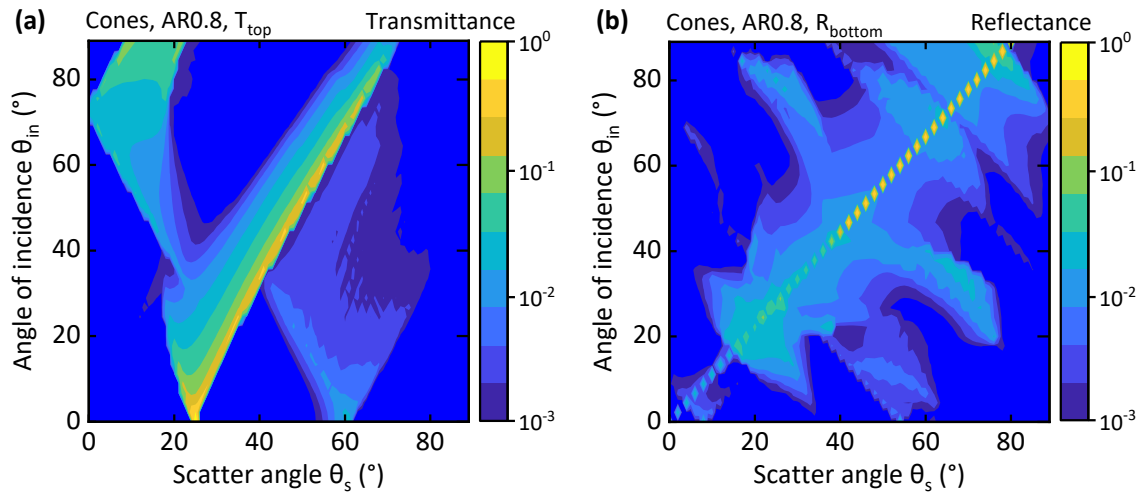


**Figure 5.5.** (a) Transmittance and (b) reflectance of cones with an aspect ratio  $AR = 0.8$ . The angular resolved transmittance and reflectance is displayed for different angle of incidence.

Efficient retro-reflection occurs, when most of the light incident from below is reflected back towards the solar cell, giving it a second chance to be absorbed. This effect is amplified, when high scatter angles  $\theta_s$  are combined with a high probability for reflectance  $R_{\text{bottom}}$  under these specific angles. To estimate the potential of different textures, a retro-reflection coefficient is defined by convoluting the angular resolved transmittance from top  $T_{\text{top}}$  with the angular resolved reflection from bottom  $R_{\text{bottom}}$ .

$$\begin{aligned}
 RR(AR) = & \frac{1}{n} \sum_{\varphi_{\text{in}} 0}^n \int_0^{2\pi} T_{\text{top}}(\theta_{\text{in}} = 0^\circ, \varphi_{\text{in}}, \theta_{\text{out}}, \varphi_{\text{out}}, AR) d\varphi_{\text{out}} \\
 & \cdot \frac{1}{n} \sum_{\varphi_{\text{in}} 0}^n \int_0^{\pi} \int_0^{2\pi} R_{\text{bottom}}(\theta_{\text{in}}, \varphi_{\text{in}}, \theta_{\text{out}}, \varphi_{\text{out}}, AR) d\varphi_{\text{out}} d\theta_{\text{out}} \quad 5.2.
 \end{aligned}$$

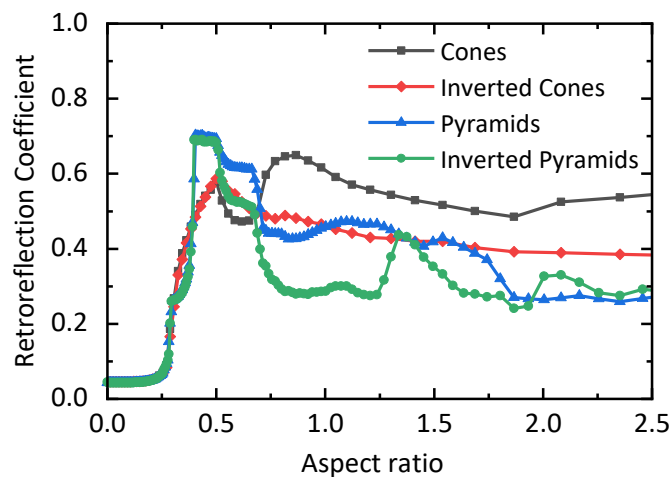


**Figure 5.6.** Retro-reflection coefficient for cones, inverted cones, pyramids, and inverted pyramids for different aspect ratios. The retro-reflection coefficient estimates the potential of different textures to redirect light reflected by the solar cell back to the solar cell.

Here, the angle of incident corresponds to  $\theta_{in}$  and the scatter angle to  $\theta_{out}$ . The calculated retro-reflection coefficient RR is displayed in **Figure 5.6**. For the planar reference, this equals a RR of 4.5%, which exactly matches the assumed probability in a system with parallel interfaces.

The RR however, strongly increases for larger AR. For pyramids and inverted pyramids, the retro-reflection is very strong for an AR = 0.5. Here, around 70% of reflected light will be redirected back towards the solar cell. The cones and inverted cones show retro-reflective properties of around 50%. Unique for the cones, is a second strong increase in the RR for an AR around 0.8. Moreover, compared to the other textures, the RR stays high (>50%) for larger AR.

## 5.4 Light harvesting by retro-reflection in solar cells

To analyze the light harvesting by improved light incoupling and trapping, the different textures are analyzed with various realistic substrates at the rear of the texture. Therefore,

- (a) a perfect absorber, accounting for front surface reflection only;
- (b) a planar silicon surface, determining the retro-reflection on specular reflecting samples;
- (c) a random upright textured silicon surface to investigate the retro-reflection on diffusive reflecting substrates;
- (d) and a semitransparent perovskite solar cell for tandem applications are considered.

The total reflectance  $R_{total}$  for normal incidence and at 600 nm for all four textures is displayed in **Figure 5.7**. The specular resolved total reflectance  $R_{total}(\lambda)$  is provided for micro-cones in **Figure 5.8**. Moreover, the simulated reflectance is compared to experimentally obtained values for micro-cone textures (points in Figure 5.7). Finally, the micro-cones textures are applied on planar and textured silicon solar cells (see **Figure 5.9**) as well as on perovskite solar cells (see **Figure 5.12**). In addition, inverted pyramid textures are shown on perovskite/silicon tandem solar cells (see **Figure 5.13**).

### 5.4.1 Minimizing reflection of different substrates with microtextures

For all textures and all substrates, the total reflectance is strongly reduced starting from AR = 0.5 compared to the planar (AR = 0) reference (see Figure 5.7 and Figure 5.8). The total reflectance  $R_{total}$  for the different textures and aspect ratios is derived by a series expansion of probability matrices for top and bottom reflectance and transmittance  $T_{top}$ ,  $R_{top}$ ,  $T_{bottom}$ , and  $R_{bottom}$  and the reflectance of the substrate  $R_{substrate}$  following the possible ray paths within the textured layer. The angular and specular resolved reflectance of the different substrates used for the calculations is computed with the optics module of the

energy yield framework (see details in chapter 4.4). The refractive indices of the c-Si and perovskite solar cells are summarized in Appendix A.

Combining the optical response of the different substrates with the ones from the different textures by following the rays of light with their specific probabilities, the total reflectance  $R_{\text{total}}$  is then given by the following series expansion:

$$R_{\text{total}} = R_{\text{top}} + T_{\text{top}}R_{\text{substrate}}T_{\text{bottom}} + \sum_{k=0}^{\infty} T_{\text{top}}(R_{\text{cell}}R_{\text{bottom}})^k R_{\text{cell}}T_{\text{bottom}}. \quad 5.3.$$

In case of a perfectly absorbing substrate (see Figure 5.7a), all textures demonstrate a steadily decreased reflectance for larger ARs. Since no light is reflected back from this substrate, the curves equate the reported front reflectance in Figure 5.2. Moreover, the  $R_{\text{total}}$  does not show any wavelengths dependence (see Figure 5.8a).

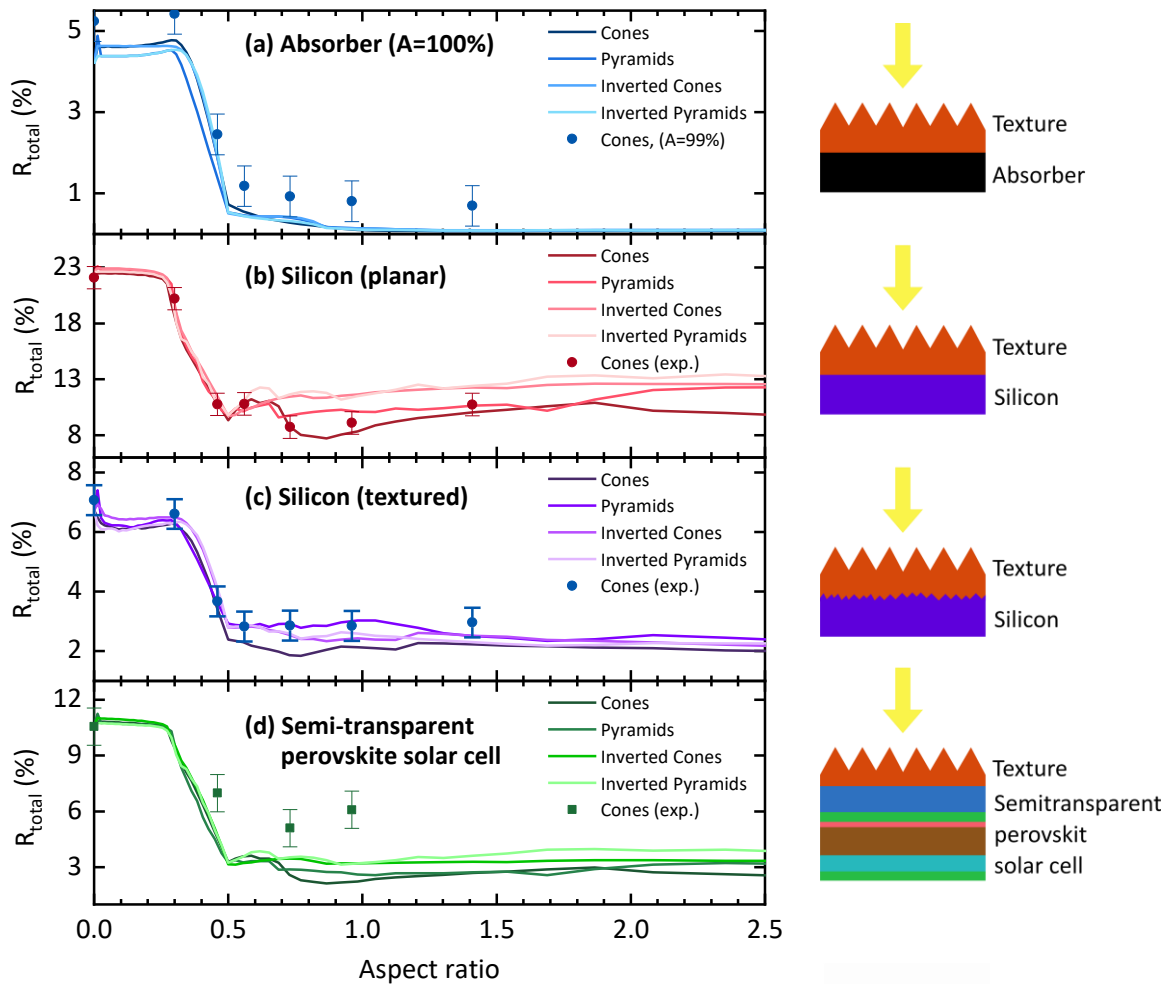


**Figure 5.7.** Total reflectance  $R_{\text{total}}$  for normal incidence of cones, inverted cones, pyramids, and inverted pyramids on (a) a perfect absorber, (b) a planar silicon layer, (c) a textured silicon layer with random upright pyramids, and (d) a semitransparent perovskite solar cell at a wavelength of 600 nm. The points are experimentally measured data of cones out of a UV curable glass-like resist (NOA88). The data in a, b and c is extracted from the collaborative work in ref. [78].

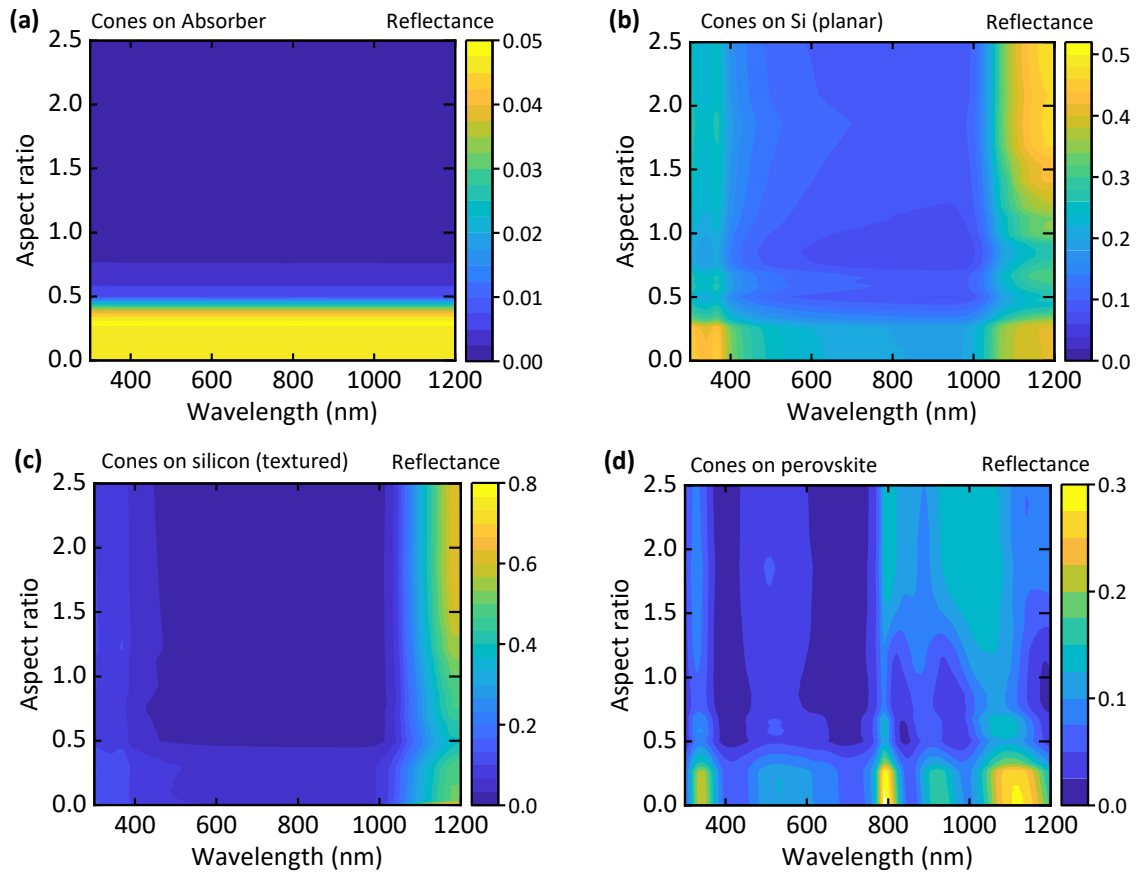


**Figure 5.8.** Specular resolved total reflectance  $R_{\text{total}}$  for different aspect ratios for micro-cones on top of an (a) perfect absorber, (b) a planar silicon, (c) a textured silicon, and (d) a semitransparent perovskite cell. The aspect ratio 0 corresponds to the respective planar reference layer.

For the planar silicon substrate, the retro-reflective behavior of the different textures comes into its own. In contrast to a perfectly absorbing substrate at the back of the texture, a planar silicon layer shows a strong specular reflection. Equipped with a planar encapsulation ( $AR = 0$ ) with refractive index  $n = 1.56$ , the planar silicon substrate reflects around 23% of the incident light at a wavelength of 600 nm. Nevertheless, similar to the absorber, all microtextures on top of the planar silicon substrate lead to a sharp minimum in  $R_{\text{total}}$  at  $AR = 0.5$ . Here, the reflectance is reduced by  $\approx 60\%_{\text{rel}}$  to  $8.5\%_{\text{abs}}$ . Whereas all textures perform equally well at  $AR = 0.5$ , the micro-cones reveal a second minimum with a reflectance of only  $8\%_{\text{abs}}$  for slightly higher  $AR$  of around 0.85. Here, the inverted cones, and both, the pyramids and inverted pyramids demonstrate an increased reflectance. For larger  $AR$  ( $>1.0$ ), the reflectance increases for all the microtextures and reaches  $\approx 10 - 13\%_{\text{abs}}$ . For longer wavelengths ( $\approx 1100 - 1200$  nm), the retro-reflective effect is decreased for high aspect ratios (see Figure 5.8b). Here, the total reflectance is increased compared to the planar reference. On the other side,  $AR$ s between 0.5 and 1.4 demonstrate a very good reduction on the overall reflectance for all wavelengths.

For a diffuse reflecting textured c-Si substrate, this second minimum of total reflectance is less pronounced and shifts to an  $AR$  of 0.75. Moreover, almost no spectral

dependency is visible for the cones on top of the textured silicon substrate (see Figure 5.8c) and increasing aspect ratios do not lead to a significant increase of the total reflectance as for the specular reflecting planar silicon. At 600 nm, all textures perform very well and reduce the reflectance by  $\approx 60\%_{\text{rel}}$ . For high aspect ratios ( $>1.5$ ) all textures demonstrate very low reflectance of  $\approx 2\%_{\text{abs}}$ .

The total reflectance  $R_{\text{total}}$  of the perovskite stack (glass/ITO/SnO<sub>2</sub>/perovskite/spiroOMeTAD/ITO) follows the trend of the planar silicon layer for a wavelength of 600 nm (see Figure 5.7d). The minimal reflectance is given by the cones with an aspect ratio of  $AR = 0.85$ . This optimum hold, as well even after considering the full spectral range of 300 – 1200 nm (see Figure 5.8d). At 600 nm, the reflectance decreases from  $11\%_{\text{abs}}$  to  $\approx 3\%_{\text{abs}}$ .

#### 5.4.2 Micro-cones on planar and textured silicon solar cells

The optical simulations promise strong reduction of the reflection losses by micro-cones with aspect ratios (AR) equal and greater than 0.5. To verify the optical simulations, the conical microtextures are fabricated by direct laser writing (DLW). The DLW process enables to create freeform architectures on the nano- and micro-scale by a two-photon polymerization process (see details in section 3.2.1 and 3.2.2 as well as in ref. [78]). The micro-cones with 25  $\mu\text{m}$  diameter are written with the commercial resist IP-S (Nanoscribe).

In order to verify the trends of the simulations, micro-cones are replicated by an intermediate PDMS mold directly on top of the different substrates (see Figure 5.7) and solar cells (see below). For the replication an UV curable resist (NOA88) is used. The points in Figure 5.7 represent measured values for replicated cones on the four different substrates. The data for the absorber, planar and textured c-Si substrate are extracted from ref. [78]. The measurements show the same trends for the different aspect ratios (0.3, 0.46, 0.56, 0.73, 0.96, and 1.41) and different substrates. For the specular reflecting planar silicon, the two minima ( $AR = 0.5$  and  $AR \approx 0.8$ ) are apparent. In addition, the decrease in  $R_{\text{total}}$  for larger AR is visible for the absorber as substrate. It should be noted that in the experiment an absorber with  $\approx 1\%$  reflectance was used, which explains the offset in Figure 5.2a.

A reduced front surface reflection can lead to an increased absorption in the absorber layer leading to an enhanced external quantum efficiency (EQE). This enhancement in the EQE results in an increase in the short-circuit current density ( $J_{\text{SC}}$ ). The efficient reduction of the front surface reflection of the air/glass interface by the microtextures is exploited in the following to improve planar and commercially alkaline-etched c-Si solar cells (see Figure 5.9).

Moreover, semitransparent perovskite solar cells are examined to enhanced absorption in the perovskite and improve the transmittance for the bottom solar cell (see next section).

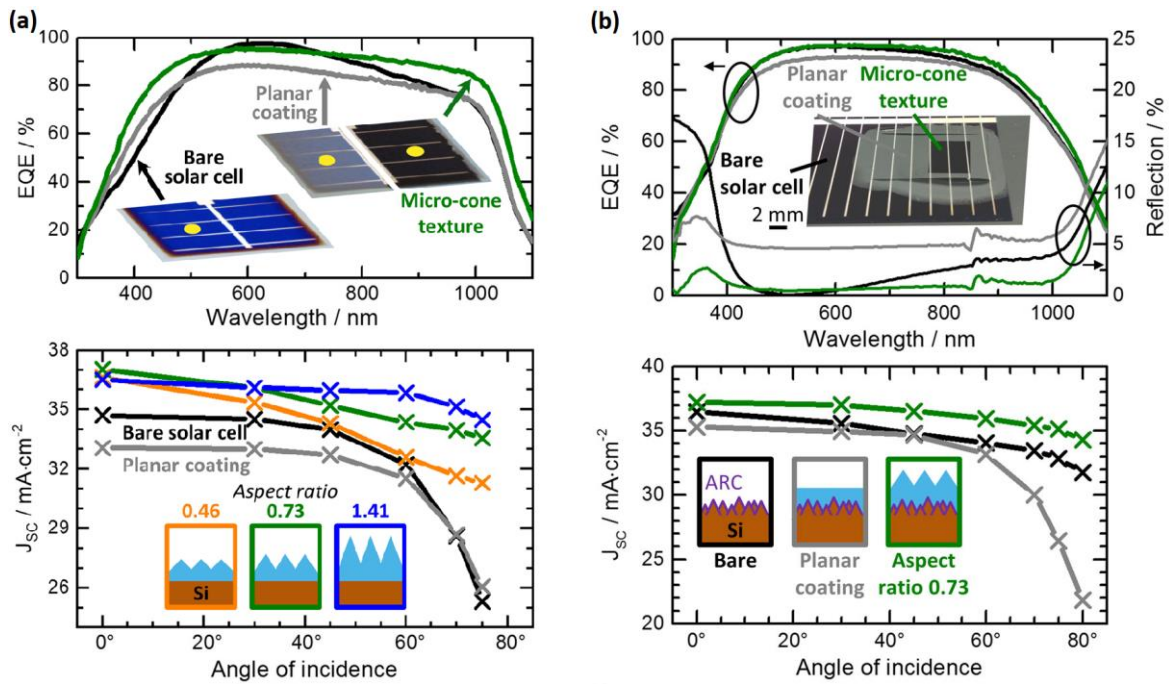


**Figure 5.9.** (a) Planar crystalline silicon (c-Si) and (b) textured c-Si solar cells with cones of different aspect ratios (AR) on top. The external quantum efficiency (EQE) increases broadband for the cones applied on top of the c-Si solar cells. The short-circuit current density ( $J_{sc}$ ) for normal incidence significantly increases compared to the planar reference as well as the bare solar cell (with an anti-reflection coating on top). Moreover, the  $J_{sc}$  of the microtextured c-Si cells demonstrates an excellent angle stability compared to the planar reference. Adapted with permission from ref. [78], © John Wiley & Sons.

Micro-cones with AR = 0.45, 0.73 and 1.41 are replicated on top of the planar silicon solar cell (see Figure 5.9a). All ARs demonstrate an improved  $J_{sc}$ . The highest  $J_{sc}$  is found for an AR = 0.73, which is close to the simulated optimum of AR = 0.85 (see above). For cones with AR = 0.73 on the planar c-Si solar cells demonstrate an enhanced  $J_{sc}$  of 12%<sub>rel</sub> compared to the planar reference. As planar reference, a planar layer of the same resist is used, which matches well with an encapsulation layer of a solar module. Since the bare solar cell is optimized with a thin-film anti-reflection coating (ARC) for air, the  $J_{sc}$  of the silicon solar cell with the planar resist layer is reduced from 34.7 mA·cm<sup>-2</sup> to 33.1 mA·cm<sup>-2</sup>.

Nevertheless, the micro-cones reduce reflection losses of the planar and the bare planar c-Si solar cell and demonstrate a strong and broadband enhancement in the EQE. Only at short wavelengths, the EQE is slightly decreased due to parasitic absorption in the resist material. Moreover, especially the improvement in the EQE for wavelengths above 1000 nm clearly demonstrates the importance of the retro-reflection properties of the micro-cones. Here, the enhancement is ≈15%<sub>abs</sub>, which cannot be explained by the ≈4%<sub>abs</sub> reduction in front surface reflection only (see Figure 5.2).

Here, strong retro-reflection and light trapping due to large transmittance angles are apparent. Moreover, it should be noted that since this enhancement of the EQE and therefore  $J_{sc}$  is only an optical effect of the microtextures, the other electrical parameters of the silicon solar cells are not changed (see Table 2).

**Table 2.** Electrical performance of the planar silicon solar cells with and without micro-cones on top. (Extracted data from the Supporting Information from ref. [78])

	PCE (%)	FF (%)	EQE- $J_{sc}$ (mAcm <sup>-2</sup> )	$V_{oc}$ (mV)
Bare (average)	$17.83 \pm 0.3$	$78 \pm 1$	$34.7 \pm 0.1$	$659 \pm 5$
Planar coating	16.8	78	33.1	651
AR = 0.31	18.2	79	35.4	651
AR = 0.46	18.8	79	36.6	649
AR = 0.56	18.5	77	36.8	653
AR = 0.73	19.4	79	37.0	665
AR = 0.96	19.2	80	36.9	649
AR = 1.41	18.7	78	36.5	656

For oblique angles of incidence, the textured planar silicon cells demonstrate a strong improvement compared to the planar reference as well (Figure 5.9a). A higher aspect ratio (AR = 1.41) turns out to be more beneficial. This matches well with the optical simulations, where higher aspect ratios demonstrated the most stable angular response. For the planar coated reference and the bare solar cell, the Fresnel reflection increases drastically for high angles. For the bare solar cell, the limited use of the thin-film ARC is clearly evident.

Since, the planar c-Si solar cells showed rather high reflection losses, the enhancement of the  $J_{sc}$  by retro-reflective light trapping is relatively high. In order to demonstrate the potential of the micro-cone textures, they are applied as well on top of state-of-the art commercially alkaline-etched c-Si solar cells. The c-Si solar cells show comparably low reflection (see Figure 5.9b). Compared to the planar reference coating, all micro-cone textures improved the  $J_{sc}$  of the c-Si solar cell. Again, the highest enhancement is given by micro-cones with AR = 0.73, which matches well to the simulated optimum of AR = 0.75. Here, the  $J_{sc}$  increases by 5.4% from 35.3 mAcm<sup>-2</sup> (planar reference) to 37.2 mAcm<sup>-2</sup> (micro-cones). This even surpasses the relative improvement by a single layer thin-film ARC on the front encapsulation (glass) cover of  $\approx 3\%$  [148]. In the EQE measurements, a broadband enhancement is visible (see Figure 5.9b). Again, it has to be notated that the micro-cones only improve the optics of the textured c-Si solar cells and therefore do not impair the electrical parameters like FF and  $V_{oc}$  (see Table 3).

**Table 3.** Electrical performance of the textured silicon solar cells with and without micro-cones on top. (Extracted data from the Supporting Information from ref. [78])

	PCE (%)	FF (%)	EQE- $J_{sc}$ (mAcm <sup>-2</sup> )	$V_{oc}$ (mV)
Bare (0.5 cm <sup>2</sup> )	13.0	72	37.9	476
Planar coating	12.3	73	35.3	478
AR = 0.31	12.2	72	35.6	476
AR = 0.46	12.9	73	36.9	479
AR = 0.56	12.7	72	36.9	477
AR = 0.73	13.0	73	37.2	478
AR = 0.96	12.9	73	37.0	479
AR = 1.41	13.0	73	36.9	482

For oblique angles of incidence, the relative enhancement increases for larger angles as well as for higher aspect ratios. The planar reference shows strong Fresnel reflections for large angle of incidence. The micro-cones demonstrate a similar stable angle behavior as the bare solar cells, but with superior  $J_{SC}$  for all angles of incidence (see Figure 5.1d).

### 5.4.3 Optical analysis of microtextures for semitransparent perovskite/c-Si tandem solar cells

The strongly reduced reflection of the examined microtextures – especially of the micro-cones – leads to a significant improvement of the absorption and thus also of the  $J_{SC}$  and PCE of the demonstrated c-Si solar cells. In the following, the use of these microtextures is discussed for semitransparent perovskite/c-Si tandem solar cells. For this, cones and inverted pyramids are chosen and analyzed by optical simulation and in experiment. Since the microtextures reduce the reflection broadband, the absorption in the perovskite layer – and moreover the transmittance into the bottom c-Si solar cell – could be enhanced significantly. This improves the overall tandem PCE.

#### Optical simulations

First, the optical response of the cones and inverted pyramids is simulated on top of a semitransparent perovskite solar cell. Therefore, the perovskite solar cell is defined by the following stack: air / glass / ITO front (135 nm) / SnO<sub>2</sub> (10 nm) / perovskite  $E_g = 1.55$  eV (550 nm) / spiro-OMeTAD (280 nm) / ITO cold (160 nm) / air. The refractive indices of all the materials are summarized in Appendix A.

The optical simulations are performed with the optics module within the energy yield (EY) framework. In this regard, the angular resolved reflectance  $R$  and transmittance  $T$  of the textured interfaces for top and bottom illumination are used to define the effective interface of the front glass cover (see section 4.4). Therefore, the optical simulations combine the microtextures with the thin-film perovskite stack.

For cones and inverted pyramids (see **Figure 5.10a** and **b**), the reflectance of the semitransparent perovskite solar cell decreases very broadband  $\approx 10\%_{abs}$ . As already illustrated in Figure 5.7d, the reflectance decreases similar for both textures with an AR of 0.5 and slightly stronger for the cones with an AR of 0.8. The reduced reflectance leads to an increase in the absorption  $A$  in the perovskite layer by  $\approx 10\%_{abs}$  for both AR and both textures. However, the enhanced light incoupling is not directly translated to the amount of transmitted light. The transmittance (weighted with the AM1.5g spectrum) into air for an AR of 0.5 increases compared to the planar reference by  $5\%_{rel}$ . For an AR of 0.8, the transmittance even reduces again, compared to the planar reference (see Figure 5.10a and **b**). Only for ARs below 0.7 the microtextures lead to an improvement in both, the absorptance in the perovskite and an improvement in the transmittance (see **Figure 5.11a**).

This discrepancy is explained by the decreased probability of light-outcoupling at the ITO/air interface due to the larger propagation angles (compare Figure 5.5a) within the perovskite layer stack. Since the textures redirect the light to larger angles within the glass, the propagation angle inside each layer and especially in the ITO rear electrode is enlarged. Due to the larger angles, the out-coupling probability decreases and a portion of the light is reflected back towards the texture.

In the case of the c-Si solar cell, the texture provides by its retro-reflective properties another chance for the light to be redirected towards the c-Si. However, for the thin-film perovskite solar cell, the upwards traveling light leads to an increase in the perovskite absorption for wavelengths below the band gap of the perovskite absorber, and much more clearly to an increase of the overall parasitic absorption within the perovskite solar cell (see Figure 5.11b).

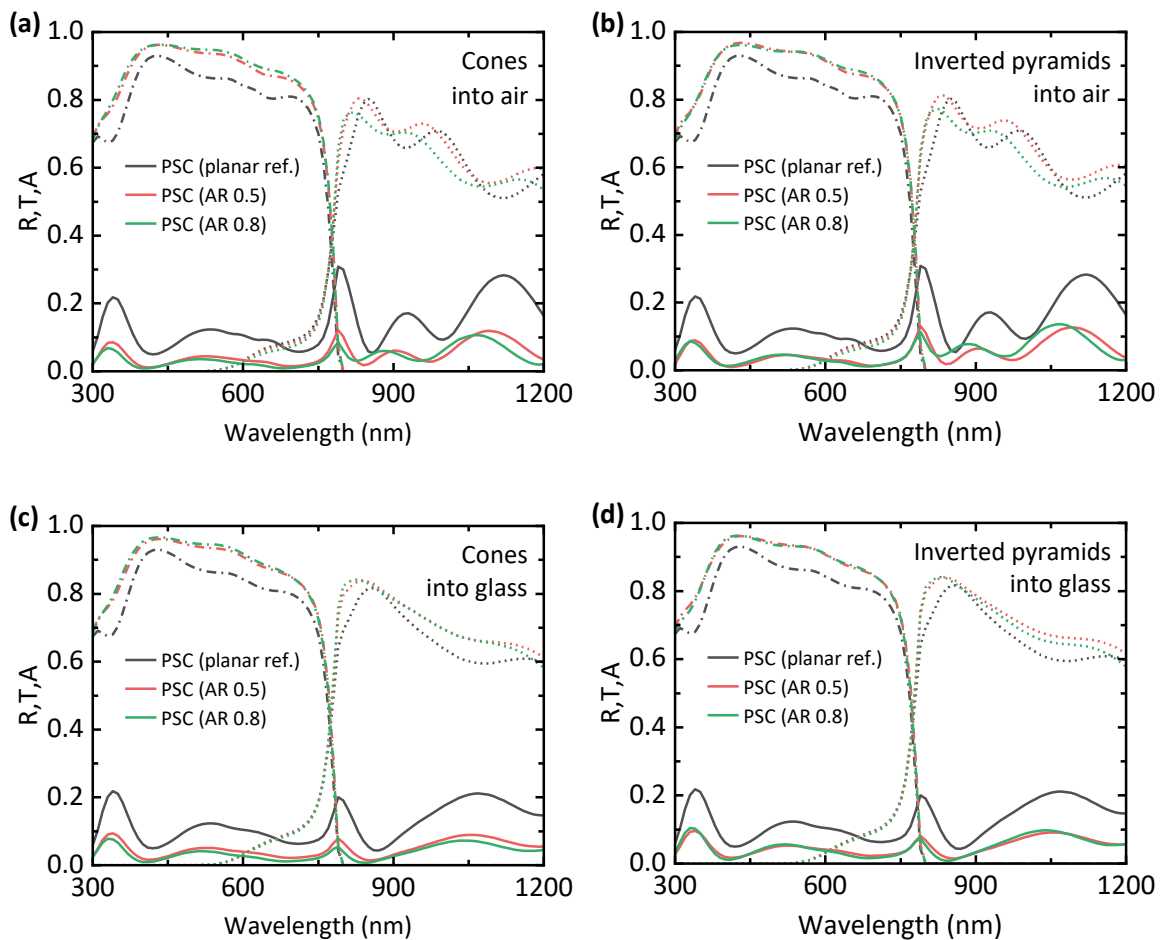


**Figure 5.10.** Reflectance  $R$  and transmittance  $T$  of the simulated semitransparent perovskite solar cell as well as the absorptance  $A$  in the perovskite layer itself. (a)  $R, T, A$  for cones and (b) inverted pyramids with  $AR = 0.5$  and  $0.8$  on top of the semitransparent perovskite solar cell. At the rear of the simulated device air is assumed. (c)  $R, T, A$  for cones and (d) inverted pyramids with  $AR = 0.5$  and  $0.8$  on top of the semitransparent perovskite solar cell. At the rear of the simulated device glass is assumed.

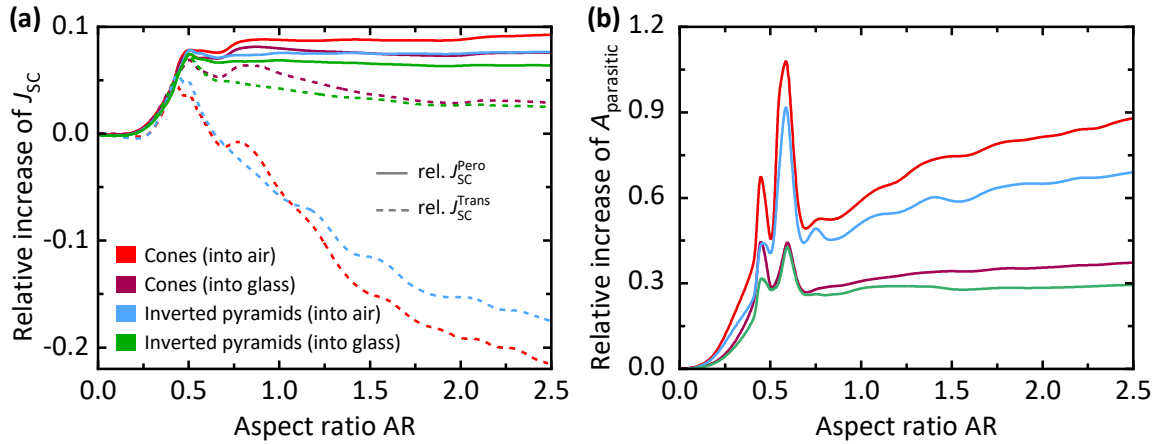


**Figure 5.11.** (a) Relative change of the short-circuit current density  $J_{SC}$  of the perovskite absorber and the transmitted light for the cones and inverted pyramids of different aspect ratios (AR) on top of the semitransparent perovskite solar cell. (b) Relative change of the parasitic absorption  $A_{\text{parasitic}}$  as a function of the AR for cones and inverted pyramids on top of the semitransparent perovskite solar cell.

In order to increase the transmittance into the bottom c-Si solar cell, the optical coupling between two sub solar cells of the tandem has to be improved. The best match will be achieved for a gradual change in the refractive index between the rear ITO of the perovskite and the front conductive oxide of the c-Si solar cell. Experimentally this is challenging and the most straightforward way would be to use existing encapsulation materials (see e.g. Figure 4.6) like ethylene-vinyl acetate (EVA), which has a refractive index close to glass ( $n = 1.5$ ). In this regard the probability to outcouple is enhanced compared to air with  $n=1$ . The transmitted light into a glass-like layer (labeled with ‘into glass’ in the Figures) increases for both microtextures and for both AR (see Figure 5.10c and d). Here, an infinite glass layer instead of air is assumed at the rear of the ITO back electrode.

In terms of relative improvement of the respective  $J_{SC}$  of the absorbed light in the perovskite top solar cell and the portion of transmitted light, the AR of 0.5 performs best for all textures and considerations (see Figure 5.11a). Here, the perovskite gains  $\approx 8\%_{\text{rel}}$  in  $J_{SC}$  (solid lines), the c-Si could gain  $\approx 5\%_{\text{rel}}$  due to the enhanced transmittance (dashed lines). Overall, the cones and inverted pyramids improve the absorptance compared to the planar reference for all ARs. The transmittance demonstrates a maximum at  $AR = 0.5$ . For  $AR > 0.5$  and in case of air as optical coupling layer (simulation performed “into air”), the transmittance decreases strongly. However, due to the better match of the refractive indices at the rear of the stack, the transmittance increases into the glass layer compared to the air as optical coupling layer. Here again, all ARs lead to an enhanced transmittance compared to the planar reference. Since more light is reaching the c-Si solar cell, this also reduces the parasitic absorption of the top perovskite solar cell (see Figure 5.11b). The strong parasitic absorption in the case of air at the rear of the ITO electrode, is mainly located in the front and rear ITO.

Overall, the inverted pyramids and cones demonstrate a solid improvement in the absorptance of the perovskite layer and below an AR of 0.7 as well in the total transmittance. In particular, at an AR = 0.5, the inverted pyramids show a comparatively lower parasitic absorption and an adequately improved transmission.

### Experimental verification

In order to experimentally examine the cones and inverted pyramids, both textures have been fabricated and implemented on top of the front glass cover of the semitransparent perovskite solar cell. In the following, the optical performance is discussed only for the transmittance into air, since it is experimentally challenging to account for a glass-like optical coupling layer at the rear. However, the final 4T tandem solar cells, are probed with an intermediate coupling layer (see next section).

The conical textures are replicated into fluorinated ethylene propylene (FEP) by a hot embossing process with a nickel mold (see ref. [149] for a detailed description), which is similar to the thermal nanoimprint lithography (TNIL) process (see section 3.2.3). The inverted pyramids are fabricated by replication of an alkaline etched c-Si wafer. This led to a thin flexible textured polydimethylsiloxane (PDMS) layer, which could be easily attached to the front glass of the semitransparent perovskite solar cell. The replicated etched c-Si wafer resulted in random inverted pyramids with an AR of 0.7.

Although the two approaches are somewhat different, the concept of the proposed working principle is examined. First, the replicated cones are tested on top of the perovskite solar cell (see **Figure 5.12a**). A similar behavior is observed in the overall reduction of the reflectance for both AR of 0.5 and 0.8. Moreover, the reduced reflectance translates to a similar enhancement in the total absorptance of the semitransparent perovskite solar cell of 7%<sub>abs</sub>. In this regard,  $R$  decreases more for the cones with AR = 0.8, which matches with the simulated results (see above).

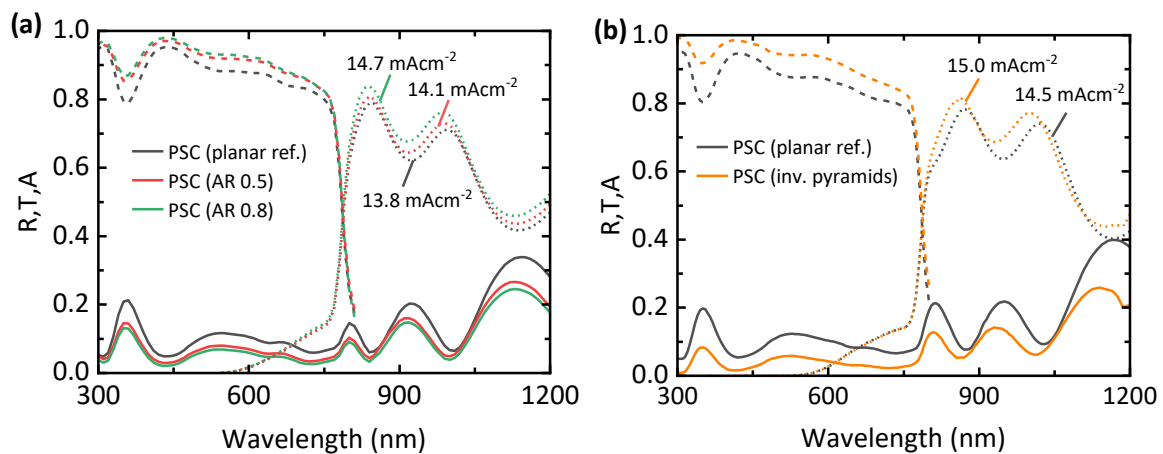


**Figure 5.12.** Measured reflectance  $R$  and measured transmittance  $T$  of the fabricated semitransparent perovskite solar cell as well as the total absorptance in the full device ( $A=1-R-T$ ). (a)  $R$ ,  $T$ ,  $A$  for cones in FEP with AR = 0.5 and 0.8 and (b) inverted random pyramids in PDMS with AR = 0.5 on top of the semitransparent perovskite solar cell glass front side.

In addition to the enhancement in the absorption, the cones increase the transmittance as well. Both ARs (0.5 and 0.8) improve the transmittance of the planar reference by 2%<sub>rel</sub> and 7%<sub>rel</sub>, respectively. It should be noted that the enhancement by the cones of AR = 0.8 measured does not perfectly match the simulations. However, the cones are replicated in FEP and attached with an index matching liquid ( $n = 1.46$ , Thorlabs G608N3) in between. The FEP has a slightly smaller refractive index ( $n \approx 1.34$  @560 nm) than the glass-like textures as it is assumed for the simulations and therefore can also contribute by an additional anti-reflective effect ( $\approx 2\%$ ), due to a smoother gradient in the refractive indices. Moreover, due to the smaller refractive index, the enlargement of the transmittance angle is deferred towards higher AR.

In addition, the replicated inverted random pyramids are tested on top of another semitransparent perovskite solar cell. Due to the constant inclination angle of the c-Si pyramids of  $54.7^\circ$ , the AR of the inverted pyramids is 0.7. Similar to the cones, the inverted pyramids inside PDMS ( $n \approx 1.42$ , @560 nm) demonstrate a strong reduction on the overall reflectance of  $\approx 10\%$ <sub>abs</sub>, which is reflected in an equivalent enhancement of the absorptance. Moreover, the transmittance of the texture applied to the front glass of the device increases by  $\approx 3\%$ <sub>rel</sub>.

To conclude, the microtextures demonstrate an improvement in the overall absorptance and transmittance of the semitransparent perovskite solar cells, and thus will improve the tandem PCE. However, in contrast to the predictions for the planar and textured c-Si solar cells, the evaluation of the total reflectance is not enough to characterize the optimum texture or aspect ratio. Due to parasitic absorption of the other layers within the thin-film perovskite solar cell, the transmittance decreases for large AR. Therefore, in terms of PCE, the optimum AR for textures with a refractive index similar to glass, is located at an AR of 0.5.

#### 5.4.4 Inverted pyramids for enhanced light harvesting in perovskite / c-Si tandem solar modules

Similar to the inverted random pyramids in PDMS with an aspect ratio (AR) of 0.7, inverted pyramids with an AR of 0.5 were tested on top of a perovskite/c-Si mini module with 4 cm<sup>2</sup> in size. The work derived from a collaboration with the group of Jef Poortmans (see Jaysankar *et al.* [150]). The inverted square pyramids are imprinted in a polyethylene terephthalate (PET) film and glued on the front glass cover of a completed semitransparent perovskite top solar cell (see **Figure 5.13a-c**).

In the semitransparent top perovskite solar cell, a CsFAPbI<sub>3</sub> perovskite absorber layer is used. The bottom solar cell is an interdigitated back contact (IBC) c-Si solar cell. The c-Si solar cell has a textured front surface consisting of random upright pyramids. In addition to the front texturing, a SiO<sub>2</sub> passivation layer and a thin SiN<sub>x</sub> anti-reflection coating are applied (for more details on the architecture see ref. [150]).

The inverted pyramid texture mainly reduces the reflectance losses at the front air/glass interface and increases the transmittance in the bottom solar cell in the range of 800 - 1200 nm (see Figure 5.13d). Whereas the short-circuit current density ( $J_{SC}$ ) in the perovskite top solar cell improves only minor by inverted pyramid textures from 20.0  $\text{mAcm}^{-2}$  to 20.1  $\text{mAcm}^{-2}$ , the improved transmittance leads to an absolute increase of 1  $\text{mAcm}^{-2}$  in current of the bottom c-Si solar cell. Here, the  $J_{SC}$  increases from 14.1  $\text{mAcm}^{-2}$  to 15.1  $\text{mAcm}^{-2}$  for the textured foil applied on the front glass cover.

An improved matching of the refractive indices between the rear ITO and the textured c-Si solar cell with an index matching liquid (refractive index  $n = 1.5$ ), the  $J_{SC}$  increases by  $\approx 11\%$  to 15.6  $\text{mAcm}^{-2}$ . This underlies once again the importance of the optical coupling layer with  $n = 1.5$  instead of air with  $n = 1$ , as it was already discussed in the previous section (see Figure 5.10 and Figure 5.11).

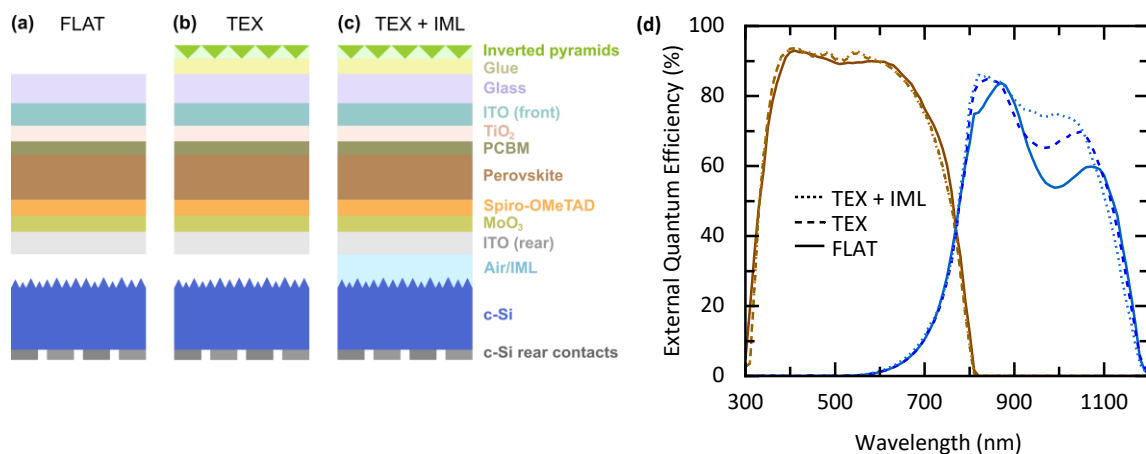


**Figure 5.13.** Schematic of the perovskite/c-Si tandem solar cell in the (a) planar (=FLAT), (b) textured (=TEX), and (c) textured configuration with additional index matching liquid (IML) between the top and bottom solar cells (=TEX+IML). (d) Measured external quantum efficiency (EQE) of the semitransparent perovskite top (brown) solar cell and the IBC c-Si bottom solar cell (blue) for the three configurations displayed in (a-c). Adapted with permission of The Royal Society of Chemistry from ref. [150].

The enhancement in the  $J_{SC}$  boosts the PCE of the bottom cell from 7.8% to 8.6% and therefore improves the overall 4T tandem efficiency from 23.1% to of 23.9% for an active area of 4  $\text{cm}^2$  and 25.3% for 0.13  $\text{cm}^2$ . This equates an enhancement of 3%<sub>rel</sub> and 10%<sub>rel</sub> tandem efficiency, respectively. These improvements match very well with the predicted improvements in the  $J_{SC}$  by the simulations and experiments in the previous section (see Figure 5.11a). Here, the enhancement in the  $J_{SC}$  also increases for the encapsulation layer with  $n = 1.5$  instead of  $n = 1$  as optical spacer layer. Besides, it should be noted that by the time of this study, this has been the highest reported PCE for a perovskite/c-Si tandem solar cell with aperture area larger than 0.5  $\text{cm}^2$ . Moreover, both, the planar 4T perovskite/c-Si tandem as well as the textured tandem exceed the PCE of the stand-alone c-Si solar cell (23.0%) used for this study.

## 5.5 Biomimetic retro-reflection

Microtextures demonstrate excellent improvements in light harvesting by reducing the front surface reflection and providing retro-reflective properties. So far, the microtextures were analyzed by optical simulations. Moreover, enhancements in the short-circuit current density ( $J_{sc}$ ) of planar and textured c-Si as well as perovskite and perovskite/c-Si tandem solar cells have been experimentally demonstrated (see section 5.4).

Up to now, microtextures have been fabricated artificially or by replication of the alkaline-etched c-Si surface (see above). However, many species in nature exhibit remarkable functionalities like ingenious surface functionalities. The research field of biomimetics examines such biological species and processes of nature with view in transferring elaborated concepts to beneficial technologies and applications for engineering usage. The development of natures' species usually has followed millions of years of evolution with the necessity of the species to evolve through natural selection. Therefore, varieties of different surface properties have already evolved by nature's evolution, which conquer a multitude of different technological challenges. In this regard, plant leaves, insects, reptiles and even marine life provides surface textures ranging from a few tens of nanometers to hundreds of micrometers [151]. Especially, plant surfaces demonstrate similar conical textures as the ones designed artificially (see above) with aspect ratios of up to  $AR = 1.2$ . The conical microtextures on the plants surfaces demonstrate a strong interaction with sunlight [152]. Hereby, leaves ensure the survival by providing energy, while the petals of the plants secure the reproduction by efficiently attracting pollinators by high color saturation [153,154].

Schulte *et al.* [151] studied the transfer of different plant textures and proposed new optical properties of plant surfaces. As a general guideline, Hünig *et al.* [155] identified the aspect ratio (AR) of various plants as key parameter for good light harvesting properties. In this regard, the AR of the conical surface elements correlate with reduced reflection losses at the air/texture interface. This observation matches very well with the simulated and measured artificial microtextures (see section 5.4).

The investigated petals of different plants demonstrate significantly different reflection properties. A selection is provided in **Figure 5.14**, the reflectance of different plant textures replicated on top of an (almost) perfectly absorber foil (d-c-fix, Konrad Hornschuch AG, D-74679, Weissbach) are shown in (a) for all angles of incidence at a wavelengths of 560 nm and in (b) spectrally resolved at an angle of incidence of  $60^\circ$ . In Figure 5.14c, the corresponding scanning electron microscopy (SEM) images display the micron-sized scale of the textures. The low AR *Papaver rhoeas* (red poppy) reduces reflectance only for large angle of incidence, compared to a planar air/glass interface. Plant textures with a higher aspect ratio ( $AR \approx 0.6$ ) demonstrate a smaller front surface reflectance (e.g. *Red naomi*, *Rosa 'El Toro'*). Since, the replicated plant textures are in the micron-scale, the effect on the reduced reflection is broadband.

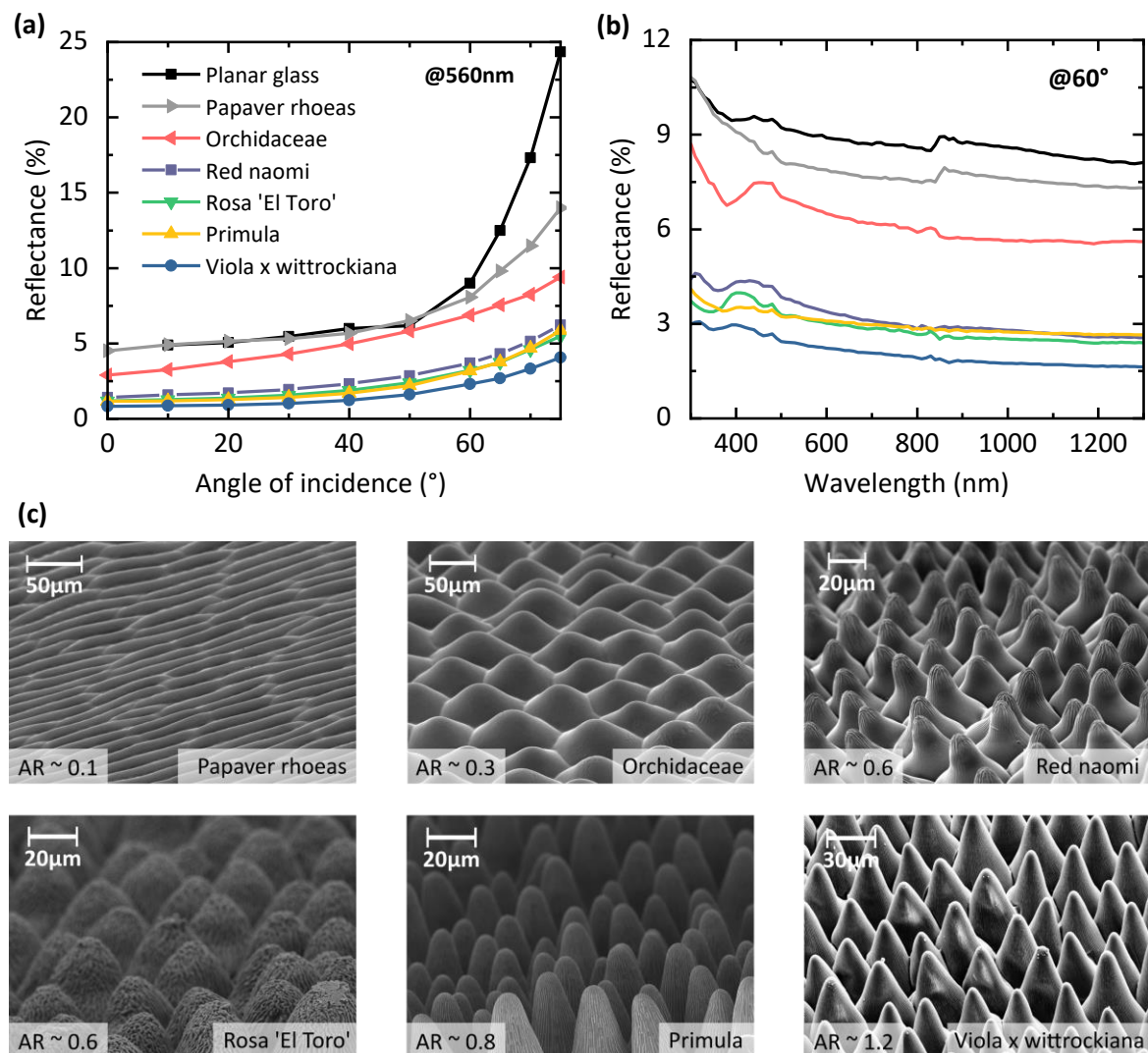


**Figure 5.14.** (a) Reflectance of different plant textures at 560 nm for different angles of incident. The textures are replicated on top of an almost perfectly absorbing foil. (b) Reflectance of same plant textures at an angle of incidence of 60° spectrally resolved. (c) The scanning electron microscopy images of the replicated plant textures give visualize the increased aspect ratio. For higher aspect ratio of the microtextures, the reflectance reduces broadband and omnidirectional. It can be seen, that the texture of the viola (*viola x wittrockiana*) shows by far the lowest reflectance. Adapted reprinted with permission from ACS Photonics 2017, [145]. © American Chemical Society.

It was found, that for all angles of incidence, the texture of the *viola x wittrockiana* petal outperforms all other plant textures. The aspect ratio of the *viola* petal is  $\approx 1.2$ . For an angle of incidence of 75°, the reflectance is only  $\approx 4\%$ . This even is slightly less than the reflectance at normal incidence ( $\approx 4.8\%$ ) of the planar reference for normal incidence and around 84% less for the same angle of incidence. Compared to the simulated cones with perfect and smooth shape, the replicated *viola* texture with cones of  $AR \approx 1.2$ , performs equally well for large angle of incidence, but still shows a measurable reflectance for near-normal incidence (see Figure 5.2). This may result from the small remaining reflectance from the absorber foil ( $R \approx 1\%$ ) and due to the measurement error of the spectrophotometer.

Compared to the perfect periodic optical simulations (see Figure 5.1), the viola texture as well as the other replicated textures exhibit a certain amount of disorder of their (mostly) conical texture elements. The disorder mainly broadens the propagation angle range for every angle of incidence. But, according to Fritz *et al.* the light harvesting performance of conical textures are almost unaffected by the perturbations size, tilt and position [147]. The strongest influence is the found in the distribution of aspect ratios, whereas the mean aspect ratio is decisive for the optical performance.

Based on these promises, the viola petal texture is studied as light harvesting texture for photovoltaic. Therefore, the texture is replicated on top of a planar c-Si solar cell (see **Figure 5.15**). The improved light harvesting properties by enhanced light incoupling and retro-reflection are analyzed in the following. Moreover, the contribution of the nano-scale wrinkles is investigated (see Figure 5.15c).

The replication of the viola petal is done by casting a PDMS mold out of the fresh viola petal. With the cured PDMS mold, a UV-curable resist (NOA88, from Norland Products Inc.) is used to replicate the viola texture directly on top of the planar c-Si solar cell. The process of replication is analog to section 5.4 and more details can be found in section 3.2.2.

Compared to the planar reference, the PCE of the c-Si solar cell is enhanced by  $\approx 6\%_{\text{rel}}$  for the device equipped with the viola texture on top (see **Figure 5.16a**). As planar reference, a planar encapsulation of the c-Si solar cell with the same resist material is used. This configuration mimics best the relevant architecture in a solar module. Even though the pristine planar c-Si solar cell had a thin film ARC (70 nm ITO layer) optimized for light incident from air, the viola textured c-Si cell, improves the PCE by  $3\%_{\text{rel}}$ . It should be noted that in comparison to the artificial cones (see above), the improvement is slightly smaller.

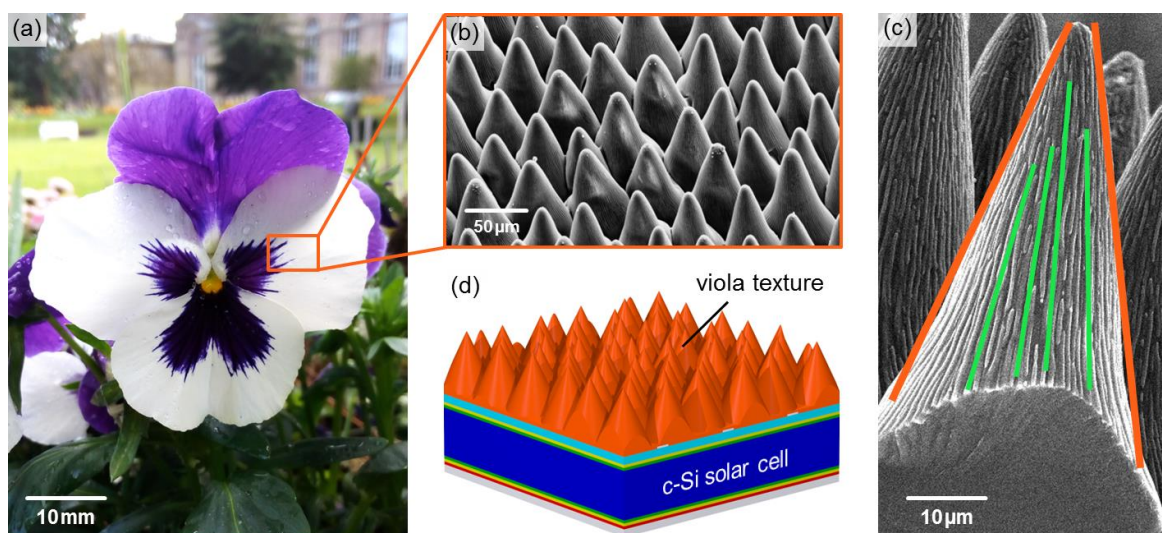


**Figure 5.15.** (a) Photograph of the viola petal (species: *Viola × wittrockiana*). A scanning electron microscopy (SEM) image of the replicated viola surface from the top (b) and side (c) illustrates the micro-cone arrangement as well as the nano-wrinkles (shown with green lines) decorating the micro-cones (bounded by orange lines). A schematic illustration (d) displays the planar heterojunction silicon solar cell with applied viola texture. Reprinted with permission from ACS Photonics 2017, [145]. © American Chemical Society.

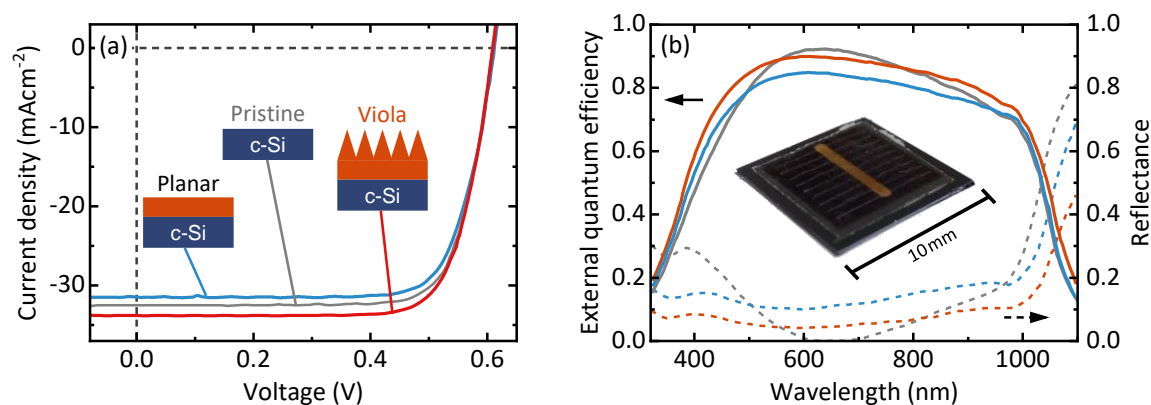


**Figure 5.16.** (a) Current density-voltage characteristic of the planar c-Si solar cells. Compared to the planar reference layer, the viola texture applied on top of the c-Si solar cell shows an enhanced current density. (b) Corresponding external quantum efficiency EQE (solid lines) and reflectance (dashed lines) of the solar cells. The inset illustrates the replicated viola surface texture on top of the device. Reprinted with permission from ACS Photonics 2017, [145]. © American Chemical Society.

This shortcoming can be contributed to multiple possibilities: (1) the overall thickness of the NOA88 layer was thicker and therefore parasitic absorption could be increased; (2) due to the disorder and natural defects on top of the replicated texture, there is an offset to the artificial defect free surface; and (3) the broadening of the transmittance angular space due to disorder as well as the nano-wrinkles (see below) may lead to a reduced retro-reflective light trapping.

However, this first demonstration clearly shows the great potential of biological textures. Similar to the artificial cones, the viola micro-texture does not affect the electrical parameters of the solar cell and only improves the light harvesting of the silicon solar cell. Therefore, the FF and  $V_{OC}$  are hardly affected by the viola-texture (see Table 4).

**Table 4.** Electrical parameter of a pristine planar c-Si solar cell as well as the planar silicon solar cell equipped with a planar resist layer of NOA88 and the viola texture within the same material.

	PCE (%)	FF (%)	EQE- $J_{SC}$ (mAcm <sup>-2</sup> )	$V_{OC}$ (mV)
Pristine	15.0	76	32.8	600
Planar	14.6	76	31.6	610
Viola texture	15.5	76	33.8	605

As shown in Figure 5.16b, the improvement of the  $J_{SC}$  by the viola texture compared to the planar and pristine device is based on a broadband reduction of reflection. The reduced reflection directly translates to a broadband increase of the external quantum efficiency of the c-Si solar cell. Although, the EQE is reduced for wavelengths  $\approx 600$  nm due to the suppression of the ARC coating on the pristine device, the overall enhancement of the viola texture is clearly visible.

The cones, found on the viola petal and therefore on the replicated viola surface texture, feature disorder in their aspect ratio. For a single aspect ratio, the texture produces a discrete intensity distribution of the transmitted light (compare Figure 5.3). To account for a broad range of different cones, a moving average over cones with aspect ratios between 0.9 and 1.5 is performed. By a moving average calculation, the multitude of aspect ratios is considered and a more realistic model is obtained. Due to the distribution in the aspect ratio of the cones, the angular resolved transmittance and reflectance broadens (see Figure 5.17e).

The disorder of the viola micro-texture redistributes the light to a broad maximum at a transmittance angle of  $\approx 30^\circ$ . For light being reflected and not absorbed in the first pass, light will travel with the same angular distribution towards the texture/air interface (Figure 5.17f). For the viola texture, around 60% of the light will be retro-reflected back towards the solar cell and gets a second chance to be absorbed. This is in good agreement with the result for single aspect ratio cones reported above (see Figure 5.6).

A key difference between the smooth artificially processed cones and the cones on the viola petal are additional surface wrinkles. The dimensions of the wrinkles reside in the order of the visible wavelength regime ( $\approx 500$  nm). Therefore, the optical working principle of the wrinkles are simulated by the finite-difference time-domain (FDTD) method, accounting for the wave-optical effects involved. The nano-wrinkles were simulated with the FDTD method for several wavelengths, planes and angles of incidences.

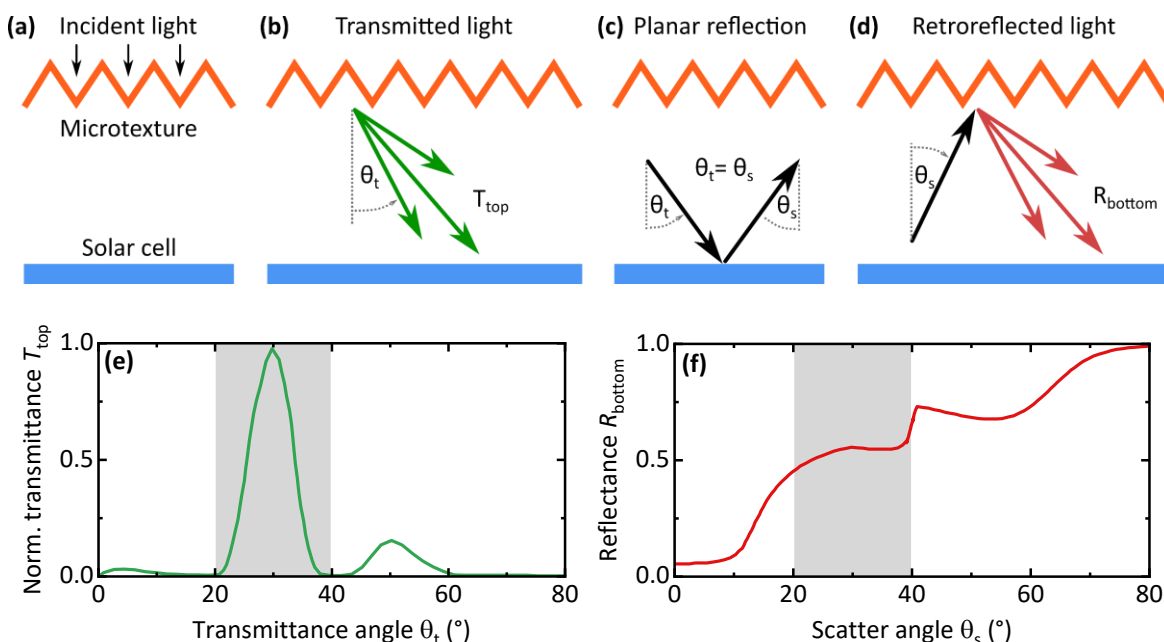


**Figure 5.17.** Moving average of ray tracing simulation on micro-cones of aspect ratios between 0.9 and 1.5, which is similar to the distribution found on the viola petals. For normal incidence, the (a) normalized angular distribution of the transmitted light broadens. (b) Light being reflected at the planar silicon solar cell efficiently will be retro-reflected for large scatter angles towards the solar cell. Adapted reprinted with permission from ACS Photonics 2017, [145]. © American Chemical Society.

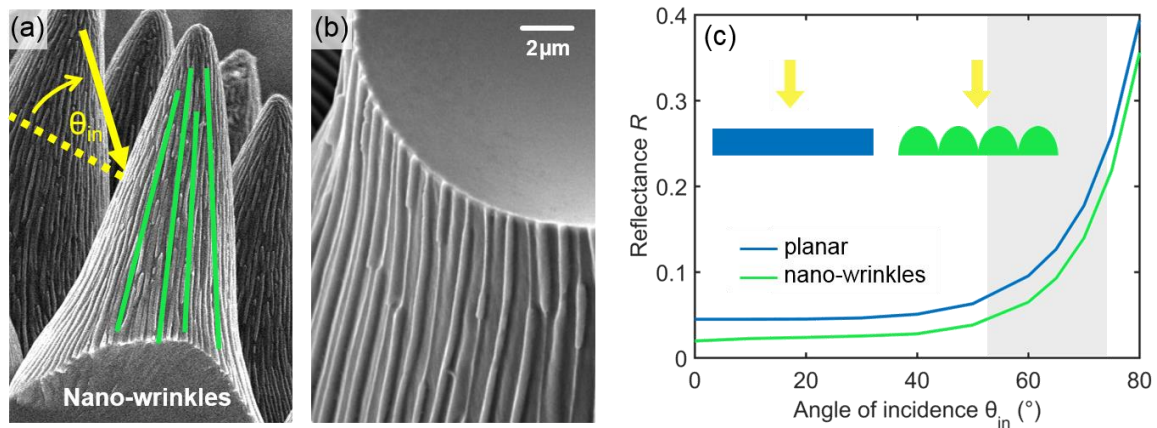


**Figure 5.18.** Reflectance of the nano-wrinkles found on the viola texture. (a) The scanning electron microscopy (SEM) image of the viola surface texture illustrates the angle of incidence  $\theta_{in}$ , which is defined to the surface normal of the wrinkles lying on the cones. (b) The zoomed in SEM image indicates the dimensions of the wrinkles. (c) Finite difference time domain (FDTD) simulations of the integrated reflectance for the nano-wrinkles compared to a planar reference layer. Adapted reprinted with permission from ACS Photonics 2017, [145]. © American Chemical Society.

By averaging the planes of incidence for each angle of incidence, the unpolarized illumination is obtained. In **Figure 5.18**, the reflectance is averaged over the relevant wavelength range of 300 – 1100 nm. It can be seen, that compared to a planar layer of same refractive index, the nano-wrinkles reflect much less of the incident light. While  $\theta_{in} = 0^\circ$  corresponds to the dashed line in Figure 5.18a, normal incidence on the viola texture is visualized by the greyed area in Figure 5.18c. Therefore, the omnidirectional decrease of reflection by the nano-wrinkles on top of the micro-cones act as an additional anti-reflection coating. Altogether, both, the anti-reflection effect of the nano-wrinkles and the enhanced light incoupling as well as retro-reflection effect of the micro cones can well explain the measured improvement in PCE of the silicon solar cell.

## 5.6 Energy yield of microtextured perovskite/c-Si tandem solar cells

In the preceding sections, the optical performance of different microtextures has been presented. Moreover, the microtextures are tested on top of c-Si single-junction solar cells and perovskite/c-Si tandem solar cells. Since the microtextures demonstrate an excellent broadband reduction of the reflectance for normal and particularly for oblique incidence, assessing the energy yield (EY) is important to probe the microtextures under realistic irradiation conditions. Therefore, in the following, the enhanced light incoupling and light-harvesting is analyzed for the perovskite c-Si tandem solar cells.

The EY for inverted pyramids with different ARs is determined in different locations (see **Figure 5.19** and **Figure 5.20**). In this regard, the annual EY is summarized for four locations with different climatic conditions: temperate (Portland, Oregon), tropical

(Miami, Florida), boreal (Chicago, Illinois), and arid (Phoenix, Arizona). For this, the same 4T monofacial tandem architecture as introduced in section 4.7 is chosen. For Figure 5.19, air is used as an optical spacer layer, for Figure 5.20 the top perovskite and bottom c-Si solar cells are connected with an optical coupling layer (e.g. encapsulation layer) with a glass-like refractive index.

The annual EY between the different locations follows the trend reported in section 4.7. In case of air as an optical spacer, the inverted pyramids on top of the perovskite/c-Si tandem solar cell only slightly enhance the overall annual EY for large AR. Moreover, at  $AR = 0.5$ , the annual EY almost decreases compared to the planar reference. This is due to the strong decrease of the EY of the c-Si bottom solar cell (illustrated by the black line in the bar plots). For all AR, the EY of the bottom c-Si solar cell does not recover to the value of the planar reference. Nevertheless, the EY of the top perovskite solar cell increases for all AR by up to 4%<sub>rel</sub> irrespective of the location. A totally different result is observed for the tandem solar cell with an optical spacer with glass-like refractive index (see Figure 5.20). Here, all ARs lead to an enhanced annual EY of up to 7%<sub>rel</sub>.

Surprisingly, both results in the EY are in contrast to the enhancement in the PCE of this 4T tandem configuration (see Figure D.1 in Appendix D). Here the tandem PCE increases strongest for an AR of 0.5 by 5.4% and 5.9% for the air and glass-like encapsulation, respectively. This improvement is maintained for the glass-like encapsulations, but breaks down in case of air between the two sub cells.

Compared to the tandem configuration with air as intermediate optical coupling layer, the glass-like layer mainly improves the transmittance of the light into the c-Si bottom solar cell. This distinct difference between air and glass as optical spacer is displayed for Miami in Figure 5.21. For the two sub-cells optical coupled with a glass-like layer, the overall EY increases due to an increase in the absorptance of the perovskite and c-Si solar cell. For an increase in the AR, the light incoupling increases and directly translates to the power generation in both sub-cells.

In case of air between the two sub-cells, the inverted pyramids on the perovskite solar cell increase the overall EY for all AR as well. However, the improvement is lower, due to the unfavorable impact on the c-Si solar cell, which mainly stems from a decrease in the transmittance (see Figure 5.22). Although the perovskite top cell demonstrates a significant improvement in the EY for all AR, the c-Si bottom solar cell shows always a lower EY. In case of inverted pyramids this suppresses any improvement for  $AR < 0.5$ . It should be noted, that this trend is also true also for micro cones (see Appendix D, Figure D.2). However, the absolute gain in the EY and specific shape (dependency on the AR) differs slightly.

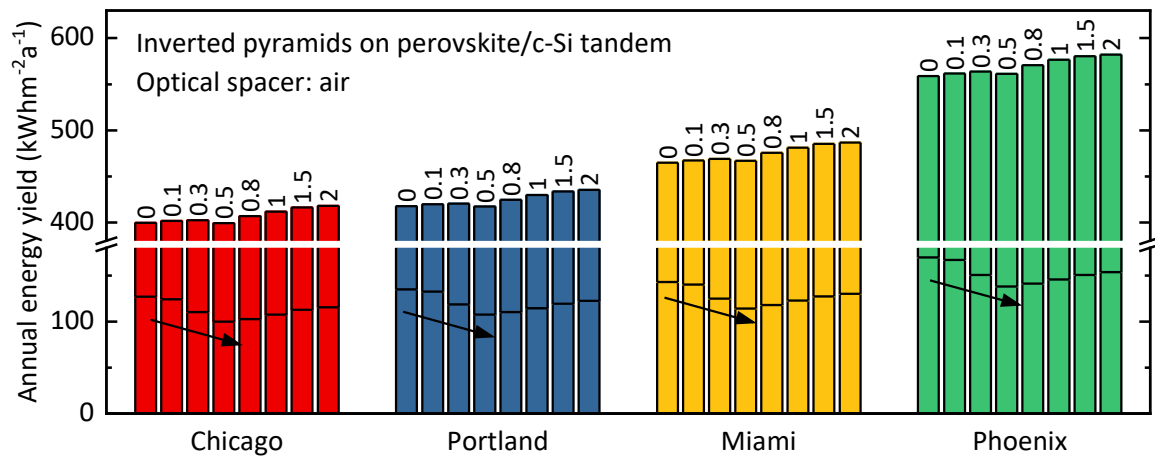


**Figure 5.19.** Annual energy yield (EY) for four different locations in the USA with different climatic conditions. The annual EY is displayed for the planar reference (aspect ratios AR=0), and for inverted pyramids on top of the front glass of the perovskite solar cell with different AR. The numbers on each bar indicate the AR of the inverted pyramids. Air is used as optical spacer in the 4T tandem architecture simulations.

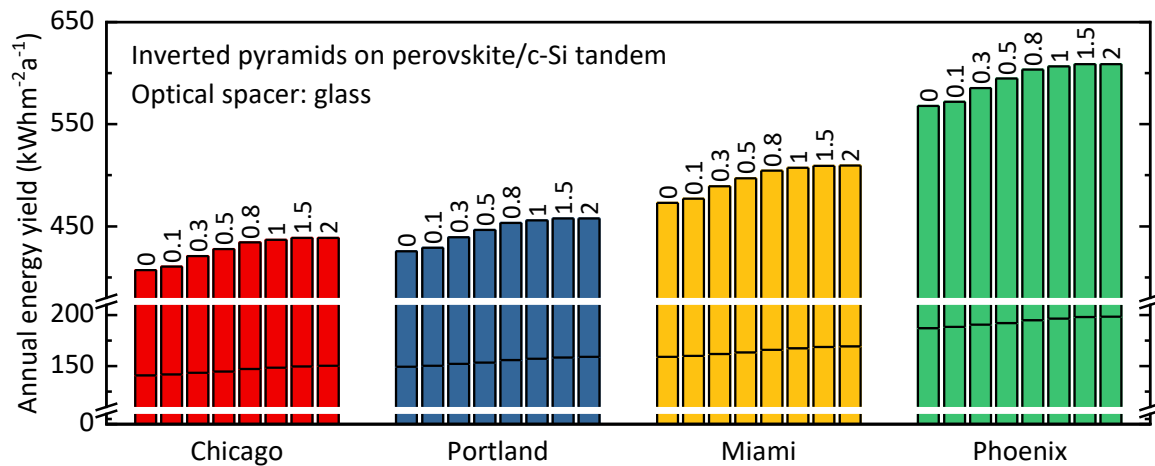


**Figure 5.20.** Annual energy yield (EY) for four different locations in the USA with different climatic conditions. The annual EY is displayed for the planar reference (aspect ratios AR=0), and for inverted pyramids on top of the front glass of the perovskite solar cell with different AR. The numbers on each bar indicate the AR of the inverted pyramids. Glass is used as optical spacer in the 4T tandem architecture simulations.

As it was already shown for normal incidence in section 5.4.3, the transmittance reduces in case of air as optical coupling layer compared to glass (see Figure 5.22a and c). Exactly this effect amplifies for oblique angles of incidence (see Figure 5.22d). For an angle of incidence of 40°, the transmittance strongly decreases for the two textured tandem solar cells and lead to a reduction in the absorption of the c-Si bottom solar cell. Whereas the tandem solar cell with a glass as optical coupling layer is not affected by the larger angle of incidence, the tandem solar cell with air as coupling layer severely loses in the EY due to a reduced power generation in the bottom c-Si solar cell.

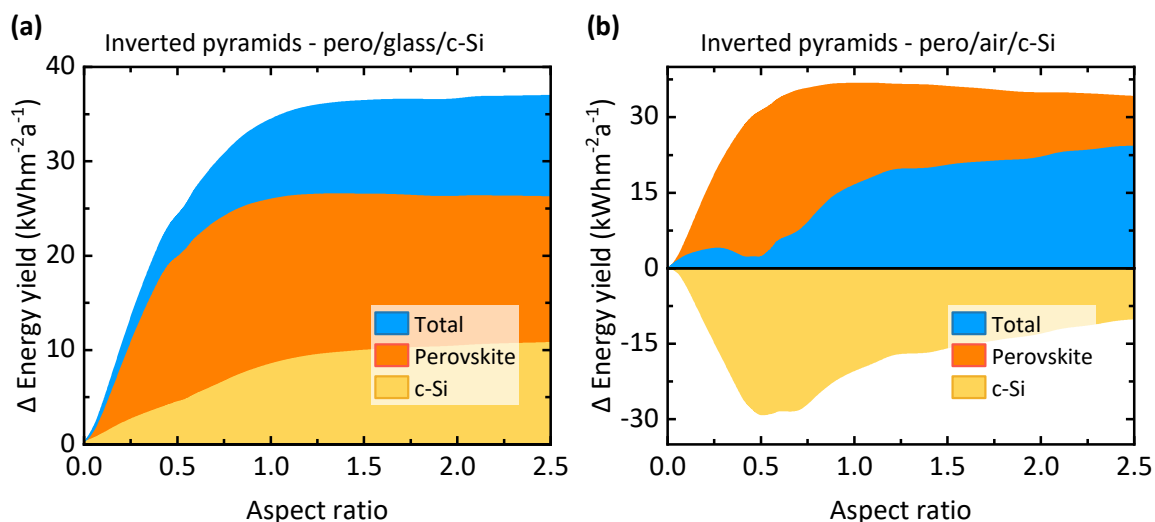


**Figure 5.21.** Change in the annual energy yield (EY) for microtextures different aspect ratios (AR). The change in the EY is displayed for the top perovskite, bottom c-Si and the sum of both. The inverted pyramids on top of the perovskite solar cell with an intermediate (a) a glass layer and (b) air gap.

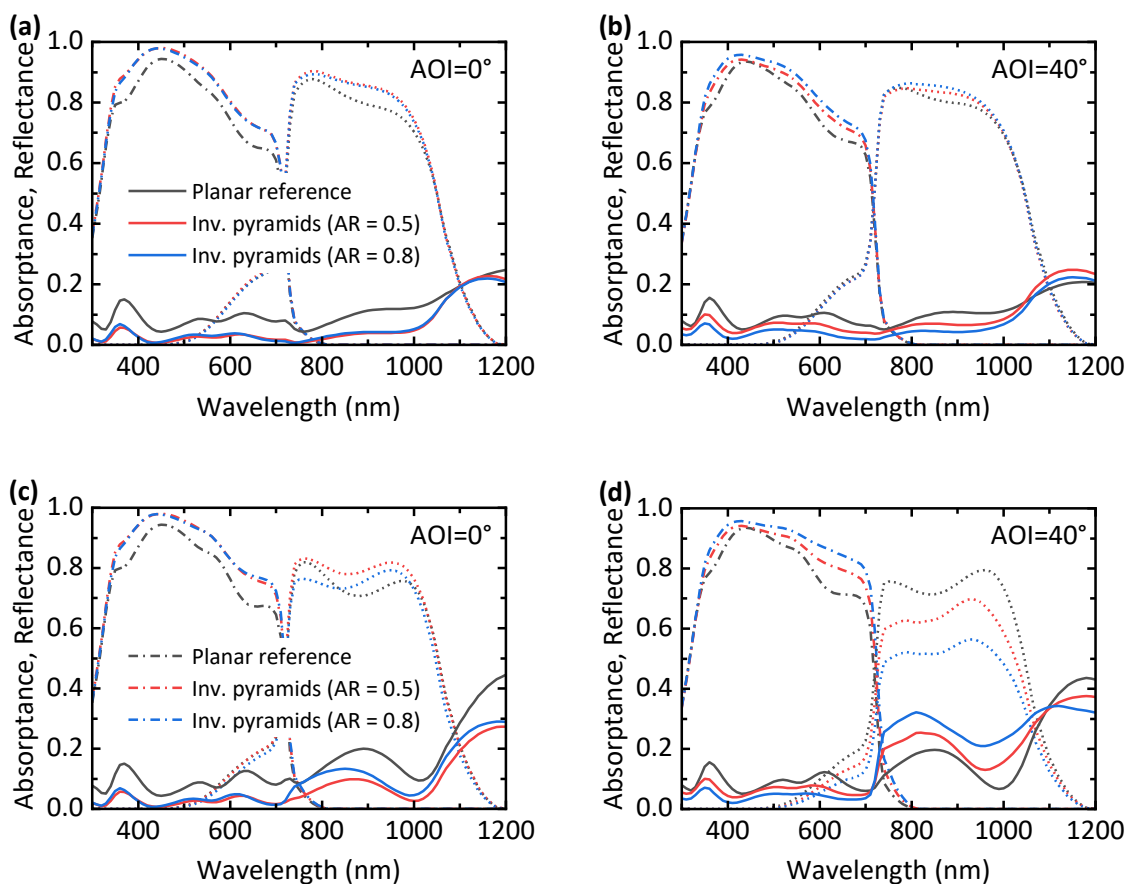


**Figure 5.22.** Absorbance and reflectance of the perovskite top and c-Si bottom solar cell in the 4T tandem architecture. The absorbance and reflectance is shown for the planar reference and inverted pyramids with AR = 0.5 and AR = 0.8 for (a) normal incidence and (b) for an angle of incidence (AOI) of 40° with glass as intermediate layer. In (c) and (d), the absorbance and reflectance is shown air as intermediate layer.

## 5.7 Summary

The microtextures demonstrate a superior reduction of reflection losses at the front planar air/glass interface, leading to excellent light incoupling and moreover superior light harvesting properties. Eliminating the front air/glass reflection, enables an absolute improvement in the current generation of around 4% for normal incidence and much higher for oblique incidence angles, which is of great importance to almost any photovoltaic technology.

Different microtextures with a broad range of aspect ratios are tested, whereas the textures are directly taken and replicated from nature (viola flower) or artificially designed and replicated. All microtextures analyzed demonstrate excellent omnidirectional and broadband light incoupling properties, reducing reflection losses to almost zero for normal incidence and about  $\approx 80\%_{\text{rel}}$  for oblique angles of  $80^\circ$ . This is utilized to enhance the current generation and thus the power conversion efficiency of planar and textured crystalline silicon as well as perovskite/silicon tandem solar cells. In this regard, planar and textured single-junction crystalline silicon solar cells demonstrate a relative increase in their power conversion efficiencies of  $\approx 12\%$  and  $\approx 5\%$  compared to the planar (encapsulated) reference, respectively. This is, in particular, due to efficient recapturing of light reflected at the solar cell by retro-reflection, which is predominantly important for the longer wavelengths. The retro-reflection ability of the microtextures scale with the reflection properties of the solar cells and therefore plays a more significant role for planar architectures as on the textured crystalline silicon solar cells.

The excellent improvements in the single-junction silicon solar cells paves the way for multi-junction perovskite/silicon solar cells. Here, implementation of inverted micro-pyramids led to strong reduced reflectance of  $\approx 10\%_{\text{abs}}$ , which boosts the four-terminal tandem power conversion efficiency up to 25.3%. Moreover, the improved light-incoupling and harvesting is demonstrated on a  $4 \text{ cm}^2$  perovskite/c-Si tandem solar module, where the 4T PCE enhances from 23.1% to 23.9%, which was at the time of this result the highest reported value for an aperture area larger than  $0.5 \text{ cm}^2$ .

Furthermore, detailed energy yield calculations reveal the importance of an optical coupling layer in between the top perovskite and bottom silicon solar cell of the four-terminal architecture. This is due to the fact that the perovskite solar cell equipped with the microtextures are sensitive to the varying angle of incidence in realistic irradiation conditions. The enlarged propagation angles inside the thin-film stack due to the microtextures reduce the outcoupling in case of a strong step in the refractive index at the rear (e.g. ITO/air). For an intermediate optical coupling layer, however, the energy yield increases for all microtextures and all aspect ratios embedded in the front glass cover and remain angle stable. It follows that the overall improvement in the annual energy yield is primarily influenced by the aspect ratio of the texture and reaches around  $6\%_{\text{rel}}$  irrespective of the considered locations.

Thus, the microtextures demonstrates significant improvements and moreover predicts excellent performance under realistic operation conditions. The concept demonstrates superior angular stability for the entire spectral range for single junction and tandem solar cells.

The presented prototypes still consist out of glass-like polymers, enabling ease of transfer to the tested architectures. However, the implementation of the proposed optical concepts into conventional photovoltaic modules, while simultaneously maintaining high durability represent a severe technological challenge. Nevertheless, first work on the implementation into the front glass cover sheet already shows the aptitude beyond the laboratory scale [30]. This so-called liquid glass approach uses silica powder in a monomeric mixture, which enables the texturing before the sintering process. After the sintering process (at 1300°C), the properties of the glass are very close to conventional fused silica. However, the liquid glass must still prove to be equally stable, robust and durable as the planar state-of-the-art encapsulation. Moreover, as it is still in an early stage of development, upscaling still needs to be further developed.

Another possibility might be the transfer of the microtextures into a foil, which then can be applied on already existing photovoltaic modules or laminated during the fabrication process. First studies already outline the potential to upscale even the presented plant surface textures [156]. Moreover, since especially the replicated plant textures feature self-cleaning properties [149], such foils would promise additional benefits. In addition to that, microtextured solar modules might find an ideal application in building integrated photovoltaics as well, where typically the largest share of irradiation comes from diffuse sun light from the sky or other buildings [95].

In summary, the proposed concepts are of great relevance for future photovoltaic modules, where a broadband antireflection coating with a superior angle tolerance is needed and it is important to minimize the first air/glass reflection, and potentially self-cleaning effects as a bonus. However, all the potential improvement and advantages needs to be set in proportion to the additional costs and effort due to the additional texturing.



## 6 Nanophotonic textures for enhanced light incoupling in perovskite/c-Si tandem solar cells

In this chapter, nanophotonic front electrodes are designed and developed to advance the light incoupling into the top perovskite solar cell and thus, to enhance the transmission into the bottom silicon solar cell in a four-terminal tandem configuration. This is achieved by effectively reducing the reflection losses at the front transparent electrode of the perovskite solar cell.

### Acknowledgements and contributions

*The following section on nanophotonic textures for enhanced light incoupling in perovskite/c-Si tandem solar cells, summarizes optical simulations performed by Katharina Goth during her master thesis [157] and the experimental results on self-assembled polystyrene nanopillars [158]. The master thesis was supervised by Raphael Schmager. The experimental work was derived in a collaborative project on nanophotonic front electrodes for the perovskite solar cells with Ihteaz M. Hossain and Yidenekachew J. Donie, who share the first authorship of the aforementioned publication. In this project, Ihteaz M. Hossain focused on the perovskite device fabrication and Yidenekachew J. Donie developed the fabrication route for the self-assembled polystyrene nanopillars. The contribution to the experimental work, were the angular dependent EQE measurements, the EY calculations and the support for the comprehension of the nanotextures' function. The c-Si bottom solar cells were provided by H. Kohlenberg and the team from Institute for Solar Energy Research (ISFH) in Hamelin and from the Institute of Electronic Materials and Devices (MBE) at Leibniz Universität Hannover.*

## 6.1 Introduction

In addition to improved light incoupling into the entire device by improving the air/glass interface through microstructures on the front glass cover (see section 5), the reflection loss at the glass and front transparent ITO electrode is examined. The reflectance loss at the front glass/ITO interface occurs – similar to the reflectance at the air/glass interface – due to the discontinuity of the refractive index between the two materials. Reducing this reflection loss promises to enhance the absorption in the perovskite absorber. Moreover, in terms of a 4T tandem application, the transmittance of low-energy photons passing through the top semitransparent perovskite solar cell could be enhanced as well. Both will increase the current generation, and thus the overall power conversion efficiency. To exploit both effects, a broadband anti-reflection interface must be designed within the solar cell layer-stack.

There are two main light management concepts to cope with this: (1) introducing a thin anti-reflection layer with refractive index in between the glass and ITO (e.g.  $\text{SiO}_{0.4}\text{N}_{0.6}$ , as suggested by ref. [26]); and (2) texturing the glass/ITO interface. With a thin additional antireflective coating, a broadband reduction of reflection loss is a challenge, since the refractive index and its dispersion must match the surrounding materials. However, with a nanotextured interface a smooth gradient of the two surrounding refractive indices is possible [27,159]. Therefore, the implementation of a nanotexture at the glass/ITO interface promises to achieve a broadband anti-reflection effect. Moreover, sufficiently high structures – compared to the thickness of the electrode and charge transport layers – will affect not only the glass/ITO interface, but all layers up to the perovskite (glass/ITO/ETL/perovskite), which account for reflection losses in the order of 5 - 20% [160].

With regard to nanotextures for perovskite PV, pre-texturing of the planar glass substrate by photo nanoimprint lithography of a transparent resist layer [161] has been demonstrated, recently. Moreover, first implementation in opaque perovskite solar cells have been reported [162]. Besides periodic arrays of two-dimensional ITO textures, disordered ITO nanorod films [163] and periodic ITO sub-wavelength gratings for Si-based thin-film solar cells have been studied in literature [164]. In addition, nanotextured ITO layers are studied for the purpose of improved light outcoupling in organic light emitting diodes [165].

In this chapter, periodic and disordered nano-holes and nano-pillars are studied to minimize the reflection loss at the glass/ITO interface in perovskite-based tandem PV. First, the potential improvement for the 2T and 4T perovskite/c-Si solar architecture is investigated using FEM-based wave-optical simulation. Compared to the planar reference, an enhancement in the power output of  $\approx 3 - 4\%_{\text{rel}}$  is found for the optimized geometry of the nanotextures. Moreover, compared to an optimized planar anti-reflection coating, the nanotextures further improve the total gain due to the better broadband match with the

geometric mean of the two surrounding refractive indices. The optimum period of the nanotextures is between 200 - 300 nm. For larger periods the incident light is subject to strong coupling to guided modes in the ITO layer (see e.g. Khan *et al.* [161] or Appendix C.2), which leads to strong parasitic absorption in the longer wavelengths.

Next, experimental realization in perovskite/c-Si tandem solar cells are demonstrated which show  $\approx 2\%$ <sub>rel</sub> enhanced 4T PCE. The nanotextured ITO electrodes are processed via a facile polymer blend lithography, which generates self-assembled patterned monolayers on a glass substrate. The obtained disordered nanopillars show similar geometrical properties as the optimized simulated periodic nanotextures. The nanotextured ITO electrode in the 4T tandem prototype significantly enhances the transmittance into the bottom c-Si solar cell, which improves the  $J_{SC}$  by 22%<sub>rel</sub>. Moreover, the enhancement even increases for oblique angles of incidence.

Finally, energy yield simulations are performed to evaluate the nanophotonic ITO electrodes under realistic operation conditions. Due to the great angular stability of the nanotextured ITO electrode in the 4T tandem solar cell compared to the planar reference, the annual energy yield increases by  $\approx 10\%$ <sub>rel</sub>.

## 6.2 Optimization of nanophotonic ITO electrodes using optical simulations

In order to enhance the PCE of perovskite/c-Si tandem solar cells, nanophotonic ITO electrodes are introduced. This is intended to increase both the share of absorbed light in the top perovskite solar cell and the amount of transmitted light below the band gap of the perovskite absorber in semitransparent perovskite solar cells. For this study, a semitransparent perovskite layer stack as illustrated in **Figure 6.1** is used. For the optical simulation, the refractive index of the wide-band gap perovskite  $\text{Cs}_{0.17}\text{FA}_{0.83}\text{Pb}(\text{Br}_{0.17}\text{I}_{0.83})_3$  with  $E_g = 1.62$  eV is chosen, since this composition has shown promising optical, thermal, and environmental stability [166]. The refractive indices of the perovskite and the other materials are summarized in Appendix A.

To quantify the potential improvement, the optical performance of the nanotextured ITO front electrode is computed in a 4T and 2T perovskite/c-Si tandem architecture (see Figure 6.1). For the planar reference in the 4T architecture, a 600 nm thick perovskite absorber is used. Increased thicknesses lead to optical improvements in the calculated  $J_{SC}$ , but might experimentally be challenging [88,167,168]. Therefore, the thickness is chosen so that it remains within the experimentally feasible range. The bottom c-Si solar cell is optically connected with an air gap to the perovskite top cell in the 4T architecture. To calculate the power output of the silicon solar cell, the transmitted light is folded with the EQE of a record c-Si single-junction solar cell (certified short-circuit current density of 43.3 mAcm<sup>-2</sup> with contact fingers) [169].

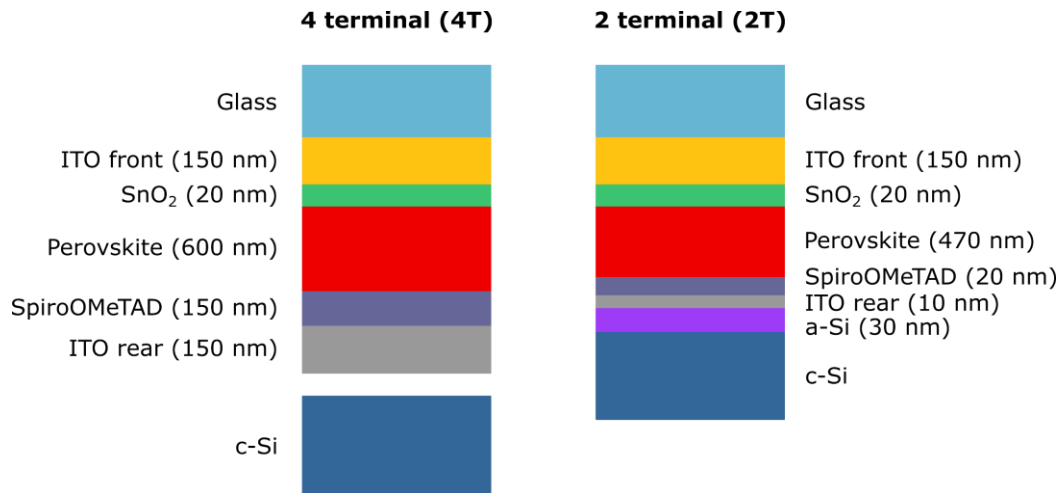


**Figure 6.1.** Schematic of the simulated layer stack in the 4T and 2T architecture. The layer thicknesses are fixed for the optimum tandem power in both architectures. In the 4T stack, the highest power is obtained for the maximum (allowed) perovskite thickness of 600 nm. In the 2T architecture, a 470 nm thick perovskite layer leads to the highest power for the planar reference.

In the 2T architecture, the concept is probed in a planar c-Si solar cell. The planar reference demonstrates the highest  $J_{SC}$  for a 470 nm thick perovskite layer. The thickness of the HTL is reduced to 20 nm and the rear ITO is acting as a 10 nm thin recombination junction between the perovskite top and the c-Si bottom solar cell (see Figure 6.1).

For the analysis of the nanophotonic ITO front electrode, two nanophotonic designs with different structural arrangements (ordered and disordered) are considered. Nanoholes and nanopillars on top of the glass superstrate. The pillars and the inverse parts of the pillars are assumed as glass in the simulation. The two designs for the ordered nanophotonic textures are displayed in **Figure 6.2**. The layers are conformably added to the corrugated glass surface.

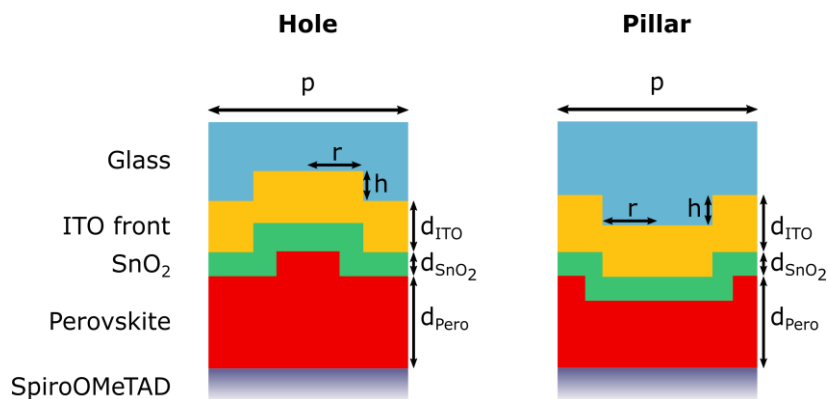


**Figure 6.2.** Schematic of the nanophotonic ITO electrodes in case of a hole and pillar indentation inside of the glass superstrate. The ITO,  $\text{SnO}_2$  and perovskite are conformally added on top of the corrugated glass surface. The interface between the perovskite and spiro-OMeTAD is assumed to be planar due to the comparably large thickness of the perovskite layer.

The interface between the perovskite and spiro-OMeTAD layer is considered to be planarized due to the significantly larger thickness of the perovskite layer. The holes (pillars) are defined by the period  $p$  of the unit cell, the radius  $r$  and the depth (height)  $h$  of the holes (pillars). The ratio between the area of the pillar ( $\pi r^2$ ) and the area of the unit cell ( $p^2$ ) is defined as the geometric fill factor (geo. FF). The geo. FF,  $p$  and  $h$  are used in the following to optimize and describe the geometry of the nano-holes and nano-pillars.

### 6.2.1 Ordered nanophotonic ITO electrode in the 4T architecture

To evaluate the performance of the “holes” and “pillars” configuration in comparison to the “planar” reference for the 4T and 2T tandem architecture, FEM-based wave-optical simulations are carried out with the commercially available software JCMsuite by JCMwave GmbH (see details in section 3.1.2).

Based on the three-dimensional electromagnetic simulations of one unit-cell of the entire perovskite solar cells, the enhancement in the  $J_{SC}$  is calculated through the absorption enhancements in the perovskite layer. The absorption increases due to the reduced reflectance at the glass/ITO/SnO<sub>2</sub>/perovskite interface. To derive the optimum geometry of the nanotextures for the 4T perovskite/c-Si tandem solar cell, the total power in the 4T tandem solar cell is estimated with the calculated  $J_{SC}$  of the perovskite and silicon solar cell:

$$P_{4T} = FF^{pero} \cdot V_{OC}^{pero} \cdot J_{SC}^{pero} + FF^{Si} \cdot V_{OC}^{Si} \cdot J_{SC}^{Si}. \quad 6.1.$$

For the electrical parameters, both (electrical) FF are assumed to be 80% and the  $V_{OC}$  are set to 1.19 V and 0.72 V for the perovskite and c-Si solar cell, respectively, which matches well with current record devices of similar band gaps [14,169,170].

#### Nanophotonic holes

Starting from a period of  $p = 300$  nm, a hole depth  $h = 120$  nm, the geo. FF is varied between 0 and 60% for the nanophotonic holes configuration. In **Figure 6.3a**, the  $J_{SC}$  and the (estimated) power of 4T tandem solar cell is plotted in relation to the geo. FF. Compared to the planar reference (geo. FF = 0%), the enhancement in  $J_{SC}$  and total power is highest at a geo. FF of around 40 - 50%.

Both, the  $J_{SC}$  in the perovskite top and the  $J_{SC}$  in the bottom c-Si bottom solar cell increases with the nanotexture. Further optimization of the geometry lead to a maximum in the power of the 4T tandem solar cell at  $p = 220$  nm, geo. FF = 60%, and  $h = 80$  nm (see **Figure 6.3f**). Here, the  $J_{SC}$  of the perovskite top solar cell increases by 4%<sub>rel</sub> from 19.8 mAcm<sup>-2</sup> to 20.7 mAcm<sup>-2</sup>. The  $J_{SC}$  of the c-Si bottom solar cell increases by 2%<sub>rel</sub> to 16.0 mAcm<sup>-2</sup>. The total power is enhanced by 4%<sub>rel</sub> from 27.9 mWcm<sup>-2</sup> to 28.9 mWcm<sup>-2</sup>. Compared to the planar reference, mainly the reflectance of the perovskite solar cell decreases up to a wavelength of 800 nm (see **Figure 6.4**).

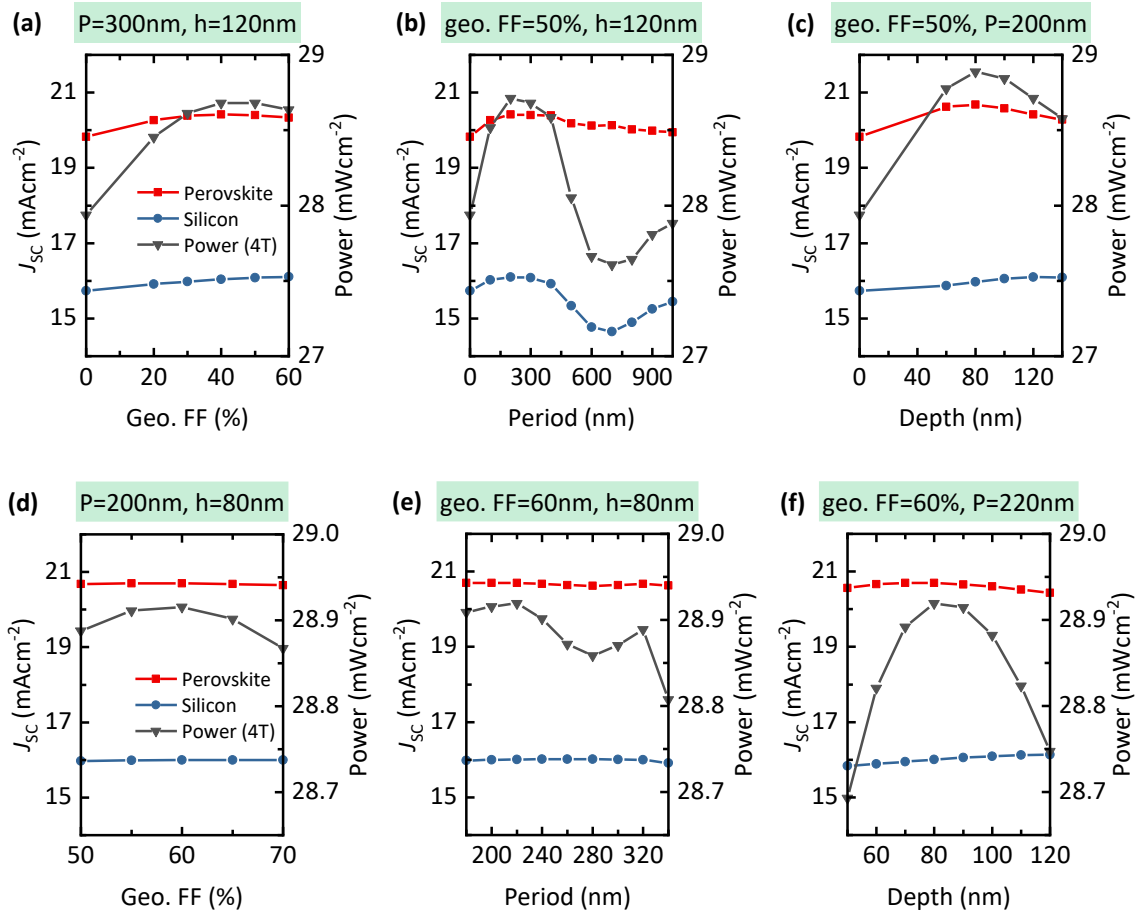


**Figure 6.3.** Optimization of the geometry of the nanophotonic ITO front electrode in the 4T perovskite/c-Si tandem architecture. (a) First, the geometric fill factor (geo. FF) is swept for the initial guess (period  $P = 300$  nm, hole depth  $h = 120$  nm). (b-c) Secondly, the period and hole depth is optimized for the optimum geo. FF found in (a). (d-f) The second round of optimization reveals a broad and robust optimum.

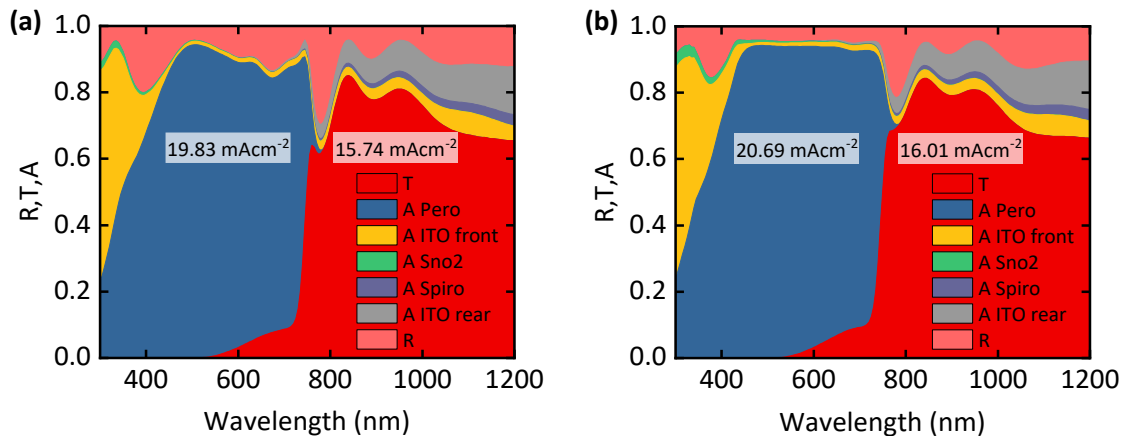


**Figure 6.4.** Reflectance  $R$ , transmittance  $T$ , and absorptance  $A$  of the individual layers of the (a) planar reference and (b) of the nanophotonic ITO device. The  $R$  and  $T$  is given for the complete stack into air. The optimum geometry ( $p = 220$  nm, geo. FF = 60%,  $h = 80$  nm) of the hole is used for the nanotextured ITO front electrode. The numbers give the short-circuit current densities ( $J_{sc}$ ) of the perovskite top solar cell and the  $J_{sc}$  of the c-Si solar cell, which is estimated via the EQE of a record c-Si solar cell (see text for details) and the transmittance (shown in this Figure).

At longer wavelengths ( $> 800$  nm) the enhancement is due to a spectral shift in the transmittance spectrum. In the short wavelengths' regime ( $< 500$  nm) parasitic absorption is increased slightly in the front ITO and  $\text{SnO}_2$  due to the nanotextures. However, the broadband reduction of reflectance is much stronger and results in an overall prominent enhancement of the  $J_{\text{SC}}$  in the perovskite and c-Si.

### Nanophotonic pillars

Besides the nanophotonic holes in the ITO layer, nanophotonic pillars were examined as well. The ideal geometry of the pillars corresponds approximately to the inverse of the holes. The optimum period is again small and the total power maximizes for a period of 200 nm. The optimum geo. FF is 35% and the pillar height is identical with the hole depth ( $h = 80$  nm). This, almost inverse relation, is discussed in more detail in the next section.

The absorptance, the transmittance and the reflectance of the nanophotonic ITO electrodes of the hole and pillar configuration (see **Figure 6.5a**) behave comparable. Only minor spectral offsets and differences can be observed. Therefore, the  $J_{\text{SC}}$  of the two designs lead to comparable values in the perovskite and c-Si absorber, respectively. Compared to the planar reference, the improvement is very similar (see Figure 6.5b) and leads to a total power of  $28.8 \text{ mWcm}^{-2}$ , which is only  $0.1 \text{ mWcm}^{-2}$  lower than the estimated power of the hole textures.

For the perovskite solar cell with the nanophotonic ITO, the reflectance is strongly reduced in between 300 nm and 850 nm. The remaining reflection loss is due to the air/glass interface. The transmittance is similar, spectrally shifted, which leads to a small increase in the  $J_{\text{SC}}$  of the c-Si solar cell from  $15.7 \text{ mAcm}^{-2}$  to  $16.1 \text{ mAcm}^{-2}$  (pillars) and  $16.0 \text{ mAcm}^{-2}$  (holes).

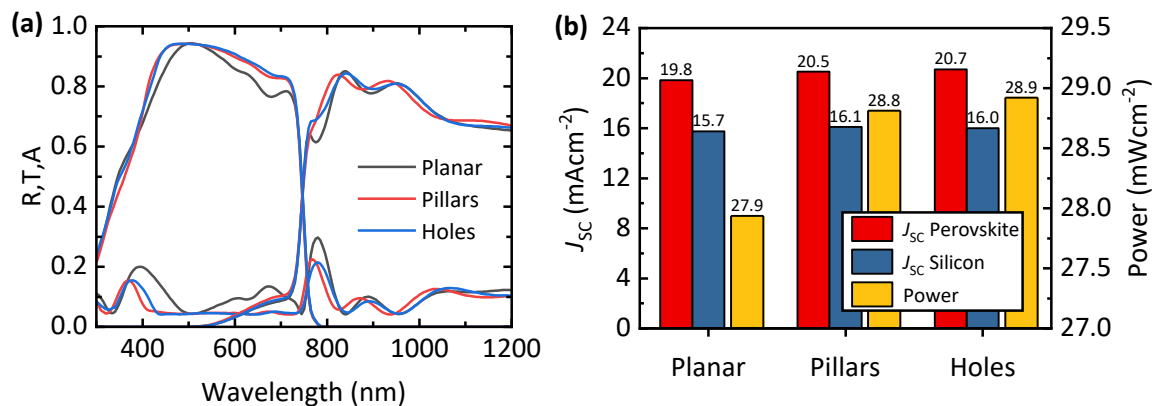


**Figure 6.5.** (a) Reflectance R, transmittance T, and absorptance A of the perovskite layer for the planar reference, the nanophotonic ITO electrode with the hole, and pillar design. (b) The corresponding short-circuit current densities ( $J_{\text{SC}}$ ) of the perovskite and c-Si solar cell as well as the estimated power of the 4T tandem. For the nanophotonic ITO electrode, the optimum of the hole and pillar design is used. Optimum for the holes:  $p = 220$  nm, geo. FF = 60%,  $h = 80$  nm; optimum for the pillars:  $p = 200$  nm, geo. FF = 35%,  $h = 80$  nm.

## 6.2.2 Ordered nanophotonic ITO electrodes in the 2T architecture

Besides the 4T architecture, also the 2T perovskite/c-Si tandem architecture has been considered for the implementation of the nanophotonic ITO front electrodes. In contrast to a 4T, a 2T tandem solar cell is electrically connected in series and therefore current matching of the perovskite and c-Si solar cell has to be considered. Furthermore, the two solar cells are directly connected to each other and do not require an optical spacer layer like the 4T concept. The optical simulations in the 2T tandem solar cell are performed up to a thin non-absorbing planar c-Si layer to estimate the optical response for the top layers of the perovskite solar cell. The absorption in the c-Si is further calculated with the Beer–Lambert law assuming a light trapping factor of 25 (see section 2.3) and a c-Si thickness of 300  $\mu\text{m}$ . The optimum geometry for the hole-textured nanophotonic ITO electrode is derived analogous to the 4T case (see above).

For the optimized nanophotonic ITO (here shown for “holes”) electrode, the  $J_{SC}$  increases by 0.5  $\text{mAcm}^{-2}$  to 19.7  $\text{mAcm}^{-2}$  compared to the planar reference (see **Figure 6.6**). The optimum geometry of the nanophotonic ITO electrode is found at  $p = 300 \text{ nm}$ , geo. FF = 50%,  $h = 100 \text{ nm}$ , which is close to the optimum of the 4T tandem solar cell. Compared to the planar reference, the power of the 2T tandem with the nanophotonic ITO is enhanced by  $\approx 3\%_{\text{rel}}$  from 29.3  $\text{mWcm}^{-2}$  to 30.1  $\text{mWcm}^{-2}$ . For comparison: the improvement in the 4T tandem solar cell was  $\approx 4\%_{\text{rel}}$ . The power in the 2T tandem is derived with the same electrical parameters as in the 4T case assuming current matching:

$$P_{2T} = 0.8 \cdot (V_{OC}^{\text{pero}} + V_{OC}^{\text{Si}}) \cdot \min(J_{SC}^{\text{pero}}, J_{SC}^{\text{Si}}) \quad 6.2.$$

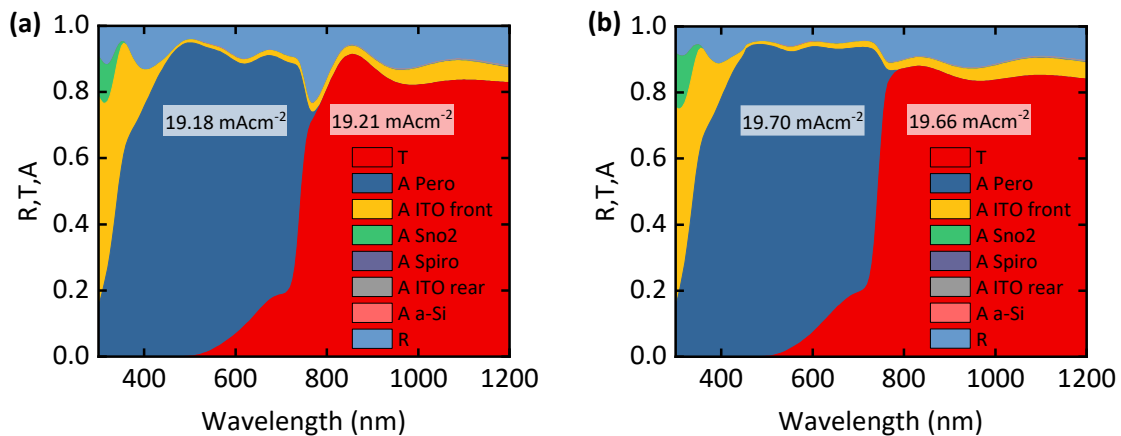


**Figure 6.6.** Reflectance R, transmittance T, and absorptance A of the individual layers of the (a) planar reference and (b) of the nanophotonic ITO device. The R and T is given for the complete stack into air. The optimum geometry ( $p = 300 \text{ nm}$ , geo. FF = 50%,  $h = 100 \text{ nm}$ ) of the hole is used for the nanotextured ITO front electrode. The numbers give the short-circuit current densities ( $J_{SC}$ ) of the perovskite top solar cell and the  $J_{SC}$  of the c-Si solar cell, which is estimated via the Beer–Lambert law assuming a light trapping factor of 25 and the transmittance into the c-Si layer (shown in this Figure).

The geometry of the hole in the nanophotonic 2T tandem is optimized with respect to current matching in both the top perovskite and the bottom c-Si solar cell. Therefore, both, the absorption of the perovskite top and the absorption of the c-Si bottom solar cell is enhanced (see Figure 6.6). The optimized planar reference has a perovskite thickness of 435 nm, whereas the nanophotonic perovskite solar cell show current matching at 420 nm.

Although the 2T perovskite/c-Si tandem solar cell with nanophotonic ITO electrodes shows a gain in total power of  $\approx 3\%_{rel}$ , a textured perovskite/c-Si interface would have greater potential [86]. Therefore, further simulations need to proof the potential of the nanotextured ITO electrodes for double-sided textured perovskite/c-Si tandem solar cells as well. However, it should be noted that for those, the implementation of the nanotextured electrode will be even more complex as in a planar perovskite/c-Si tandem.

### 6.2.3 Disordered nanophotonic ITO electrodes in the 4T architecture

For experimental reasons (see section 6.3 below), disordered gratings with similar feature sizes are also analyzed in the following. Since the optimum periods are small compared to the wavelengths range of interest (300 – 1200 nm), the nanotexture mostly act as an effective medium to the incident light. Therefore, a disordered nanophotonic ITO front electrode should demonstrate similar results as a periodic.

The disordered nano-holes are generated by a simple algorithm (see master thesis of K. Goth in ref. [157]). In a first step, three random numbers are generated, which describe the displacement, the angle of the displacement direction and the radius of the circle. The displacement is defined with respect to a hexagonal grid. In the second step, overlapping circles get removed. In the FEM simulations, a unit cell of  $1.9 \mu\text{m} \times 1.9 \mu\text{m}$  is chosen with periodic boundary conditions. A number of three simulations for each FF are performed and the average is reported below.

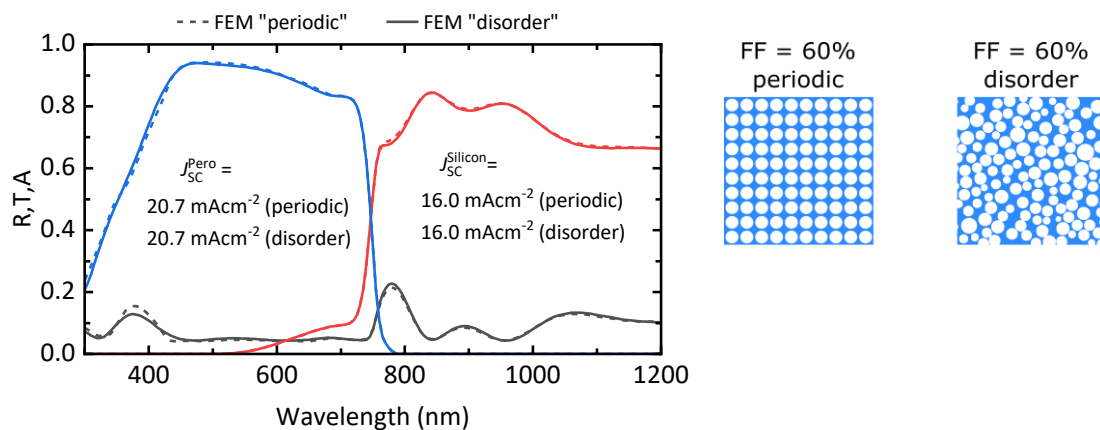


**Figure 6.7.** Reflectance R, transmittance T, and absorptance A of the periodic and disorder nanophotonic ITO device with the same geo. FF of 60%. The period of - and the average inter-distance between the - holes is 220 nm, respectively. The depth of the holes is 80 nm in both cases. Due to the small size of the holes, the disorder and periodic configuration demonstrate a very similar optical behaviour.

For equal geo. FF, and average inter-distances of the nano-holes, the nanophotonic ITO front electrodes demonstrate the very same  $J_{SC}$  in the top perovskite solar cell (see **Figure 6.7**). This confirms the assumption that the textured interface acts as a layer with an effective refractive index and diffraction can be disregarded.

Similarly, for smaller geo. FF, both, the  $J_{SC}$  in the bottom c-Si silicon and the  $J_{SC}$  in the top perovskite solar cell correspond to the periodic equivalents (see **Figure 6.8**). For increasing geo. FF, the reflectance at  $\approx 400$  nm and  $\approx 800$  nm reduces. Therefore, the absorptance  $A$  and thus the  $J_{SC}$  in the top perovskite and bottom c-Si solar cell enhance. Again, the numbers match to their respective periodic contestants.

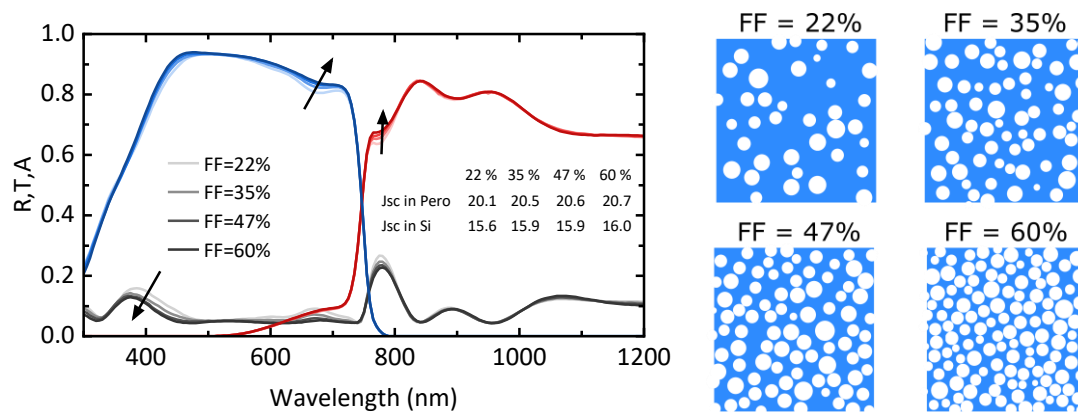


**Figure 6.8.** Reflectance  $R$ , transmittance  $T$ , and absorptance  $A$  of the disorder nanophotonic ITO device with the various geo. FF of between 22% and 60%. The average inter-distance between the holes is 220 nm. The depth of the holes is 80 nm. For increasing geo. FF, die short-circuit current density  $J_{SC}$  increases in the top perovskite and bottom c-Si solar cell – equivalent to the periodic configuration.

#### 6.2.4 Effective medium approach for nanophotonic ITO electrodes

In the preceding sections, the best geometries of the nanotextures have been derived. The optimum performance of the 4T tandem solar cell with the nanophotonic ITO electrode in the top perovskite solar cell is determined for a similar hole depth and pillar height of 80 nm. Moreover, the period performing the best, 220 nm and 200 nm for the holes and pillars, respectively. Therefore, the periodic grating of holes and pillars is smaller than the wavelengths of the considered solar irradiance (300 - 1200 nm). Consequently, the corrugated glass/ITO/SnO<sub>2</sub>/perovskite interface(s) mostly act as an effective medium to the propagating light. Moreover, due to the small period, no coupling of the light to guided modes is observed in the transmittance spectrum of the nanophotonic ITO devices (see section 7.3).

For the holes and pillars (see **Figure 6.9**), the previous simulations of the nanotextured ITO electrodes with the FEM are compared to planar TMM simulations where the textured interfaces are substituted by effective refractive indices (labeled: 'EM'). Compared to the FEM, the reflectance  $R$  and transmittance  $T$  of holes (see Figure 6.9a) and pillars (see Figure 6.9b) simulated with the EM approximation show a very good agreement. Only the

absorptance of the perovskite layer is overestimated in the short wavelength regime ( $< 500$  nm). This leads to an overestimated  $J_{SC}$  of  $20.8 \text{ mAcm}^{-2}$  for the holes and pillars with the EM approach. This offset is due to the fact that for the short wavelengths (300 - 500 nm), the EM approach is no longer valid and the periodic grating leads to diffractive effects. Moreover, in the EM approximation, the perovskite volume is part of two effective layers (see Figure 6.9) and thus the contribution to the actual perovskite volume is estimated by the volume ratio and the absorption coefficient of the perovskite and the respective other component (ITO and  $\text{SnO}_2$ ). However, the approximation shows an excellent agreement in the longer wavelengths range ( $> 500$  nm).

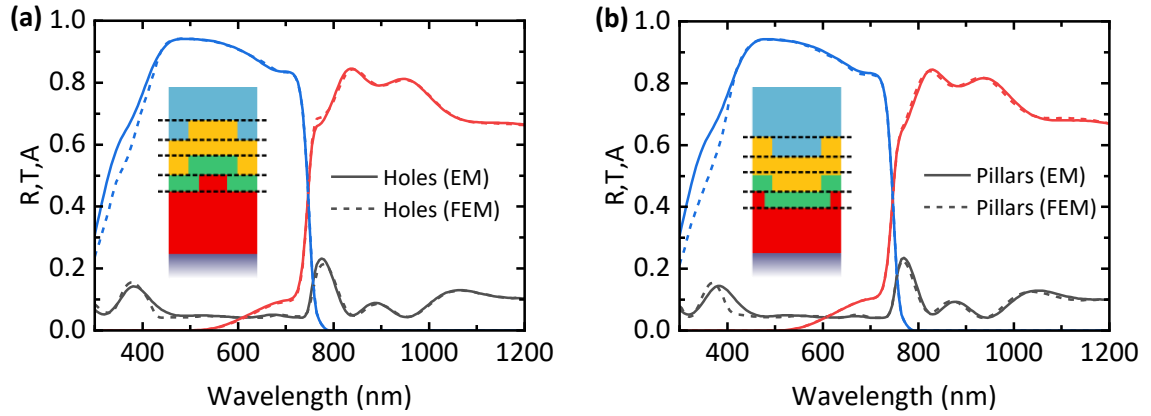


**Figure 6.9.** Comparison between FEM simulations of the nanotextures to planar TMM simulations ('EM'), where the corrugated interfaces are replaced by effective medium according the Equation 6.3. The reflectance  $R$  and transmittance  $T$  of (a) holes and (b) pillars show good agreement. Only the absorptance of the perovskite layer is overestimated in the short wavelength regime ( $< 500$  nm) by the EM approximation.

For the TMM calculations, the effective refractive index of the substituting layers is estimated by the geo. FF and the complex refractive indices of the layers defining the mixed volume (see ref. [171] and [157] for a detailed derivation):

$$n_{\text{eff}} = \frac{1}{\sqrt{\frac{\text{FF}}{n_{i+1}^2} + \frac{(1 - \text{FF})}{n_i^2}}}. \quad 6.3.$$

Since both nanotextures can be approximated with an effective medium, the anti-reflective effect of the nanophotonic ITO electrode is similar as to a typical thin-film antireflection coating (ARC). For a perfect ARC, the reflected light destructively interferes for the geometric mean of the two surrounding refractive indices:

$$n_{\text{ARC}} = \sqrt{n_1 \cdot n_2}. \quad 6.4.$$

Due to the dispersion, it is challenging to match this condition for the full spectrum. Compared to the optimum refractive index for an ARC  $n_{\text{ARC}}$ , the effective refractive index  $n_{\text{eff}}$  hardly shows any deviation (see **Figure 6.10a**). Here, both refractive indices are

calculated for the nanotextured glass/ITO interface. The excellent agreement of both describes the superior optical properties of the nanotextured ITO front electrodes compared to the planar reference, where the transition is from glass to ITO (see Appendix A for the refractive index data).

However, also planar ARCs are proposed to compete with the reflectance losses at the glass/ITO interface [26]. In this regard, e.g. silicon oxynitride ( $\text{SiO}_{0.4}\text{N}_{0.6}$ ) is suggested, since its optical band gap is  $> 5$  eV, making it transparent for a broad spectral range [172]. Nevertheless, the refractive index is not as perfect as  $n_{\text{ARC}}$  and significantly deviates from  $n_{\text{eff}}$ . Therefore, a smaller increase in the absorptance in the perovskite layer as well as in the overall transmittance is achieved for an optimized thickness of 80 nm (see Figure 6.10b). In this regard, the  $J_{\text{SC}}$  of the perovskite reaches  $20.3 \text{ mAcm}^{-2}$  and the  $J_{\text{SC}}$  in the c-Si  $15.8 \text{ mAcm}^{-2}$ , which is still  $\approx 2\%_{\text{rel}}$  less than the nanophotonic hole configuration of the ITO electrode.

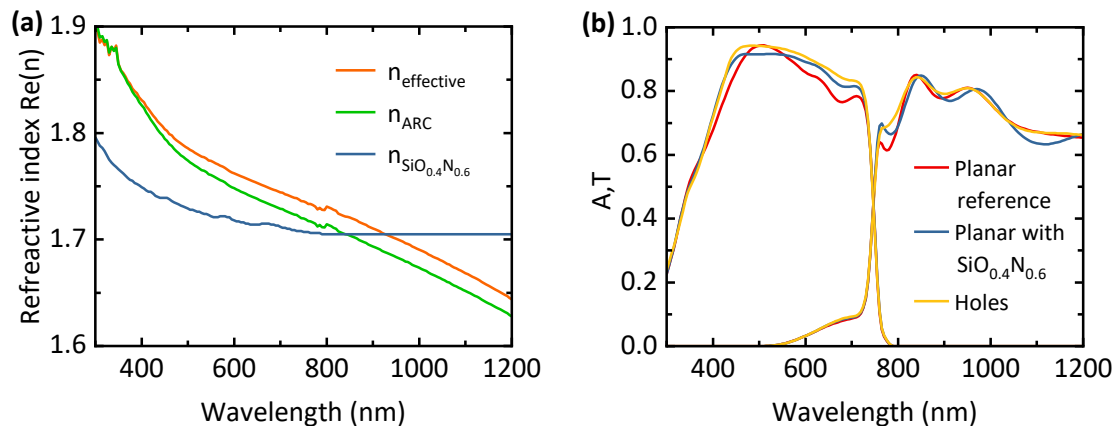


**Figure 6.10.** (a) Refractive index of a perfect antireflection (AR) coating between glass and ITO and the effective refractive index of the nanotextured glass/ITO interface. (b) Absorptance  $A$  and transmittance  $T$  of the planar reference compared to the optimum (for holes) nanotextured ITO front electrode and the device with a 80 nm thick AR coating with  $\text{SiO}_{0.4}\text{N}_{0.6}$  between the glass and ITO

### 6.3 Disordered nanophotonic front electrodes for perovskite-based multi-junction PV

In order to examine the predicted enhancements of the nanotextured ITO front electrodes derived by the simulations in the previous section, nanophotonic ITO front electrodes are experimentally fabricated. The nanophotonic ITO front electrodes are probed in 4T perovskite/c-Si tandem solar cells, whereas the architecture of the semitransparent perovskite solar cells (see **Figure 6.11**) is very similar to the above simulated (compare Figure 6.1) and consists of ITO,  $\text{SnO}_2$ ,  $\text{Cs}_{0.1}(\text{MA}_{0.17}\text{FA}_{0.83})_{0.9}\text{Pb}(\text{I}_{0.83}\text{Br}_{0.17})_3$ , spiro-OMeTAD,  $\text{MoO}_x$ , and ITO as the rear electrode. To probe the performance of the nanophotonic ITO electrodes in the semitransparent perovskite solar cells, disordered nanophotonic ITO

electrodes are processed. In the following, nanopillars are chosen and analyzed within the front electrode of a semitransparent perovskite solar.

To fabricate disordered nanopillars, a rapid and cost-effective polymer blend lithography method is used to generate self-assembled patterned monolayers on a glass substrate [173,174]. For the pattern generation, the phase separation of two immiscible polymers is used [175,176]. In this regard, a blend of polystyrene (PS) and poly(methyl methacrylate) (PMMA) is dissolved in methyl ethyl ketone (MEK) at 100°C for 1 h. After spin coating the polymer-blend on top of a glass substrate, the layers are exposed to O<sub>2</sub> plasma to cross-link the PS polymer. By developing the samples in acetic acid, the PMMA is removed and self-assembled cross-linked PS nanopillars remain on the glass substrate. By controlling the spin-coating parameters, humidity, molar masses of the two polymers and the mass ratio, the size distribution of nanopillars can be controlled. Details on fabrication via polymer blend lithography are reported in references [173,175] and the corresponding coauthor publication of this work: reference [158].

In general, the mean distance between the nanopillars can be adjusted via the ratio of the PS in the blend mixture. A reduction of the PS leads to an increased average inter-distance between the nanopillars (see **Figure 6.12a** and b). Even larger inter-distances of ≈550 nm are obtained by increasing the molecular weight of the PS (see Figure 6.12c). In addition to the increase in the average inter-distance, the mean diameter of the nanopillars increases as well. Nevertheless, a similar average height of the nanotextures (110 nm - 135 nm) is obtained by the different process parameters.

Subsequent to the polymer blend lithography, the obtained disordered nanopillars are conformally coated with a layer of ITO. Whereas the optical performance is decreased for larger inter-distances of the nanopillars, the sheet resistance improves. In Figure 6.12e, the optical characteristics are shown for the three configurations with different nanopillar inter-distances. The nanotextured ITO electrode shows the highest transmittance and lowest reflectance for the smallest nanopillar inter-distance of 210 nm, which matches perfectly with the simulated optimum period of 200 nm (see Figure 6.5).

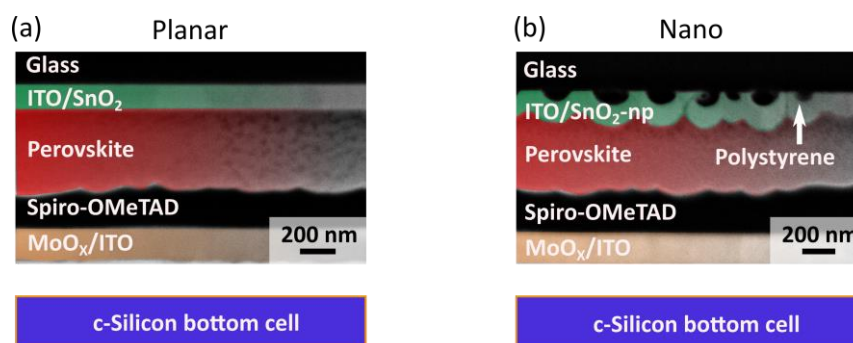


**Figure 6.11.** Scanning electron microscope (SEM) image of the cross section of (a) planar and (b) nanotextured perovskite solar cell. The disordered nanopillars on top of the glass substrate consist of polystyrene (PS). The ITO is conformally coated on top. Adapted with permission from ref. [158], © 2020 Optical Society of America.

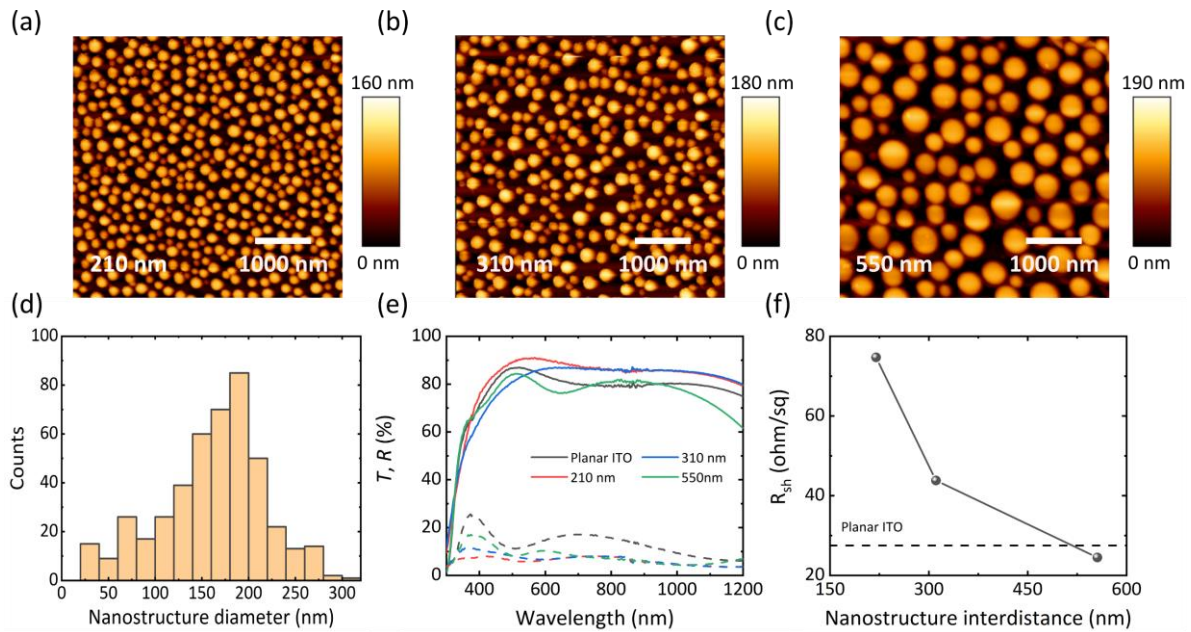


**Figure 6.12.** (a-c) Atomic force microscopy (AFM) images of the nanostructured ITO electrode for average inter-distance between the nanostructures of (a) 210 nm – optimized, (b) 310 nm and (c) 550 nm. (d) Statistical analysis of the diameter of the nanostructures in the optimized nanostructured ITO electrode derived from AFM measurement. (e) Transmittance  $T$  and reflectance  $R$ , and (f) sheet resistance ( $R_{sh}$ ) of the planar ITO electrode and the NS ITO electrode for average inter-distance between the nanostructures of: 210 nm, 310 nm and 550 nm. Adapted with permission from ref. [158], © 2020 Optical Society of America.

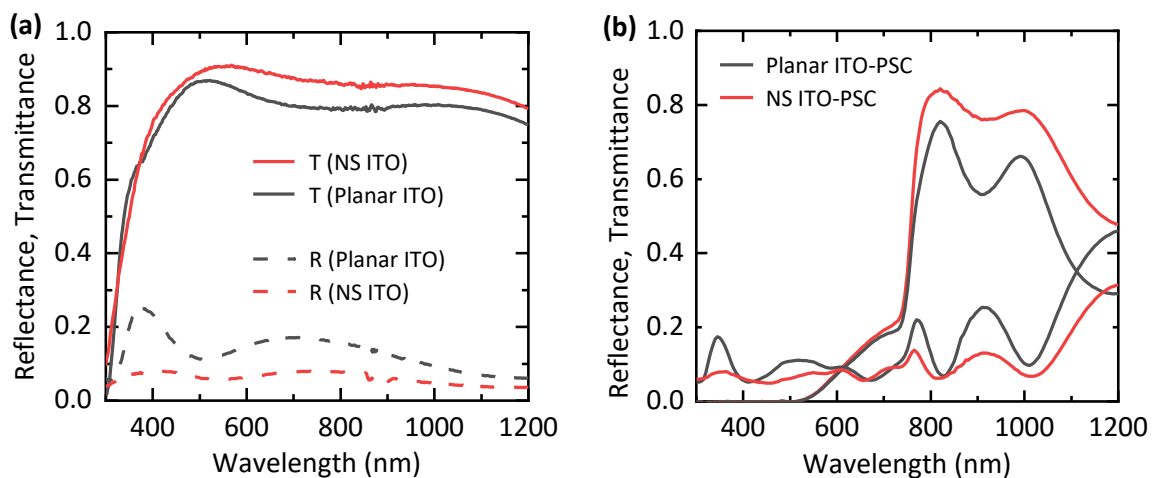


**Figure 6.13.** Reflectance and transmittance of the planar and nanotextured ITO electrode (a) on glass and (b) of the semitransparent perovskite solar cell (glass/ITO/SnO<sub>2</sub>/perovskite/spiro-OMeTAD/MoO<sub>x</sub>/ITO). Adapted with permission from ref. [158], © 2020 Optical Society of America.

For larger inter-distances of the nanopillars the reflectance increases over the complete spectrum (300 nm – 1200 nm). In contrast to the optical improvement, the sheet resistance increases from 27  $\Omega/\text{sq}$  for the smallest nanopillar inter-distance to 73  $\Omega/\text{sq}$  (see Figure 6.12f). However, the overall results (see below), indicate that the increase in the sheet resistance does not play a significant role and the smaller average nanopillar inter-distance is desired due to the greatly improved transmittance (see Figure 6.12e).

The experimentally processed and optically best-performing nanotextures are close to the predicted optimum by the simulations for ordered nano-pillars of  $FF \approx 35\%$ ,  $p \approx 200$  nm, and  $h \approx 80$  nm. The diameter of the optimized nanostructures varies between 25 nm - 300 nm (see Figure 6.12d) and the average inter-distance between the nanostructures is  $\approx 210$  nm. The average height of these nanostructures is  $\approx 130$  nm. The subwavelength inter-distance between the nanostructures induces an effective gradual matching of the refractive indices, which reduces the reflection losses compared to a planar ITO front electrode (see **Figure 6.13a**). Therefore, the weighted transmittance (300 nm - 1200 nm) is enhanced by  $\approx 7\%_{\text{rel}}$  compared to the planar reference.

This nanotextured ITO front electrode is then embedded in semitransparent perovskite solar cells. In the devices, the transmittance for energies below the band gap ( $> 780$  nm) shows a strong and broadband improvement (see Figure 6.13b). Thus, the EQE of the bottom c-Si solar cell is enhanced by  $2.9 \text{ mAcm}^{-2}$  ( $\approx 23\%_{\text{rel}}$ ). In addition, the reduced reflectance losses in the visible spectrum ( $< 780$  nm) leads to an enhanced  $J_{\text{SC}}$  in the perovskite solar cell by  $\approx 2\%_{\text{rel}}$  (see **Figure 6.14**).

However, the  $V_{\text{OC}}$  of semitransparent perovskite solar cell with the nanotextured ITO front electrode decreases by  $\approx 40$  mV (see Figure 6.14b and Table 5), which is also evident in the increased non-radiative recombination (see PL measurements in ref. [158]). Compared to the planar reference, the charge carrier lifetime is increased from 5.8 ns to 8.2 ns in the device with the nanotextured ITO front electrode. The increased non-radiative recombination is observed by time-resolved photoluminescence (PL) spectroscopy of the planar and nanotextured perovskite solar cells. The rise in the carrier lifetime can be linked to the enhanced surface area or to a poor NS ITO/SnO<sub>2</sub> or SnO<sub>2</sub>/perovskite interface due to the texture. Compared to the planar reference, the series resistance of the device with the nanotextured ITO front electrode also increases from  $\approx 70 \Omega$  to  $\approx 81 \Omega$ . However, the planar reference perovskite solar cells and the devices with the nanotextured ITO front electrodes demonstrate both a stable power output (nano: 15%, planar: 16%), see MPP tracking in ref. [158]).

**Table 5.** Electrical parameters of the top, bottom and 4T tandem solar cell for the planar and nanotextured ITO front electrode. Adapted with permission from ref. [158], © 2020 Optical Society of America.

Parameters/ Device Architecture	Planar ITO- PSC	NS ITO- PSC	c-Si: standalone	c-Si: Planar	c-Si: NS	4T Planar ITO-PSC/c-Si tandem	4T NS ITO-PSC/c-Si tandem
$V_{\text{OC}}$ (V)	1.12	1.08	0.70	0.67	0.67	-	-
$J_{\text{SC}}$ ( $\text{mAcm}^{-2}$ )	19.6	20.0	38.9	12.8	15.7	-	-
FF (%)	78	73	80	80	80	-	-
PCE (%)	17.1	15.9	21.8	6.8	8.5	23.9	24.4
SPCE <sup>1</sup> (%)	16.0	15.0	-	-	-	22.8	23.5

<sup>1</sup> The stabilized power conversion efficiency (SPCE) for tandem devices is calculated from the PCE of the top semitransparent PSC (after 5 min) and the PCE of the bottom c-Si solar cell at the maximum power point.

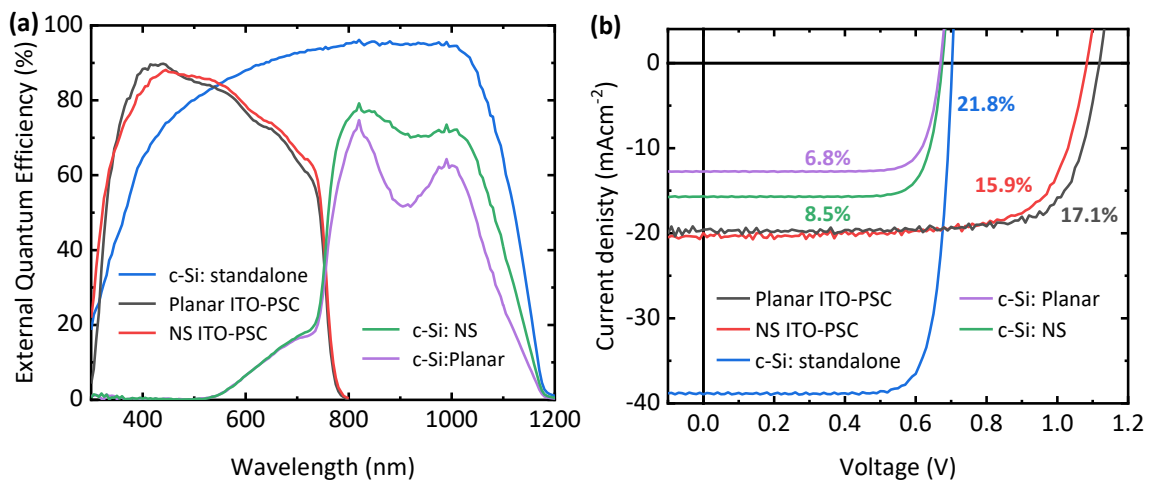


**Figure 6.14.** (a) External quantum efficiency (EQE) and (b) current density – voltage (IV) characteristics of the c-Si standalone, the planar ITO perovskite solar cell (PSC), and the PSC with the nanotextured ITO front electrode (NS ITO). Moreover, the filtered (by the planar and nanotextured perovskite solar cell) c-Si solar cell EQE and IV are provided. Adapted with permission from ref. [158], © 2020 Optical Society of America.

Moreover, the enhancement in the transmittance – although the PCE of the top perovskite solar cell is reduced in the case of a nanotextured ITO front electrode – leads to an improvement in the overall 4T tandem PCE by 1.7%<sub>abs</sub>. In this regard, the 4T tandem PCE increases from 23.9% (planar) to 24.4% (nano). In addition to that, also the overall stabilized PCE is improved from 22.8% (planar) to 23.5% (nano).

In the mechanical stacked 4T (with an air gap between the perovskite and silicon solar cell), an interdigitated back contact (IBC) c-Si solar cell is used (see ref. [158] for more details on the c-Si architecture). The c-Si solar cell shows a standalone PCE of 21.8% (see Figure 6.14 and Table 5). In the 4T tandem configuration, this c-Si bottom solar cell yields a PCE of 8.5% (nano) compared to a PCE of 6.8% (planar). This significant improvement of the 4T perovskite/c-Si tandem solar cell of the overall tandem PCE by 1.7%<sub>abs</sub> is mainly due to the superior increase in the transmittance. Assuming a similar  $V_{OC}$  and FF for the perovskite top cell with the nanotextured ITO front electrode as the planar reference, the PCE in such a 4T tandem device could be enhanced up to  $\approx 26\%$  (+8.7%<sub>rel</sub>), thus indicating the great potential of the nanotextured ITO electrodes.

Therefore, improving the  $V_{OC}$ , is of highest importance for real tandem applications with the nanotextured ITO electrodes. The loss in  $V_{OC}$  is mainly due to increased non-radiative recombination's due to the textured interfaces (ITO, SnO<sub>2</sub> and perovskite). Therefore, the fabrication of the nanotextured perovskite solar cells needs to improve. In particular, the interfaces due to the nanotexturing. One potential strategy is the evaporation of the electron transport layer, leading to a more uniform coverage of the nanotextured ITO layer compared to the solution processed thin-film [109].

Moreover, the current deposition techniques of the front ITO need to be optimized to avoid formation of small cracks in the nanotextured ITO electrodes and thus increase the sheet-resistance. In particular, highest sheet-resistance is obtained for the smallest

nanotextured ITO electrodes with an average inter-distance of  $\approx 210$  nm (see Figure 6.11b). In addition and in order to reduce the sheet-resistance further, also metal grids could be applied [177]. However, a small sheet resistance is indispensable for larger active areas paving the way towards realistic module sizes. Therefore, it is highly encouraging to resolve the remaining challenges of the electrical properties of the nanotextured perovskite solar cells and exploit by future work the full potential of this nanophotonic concept.

In order to scale up the concept to relevant module sizes, not only the electrical properties of the nanotextured ITO electrodes have to be considered, but also the manufacturing process of the nanotextures. The current polymer blend lithography promises to go to larger scale (4 – 5-inch wafer-size), however, due to the spin coating there will be an upper limit. Therefore, the pattern needs to be either transferred to a roll-to-roll process [178] or the texture needs to be fabricated differently. The latter seems to be possible via inject-printing [179]. Which would integrate well in all-inkjet printed perovskite solar cells, currently heavily investigated [180–182].

Moreover, a direct implementation of the nanotextures into the glass substrate would enable higher process temperatures for the perovskite solar cell and especially for the front ITO. With a higher process temperature, a more transparent ITO can be achieved [183,184]. Circumventing the use of polystyrene might also be important for the long-term stability of the device, since polystyrene might be susceptible for photodegradation [185]. A potential replacement might be the transferring the textures into the glass directly by etching [186] or a liquid glass approach [30].

Besides, it should be noted that in contrast to the simulated model architecture, the enhancement of the transmittance into the silicon bottom solar cell increases from  $\approx 2\%_{\text{rel}}$  to  $\approx 22\%_{\text{rel}}$ . Nevertheless, the enhancement in the top perovskite solar cell is comparable. The large discrepancy between the simulated and measured transmission arises mainly due to the better match of the refractive indices in the simulated layer stack. In particular, the refractive index of the front ITO in the simulations was chosen very optimistically, leading to an already high transmission in the planar reference. However, this shows that an optimization of the current ITO front electrode in terms of refractive index is of paramount importance. In addition, indium zinc oxide (IZO) or hydrogenated indium oxide (IOH) might be suitable replacement to minimize parasitic near-infrared absorption losses in the electrodes [160]. First simulations and experiments with IZO show this impressively (see Appendix B) by increasing the transmittance below the band gap of the perovskite around 15 - 20%<sub>abs</sub>. However, as seen by the optical simulations provided in chapter 6, even for an optically improved front electrode ('ITOHol13', see Appendix A), the nanotexturing still leads to considerably enhancements in the overall tandem power conversion efficiency. This is due to the fact that the effective refractive index of the corrugated layer still can be better matched to the one of a perfect anti-reflection coating by tuning the geometry of the nanotextures (see section 6.2.4).

## 6.4 Energy yield estimation of nano-patterned ITO electrode-based perovskite/c-Si tandem PV

So far, the  $J_{SC}$  of the perovskite top and c-Si bottom solar cell as well as the respective tandem efficiency are reported for normal incidence. The key to estimate the realistic device performance is the estimation of the energy yield (EY), which takes into account the performance of the tandem module under oblique angles and especially realistic irradiation conditions. In the following, the EY of the perovskite/c-Si 4T tandem solar cells with the nanotextured ITO front electrode are compared to their planar reference. Therefore, the angular dependence of the 4T tandem solar cell is experimentally measured. To estimate the potential of the nanotextured electrodes, the electrical ( $V_{OC}$ ,  $J_{SC}$  and FF) of the top cells are assumed to be the same and angular dependent EQE data is used as input for the EY modelling.

Whereas the  $J_{SC}$  of the top perovskite solar cell with the nanotextured ITO electrode does not show a strong difference in the angular dependency compare to the planar reference, the  $J_{SC}$  of the bottom c-Si solar cell with the nanotextured ITO electrode demonstrates an improved angular stability (see **Figure 6.15a**).

The decrease for higher angles of incidence is more pronounced for the planar reference. For angles up to  $60^\circ$ , the  $J_{SC}$  reduces to 84% in the c-Si solar cell in the planar configuration. For the perovskite solar cell equipped with the nanophotonic ITO electrode on top, the  $J_{SC}$  of the c-Si solar cell still is  $> 90\%$  for an angle of incidence of  $60^\circ$  (see **Figure 6.16a**).

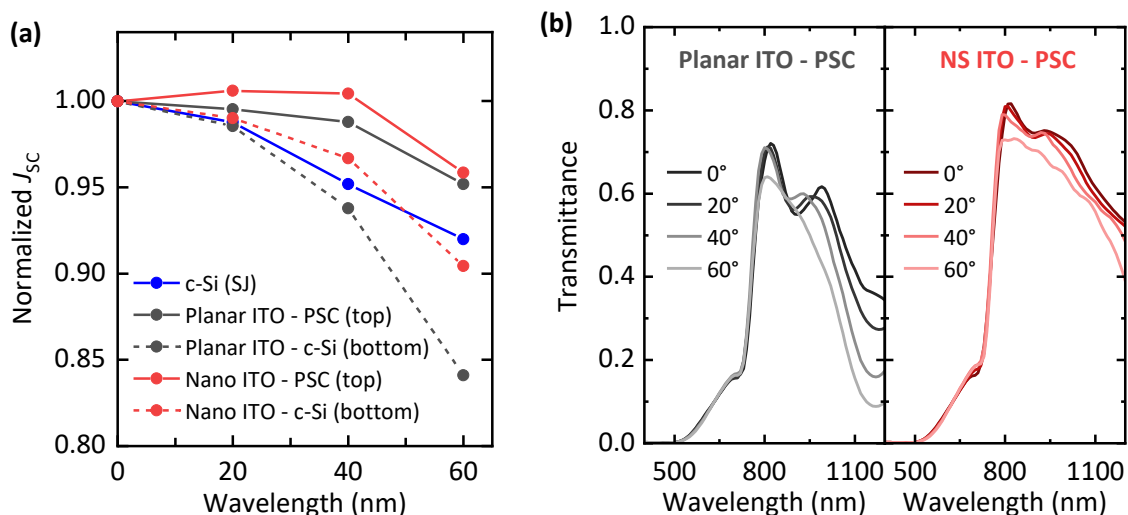


**Figure 6.15.** (a) normalized short-circuit current density  $J_{SC}$  of the single-junction c-Si solar cell, the perovskite and c-Si solar cells in 4T configuration for a planar and nanotextured ITO front electrode. (b) Transmittance of the perovskite solar cell equipped with planar and a nanotextured ITO front electrode. Adapted with permission from ref. [158], © 2020 Optical Society of America.

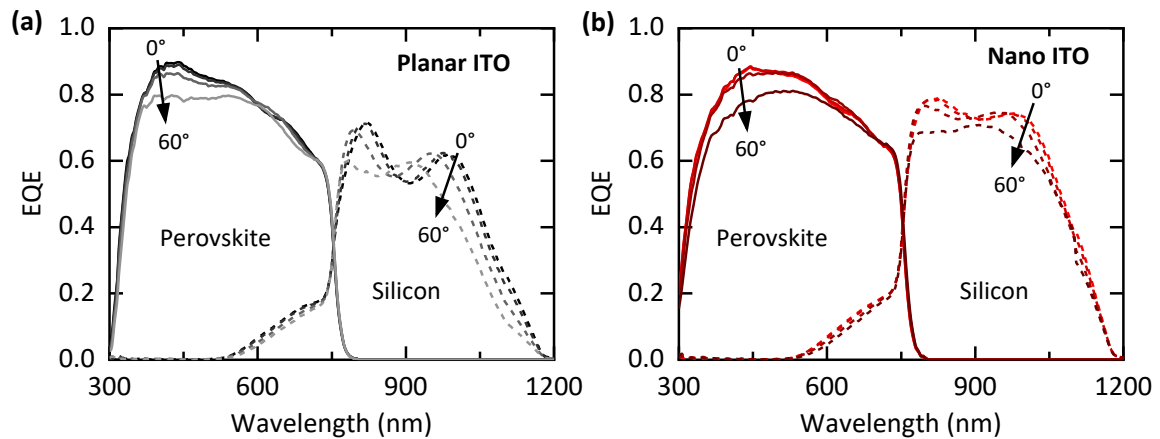


**Figure 6.16.** External quantum efficiency (EQE) of the perovskite solar cell equipped with (a) planar and (b) a nanotextured ITO front electrode and the c-Si solar cell in the 4T configuration for different angle of incidence. In case of the nanotextured ITO electrode, the improved transmittance leads to an enhanced EQE in the c-Si solar cell. Adapted with permission from ref. [158], © 2020 Optical Society of America.

Compared to the planar reference, the absolute gain due to the nanotexture in the c-Si bottom solar cell of the 4T architecture is  $3.7 \text{ mAcm}^{-2}$ . This is due to the improved transmittance of the nanophotonic ITO electrode – particularly for larger angles of incidence, which also result in a significantly improved EQE of the bottom c-Si solar cell (see Figure 6.16). The EQE of the top perovskite solar cell turns out similar for the planar (a) and nanotextured ITO front electrode (b). Due to the enhanced overall transmittance for wavelengths  $> 780 \text{ nm}$ , the EQE in the bottom c-Si solar cell increases. Especially at a wavelength of  $910 \text{ nm}$  the dip in EQE flattens out. Moreover, above  $950 \text{ nm}$ , no decrease in the EQE for larger angles is observed, which is due to the improved optical transmittance (see Figure 6.16b).

Therefore, the realistic enhancement due to the nanotextured ITO electrode might be even stronger than estimated for normal incidence. The output power during a single day January 3<sup>rd</sup>) in Phoenix, USA, reflects the improved 4T tandem performance (see **Figure 6.17a**). The relative gain during the course of the day is above 30% in the c-Si bottom and  $\approx 5\%$  in the top perovskite solar cell. In the early morning (sunrise) and evening (sunset), the c-Si solar cell benefits even more from the improved transmittance for larger angles of incidence. This is due to the fact that the simulated solar module is elevated at optimal tilt and the angle of incidence on the solar module is lowest during noon.

Moreover, the EY is calculated for four different locations in the USA with different climatic conditions: boreal (Chicago, Illinois), temperate (Portland, Oregon), tropical (Miami, Florida), and arid (Phoenix, Arizona). Since each of the locations have their specific climate (share of direct and diffuse irradiance, temperature, latitude), the annual EY is different for the selected locations (see Figure 6.17b). However, the relative enhancement of the EY due to the nanotextured front electrode in the 4T tandem solar cell is  $\approx 10\%_{\text{rel}}$  irrespective of the location. This also exceeds the estimated enhancement of  $8.7\%_{\text{rel}}$  for standard test conditions (normal incidence, AM1.5). In comparison to the planar

reference, the perovskite sub-cell with the nanotextured ITO electrode considered as single-junction, improved by  $\approx 3\%_{\text{rel}}$ . Compared to the single-junction c-Si solar cell used in the tandem configuration, the nanotextured 4T tandem is improved by 14 - 15% $_{\text{rel}}$ . Therefore, the EY study reveals that nanotextured electrodes bear an exciting potential to improve the generated power output of perovskite-based tandem PV.

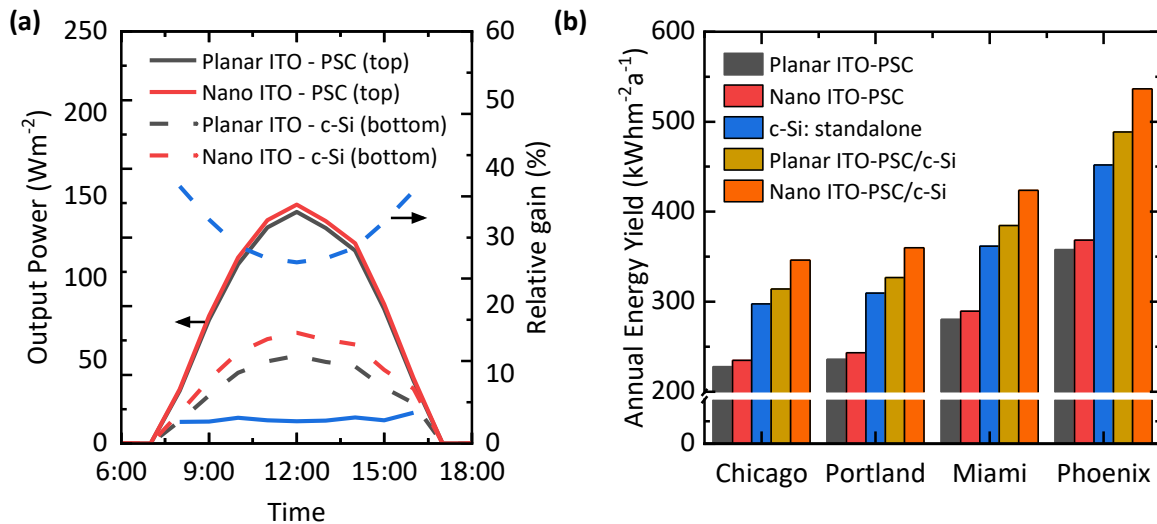


**Figure 6.17.** Energy yield calculations of the perovskite/c-Si 4T tandem solar cells with a nanotextured ITO front electrode compared to the planar reference. (a) Power output of the sub-cells and relative improvement over the course of one day. (b) Annual energy yield for four locations with different climatic conditions: boreal (Chicago, Illinois), temperate (Portland, Oregon), tropical (Miami, Florida), and arid (Phoenix, Arizona) of the sub-cells and the 4T tandem configurations. The EY improves by  $\approx 10\%_{\text{rel}}$  independent from the location. Adapted with permission from ref. [158], © 2020 Optical Society of America.

## 6.5 Summary

In the present chapter, nanophotonic front electrodes are designed and developed to improve the light incoupling into the top perovskite solar cell and to enhance the transmission into the bottom crystalline silicon (c-Si) solar cell in a four-terminal (4T) tandem configuration. In this regard, the nanophotonic front electrodes effectively reduce the reflection losses of the front transparent indium tin oxide (ITO) electrodes.

Electromagnetic simulations of the nanotextures lead to optimum periods in the range of 200 nm, and therefore shifting the dimension into the range of the effective medium approximation. The simulations indicate an improvement by the nanotextured front electrodes in the current generation and thus in the tandem power conversion efficiency (PCE) of perovskite/c-Si tandem by  $\approx 4\%_{\text{rel}}$ . Due to the small periods, nano-holes and nano-pillars lead to very similar improvements. The light effectively sees an average refractive index and the corrugated interface(s) up to the perovskite mostly act as an effective medium to the propagating light. For the optimum geometry, the effective refractive index of the corrugation matches well between the ones of glass and ITO and therefore

outperforms commonly employed single layer anti-reflection coatings for the full spectral range.

The nanophotonic electrodes, moreover, are implemented in prototype 4T perovskite/c-Si tandem solar cells, demonstrating an improvement of  $\approx 2\%_{\text{rel}}$ . In the experimental realization, disordered nanopillars are fabricated on the glass substrate with a rapid and cost-effective polymer blend lithography method. Via phase separation of two immiscible polymers (PMMA and PS), self-assembled patterned monolayers are produced. Due to the small period, simulation predicted equivalent enhancements by disordered nanotextures as for the periodic counterparts. For the same geometric fill factor, the same enhancements are calculated.

Compared to the simulated devices, the improvement in the bottom solar cell due to the enhanced transmittance is more prominent ( $22\%_{\text{rel}}$  vs.  $2\%_{\text{rel}}$ ). Moreover, the perovskite top solar cell only gains  $\approx 0.4 \text{ mAcm}^2$ , which is less than the  $\approx 0.9 \text{ mAcm}^2$  predicted by the simulations. However, it should be noted that in the simulated architecture, the refractive index of the front ITO matches better between the glass and  $\text{SnO}_2$ . Therefore, the transmittance of the planar reference is already higher. However, this teaches two things: firstly, the development of an improved front transparent electrode is of paramount importance, and secondly, even with an optically improved front transparent electrode, the nanotexturing still leads to considerably enhanced tandem PCEs.

Although, the tandem PCE is enhanced by  $2\%_{\text{rel}}$ , in the experiment, one remaining challenge in the experiment is to overcome the loss in open-circuit voltage. For this, further optimization is needed to mainly reduce the non-radiative recombination's induced by the textured interfaces. One potential strategy is the evaporation of the electron transport layer, leading to a more uniform coverage of the nanotextured ITO layer compared to a solution processed thin-film. Moreover, the sheet resistance is comparably high for real tandem devices. This have to be solved by the optimization of the ITO deposition, which in the current state still leads to cracks in the nanotextured ITO films.

Nevertheless, nanophotonic electrodes demonstrate a superior angular stability. Assuming similar electrical parameters of the nanotextured and planar perovskite devices reveal a  $\approx 10\%_{\text{rel}}$  improvement in the annual EY compared to the planar reference. This even surpasses the 9% enhancement for standard test conditions (normal incidence). In addition, the nanophotonic electrodes are not suspect to any spectral dependence and do not show any significant dependency of the different climatic and irradiation conditions. For all four locations, the relative increase in the annual EY remains constant. Therefore, it is highly encouraging to resolve the remaining challenges of the electrical properties of the nanotextured ITO front electrodes for the perovskite solar cells and exploit by future work the full potential of this nanophotonic concept.



## 7 Nanophotonic perovskite solar cells with improved light trapping

In this chapter, the light trapping properties of nanopatterned perovskite absorber layers are investigated. The nanotexture inside the perovskite leads to the coupling of incident light to quasi-guided modes and thus enhances the absorption inside the perovskite layer. The coupling of the incident light to specific modes allows to primarily control and enhance the absorption in the weaker absorbing regimes close to the band gap of the perovskite solar cells.

### Acknowledgements and contributions

*The majority of the results reported in this section on the nanophotonic perovskite solar cells have been published in references [49,50,187]. These first-author publications encompass the optical design and simulations on nanophotonic perovskite solar cells and experimental implementation in working perovskite solar cells. The experimental work was assisted by the two master students: Dong Jae Lee [188] and Artyom Assadillayev [189]. Whereas Dong Jae Lee conducted mostly initial results on planar imprinted perovskite layers, Artyom Assadillayev focused on optimized parameters for the nanoimprint of the perovskite layers. For the numerous nanoimprinted perovskite solar cells, Ihteaz Hossain, Fabian Schackmar, Jonas Schwenger, Somayeh Moghadamzadeh, Saba Gharibzadeh, Tobias Abzieher and Amjad Farooq assisted to process the perovskite absorber, electron and hole transport layers. The two master theses on the nanoimprinted perovskite layers and the project on nanoimprinted perovskite solar cells were initiated and supervised by Raphael Schmager.*

## 7.1 Introduction

In addition to the presented light incoupling textures at the front glass cover of PV modules and the nanotextured front electrodes in perovskite solar cells, the patterning of the perovskite absorber material itself is investigated in the following. By the patterning of the absorber layer with periodic textures, the coupling of incident light to quasi-guided modes can be achieved. This increases the absorption and therefore the short-circuit current density ( $J_{SC}$ ). Moreover, the coupling to specific modes allows to control and enhance the absorption in the weaker absorbing regimes close to the band gap of the perovskite solar cells.

Various techniques to pattern the perovskite layers have been proposed in literature: (1) focused ion beam lithography [190–193], (2) electron beam etching [194–196], (3) recrystallization through phase transformation [197,198], and (4) thermal nanoimprint lithography (TNIL) [187,199–203]. From those, the TNIL is the most promising, since it allows patterning of nanostructures at both large scale and high throughput, which is crucial for up-scalable fabrication technologies such as roll-to-roll processing [178,204]. During the TNIL, the perovskite recrystallizes due to the applied heat and pressure yielding to an improved crystal structure that exhibits fewer surface defects [200]. In contact with a textured mold, the perovskite layer is directly patterned by the TNIL.

So far, the main focus in research has been on nano-patterning the perovskite layer for the purpose of optically-pumped lasing [191,200,201], light-emitting diodes [197] and nanostructured photodetectors [199]. Only recently, nanoimprinted perovskite solar cells with improved  $J_{SC}$  have been reported, which show a broadband enhancement of the external quantum efficiency [203,205]. In this regard, Kim *et al.* identified that the uniaxial compression leading to an enhanced crystal quality and Wang *et al.* described the nanophotonic light trapping by diffraction of incident light at the textured perovskite interface. However, the coupling of incident light to quasi-guided modes was not discussed in detail. The following chapter builds on these studies and provides detailed experimental and simulative analysis of the light coupling to quasi-guided modes in nanoimprinted perovskite solar cells.

First, optical simulations on the light coupling to quasi-guided modes in the nanophotonic perovskite solar cells are discussed and optimized geometrical parameters are derived for periodic holes inside the perovskite layer. The nanophotonic perovskite solar cells improve the  $J_{SC}$  by 5 - 6%<sub>rel</sub> compared to their planar references.

Next, experimental results on nanophotonic perovskite solar cells are reported. Therefore, the perovskite layers are nanoimprinted with a facile TNIL process. These nanoimprinted perovskite solar cells demonstrate an enhanced  $J_{SC}$  with respect to their planar references by  $\approx 2\%$ <sub>rel</sub>. The enhancement in  $J_{SC}$  by the coupling of the incident light to quasi-guided modes, enhancing the absorption near the band gap of the perovskite is analyzed in detail. Due to the nanoimprint, the electrical parameters of the perovskite

solar cells remain unchanged and more importantly, the presented nanoimprinted perovskite solar cells show a stable power output.

Since the implemented photonic grating in the perovskite layers might be susceptible for oblique incidence of light, the angular dependent performance of the nanophotonic perovskite solar cells is analyzed. Finally, energy yield simulations are performed to evaluate the nanophotonic perovskite solar cells under realistic operation conditions.

## 7.2 Nanophotonic perovskite solar cells

In order to increase the short-circuit current density ( $J_{sc}$ ) in perovskite solar cells, the absorption in the perovskite layer has to be enhanced. Enhancing the absorption inside the perovskite thin-film solar cell can be achieved by exciting quasi-guided resonances inside the photo-active layer to which the incident light can couple [206]. These resonances lead to a stronger concentration of the electromagnetic field inside the perovskite absorber. In this regard, a nanophotonic grating inside the perovskite layer is designed, which effectuates the coupling and therefore leads to improved absorption within the perovskite absorber layer.

In order to achieve this, a nanophotonic modification by a cylindrical patterning of the absorber layer is proposed as illustrated in **Figure 7.1**. In the following, three configurations are discussed: (1) a planar reference, (2) a cylindrical indentation, and (3) a hole inside the perovskite layer (see Figure 7.1). Whereas the “indentation” corresponds to a hole inside the perovskite absorber layer with a certain height  $h$ , the “hole” represents the maximum possible indentation.

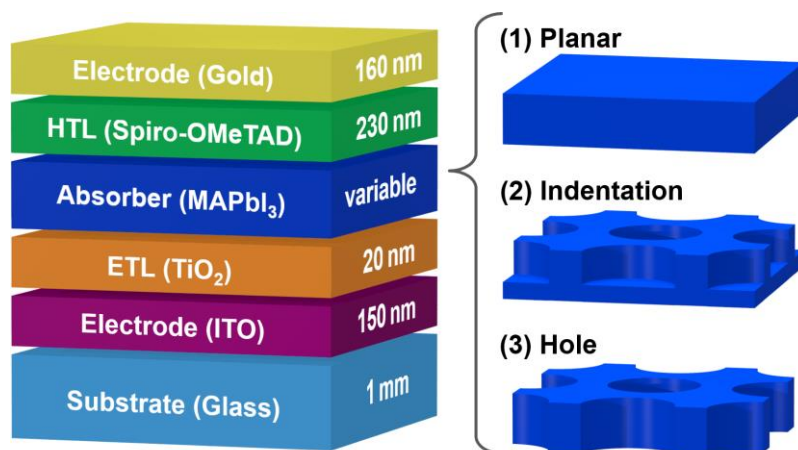


**Figure 7.1.** Schematic of the layer stack with corresponding layer thicknesses of the simulated perovskite solar cell. Three different configurations of the active layer are simulated: (1) a planar reference, (2) a cylindrical indentation into the perovskite layer of variable depth; and 3) a hole geometry which corresponds to the maximum cylindrical indentation. Adapted with permission from ref. [49], © 2019 Elsevier.

In order to evaluate the performance of the “indentation” and “hole” configuration in comparison to the “planar” reference, wave-optical simulations are carried out with the commercially available software Comsol Multiphysics® (see details in section 3.1.2). Based on the three-dimensional electromagnetic simulations of a unit cell of the full perovskite solar cells, the enhancement in the short-circuit currents are calculated by the absorption enhancements in the perovskite layer. The simulations are performed with a plane wave starting inside the lossless glass layer. The obtained data is afterwards corrected by the air/glass reflectance. Therefore, only the optical enhancement is simulated and evaluated. Nevertheless, it should be noted that the increased perovskite surface due to the nanophotonic grating inside the layer, is expected to enhance carrier recombination. However, due to self-passivation of the perovskite layer, these losses are expected to be small [207]. Besides, the potential improvement of the open-circuit voltage  $V_{OC}$  due to the decreased thickness is neglected in this study as well [208]. In addition, the experimental realization (see section 7.4) of nanophotonic perovskite solar cells shown that the electrical parameters remain largely the unaffected by the corrugation.

The planar reference layer stack considered in this study (see Figure 7.1) comprises indium tin oxide (ITO) as well as gold as a rear electrode. The well-established methylammonium lead triiodide perovskite ( $\text{MAPbI}_3$ ) is used as absorber material, since it was at the time of this study the most researched lead halide perovskite and exhibits very similar optical properties to the various types of multi-cation perovskites that are used in today’s record solar cells [167,168,209]. The charge transport layers are titanium dioxide ( $\text{TiO}_2$ ) and 2,2',7,7'-tetrakis[N,N-di(4-methoxyphenyl)amino]-9,9'-spirobifluorene (spiro-OMeTAD). The refractive indices of the perovskite absorber and the other materials used for the optical simulations are summarized in Appendix A.

Compared to the planar reference, the nanophotonic indentation and hole configurations demonstrate a significantly enhanced  $J_{SC}$  (**Figure 7.2**). For different initial perovskite thicknesses  $d_{\text{Pero}}$  the corresponding  $J_{SC}$  is calculated. Therefore, the volume of the perovskite absorber in the nanophotonic configurations equals the same volume as the volume in the planar reference with the respective same initial thickness  $d_{\text{Pero}}$ . For a conventional perovskite absorber thickness<sup>1</sup> of  $\approx 300$  nm, the  $J_{SC}$  is enhanced by  $\approx 1.0 \text{ mAcm}^{-2}$  and  $\approx 1.2 \text{ mAcm}^{-2}$  for the hole and indentation, respectively (see Figure 7.2). This corresponds to a relative improvement of 4.7% and 5.6%. The geometry of the nanophotonic perovskite layers is defined by the optimization shown further below. In Figure 7.2, the geometric fill factor is set to 40% and the period is fixed at 380 nm for both the hole and indentation with depth of 120 nm.

---

<sup>1</sup> It should be noted that the thicknesses of the record devices evolved from  $\approx 300$  nm towards 400 - 500 nm during the period of this work.

---

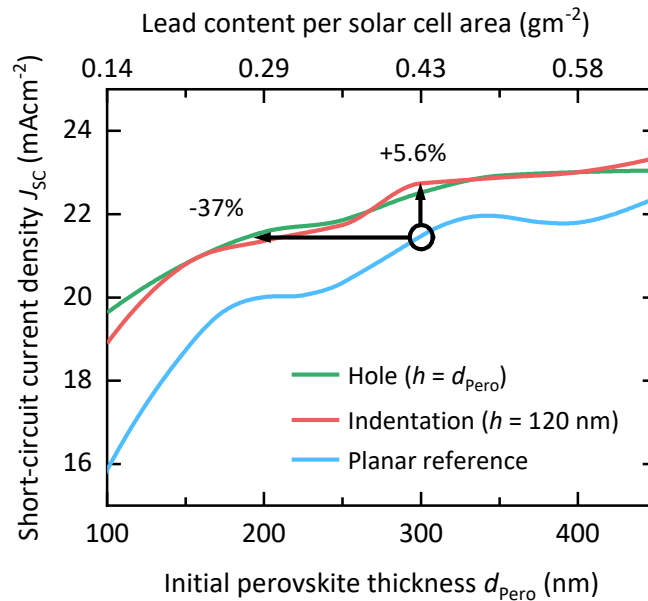


**Figure 7.2.** Short-circuit current density  $J_{\text{sc}}$  of the hole and indentation configuration of the nanophotonic perovskite solar cell compared to the planar reference for different perovskite layer thicknesses  $d_{\text{perovskite}}$ . The perovskite thickness is proportional to the lead content per area in the device [210]. The nanophotonic configurations have a period of 380 nm and a geometric fill factor of 40%. Adapted with permission from ref. [49], © 2019 Elsevier.

Next to the enhanced  $J_{\text{sc}}$  of the nanophotonic perovskite solar cells, nanophotonic perovskite solar cells with significantly lower absorber thickness can yield the same or even higher  $J_{\text{sc}}$  than their planar counterparts. In this regard, it is possible to reduce the perovskite absorber volume while maintaining high  $J_{\text{sc}}$ . A reduced absorber volume directly leads to a reduced lead content in the perovskite solar cell (expressed in  $\text{gm}^{-2}$ ). For the considered 300 nm thick perovskite layer, the nanophotonic perovskite solar cell demonstrate the same  $J_{\text{sc}}$  for a 33% (indentation) and a 37% (hole) reduced amount of perovskite material. Compared to the planar reference with  $0.43 \text{ gm}^{-2}$ , this equals a lead content of  $0.29 \text{ gm}^{-2}$  and  $0.27 \text{ gm}^{-2}$ , respectively.

As mentioned, reducing the amount of perovskite material in the perovskite solar cells, directly links to a reduced amount of harmful lead in the devices. The reduction and the replacement of the harmful lead in the perovskite solar cells is still a key challenge and is heavily investigated in current research [211–213]. At present, the most prominent routes to mitigate lead are the (partial) substitution of the lead by a group IV element, like tin or germanium and its replacement by a double perovskite structure, where lead is replaced by a heterovalent substitution with noble metals [214].

For this reason, intensive research is currently being carried out on lead-free perovskite solar cells, as well as on a partial replacement of the Pb by Sn or Ge [215]. One of the goals is to fall below the - still unspecified - maximum permissible values for Pb use in perovskite PV while maintaining the stability and the high PCEs. In this regard, it should be noted that the limit for environmental contamination depend heavily on the distribution of the

degraded perovskite material in exposed soil or groundwater, and legislation still needs to be enacted.

Therefore, being able to reduce the lead content, while maintaining high PCE, nanophotonic perovskite solar cells are an excellent alternative to the partial replacement of Pb with Sn or Ge. The reason for this is that the nano-structuring of the perovskite absorber is independent of the perovskite absorber composition used and thus offers access to all possible perovskite compositions. For example, perovskite solar cells with different band gaps can benefit from this. Moreover, a combination of the partial replacement by Sn or Ge may be a conceivable strategy.

The enhanced  $J_{SC}$  in the nanophotonic perovskite solar cells is represented in the enhanced absorption in the perovskite layer. In **Figure 7.3**, the absorption of the two nanophotonic configurations: “holes” (Figure 7.3a and c) and “indentation” (Figure 7.3b and d) with a depth of 120 nm is compared to the planar reference device. Here, an indentation is with a depth of 120 nm is studied. A full optimization of the indentation depth is discussed in Figure 7.6. The comparison is shown for an initial perovskite absorber thickness of 200 nm (Figure 7.3a and b) and 300 nm (Figure 7.3c and d). The enhancement in the  $J_{SC}$  (summarized in Figure 7.3e) is due to the coupling of incident light to quasi-guided modes in the perovskite thin-film. This coupling is represented in distinct peaks in the absorption spectra near the band gap of the perovskite (close to 800 nm). Since the absorption is (comparably) weak in the planar reference close to the band gap, strong enhancements are visible.

For shorter wavelengths (600 - 750 nm), much broader enhancements are present in the absorption spectra of the nanophotonic perovskite solar cells. Most interestingly, the absorption near the band gap surpasses the absorption of the planar reference neglecting all parasitic absorption and is close to the Yablonovitch limit. For the Yablonovitch limit, perfect Lambertian light trapping is assumed and parasitic absorption as well as surface reflections at the air-glass interface are neglected. For shorter wavelengths (< 500 nm), the nanophotonic perovskite solar cells with a complete hole, demonstrates a strong loss in the absorption, which is linked to an increased parasitic absorption – mainly in the spiro-OMeTAD layer (see **Figure 7.4a**). For decreased indentation depth, the parasitic absorption is reduced and the absorption equals the planar case (see Figure 7.4b).

The increased parasitic absorption of spiro-OMeTAD layer is also visible in the distribution of the electric field intensity for such short wavelengths (e.g. 355 nm) shown in **Figure 7.5a**. At 355 nm, the perovskite layer is strongly absorbing the incident light and no quasi-guided modes are supported. However, in the “hole” configuration, the void of the hole is filled by spiro-OMeTAD, which starts absorbing once reached by the electromagnetic wave.

For longer wavelengths, 675 nm (see Figure 7.5b) and 795 nm (see Figure 7.5c), distinct periodic patterns in the electric field intensity are apparent for the nanophotonic

perovskite solar cells, which clearly correspond to the field enhancement through specific quasi-guided modes. Since the light absorption scales quadratically with the electric field intensity, the enhanced field intensity leads to strong enhancements in the absorptance (see Figure 7.3a and b). Similar patterns are apparent at distinct wavelengths demonstrating enhanced absorption in the case of a 300 nm initial perovskite layer thickness as shown in Figure 7.3c and d.

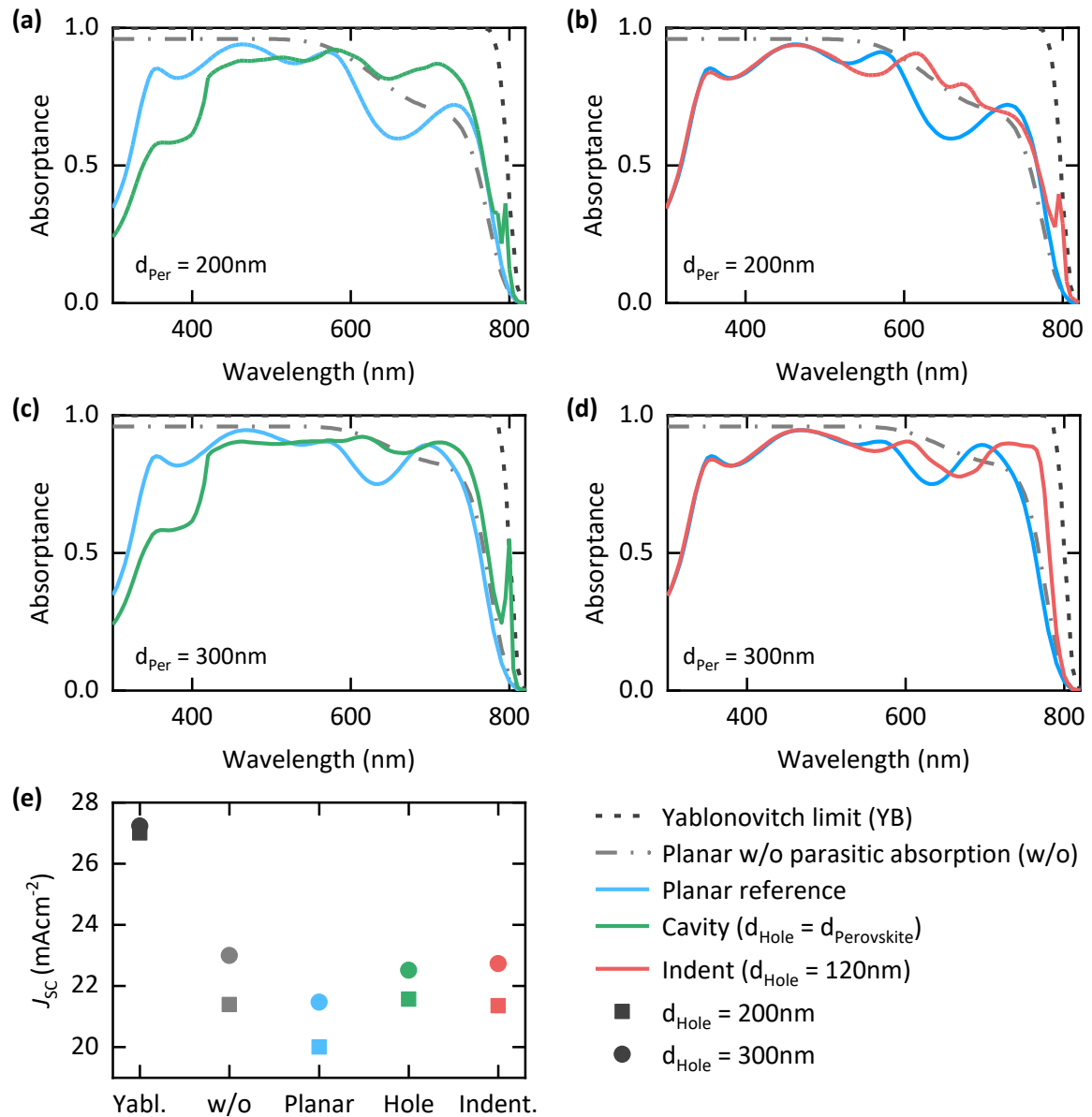


**Figure 7.3.** Simulated absorptance in the perovskite layer for the planar perovskite solar cells for a 200 nm (a, b) and a 300 nm (c, d) thick perovskite layer compared to the corresponding cavity and indentation configuration. Compared to the theoretical Yablonoitch limit, parasitic absorption in the perovskite solar cell reduces the overall absorption. (e) Both nanophotonic perovskite solar cells demonstrate similar  $J_{\text{sc}}$  as the planar reference without parasitic absorption. The displayed nanophotonic patterns employ a geometric fill factor of 40% and a period of 380 nm. Adapted with permission from ref. [49], © 2019 Elsevier.

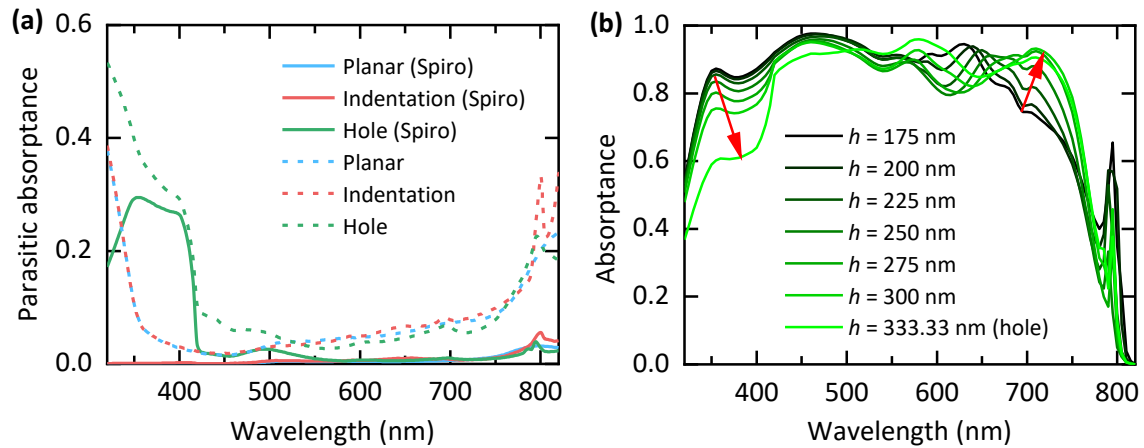


**Figure 7.4.** (a) Parasitic absorbance in the full device (bold) and in the spiro-OMeTAD layer (dotted) of the hole configuration, the indentation and the planar configuration. (b) Enhanced parasitic absorption in the hole configuration compared to the indentation and planar perovskite solar cells. The strongest loss is due to light absorption in the Spiro-OMeTAD layer at shorter wavelengths up to 420 nm. Adapted with permission from ref. [49], © 2019 Elsevier.

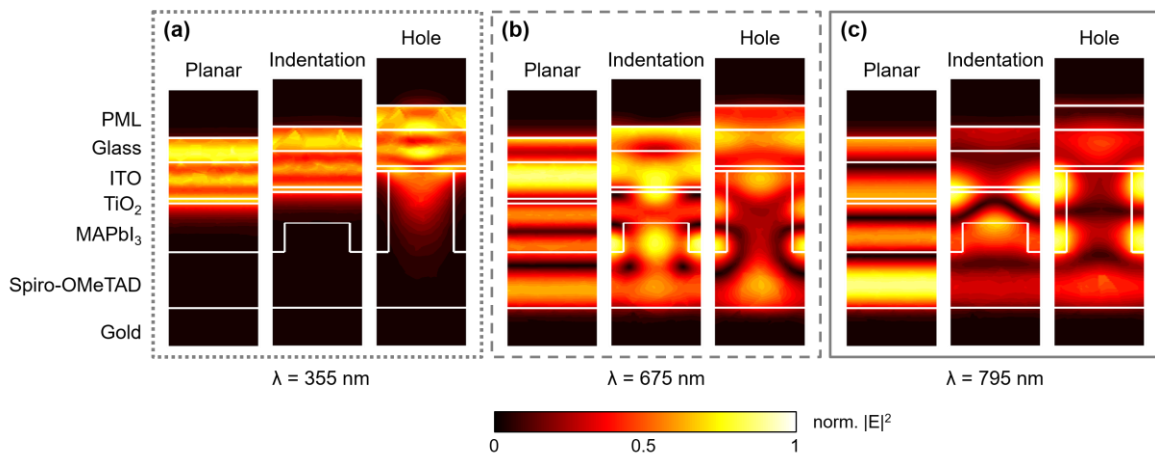


**Figure 7.5.** Normalized electric field intensity  $|E|^2$  distribution for incident wavelength of (a) 355 nm, (b) 675 nm, and (c) 795 nm for a 200 nm planar reference and the corresponding nanophotonic representations of the indentation and hole. A cross-section through the 3D unit cell of the nanophotonic perovskite solar cell is shown. To suppress back reflections, an additional perfectly matched layer (PML) is included at the top of the solar cell stack. For longer wavelengths, the characteristic patterns in the electrical field intensity for quasi-guided modes are present in the perovskite absorber layer. Adapted with permission from ref. [49], © 2019 Elsevier.

To maximize the  $J_{\text{SC}}$  in the nanophotonic perovskite solar cells, the geometrical parameters of the cylindrical indentations and holes are tuned. The optimization of the period  $P$ , the geometric fill factor FF, and the indentation depths  $d$  of the cylinders is illustrated in **Figure 7.6**. Compared to the planar reference, almost each set of parameters of the nanophotonic perovskite solar cells demonstrates an improved  $J_{\text{SC}}$ . The parameters are varied for three different perovskite initial thicknesses: 100 nm, 200 nm, and 300 nm. Within one of the subfigures, each of the three curves has the same initial perovskite layer thickness and therefore the same perovskite absorber volume.

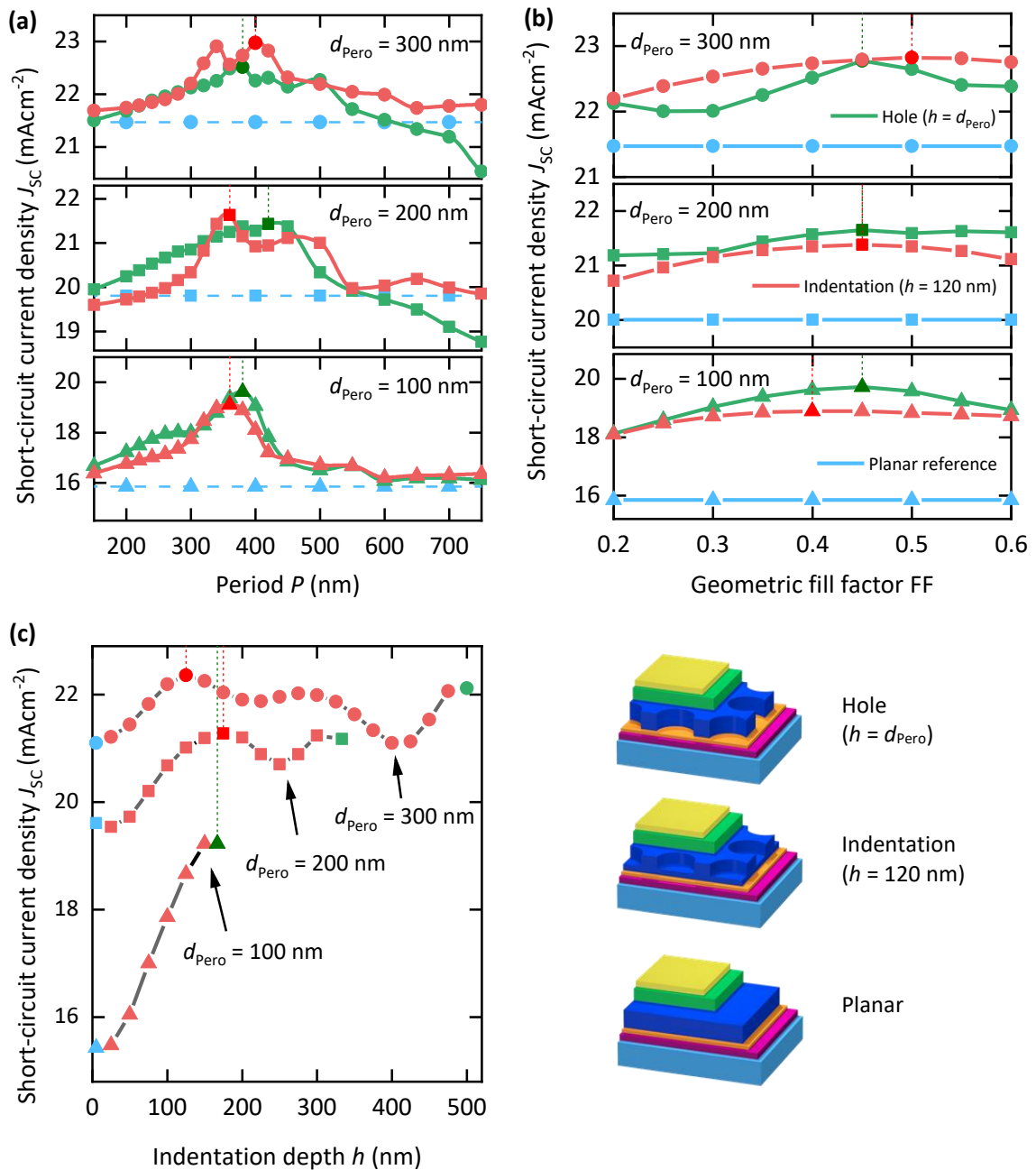


**Figure 7.6.** Short-circuit current density  $J_{sc}$  derived from the absorption in the perovskite layer of three different (initial) perovskite layer thicknesses  $d_{\text{perovskite}} = 100$  nm, 200 nm and 300 nm. The  $J_{sc}$  is calculated by the simulated absorbance. Two periodic configurations: “holes” and “indentation” are compared to the planar reference. The  $J_{sc}$  is compared for (a) different periods  $P$ , (b) different geometric fill factors  $FF$ , and (c) different indentation depths  $h$ . Whereas an indentation of 0 nm equals the planar reference and the maximum indentation per thickness corresponds to the “hole” configuration. All simulations are performed at  $P = 380$  nm and  $FF = 40\%$  if not defined differently by the sweep. Adapted with permission from ref. [49], © 2019 Elsevier.

Regardless of the perovskite thickness, the nano-pattern inside the perovskite layer enhances the  $J_{sc}$  of the nanophotonic perovskite solar cells. The optimum period (see Figure 7.6a) for both, the indentation with a depth of  $h = 120$  nm and the hole configuration, is found at  $\approx 400$  nm. In particular, the coupling of light to guided or quasi-

guided modes in the perovskite layer can be influenced by the period of the two-dimensional grating. In this regard, the light couples into modes by different grating diffraction orders, depending on the incidence angle and the wavelength. A guided mode analysis of the planar perovskite solar cell architecture is performed and illustrated in **Figure 7.7**. Since the extinction coefficient of the perovskites decreases near the band gap, enhancing the absorption in this spectral region is beneficial. Therefore, coupling is analyzed in the most relevant wavelength range above 600 nm (Figure 7.7b). The coupling of the incident light to these modes is expected for spatial frequencies of the grating matching the propagation constant of quasi-guided modes. The dispersion relation for the TE<sub>0</sub> and TM<sub>0</sub> mode discloses potential coupling to those modes in the perovskite layer for periods in the range between 300 nm and 500 nm. This matches very well with the found optimum period in Figure 7.6a.

The geometric fill factor for the sweep over the periods is set to FF = 40%, which is very close to the optimum FF. For the indentation, the optimum in the geometric fill factor shifts from 40% to 50% for an increased initial perovskite layer thickness from 100 nm to 300 nm. For the hole configuration, the maximum  $J_{SC}$  is always at a geometric fill factor of 45% (see Figure 7.6b).

For shallow indentations inside the perovskite absorber layer, the nanophotonic perovskite solar cell shows only minor enhancements in the  $J_{SC}$ . In Figure 7.6c, the indentation depth is varied from zero (“planar”) to the maximum possible for each of the distinct initial perovskite absorber thicknesses (“hole”). The strongest enhancements are found for indentations around 120 nm, which is valid for all three initial perovskite thicknesses. Whereas the relative improvement in  $J_{SC}$  observed for the indentation is less for the thicker layers, the relative gain for the 100 nm thin perovskite layer reaches 23.9%. However, this demonstrates, that a strong perturbation by the nanophotonic grating in the thinner perovskite layer is necessary to maximize absorption of light.

For thicker perovskite absorber layers, already a partial corrugation is sufficient to achieve the optimum  $J_{SC}$  and the indentation turns out to be superior. For an indentation depth larger than  $h = 120$  nm, the  $J_{SC}$  oscillates and does not increase further. Moreover, the complete indentation (“hole” configuration), is experimentally not feasible due to the shunting of the device by connecting the ETL with the HTL. Nevertheless, it is kept as an upper (optical) limit for the hole depth in the simulations.

The optimized geometry of the nanophotonic perovskite solar cells is derived therefore for periods around 300 – 500 nm, a geometric fill factor of 40 – 50% and a minimum indentation depth of  $\approx 100$  nm. It should be noted that the optimum FF shifts from 40% at 100 nm initial perovskite layer thickness to 50% for a 300 nm perovskite thickness in case of the experimentally feasible indentation. However, the difference is below  $0.1 \text{ mAcm}^{-2}$ , which means that the optimum found is reasonably broad. This in turn motivates the experimental implementation (see next section). In addition, for large indentation depths,

the possible gain in the  $J_{SC}$  is neglectable. Moreover, for some specific configurations (e.g. a depth of  $\approx 400$  nm for the initial perovskite thickness of 300 nm) the nano-patterning even proves to be disadvantageous. Finally, the broad range of suitable periods and the remarkable gain ( $\approx 5 - 6\%_{rel}$ ) in the  $J_{SC}$  in the nanophotonic perovskite solar cells is auspicious for experimental realization.

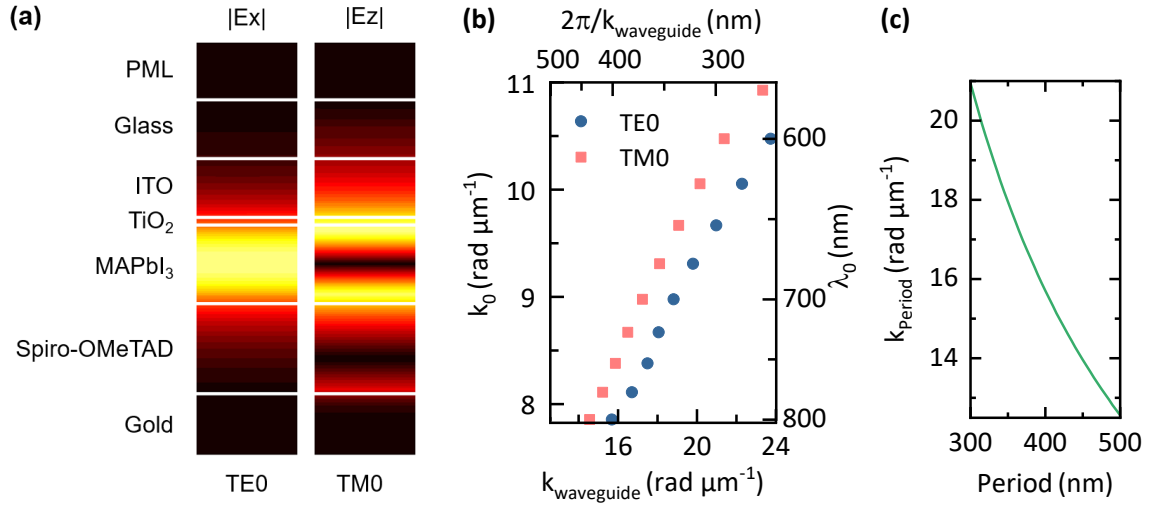


**Figure 7.7.** (a) The electric field intensity of the TE0 and TM0 mode at  $k_0 = 8.3 \text{ rad } \mu\text{m}^{-1}$ . (b) Guided mode analysis of the planar reference architecture with a 100 nm thick perovskite layer. The TE0 and TM0 mode for different propagation constants  $k_{\text{waveguide}}$  and free space wave vector  $k_0$ . The potential region of absorption enhancement in the perovskite layer reside mainly above 600 nm. (c) The periodic grating displays good overlap for periods around 400 nm. Adapted with permission from ref. [49], © 2019 Elsevier.

### 7.3 Nano-patterning of the perovskite absorber layer

The simulated enhancements in the  $J_{SC}$  provides good prospects for an experimental realization of nanophotonic perovskite solar cells. To nano-pattern the perovskite solar cells, the thermal nanoimprint lithography (TNIL) is used as described in more detail in section 3.2.3. To build nanoimprinted perovskite solar cells, the layer stack of the perovskite solar cell is processed up to the perovskite layer. The annealed sample (see section 3.2.4) is then imprinted with an in-house developed hot embossing machine. The machine operates in ambient air, but can purge the process chamber with nitrogen or even evacuate it once the sample is inside (see section 3.2.3). Nevertheless, it is not possible to avoid exposure of the perovskite layer to ambient and humid air, i.e. during the transfer inside the chamber. Subsequently, the nanoimprinted perovskite sample is completed to full solar cell devices by the deposition of the hole transport layer spiro-OMeTAD and a gold electrode.

## Planar imprinted perovskite layers

In order to test the TNIL and to derive a suitable parameter window, planar imprints of the perovskite layers have been performed first. The planar imprint of the perovskite layer results in a significant increase in the mean grain size by  $\approx 15\%$ <sub>rel</sub> with increased temperatures (see **Figure 7.8**). At a temperature of 90°C, there is a small trend in the optimum pressure. For a pressure of  $\approx 30$  MPa during the TNIL process, the grain size maximizes. However, the influence of the applied pressure decreases further at 100°C. Moreover, at sufficiently large temperatures ( $\approx 100^\circ\text{C}$ ), an increasing pressure leads to smoother layers (see **Figure 7.9**). The root mean square (RMS) roughness of the planar imprinted perovskite surface decreases from  $\approx 47$  nm to  $\approx 28$  nm. A similar trend of decreased surface roughness is also found in the lamination of perovskite solar cells, whose basic process resembles the planar imprint (see **Figure 8.7** for the temperature dependent decrease of the roughness in laminated solar cells).

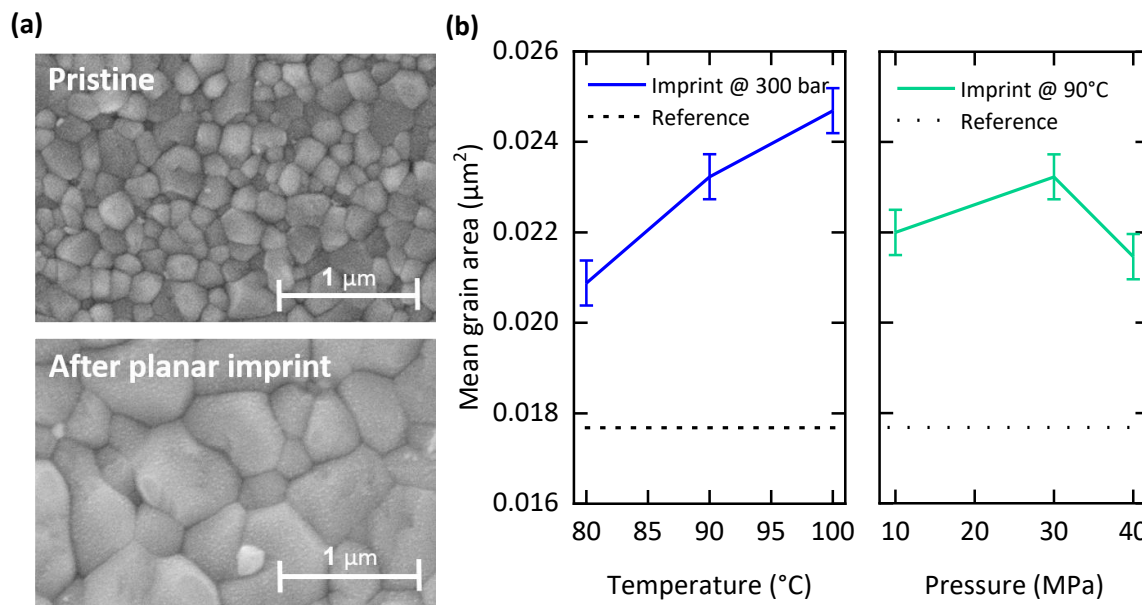


**Figure 7.8.** (a) Scanning electron microscopy (SEM) of a pristine perovskite layer and the same layer after a planar imprint at 30 MPa and 100°C. (b) The mean grain area of different planar imprinted perovskite layers is increased compared to the pristine reference. For elevated temperatures, the grain area increases significantly.

Although the perovskite surface is exposed to ambient atmosphere before and after the TNIL process, the perovskite layer shows no signs of degradation (see ‘pristine’ in **Figure 7.10**). Until up to 100°C, only the characteristic diffraction peaks from the crystal planes of the triple cation perovskite as well as the ITO and SnO<sub>2</sub> are visible.

Furthermore, it is hypothesized that this is due to the planar stamp acting as protective layer during the TNIL and helps to avoid any gaseous degradation products to escape [202]. Since the edges are not completely sealed, we observe the degradation of the perovskite at elevated temperatures – starting at 110°C. This becomes visible optically – the

perovskite film turns yellow (see pictures in Figure 7.10) – and by the rising diffraction peaks of the lead iodide  $\text{PbI}_2$  at  $12.6^\circ$  in the X-ray diffraction (XRD) pattern (see Figure 7.10).

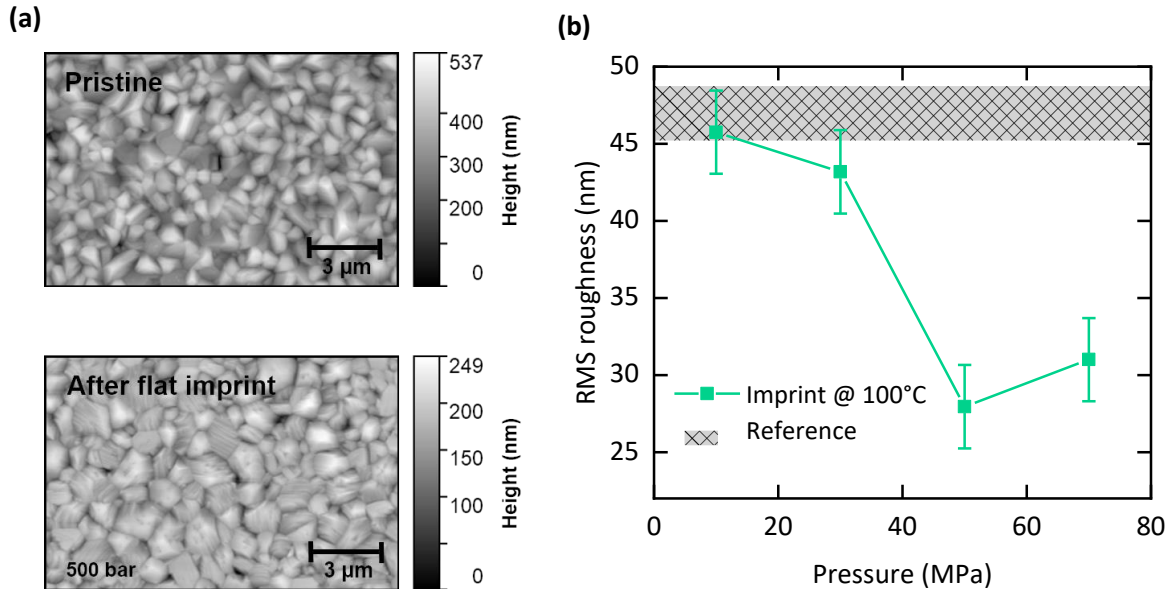


**Figure 7.9.** Atomic force microscopy images (AFM) of a pristine perovskite layer and a planar imprinted perovskite layer at 50 MPa and  $100^\circ\text{C}$ . (b) The root mean square (RMS) roughness is decreased for higher imprinting pressures at an imprint temperature of  $100^\circ\text{C}$ .

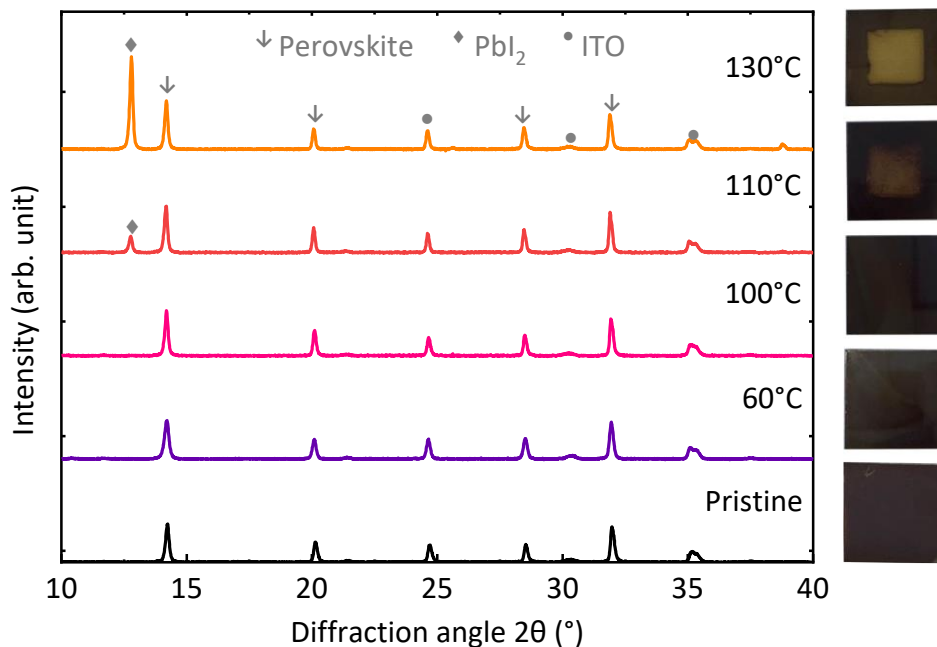


**Figure 7.10.** X-ray diffraction (XRD) pattern for a pristine perovskite layer on top of ITO compared to four different heated perovskite layers. The characteristic diffraction peaks for the triple cation perovskite are visible in the XRD diffractogram for different temperatures ( $60^\circ\text{C}$  up to  $130^\circ\text{C}$ ). For temperatures above  $100^\circ\text{C}$ , an additional  $\text{PbI}_2$  peak is arising at  $12.6^\circ$ .

## Nanoimprinted perovskite layers

The change in the mean grain size is a direct indication that the perovskite layer recrystallizes during the planar imprint and therefore is able to recrystallize during a nanoimprint as well. Moreover, the hot pressing is not anticipated to change the perovskites' composition during the TNIL process [216], which is shown in the previous section (see Figure 7.10). Only a change in the morphology is visible by the increased grain sizes (see Figure 7.8).

In order to transfer a periodic grating inside the perovskite layer, a textured stamp is used. The stamps consist of a textured OrmoStamp® (UV-curable photoresist) layer on top of a glass substrate. They are processed by the replication via PDMS of a master mold (silicon wafer) fabricated by electron-beam lithography. The details on the fabrication of the stamps is described in more detail in section 3.2.2.

Various periods of the periodic arrangement of the cylindrical pillars are processed. Overall, the replicated OrmoStamp® molds reveal good quality – although the geometric fill factor is slightly reduced (30 - 40%) compared to the master mold (FF = 40%). In **Figure 7.11** the atomic force microscopy (AFM) images of two exemplary stamps with different periods ( $P = 480$  nm and  $P = 410$  nm) are shown. The square lattice of the periodic pillars is clearly visible and the replication leads to a pillar height of  $\approx 180$  nm in both cases.

The TNIL on the perovskite surface is performed on the annealed perovskite layers. The optimum temperature for the TNIL process is found at  $\approx 100^\circ\text{C}$ . The pressure is set to 30 MPa. Once the sample (including the process chamber) reached the imprint temperature, the pressure is increased from a small touching force (equals a pressure of  $\approx 1 - 5$  MPa) to the actual imprint pressure. The imprint pressure is applied for 10 min at the imprinting temperature and until the sample is cooled down to room temperature. The cooling and heating are performed actively with cooled or heated oil inside the upper and lower plate of the imprinting machine (see section 3.2.3 for more details on the TNIL).

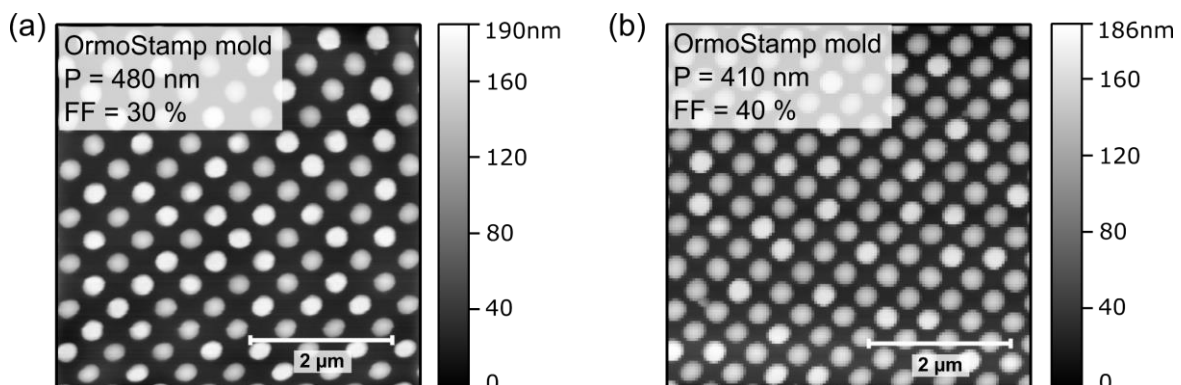


**Figure 7.11.** Atomic force microscopy of the OrmoStamp molds used for the thermal nanoimprint lithography. The pillar texture is well replicated on top of a glass substrate. In (a), the two-dimensional grating demonstrates a geometric fill factor of  $\approx 30\%$ , in (b) a geometric fill factor of  $\approx 40\%$ . The periods are 480 nm and 410 nm, respectively. The height of the pillars is equivalent in both textures.

The layer stack up to the perovskite layer is thermally imprinted with three arrays with periodic gratings of the same size (3.5 mm x 4.5 mm) covering the active areas (3 mm x 3.5 mm) of the device (see **Figure 7.12**). The fourth active area on each substrate is imprinted with a planar surface – and therefore used as a reference. In the photograph, the reflected light of the surrounding illumination generates strong diffractive effects due to the grating inside the perovskite layer. Dependent on the viewing angle and on the period, different diffraction orders are present and a strong color impression is visible. On the three different samples, each pixel has a different period.

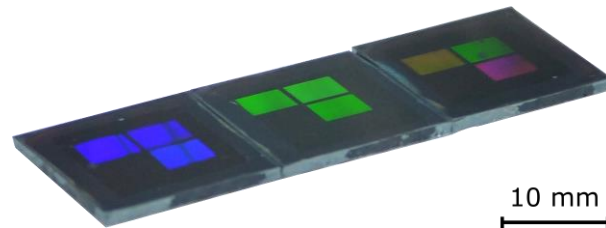


**Figure 7.12.** Photograph of periodic grating imprinted perovskite layers. Each pixel has a different period. From left to right: {300 nm, 380 nm, 460 nm}, {440 nm, 460 nm, 480 nm}, {350 nm, 360 nm, 370 nm}. Therefore, light incident onto the perovskite surface is efficiently diffracted to the viewer, giving different color impressions.

A scanning electron microscopy (SEM) image of such imprinted perovskite layers shows the change of the surface morphology of the perovskite layer in detail (see **Figure 7.13**). For the planar imprint (a), the boarder between the silicon stamp and the pristine perovskite layer is clearly visible. For the planar imprint, the roughness of the perovskite surface significantly decreases. For the nanoimprinted layer in (b), the holes inside the perovskite are well replicated. Again, the image shows the boarder of the nanotexture and the planar region of the TNIL. For a larger period, the AFM image reveals comparably large grains with holes inside them (see Figure 7.13c).

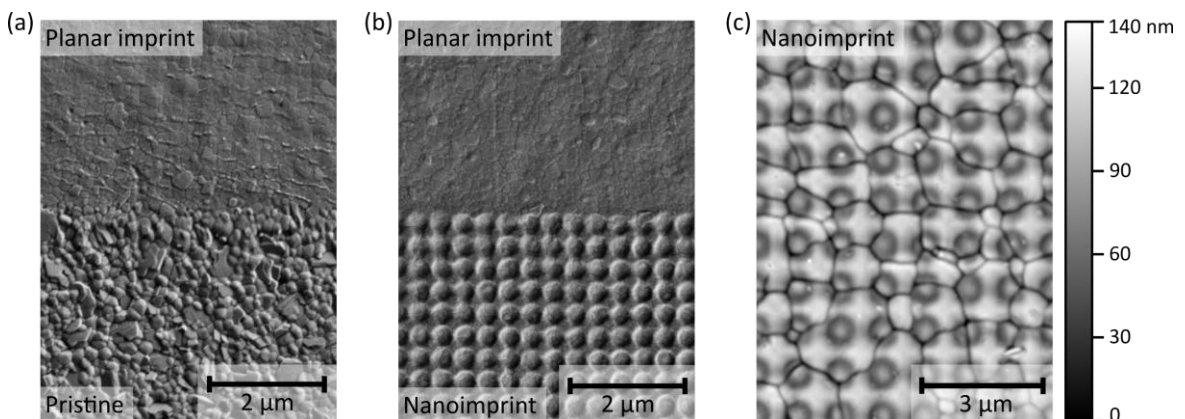


**Figure 7.13.** Scanning electron microscopy image of a (a) planar hot-embossed and (b) nanoimprinted perovskite surface. (c) AFM image of large period imprinted. The imprinting has been performed at  $\approx 300^\circ\text{C}$  for 10 min at a temperature of  $100^\circ\text{C}$ .

As reported above, the temperature of the TNIL process has the strongest influence on the recrystallization of the perovskite thin-film. For increased temperature, the indentation depth of the holes inside the perovskite layer is increased. At temperatures  $\approx 90^\circ\text{C}$  to  $100^\circ\text{C}$  the imprint depth inside the perovskite is converging towards the actual pillar height on the stamp (see **Figure 7.14a**). Whereas the imprint quality of the perovskite layer is very poor for low temperatures ( $\approx 50^\circ\text{C}$ ), the quality increases dramatically and is very good at  $100^\circ\text{C}$  (see Figure 7.14b and c). In the line profile of the AFM scan for  $50^\circ\text{C}$  the shallow imprint is clearly visible (see Figure 7.14c).

For a deeply ( $\approx 160 - 180 \text{ nm}$ ) nanoimprinted perovskite layer with periods of (a)  $480 \text{ nm}$ , (b)  $460 \text{ nm}$  and (c)  $440 \text{ nm}$ , the AFM images are shown in **Figure 7.15**. The imprint quality is very good and relatively homogeneous over the complete  $15.75 \text{ mm}^2$  surface area of each of the grating fields. This was checked by scanning with the SEM over the whole area.

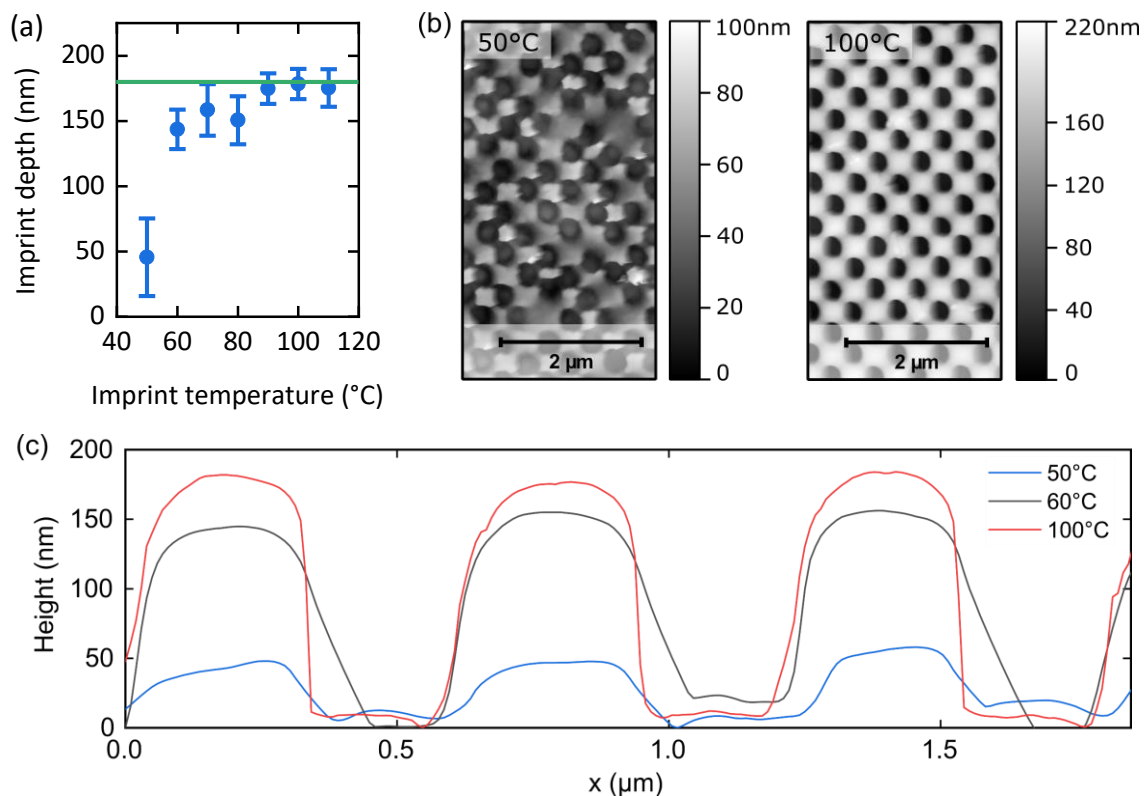


**Figure 7.14.** (a) Imprint depth for a nanoimprinted perovskite layer for different temperatures. The pillar height of the textured mold is  $180 \text{ nm}$ . For increasing temperature, the imprint depth is converging to the height of the pillars on the mold (green line). (b) Atomic force microscopy (AFM) images of the nanoimprinted perovskite layer at  $50^\circ\text{C}$  and  $100^\circ\text{C}$  at a pressure of  $30 \text{ MPa}$  each. For temperatures below  $60^\circ\text{C}$ , the nanoimprint reveals defects in the textured perovskite surface. (c) Line profile as a function of the lateral position  $x$  for three different temperatures. Adapted with permission from ref. [50], © 2019 Elsevier.

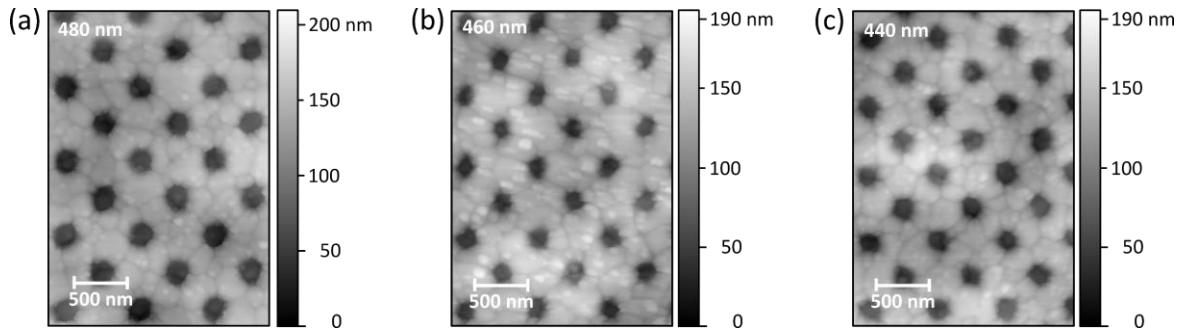


**Figure 7.15.** Atomic force microscopy images of the three nanoimprinted perovskite layers with a period of (a) 480 nm, (b) 460 nm and (c) 440 nm. The geometric fill factor is around 10-30%.

The AFM images presented are representative for the imprint quality. However, the replicated grating of nanoholes inside the perovskite surface demonstrate a geo. FF of 10 - 30% only. The periodic stamps for the TNIL had a geometrical FF of  $\approx 30 - 40\%$ . Therefore, a strong loss in geo. FF from the original silicon master mold (FF = 40%) to the perovskite layers is observed.

Moreover, it should be noted that there is no severe loss of perovskite material during the TNIL when operated below the decomposition temperature. The displaced perovskite material by the nanoimprint of the perovskite layer translocates to the remaining volume next to the holes. Therefore, the effective thickness of the perovskite bulk (including the parts of the surrounding of the nano-holes) increases with increasing imprinting depth and geometrical FF of the holes (see **Figure 7.16a**). With an FF of  $\approx 10 - 20\%$  and the depth of the holes of 160 - 180 nm, the calculated effective thicknesses match the experimentally measured heights of the perovskite layers.

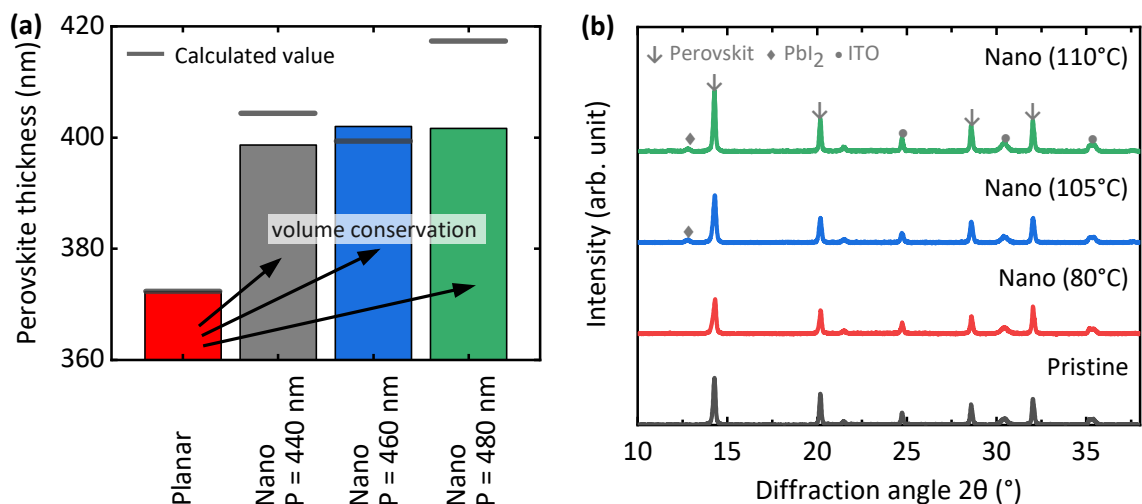


**Figure 7.16.** (a) The effective thickness of the perovskite layer is increased at the position of the nanoimprint. The increase is due to the conservation of the perovskite volume during the TNIL. The pristine 370 nm thick perovskite layer increases by roughly 30 nm for the nanoimprint with depth of 160 nm - 180 nm and a geometrical FF of 10-30%. (b) X-ray diffraction pattern (XRD) of different nanoimprinted perovskite solar cells at different temperature. Adapted with permission from ref. [50], © 2019 Elsevier.

Similar to the planar imprint of the perovskite layers at elevated temperatures up to 100°C, the nanoimprint of the perovskites does not show any degradation due to the TNIL process (see Figure 7.16b). The crystal structure of the triple cation perovskite remains unaltered for elevated temperatures. Starting at  $\approx 105^\circ\text{C}$ , a small lead iodide  $\text{PbI}_2$  diffraction peak appears.

Compared to the planar imprinted perovskite layer, the photoluminescence (PL) intensity is enhanced by  $\approx 80\%$  for the nanoimprinted layers (see **Figure 7.17**). The PL spectrum is measured from the perovskite layer on top of glass/ITO/ $\text{SnO}_2$ /. The PL emission peak is located near the band gap of the triple cation perovskite ( $\approx 1.62$  eV). The absolute enhancement is comparable for all the three different grating periods. The enhancement is due to the improved light out-coupling of the grating texture compared to the planar perovskite layer. Moreover, the enhanced light out-coupling is dependent on the grating design and varies with the period. Owing to the reciprocity of the light path, the emitted light by the PL emission is enhanced for energies below the band gap (wavelengths  $> 795$  nm). This results in a second PL peak in the emission spectrum of the three periodic nanoimprinted perovskite layers. For energies above the band gap, the absorption dominates and suppresses any emission enhancement due to the enhanced light out-coupling.

In addition, the charge carrier lifetimes remain constant ( $\approx 50$  ns) for all the different imprints and the planar reference perovskite layers. Therefore, we conclude from the time-resolved PL (TRPL) (see Figure 7.17b) that the charge carrier dynamics of the nanoimprinted perovskite layers are not altered. This is beneficial for the perovskite solar cells, with nanoimprinted perovskite layers (see below).

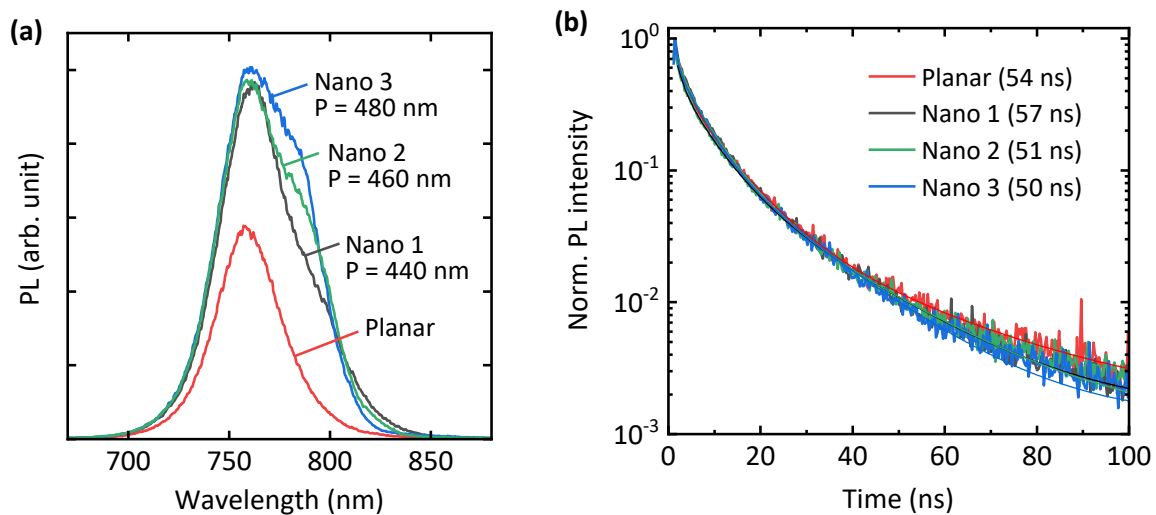


**Figure 7.17.** (a) Photoluminescence (PL) spectrum of a planar perovskite layer compared to the PL spectra of three nanoimprinted perovskite layers with periods. (b) Time-resolved photoluminescence (TRPL) of the planar and nanoimprinted perovskite layers shows a similar decay. The PL and TRPL measurement of the planar and the nanoimprinted perovskite layers are measured on glass/ITO/ $\text{SnO}_2$ . Adapted with permission from ref. [50], © 2019 Elsevier.

In terms of optical performance, the nanoimprinted perovskite layers on top of glass/ITO/SnO<sub>2</sub>/ demonstrate a decreased reflectance for wavelengths close to the band gap ( $\approx 700$  nm) as well as below the band gap ( $\approx 800$  nm). In **Figure 7.18**, the measured reflectance for two samples with three different periods each are illustrated. Compared to the planar reference layer, the reflectance shows sharp features corresponding to coupling of the incident light to distinct waveguide modes in the device. Therefore, different grating periods demonstrate slightly shifted features in the transmittance spectrum (see Figure 7.18). This decrease in reflectance can be correlated to an enhanced absorption in the device. For wavelengths below the band gap this is linked to an increased parasitic absorption – for wavelengths above the band gap this may correspond to an enhanced absorption in the perovskite layer, which has been demonstrated by the simulations shown above.

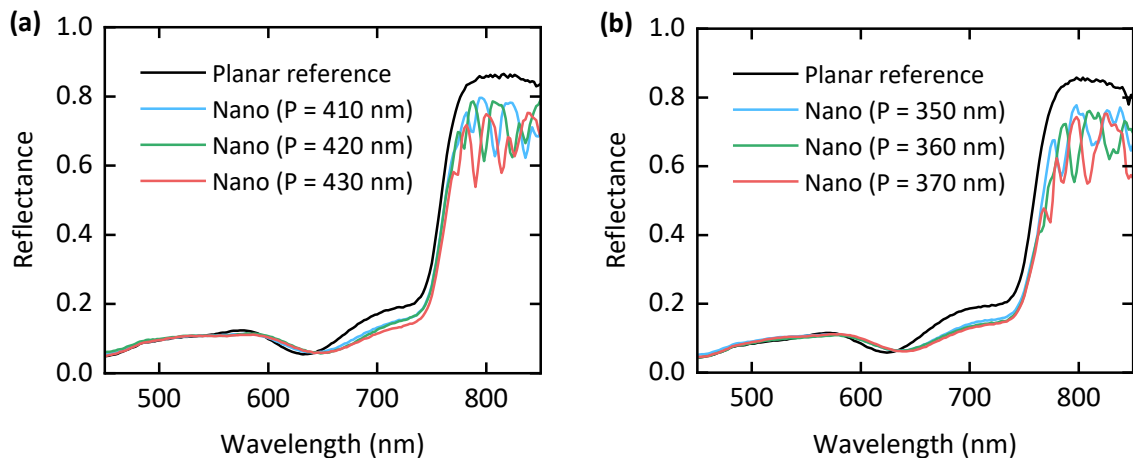


**Figure 7.18.** Reflectance of two nanoimprinted glass/ITO/SnO<sub>2</sub>/perovskite samples with different periods. The reflectance is measured by illuminating from the glass side. The planar reference demonstrates a higher reflectance than the periodic textured perovskite layers. The nanoimprinted perovskite layers demonstrate the coupling of the incident light to quasi-guided modes in the device.

## 7.4 Nanoimprinted perovskite solar cells

The concept of nanoimprinting the perovskite layer is now further transferred to nanoimprinted perovskite solar cells. The change in transmittance is a valid indication together with the enhanced PL emission that the nano-texturing enhances the light coupling to quasi-guided modes in the device. After the TNIL process, the textured perovskite surface is covered with the HTL spiro-OMeTAD by spin coating (see **Figure 7.19**). Therefore, 80 mg/mL spiro-OMeTAD (Luminescence Technology) solution doped with 17.5  $\mu$ L of lithium bis-(trifluoromethanesulfonyl) imide (520 mg/mL in acetonitrile) and 28.5  $\mu$ L of 4-tert-butylpyridine was diluted in cyclohexanone (volume ratio 6:1) and spin-coated at 3000 rpm for 30 s in ambient atmosphere.

In comparison to the conventional process (described in section 3.2.4), the cyclohexanone is added to enhance the wettability of the spiro-OMeTAD solution on top of the textured perovskite surface (see left image in **Figure 7.20**) [217]. Compared to a planar perovskite surface, the nanotextured layer leads to a larger contact angle of the spiro-OMeTAD solution, which results in a roll-off of most of the solution, and thus in very inhomogeneous layers (see right image in Figure 7.20).

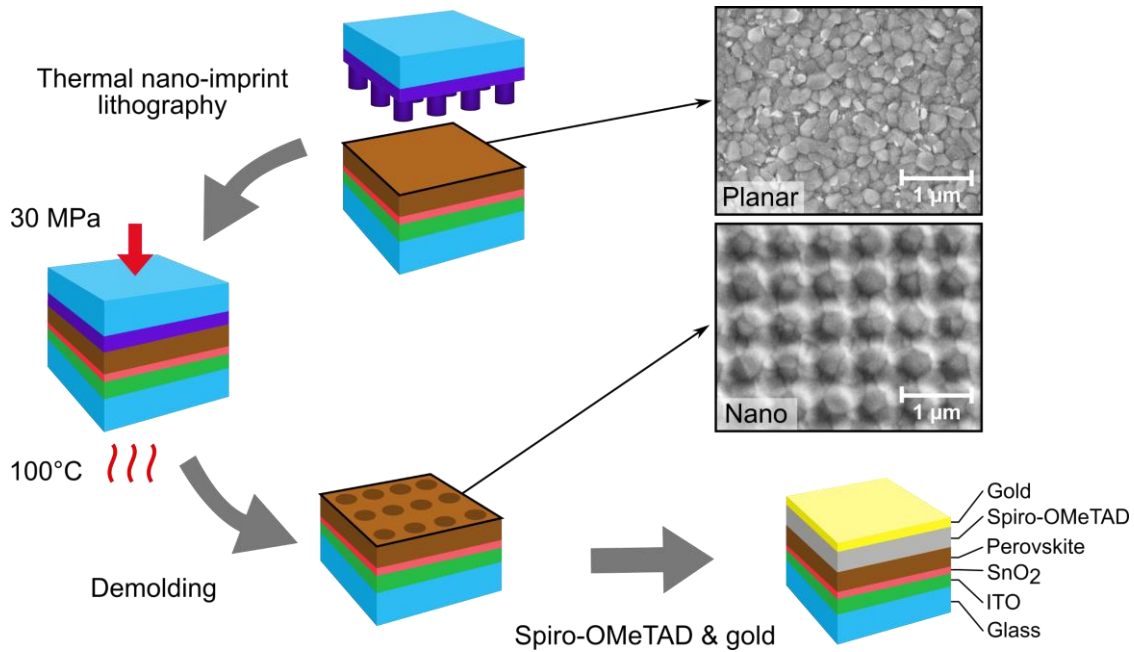


**Figure 7.19.** Schematic of the thermal nanoimprint lithography (TNIL) process. The perovskite layer of the perovskite solar cell is imprinted with a two-dimensional periodic grating. A patterned glass substrate with OrmoStamp is used as stamp for the TNIL process. Due to recrystallization during the TNIL process at 30 MPa and 100°C, the perovskite thin-film recrystallizes in the shape of the 2D grating. The insets show a top-view scanning electron microscope (SEM) image of a planar and a nanoimprinted (“Nano”) perovskite layer with a period of 480 nm. Adapted with permission from ref. [50], © 2019 Elsevier.

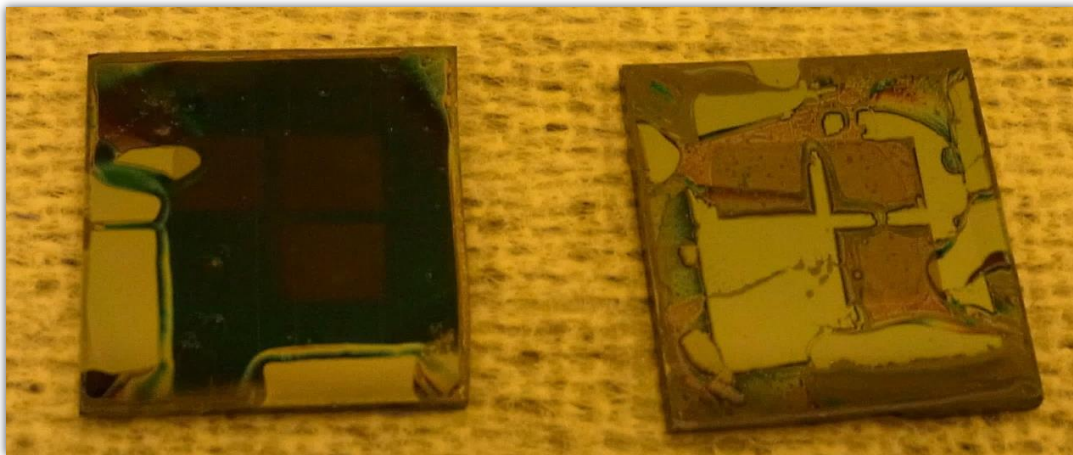


**Figure 7.20.** Coverage of the spiro-OMeTAD layer on top of a textured perovskite solar cell with (left) and without (right) cyclohexanone in the spiro-OMeTAD solution.

Subsequent to the spiro-OMeTAD deposition, a 60 nm thick gold electrode is evaporated using a thermal evaporator. The spiro-OMeTAD layer and the gold electrode cover the nanoimprinted perovskite layer very well (see **Figure 7.21** and **Figure 7.22**). The spiro-OMeTAD layer planarizes the nanotextured surface of the perovskite layer. Moreover, the cylindrical holes of the nanoimprinted perovskite layer are filled by the spiro-OMeTAD.

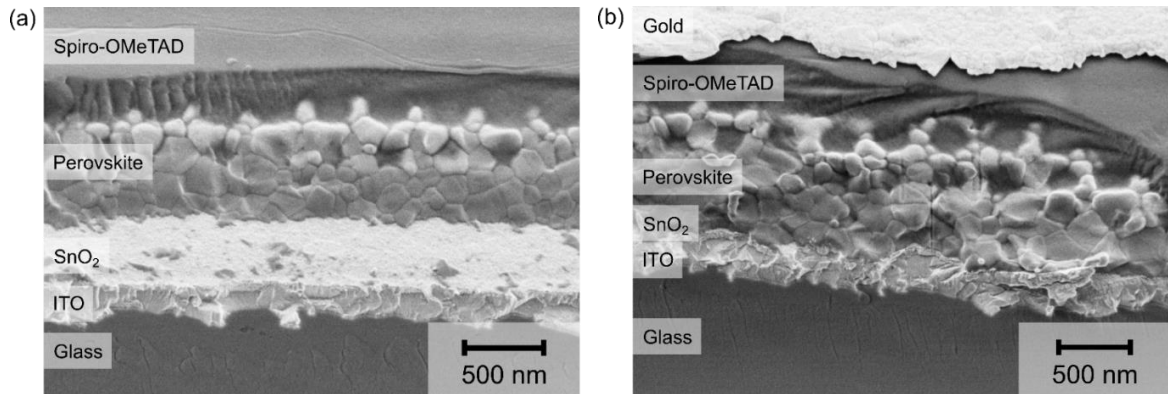


**Figure 7.21.** Scanning electron microscopy (SEM) images (a) and (b) of the nanoimprinted perovskite solar cell at a different positions. The SEM image is captured for an inclination angle of  $45^\circ$ . The cross-sectional view displays all layers of the stack. The cylindrical holes of the nanoimprinted perovskite layer are infiltrated by the spiro-OMeTAD and fill up the holes. Therefore, the spiro-OMeTAD/gold interface is planarized. Adapted with permission from ref. [50], © 2019 Elsevier.

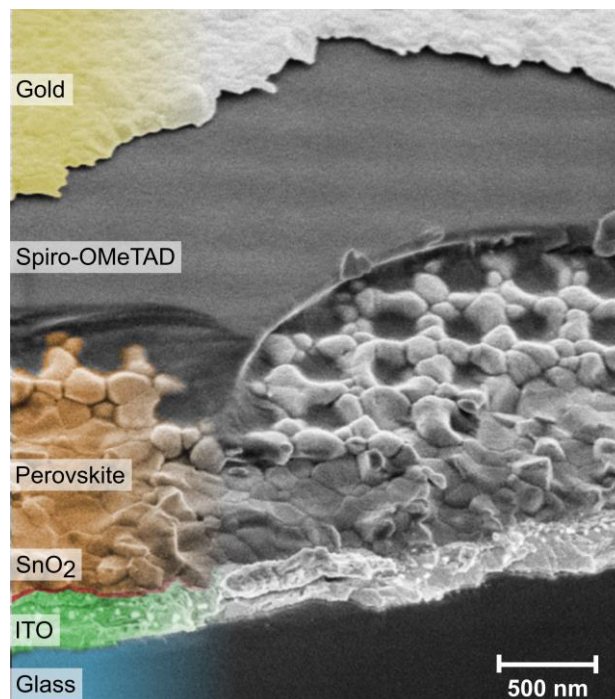


**Figure 7.22.** Scanning electron microscopy (SEM) image of a nanoimprinted perovskite solar cell at an inclination angle of  $45^\circ$ . The nanoimprinted perovskite solar cell has a period of 480 nm. The cross-sectional view displays all layers of the stack. The cylindrical holes of the nanoimprinted perovskite layer are filled with spiro-OMeTAD. Adapted with permission from ref. [50], © 2019 Elsevier.

Nanoimprinted perovskite solar cells are processed with a period of 480 nm, 460 nm, and 440 nm (see AFM and SEM characterization of exactly this device in Figure 7.15, Figure 7.16, and Figure 7.22). The nanoimprinted perovskite solar cells with a period of 480 nm and 440 nm performed equally well and demonstrate an improved  $J_{SC}$  of  $\approx 2\%$ <sub>rel</sub> compared to the planar references.

In the following, the nanophotonic perovskite device with a period of 480 nm is depicted. In **Figure 7.23a**, the current density – voltage characteristics of champion nanoimprinted perovskite solar cell and planar reference is shown. The  $J_{SC}$  increases from  $19.1 \text{ mAcm}^{-2}$  to  $19.4 \text{ mAcm}^{-2}$ . This improvement is due to the enhanced EQE (see Figure 7.23b) of the nanophotonic perovskite solar cell in the weakly absorbing spectral region of the perovskite solar cell ( $> 680 \text{ nm}$ ). The two-dimensional periodic grating inside the perovskite layer enhances the coupling of incident light to the quasi-guided modes in the perovskite layer and therefore increases the absorption. The increased absorption is due to the increased electromagnetic field intensity within the perovskite layer for certain wavelengths (see the simulated electric field intensity in Figure 7.5).

The enhanced EQE between 680 and 790 nm is linked to the reduced reflectance (see Figure 7.23b). At 795 nm and below the band gap, the coupling becomes visible by sharp features in the reflectance spectra (Figure 7.18b). Above the band gap, the resonances in the reflectance spectrum are due to parasitic absorption in the nanophotonic perovskite solar cell.

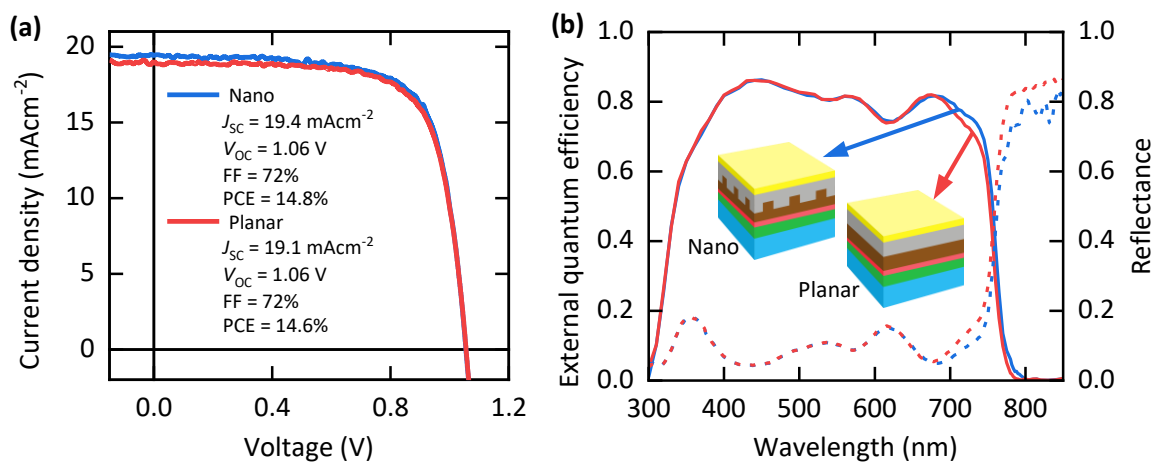


**Figure 7.23.** (a) The current density-voltage ( $J$ - $V$ ) characteristic of the planar and nanoimprinted perovskite solar cell with a period of 480 nm. The nanoimprinted perovskite solar cell demonstrates an improved short-circuit current density ( $J_{sc}$ ). (b) External quantum efficiency and reflectance spectra of the planar and nanoimprinted perovskite solar cells. The nanoimprinted perovskite solar cell shows enhanced absorption and current generation close to the band gap. For energies below the band gap ( $>790 \text{ nm}$ ) discrete peaks are visible in the reflectance measurement. Adapted with permission from ref. [50], © 2019 Elsevier.

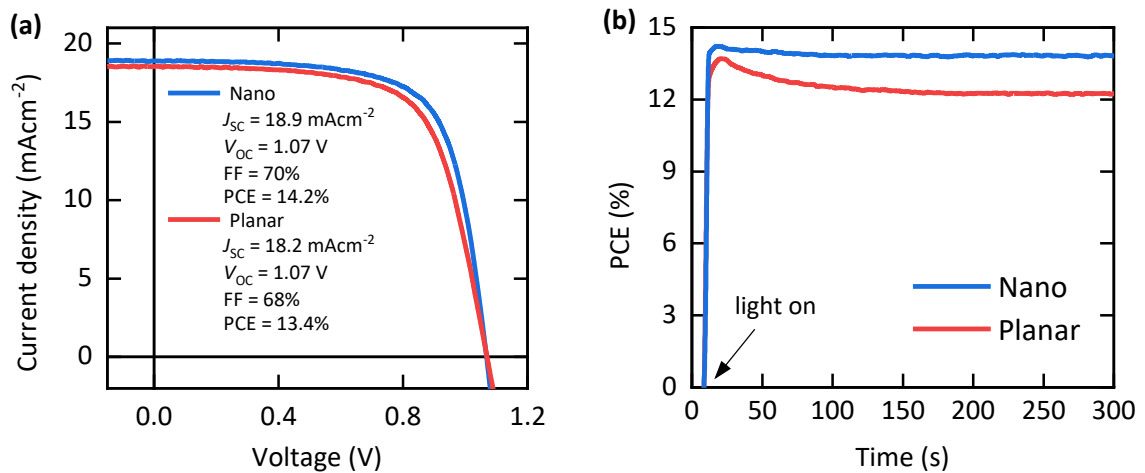


**Figure 7.24.** (a) Current density – voltage characteristics of the nanophotonic and planar perovskite solar cell. The open-circuit voltage ( $V_{OC}$ ) and the fill factor (FF) are hardly affected by the nanoimprint. The period of the grating is 410 nm. (b) Maximum power point (MPP) tracking of a planar and nanophotonic perovskite solar cell. Both cells reach a stable power conversion efficiency (PCE) within 300 s. Adapted with permission from ref. [50], © 2019 Elsevier.

Since the fill factor (FF) and open circuit voltage ( $V_{OC}$ ) are not affected by the nanoimprint (see Figure 7.18a), the improvement of the  $J_{SC}$  due to the improved EQE directly leads to an improved PCE of  $\approx 1\%_{rel}$ . Moreover, the TNIL does not affect the stability of the perovskite solar cells. On a different nanoimprinted perovskite solar cell (with a period of 410 nm), a maximum power tracking is performed. Compared to the planar perovskite solar cell on the same device, which was thermal nanoimprinted at 100°C and 30 MPa for  $\approx 10$  min, the nanophotonic solar cells show a similar stable power output (see **Figure 7.24**).

The above reported enhanced  $J_{SC}$  in the nanoimprinted perovskite solar cells is due to the coupling of the incident light to quasi-guided modes in the perovskite absorber. The improved  $J_{SC}$  is mainly because of a spectrally broad (80 nm) enhancement in the EQE near the band gap of the perovskite.

Reducing the period of the nanophotonic grating inside the perovskite absorber to 410 nm leads to strong and sharp enhancements in the EQE (see **Figure 7.25a**), as already have been shown by the simulations (see Figure 7.3c). Here, a distinct quasi-guided mode is prominent for normal incidence at 784 nm. Although the enhancement is strong near the band gap, the overall improvement in the  $J_{SC}$  is comparably weak. Nevertheless, the coupling is also visible in the reflectance spectrum, which matches very well with the excited modes. In addition, for larger angles of incidence of up to 60° of incidence, this mode is still present.

It should be further noted that in order to increase the spectral width of the coupling, disordered nanotextures have been successfully implemented as well (see Appendix C.1). For an average diameter around 400 nm, the  $J_{SC}$  enhances by  $\approx 3\%_{rel}$ . However, the overall

PCE remained low (at  $\approx 10\%$ ) due to poor electrical performance in both the planar reference and the nanoimprinted devices.

Nevertheless, the experimentally fabricated nanoimprinted perovskite solar cells demonstrate similar coupling to quasi-guided modes close to the band gap, as shown by the simulated nanophotonic perovskite solar cells. However, an offset in the coupling strength as well as in the overall enhancement in terms of  $J_{SC}$  is visible. However, there are a number of reasons for this. Firstly, slightly thicker perovskite layers were used in the experiments ( $\approx 370$  nm), which limit to potential enhancements in the short-circuit current density to around 5%. Secondly, there is a loss of the geo. FF during the transfer from the master molds (40%) into the perovskite layers (only  $\approx 10 - 30\%$ ). In retrospect, the choice of the geometric fill factor on the master lattices was somewhat unfavorable chosen with 40%, since simulation revealed that slightly thicker perovskite layers have their optimum geo FF. close to 50%.

In addition, the transfer of the concept from opaque single-junction perovskite to perovskite/c-Si tandem solar cells indicates that the strong coupling to guided-modes in the longer wavelengths reduce the transmission into the bottom c-Si solar cell (see Appendix C.2). Nevertheless, the top perovskite solar cell still benefits by an increase in the  $J_{SC}$ . However, the improvement will be mostly attenuated by the decrease in transmittance.

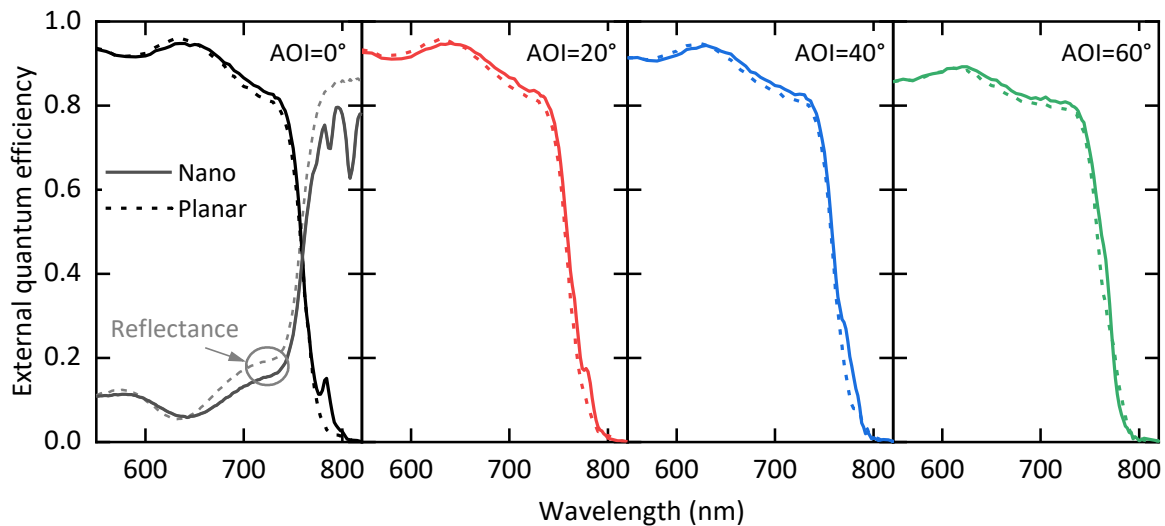


**Figure 7.25.** External quantum efficiency (EQE) – normalized to the maximum of the  $0^\circ$  angle of incidence (AOI) measurement at 450 nm – of a planar and nanoimprinted perovskite solar cell near the band gap. The nanoimprinted perovskite layer has a period of 410 nm. The enhanced absorption is visible at 784 nm by a sharp feature in the external quantum efficiency. For increasing AOI, the mode shifts towards shorter wavelengths. Adapted with permission from ref. [50], © 2019 Elsevier.

## 7.5 Energy yield estimation of nanophotonic perovskite solar cells

So far, only the  $J_{SC}$  for normal incidence of the nanophotonic perovskite solar cells has been discussed in detail. In the experiment, it was demonstrated that the coupling to quasi-guided modes remains for larger angle of incidence as well (see Figure 7.25). However, since especially periodic nanophotonic textures are suspected to be subject to a significant angular dependent optical response, oblique angles of incidence have been analyzed as well. The angular dependent absorption of the nanophotonic perovskite solar cells is further compared to their planar reference in terms of energy yield (EY). The EY is the key figure-of-merit for realistic estimation of device performances, since it accounts for the performance of the solar cells under realistic irradiation conditions, covering all angles of incidence.

The angular dependent  $J_{SC}$  of the planar reference, indentation and hole configuration are displayed in **Figure 7.26a** for an initial perovskite absorber thickness of 200 nm and 300 nm. Compared to the planar reference, the nanophotonic perovskite solar cells exhibit a strong enhanced  $J_{SC}$  for both absorber thicknesses for all angles of incidence. Whereas the hole configuration surpasses the indentation for normal incidence, the  $J_{SC}$  is lower for larger angles of incidence for the 200 nm initial perovskite absorber thickness. In case of the 300 nm perovskite layer, the angular behavior is exactly opposite and the indentation shows a superior angular stability.

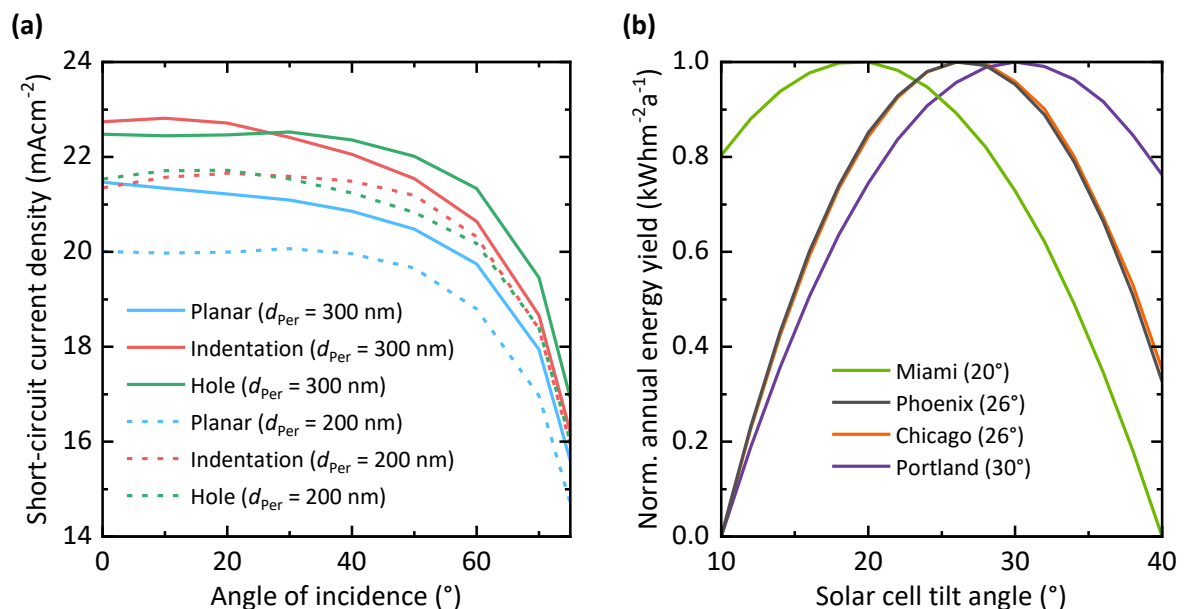


**Figure 7.26.** (a) Short-circuit current density  $J_{SC}$  for different angles of incidence. The  $J_{SC}$  is displayed for the planar reference, the hole and indentation configuration with a 200 nm and a 300 nm initial perovskite layer thickness. (b) The normalized annual energy yield over the solar cell tilt angle the planar configuration with a perovskite layer thickness of 300 nm. The different locations, show a different optimal tilt.

The EY is calculated for four different locations in the USA with different climatic conditions. For these locations, the annual EY is calculated for different solar cell tilt angles. For a south-facing planar reference, the optimal tilt for Chicago (Illinois), Portland (Oregon), Miami (Florida) and Phoenix (Arizona) is illustrated in Figure 7.26b. The optimal tilt is  $\approx 15^\circ$  less than the latitude of the boreal and temperate locations (Chicago  $41.8^\circ$  and Portland  $45.5^\circ$ ) and  $\approx 5^\circ$  less than the latitude of the tropical and arid locations (Miami  $25.8^\circ$  and Phoenix  $33.4^\circ$ ). Since every location has its specific climate, the annual EY is different for the selected locations (see **Figure 7.27**). Here, the EY is illustrated for the 200 nm and 300 nm initial perovskite layer thickness, respectively. The partial indentation of 120 nm performs superior for the thin initial perovskite thickness. Here, the annual EY improves for all locations  $\approx 7\%$  (in Phoenix only  $\approx 6\%$ ).

For the thicker 300 nm initial perovskite layer, the hole configuration enhances the annual EY similar by 5 - 6%. The difference between the hole and indentation is due to the different angular stabilities for each of the configurations. However, it should be noted that the hole configuration would lead to a shunting in real devices and is depicted only as an upper limit of indentation. Nevertheless, the enhancements in the annual EY of the nanophotonic perovskite solar cells with holes and indentations are similar, and therefore, a partial indentation of  $\approx 120$  nm proves to be sufficient.

Equally impressive is the comparison between the planar 300 nm reference to the nanophotonic configurations. In contrast to the 150% thicker planar reference, which corresponds to 150% higher lead content, the two thin (200 nm) nanophotonic perovskite solar cells lead to a higher EY. Even though the  $J_{SC}$  for normal incidence are fairly equal, the EY surpasses the EY of the thicker planar reference still by  $\approx 2\%_{rel.}$

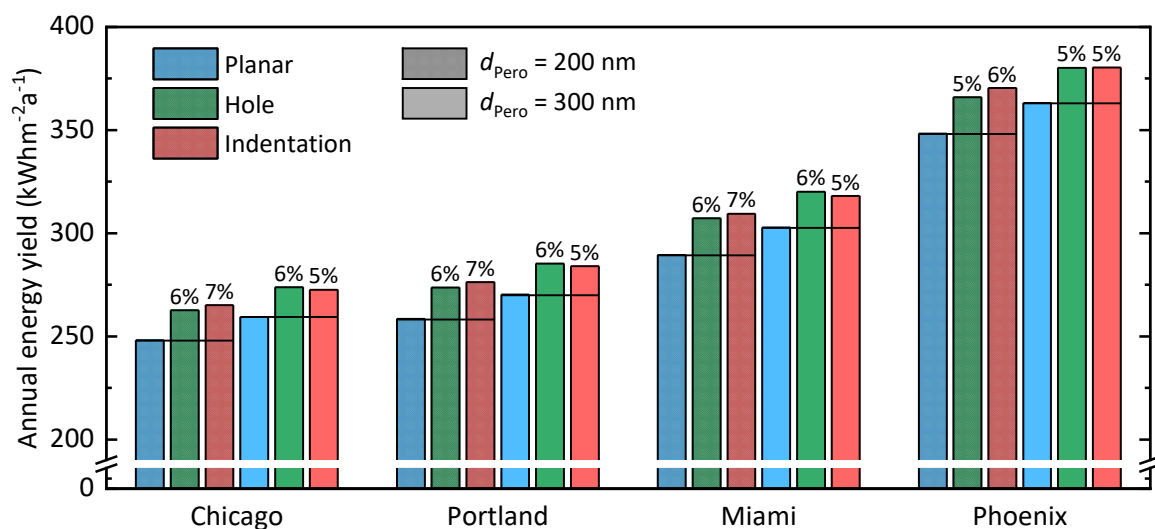


**Figure 7.27.** Annual energy yield (EY) for four different locations in the USA with different climatic conditions. The annual EY is displayed for the planar reference, the hole and indentation nanophotonic perovskite solar cells. For each of the three devices, the EY is calculated for a 200 nm and 300 nm initial thickness of the planar perovskite layer.

## 7.6 Summary

In this chapter, the patterning of the perovskite absorber material has been investigated by optical simulations and initial experimental prototypes are demonstrated.

First, the optimum geometry of the nanophotonic absorber is derived. For a period of 380 nm and a geometric fill factor of  $\approx 40\%$ , the nanophotonic perovskite solar cells promise to improve the short-circuit current density ( $J_{SC}$ ) by 5 - 6%<sub>rel</sub> compared to their planar references. For the pattern inside the perovskite layer, holes and indentations are analyzed. It is shown that the nanophotonic perovskite solar cells improve the absorption and therefore the  $J_{SC}$  in the perovskite solar cells by the coupling of the incident light to quasi-guided modes in the perovskite layer. The coupling of light to quasi-guided modes in the weakly absorbing spectral region of the perovskite absorber leads to distinct enhancements in the absorption spectra of the nanophotonic perovskite solar cells.

Next, the nanophotonic perovskite solar cells are experimentally realized by thermal nanoimprint lithography (TNIL). The TNIL allows to imprint the perovskite layer with a textured mold. During the imprint of the perovskite layer, the perovskite recrystallizes. The optimal parameters for the imprint are a temperature  $\approx 100^\circ\text{C}$ , and a pressure  $\approx 30$  MPa. The nanoimprinted perovskite solar cells demonstrate an enhanced  $J_{SC}$  with respect to their planar references by  $\approx 2\%$ <sub>rel</sub>. The origin of the enhancement is alike to the simulated devices due to the improved coupling of the incident light to quasi-guided modes in the perovskite, which lead to distinct absorption enhancements. Most importantly, the electrical parameters like  $V_{OC}$  and FF of the nanoimprinted perovskite solar cells remain unchanged compared to the planar references. Furthermore, the nanoimprinted perovskite solar cells demonstrate a stable power output.

Although, the overall enhancements in power conversion efficiency (PCE) are yet limited to  $\approx 1\%$ <sub>rel</sub> in the experimental study, the coupling of the incident light to quasi-guided modes in the perovskite absorber has been verified. The discrepancy to the predicted enhancements by the simulated nanophotonic perovskite solar cells is mainly due to the smaller geometric fill factors of the imprinted periodic holes in the perovskite layer ( $\approx 20 - 30\%$ ). Therefore, further optimizations are needed to achieve higher geometric fill factors reaching the proposed optimized values of 40 - 50%, while maintaining impeccable imprints in the perovskite thin film.

In addition, the transfer of the concept from opaque single-junction perovskite to perovskite/c-Si tandem solar cells is discussed. Strong enhancements in the top perovskite solar cell are found for similar geometries. However, the overall improvement in the tandem PCE will be mostly attenuated by the decrease of transmittance into the bottom c-Si solar cell. Potentially, the decrease could be attenuated by moving towards disordered gratings inside the perovskite layer. Although first experiments reveal promising enhancements in the  $J_{SC}$  of opaque single-junction devices by  $\approx 3\%$ , the concept needs to be tested in semitransparent devices as well.

Finally, the EY of the nanophotonic perovskite solar cells is calculated for four different locations with different climatic conditions, which is crucial to assess the realistic potential of the nanophotonic perovskite solar cells. Especially, since periodic nanophotonic textures are usually prone to angular dependent optical response. For all different locations, the EY is enhanced by 5 - 7% for the nanophotonic configurations compared to the planar reference. This enhancement is in accordance with the enhancements in the  $J_{SC}$  calculated for standard test conditions.

In addition, the nanophotonic perovskite solar cells enable a facile way to mitigate the environmentally harmful lead content in perovskite solar cells. In this regard, the nanophotonic devices maintain the  $J_{SC}$  and even enhance the annual EY by  $\approx 2\%_{rel}$ , while simultaneously reduce the perovskite thickness about  $33\%_{rel}$ . Therefore, the nanophotonic perovskite solar cells might not also enhance the overall EY, but could serve to reduce the amount of the harmful lead.

## 8 Laminated perovskite solar cells

In this section, a novel fabrication route for perovskite solar cells is discussed. In this regard, the lamination of two separately processed perovskite half-stacks is presented. The laminated perovskite solar cells enable to access novel device architectures and provide new degrees of freedom in the choice of electron and hole transport layers. Moreover, the lamination route is also seen as an exciting concept for perovskite-based tandem solar cells.

### Acknowledgements and contributions

*The following section on laminated perovskite solar cells has already been published in reference [218] by Raphael Schmager and Julie Roger as shared first authors. The coauthors of this publication: Jonas A. Schwenger, Fabian Schackmar, Tobias Abzieher, Mahdi Malekshahi Byranvand, and Bahram Abdollahi Nejand supported the experimental work. The presented data in the following chapter mainly originates from this publication, and the master theses of Julie Roger [219] and Nitish Rai [220]. The project on laminated perovskite solar cells was initiated and supervised by Raphael Schmager.*

## 8.1 Introduction

Perovskite-PV is a steadily and continuously growing field of research. Significant progress in recent years has been driven by a multitude of developments and optimizations. On the one hand, the optimization of the composition [9,10] and morphology [221] of the absorber layer was a key to success. On the other hand, progress has been achieved through advances in device architectures [11,12], the incorporation of passivation layers [13,14] and the optimization of the semitransparent electrodes [160] and of the hole- and electron transport layers [15,16]. Nevertheless, fundamental challenges remain to be solved [222]. These include the toxicity of lead-containing perovskites and, above all, the limited stability of the individual layers of perovskite solar cells. In this regard, it is important that the perovskite absorber, the charge transport layers, and the electrodes are resistant to moisture, light and thermal stress.

A promising strategy to attain mostly the thermal stability of perovskite solar cells is to replace the organic transport layers with inorganic ones. In this regard, the hole transport layers copper iodide (CuI), copper thiocyanate (CuSNC) and nickel oxide ( $\text{NiO}_x$ ) have been shown to increase intrinsic chemical stability with respect to the commonly used organic HTL spiro-OMeTAD [15,223–225]. In addition, the electron transport layers like zinc oxide (ZnO), tin oxide ( $\text{SnO}_2$ ) and mesoporous titanium dioxide ( $\text{TiO}_2$ ) are known to be intrinsically stable and have been demonstrated to result in highly efficient and stable perovskite solar cells [226–230]. However, the conventional layer deposition significantly limits the combination of materials, deposition techniques and the choice of device architectures. The reason for this is the inability to deposit some layers on top of other layers. For solution-based processes, the underlying layer must be robust against the solvent used for the next layer (see **Figure 8.1**). In addition, the wetting of the solution on the surface is crucial for a full coverage and uniform layer thickness during spin coating. For vacuum-based processes like physical vapor deposition (PVD) and chemical vapor deposition (CVD), high temperatures, radicals and ion bombardment must be limited due to possible damage of the underlying layers [26,231,232].

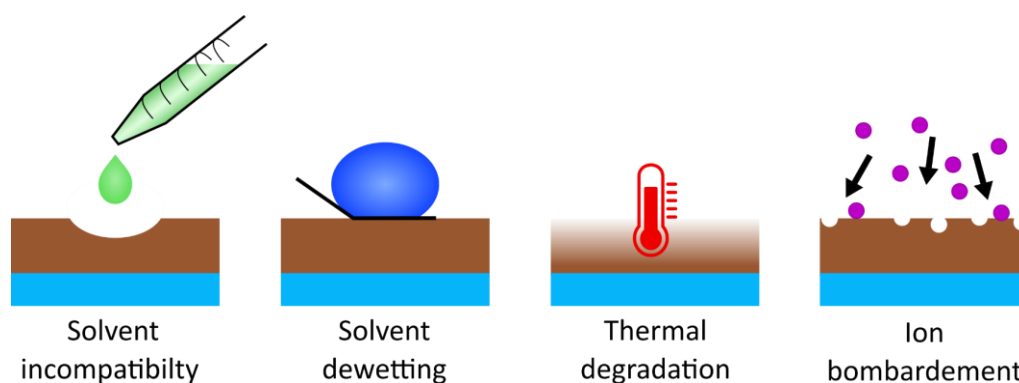


**Figure 8.1.** Illustration of process-induced incompatibilities of layer deposition techniques.

In this regard, metal-oxide- or fullerene-based buffer layers are usually deposited as protective layers before processes like sputtering, atomic layer deposition or electron-beam evaporation [233–236]. As a consequence, not all combinations of ETLs and HTLs are accessible in a straightforward manner.

In order to master these challenges, a number of laminating processes were presented in literature. Incidentally, the lamination of carbon nanotube networks [237] and graphene electrodes [238], flexible titanium substrates on titanium dioxide electron-transport layers [239], mesh-like silver networks [240] and self-adhesive nickel meshes on polyethylene terephthalate (PET) on a poly(3,4-ethylenedioxythiophene) polystyrene sulfonate (PEDOT:PSS) have been introduced. In addition, the lamination of wet organic charge transport layers (CTLs) on top of the perovskite have been demonstrated for tandems [241,242] and semitransparent flexible perovskite solar cells [243]. Furthermore, the lamination of dry organic layers on top of each other [244–246] and directly on the perovskite absorber have been presented [247]. Recently, Dunfield *et al.* demonstrated the lamination of two MAPbI<sub>3</sub> layers on top of each other [248]. However, the laminated perovskite solar cells in this proof-of-concept work still showed comparably low PCEs (<11%) that was mostly limited by a significant series resistance.

In contrast to Dunfield *et al.*, this work reports on the lamination of perovskite solar cells below the annealing temperatures of the perovskite polycrystalline film. Therefore, the lamination is not formed via the degradation pathway (see Equation 1 in ref. [248]) at lamination temperatures of around  $\approx 150^\circ\text{C}$ , but by a recrystallization during the hot pressing at  $\approx 90^\circ\text{C}$  (see Figure 8.7 and section 7.2). Moreover, the two half stacks are laminated at the perovskite / HTL interface and the influence of a thin poly(triarylamine) polymers (PTAA) buffer<sup>1</sup> layer between the perovskite and HTL interface is analyzed. Since, the both perovskite half-stacks are processed independently, it enables the opportunity to access device architectures that are generally inaccessible by conventional processing methods. Since this is the case for device architectures with two inorganic CTLs, a combination of two inorganic CTLs is presented in this work: (sputtered) NiO<sub>x</sub> and SnO<sub>2</sub>, which are promising due to their intrinsic stability.

In the following sections, this work provides a detailed discussion on the process of laminating the perovskite solar cells via hot pressing. The process parameters are studied and the influence of pressure, lamination time and temperature are evaluated. Furthermore, the results on our champion devices are discussed. Finally, flexible and semitransparent laminated perovskite solar cells as well as a combination of both are demonstrated.

---

<sup>1</sup> PTAA is also an HTL. The term “buffer” is used to distinguish PTAA from the NiO<sub>x</sub> HTL.

## 8.2 Hot pressing of perovskite solar cells

The laminated perovskite solar cells are manufactured via hot pressing two separately-processed half-stacks together (see **Figure 8.2**). Due to the separate fabrication of the two perovskite half-stacks, it is possible to enable device architectures and material combinations, which are usually inaccessible by conventional processing methods. In this study,  $\text{SnO}_2$  and  $\text{NiO}_x$  are used as ETL and HTL, respectively. As absorber, the triple cation perovskite  $\text{Cs}_{0.1}(\text{MA}_{0.17}\text{FA}_{0.83})_{0.9}\text{Pb}(\text{I}_{0.83}\text{Br}_{0.17})_3$  is used. As a buffer layer to enhance mechanical and electrical contact a thin PTAA buffer layer is utilized between the perovskite and HTL. All details on the device and layer fabrication can be found in section 3.2.4.

After the two substrates are prepared, they are brought into contact and placed on the lower plate of the hot press (see **Figure 8.3a**). It should be noted that the hot pressing is performed with the same machine as for the TNIL described in sections 3.2.3 and 7.3. The hot pressing can be subdivided into three phases: (1) the heat up of the plates and sample, (2) the lamination and (3) the cool down before the laminated perovskite solar cell can be released. The two perovskite half-stacks are laminated at a temperature of  $90^\circ\text{C}$  and a pressure of 50 MPa for a duration of 5 min. Owing to the machine specifications, the precision of the temperature, pressure is  $\pm 2^\circ\text{C}$ ,  $\pm 5$  MPa. In **Figure 8.3b** a typical process diagram is displayed for the pressure and temperature during the lamination. To compensate for minor imperfections or unevenness's in the complete stack, a silicon wafer and two aluminum foils are placed between the substrate and the metal plates of the hot press on both of the two substrates (see **Figure 8.3a**).

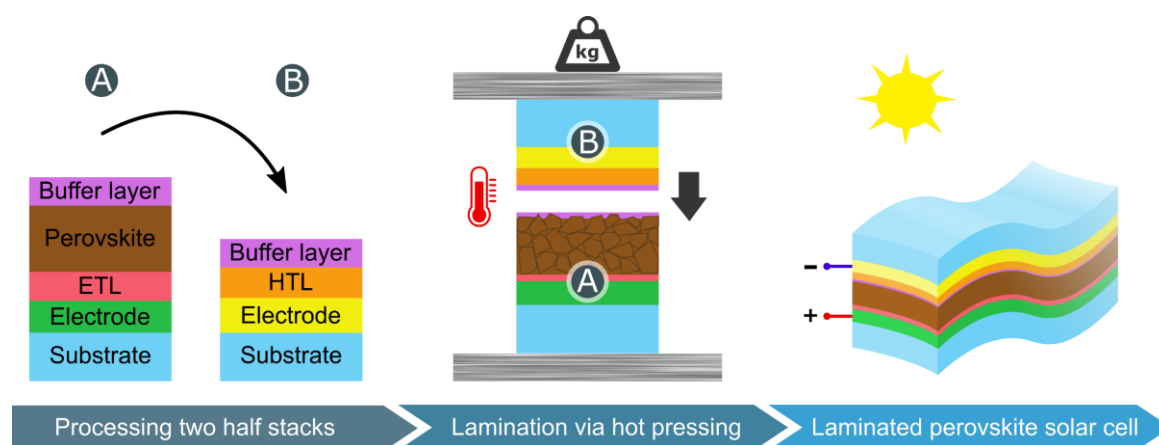


**Figure 8.2.** Illustration of the lamination process. First, two perovskite half-stacks are processed separately. Subsequently, the two half-stacks are laminated together in a hot-pressing step at temperatures of  $\approx 90^\circ\text{C}$  and a pressure of  $\approx 50$  MPa. After the lamination, the two half-stacks form an intimate electrical contact at the laminated interface. Adapted with permission from ref. [218], © John Wiley & Sons.

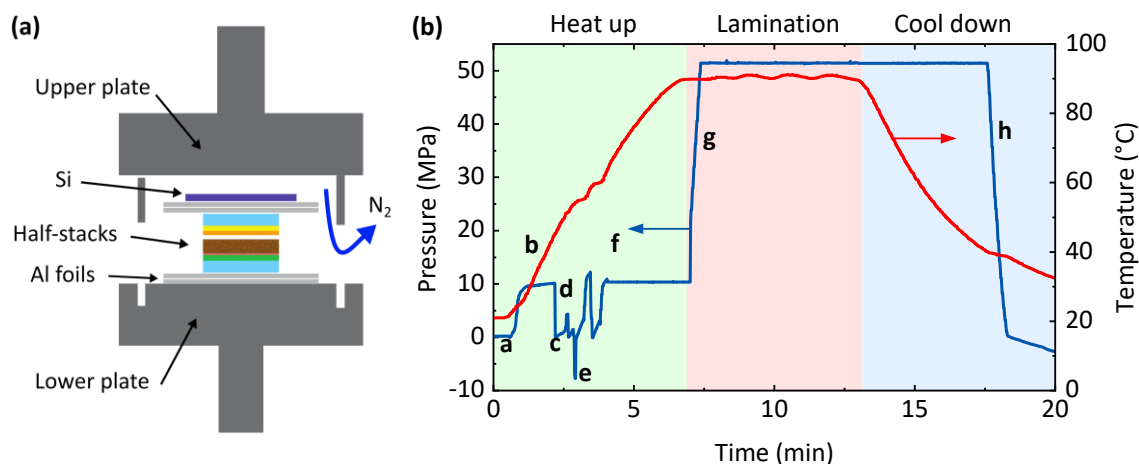


**Figure 8.3.** Process diagram of the hot pressing to laminate two perovskite half-stacks. The process can be subdivided in three phases. During the heat up phase, the two half-stacks are in contact and the chamber is closed. The pressure is increased to  $\approx 50$  MPa once the two half-stacks reach the lamination temperature of  $\approx 90^\circ\text{C}$ . After 5 min the pressure the cool down is initialized. The pressure is released after the sample reached  $40^\circ\text{C}$ . Adapted with permission from ref. [218], © John Wiley & Sons.

During heat up, the upper and lower metal plates are moving together (a) with a speed of  $2.0\text{ mm}\cdot\text{min}^{-1}$ . While the plates are moving together, the temperature steadily increases from room temperature to  $\approx 90^\circ\text{C}$ . Additionally, the chamber is flushed with nitrogen to lower the water and oxygen content in the process chamber during the lamination process, which both are known to degrade the perovskite layer.

Once the upper and lower plate close, the force on the plates increases (b) due to the trapped air inside the sealed upper and lower plate (see Figure 8.3a). At around 1 mm apart from the touching point, the pressure is set to zero (c) and the moving speed of the plates is reduced to  $0.5\text{ mm}\cdot\text{min}^{-1}$  to assure a gentle touch of the sample arrangement with the top metal plate. A sharp increase in pressure (d) indicates the touching (touching force  $\approx 100\text{ N}$ ) of the plates and sample.

After touching, the chamber is repeatedly evacuated and flushed with nitrogen to minimize the oxygen and moisture content in the chamber. Until the temperature reached  $90^\circ\text{C}$ , the sample is held at a constant pressure of  $\approx 10$  MPa (f). The lamination of the two half-stacks is initiated at  $90^\circ\text{C}$ , where to pressure increases to 50 MPa. The lamination is performed for 5 min at constant pressure and temperature. The laminated perovskite solar cell is then released (h) after the temperature is cooled down to  $40^\circ\text{C}$ .

### 8.3 Contact design

The architecture of the laminated perovskite solar cells builds up on the contact design used within the “Taskforce Perovskite” group at KIT. The active areas ( $10.5\text{ mm}^2$ ) of the perovskite solar cells are defined by the overlap of the ITO stripes with the orthogonal rear gold stripes. Conventionally, the solar cells are probed at the rear gold contacts. The outer

gold contacts are connected with the rear; the middle gold contact contacts the front ITO electrode. In case of laminated perovskite solar cells, the rear side is not easily accessible, since the rear contacts are embedded between the two substrates (see Figure 8.2).

Therefore, the size of the rear substrate is reduced to enable access to the front ITO contacts. **Figure 8.4** displays the contacts and layers of the top (a-e) and bottom (f-g) half-stack of the perovskite solar cell. The laminated perovskite solar cell (h) is probed on the gold pads, which are evaporated on top of the ITO (e) to enhance electrical contact between the probes and the ITO as well as between the rear gold electrode on substrate 2 and the outer ITO stripe on substrate 1. The gold pads ( $\approx 40$  nm) in (e) are evaporated after removing the perovskite on the edges (d) with GBL. For the second substrate, a flexible PEN foil is used. Before the lamination, the edges of substrate 2 are cut off (g).

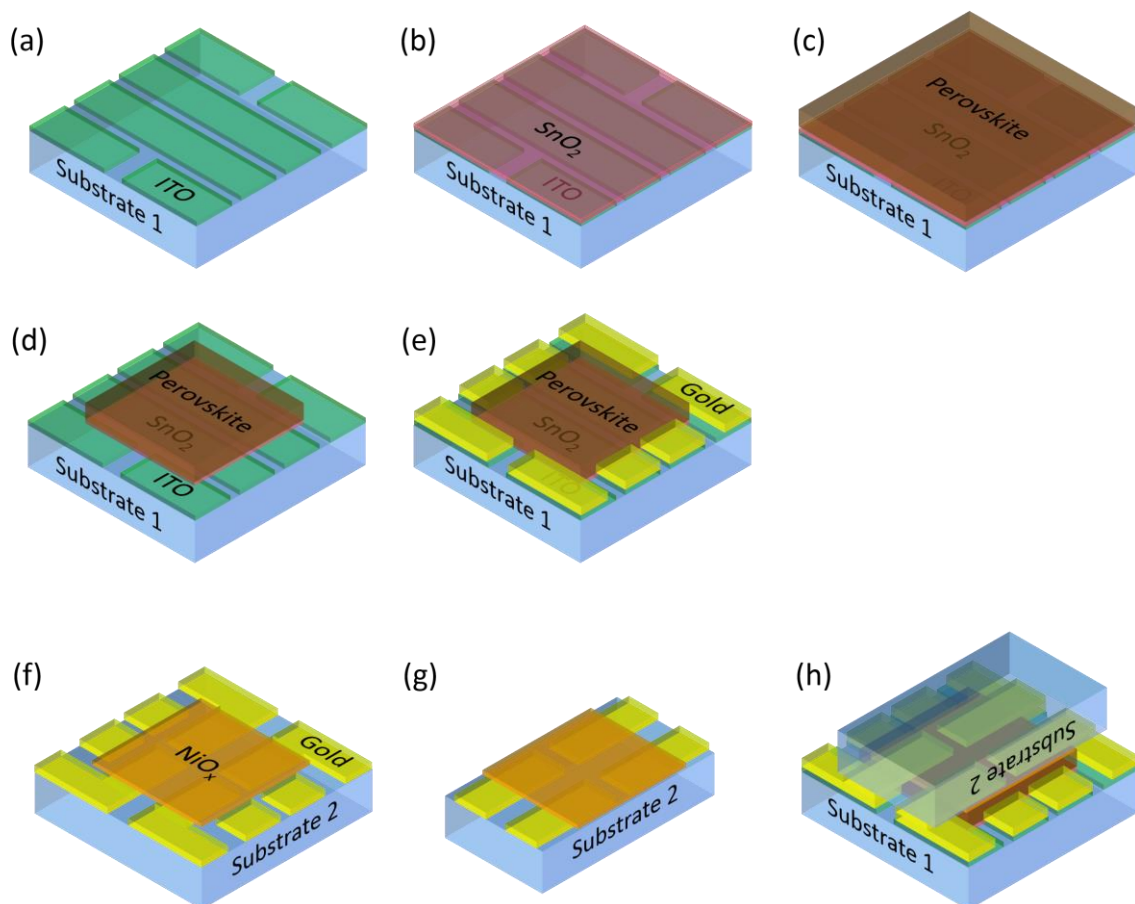


**Figure 8.4.** Contact design of the laminated perovskite solar cells. (a) Structured ITO on a glass substrate is used as a front electrode. (b)  $\text{SnO}_2$  as ETL and (c) the perovskite absorber are swiped off (d) to expose the ITO again. (e) Gold pads are evaporated on the edge of the ITO to enhance electrical contact. (f) A gold electrode and a  $\text{NiO}_x$  HTL are evaporated on top of the second substrate. As second substrate, a flexible PEN foil is used and (g) the edges are cut off. (h) Substrate 2 is flipped and brought into contact with the layers of substrate 1.

## 8.4 Influence of hot-pressing parameters

To optimize the performance of the laminated perovskite solar cells, the influence of the different input parameters of the hot pressing on the solar cell performance are examined. In the following, the pressing pressure, the duration of the lamination, the cooling profile, the atmosphere in the lamination chamber, the temperature and an additional buffer layer are analyzed. Additionally, the surface roughness of the flexible substrates plays an important role for the layer quality and will be discussed.

### 8.4.1 Surface roughness of the substrates

The layer thicknesses of the thin-film perovskite solar cell are in the order of ten to a few hundred of nanometers. In case of the laminated perovskite solar cells, a second substrate is introduced and carries the gold electrode and the HTL. Due to experimental difficulties, a flexible film is chosen for the second substrate. Alternatively, very planar glasses are required for the glass/glass configuration to prevent cracks of one or both substrates. Furthermore, completely flexible laminated perovskite solar cells were investigated as well and two flexible substrates are required.

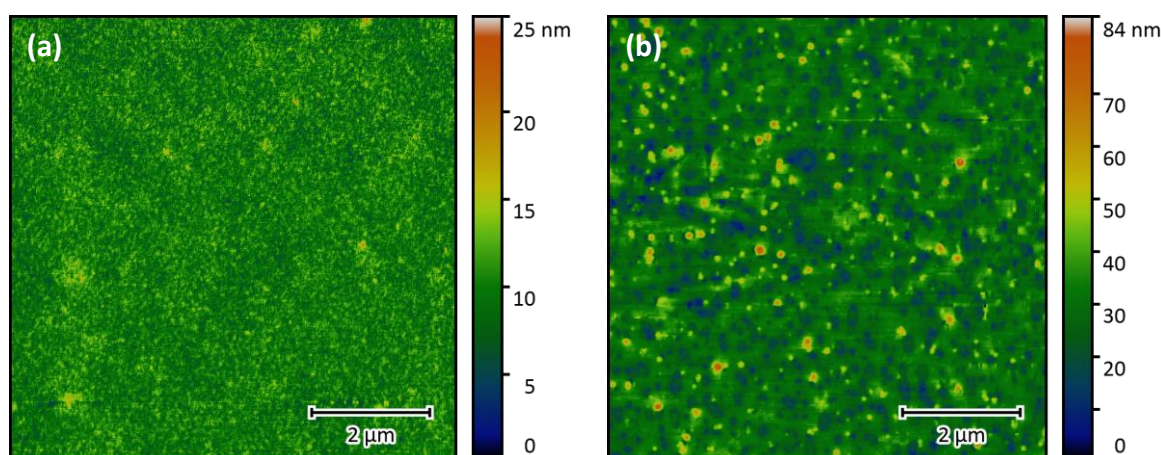


**Figure 8.5.** AFM image of the 100  $\mu\text{m}$  TEONEX Q65HA PEN foil. (a) The front side shows a RMS of  $\approx 1.7$  nm and (b) backside a RMS of  $\approx 7.2$  nm. The front side do not show any high features, whereas the backside has pointy features of  $\approx 50$  nm height.

Next to the flexibility, it is imperative that the surfaces of both substrates provide a low surface roughness. This is because sharp and high features ( $>50$  nm) on the substrate will destroy the thin layers during the lamination or lead to non-uniform coverage of the layers. Especially sharp and pointy features lead to shortcuts in the device. Such features are usually found on foils (see ref. [219]). Therefore, the extremely smooth front surface of the TEONEX Q65HA PEN foil from TEIJIN FILM SOLUTIONS is used. In **Figure 8.5** the AFM image of the front- and backside of this PEN foil is illustrated. The root mean square (RMS) surface roughness is  $\approx 1.7$  nm for the front side and  $\approx 7.2$  nm for the rear side. The front

side is therefore comparable to a planar glass substrate and does not show any sharp pointy features ( $\approx 50$  nm height) like e.g. the backside.

### 8.4.2 Lamination temperature

The most crucial parameter for the lamination process of the perovskite solar cells is the temperature. Since the lamination of the perovskite solar cells is dependent on the recrystallization of the perovskite absorber, the best performance is expected in the same temperature range as the TNIL (see sections 3.2.3 and 7.3), which is around  $\approx 90^\circ\text{C}$ . Indeed, the highest PCE of the laminated perovskite solar cells is found at this temperature (see **Figure 8.6a**). The main reason for the increase in PCE is an increase in FF due to an improvement in the series and shunt resistance (see **Figure 8.6b** and Table 6).

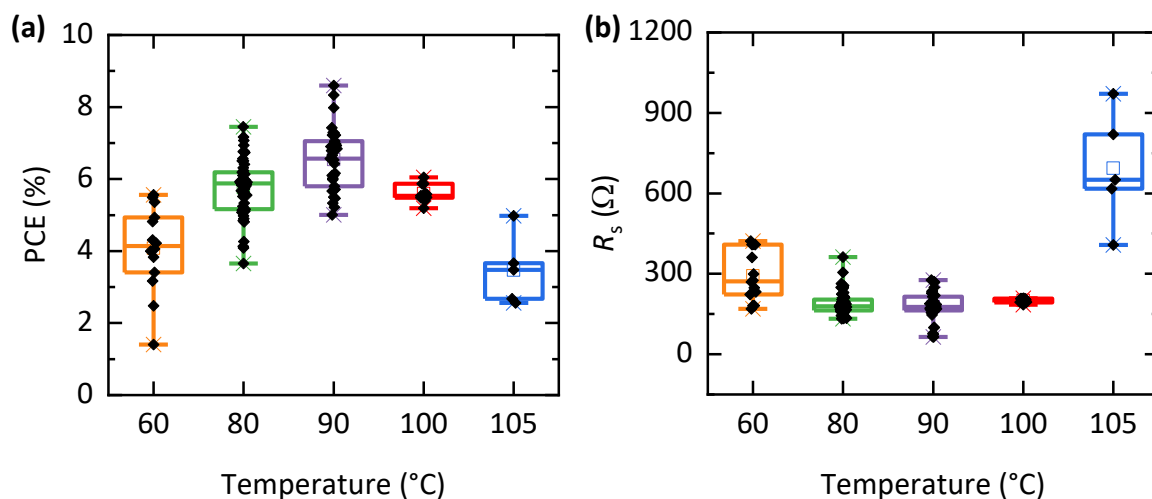


**Figure 8.6.** (a) Power conversion efficiency (PCE) and (b) Series resistance  $R_s$  of laminated perovskite solar cells with different lamination temperatures. The lamination is performed at the  $\text{NiO}_x$  / perovskite interface. The optimum device performance is found at  $90^\circ\text{C}$ . Here, the lowest  $R_s$  is measured. Adapted with permission from ref. [218], © John Wiley & Sons.

At  $60^\circ\text{C}$  and below, the perovskite does not show any visible recrystallization. The FF and other electrical parameters remain low (see Table 6). Above  $100^\circ\text{C}$ , the perovskite absorber starts degrading what is detrimental to device performance. The recrystallization of the perovskite during the lamination is studied for the different lamination temperatures. Therefore, the laminated perovskite solar cells are delaminated again. The exposed perovskite surface is then analyzed by AFM measurements. In **Figure 8.7a**, the AFM images for  $60^\circ\text{C}$  up to  $100^\circ\text{C}$  are displayed. For increasing lamination temperature, the RMS roughness of the perovskite surface is decreasing (see **Figure 8.7b**) from 12.3 nm to 2.4 nm. Starting at  $\approx 90^\circ\text{C}$ , the perovskite surface suddenly looks very different and becomes very flat. Although less defects and holes are visible at the sample laminated at  $100^\circ\text{C}$ , the average electrical performance decreases again (**Figure 8.6** and Table 6). One potential reason for this might be decomposition of the perovskite absorber for too high

lamination temperatures. In Figure 8.7c, the XRD pattern is displayed and the characteristic diffraction peaks from the crystal planes of the triple cation perovskite are visible for temperatures up to 90°C. For temperatures above 90°C, a significant  $\text{PbI}_2$  diffraction peak is noticeable, indicating the decomposition of the perovskite into  $\text{PbI}_2$  and other compounds during the lamination process.

**Table 6.** Electrical parameters of laminated perovskite solar cells for different lamination temperatures.

$T$ (°C)	PCE (%)	FF (%)	$J_{SC}$ ( $\text{mAcm}^{-2}$ )	$V_{OC}$ (V)	$R_{SH}$ ( $\text{k}\Omega$ )	$R_s$ ( $\Omega$ )
60	$4.1 \pm 1.1$	$32.8 \pm 3.6$	$16.3 \pm 1.4$	$0.75 \pm 0.14$	$0.13 \pm 0.05$	$30 \pm 9$
80	$5.8 \pm 0.8$	$38.9 \pm 3.0$	$18.3 \pm 1.3$	$0.81 \pm 0.05$	$0.19 \pm 0.07$	$20 \pm 4$
90	$6.5 \pm 0.8$	$42.5 \pm 6.0$	$19.0 \pm 1.0$	$0.82 \pm 0.06$	$0.27 \pm 0.13$	$19 \pm 6$
100	$5.6 \pm 0.2$	$39.3 \pm 0.7$	$16.5 \pm 0.8$	$0.87 \pm 0.01$	$0.16 \pm 0.01$	$21 \pm 1$
105	$3.5 \pm 0.9$	$23.4 \pm 3.1$	$16.0 \pm 1.7$	$0.81 \pm 0.02$	$0.08 \pm 0.03$	$73 \pm 20$

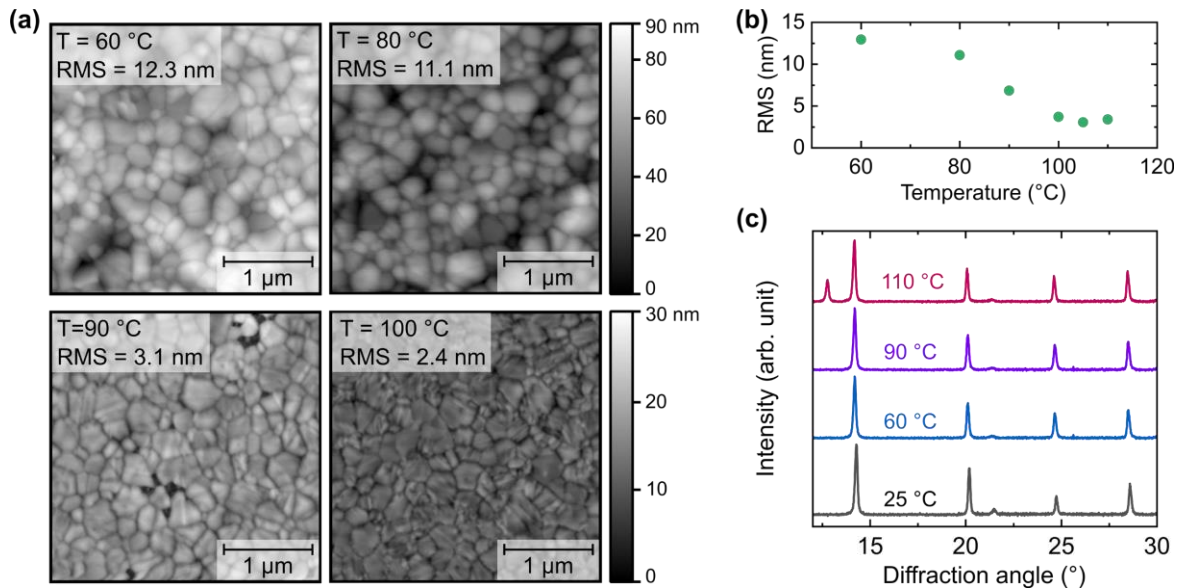


**Figure 8.7.** (a) AFM images of the perovskite surface of delaminated perovskite solar cells, which were laminated at different temperatures. The delamination is performed at the perovskite /  $\text{NiO}_x$  interface. (b) The RMS roughness of the perovskite surface decreases with the lamination temperature. (c) For temperatures below 110°C, the XRD pattern of the triple cation perovskite does not indicate decomposition or degradation. Adapted with permission from ref. [218], © John Wiley & Sons.

### 8.4.3 Influence of other process parameters on the device performance

For the lamination process, the influence of the atmosphere (ambient air, vacuum and nitrogen) in the lamination chamber is crucial. The atmosphere can be controlled with a vacuum pump and a nitrogen inlet. Since humidity in the ambient air is known to degrade the perovskite layer, only the lamination under vacuum and nitrogen is tested [249]. In **Figure 8.8a**, the FF of laminated perovskite solar cells are displayed for hot pressing under vacuum and in nitrogen atmosphere. The FF is chosen as a first figure of merit for the electrical properties of the laminated devices. Compared to the laminated perovskite solar

cells in vacuum, the devices laminated in a nitrogen atmosphere demonstrate an improved FF. This could be due to the fact that the decomposition reaction of the perovskite to hydrogen iodide HI(g) and lead iodide  $\text{PbI}_2(\text{s})$  accelerates in a vacuum. However, it should be noted that the FF is comparatively small and by the time of this observation, the process parameters were not yet optimized. Therefore, further investigations need to proof this hypothesis.

Whereas the pressing pressure during the lamination of the perovskite solar cells shows an increase in FF for higher pressures (Figure 8.8b), there is no obvious trend visible in the time of the lamination (Figure 8.8c). Since pressures above 50 MPa lead (above-average) to cracks or complete destruction of the rigid glass substrates, higher pressures are excluded from the analysis [219,220]. In addition to that, two different cooling profiles are tested. First, the cooling is initialized, while the pressing pressure is still applied (w/ load). Once a certain threshold ( $40^\circ\text{C}$ ) is reached, the pressure is released and the chamber opens. For the second method, the cooling is initialized after releasing the pressing pressure (w/o load). However, the sample is not removed until the threshold temperature is reached. In Figure 8.8d, the cooling under load (w/ load) demonstrates a higher FF.

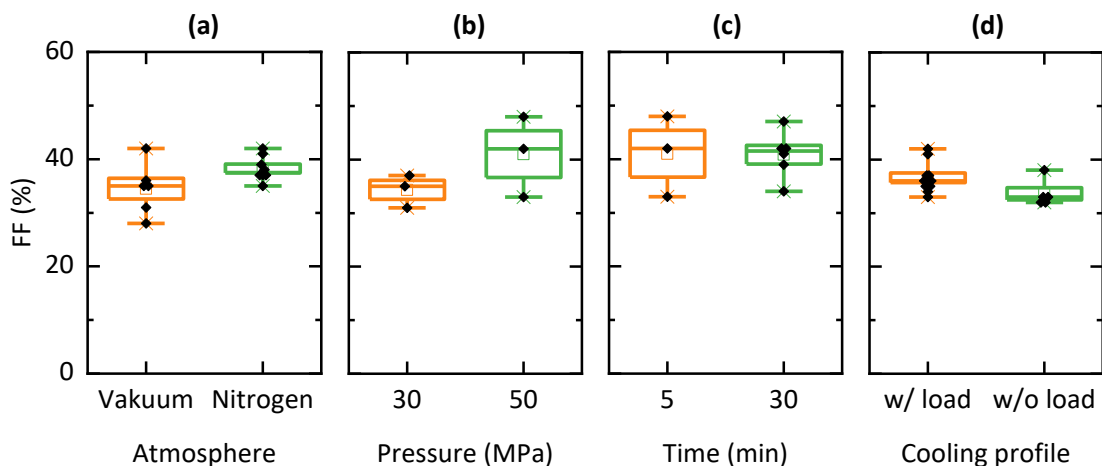


**Figure 8.8.** Effect of different lamination parameters on the FF of the laminated perovskite solar cells. (a) A nitrogen atmosphere inside the process chamber is preferred over a vacuum. (b) A pressure of  $\approx 50$  MPa increases the FF. (c) The duration of the lamination pressure does not affect the FF. (d) For the cooling profile it is preferable to keep the load during the cooling of the laminated perovskite solar cell.

#### 8.4.4 Introducing a buffer layer between the perovskite and HTL

The preliminary investigations have shown that the FF of the laminated perovskite solar cells is comparably low. This implies a high series  $R_s$  and low shunt resistance  $R_{sh}$ . A possible reason for this might be still a poor interface between the two laminated perovskite half-stacks. Therefore, the implementation of a thin buffer layer is intended.

In this regard, the key to the lamination process is found for a thin PTAA buffer layer between the perovskite and  $\text{NiO}_x$  HTL. The buffer layer increases the mechanical and

electrical contact between the two half-stacks. The improved mechanical contact between the laminated layers leads to 36% less nonfunctional laminated perovskite solar cells (see Figure S4, Supporting Information in ref. [218]). With the PTAA layer on both sides, the mean PCE of the devices enhances by 6.9%<sub>abs</sub> as compared to the laminated perovskite solar cells without the PTAA layer (see **Figure 8.9**). It is presumed that the thin PTAA layer enhances electrical contact by filling remaining holes in between the recrystallized perovskite layer and NiO<sub>x</sub> HTL. The improvement is visible in all the electrical parameters, like the FF, series and shunt resistance (see Table 7). In the champion device, the series resistance drops from ≈180 Ω to 66 Ω.

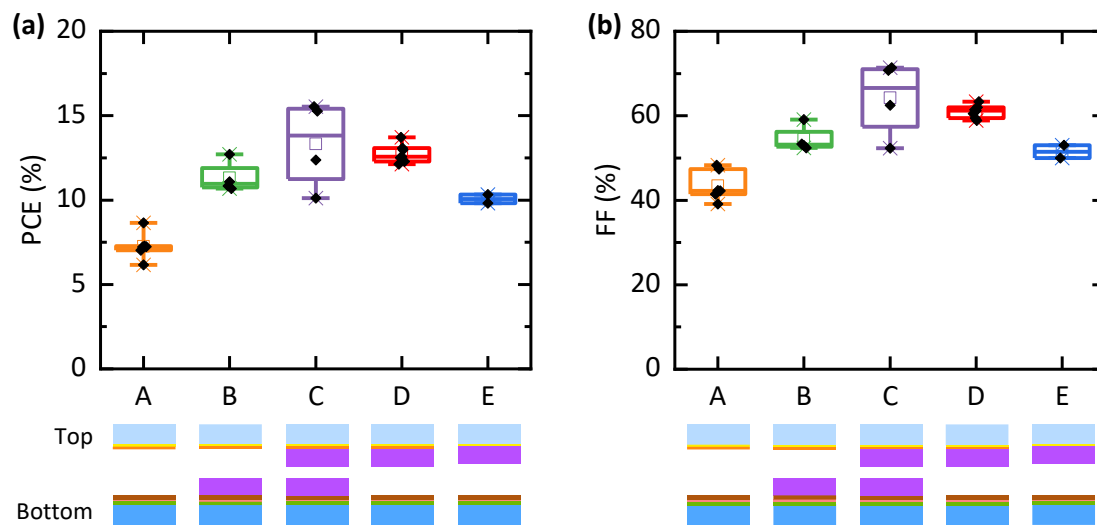


**Figure 8.9.** Electrical characterization of the laminated perovskite solar cells with a PTAA buffer layer at the perovskite / NiO<sub>x</sub> interface. (A) No PTAA is used, (B) PTAA is deposited on top of the perovskite layer, (C) on top of the NiO<sub>x</sub> and perovskite layer, and (D) only on top of the NiO<sub>x</sub> layer prior to the lamination process. (E) Only PTAA without NiO<sub>x</sub> is used. Adapted with permission from ref. [218], © John Wiley & Sons.

**Table 7.** Electrical parameters for laminated perovskite solar cells with a PTAA buffer layer at the perovskite / NiO<sub>x</sub> interface for the four configurations illustrated in Figure 8.9.

Config.	PCE (%)	FF (%)	$J_{sc}$ (mAcm <sup>-2</sup> )	$V_{oc}$ (V)	$R_{SH}$ (kΩ)	$R_s$ (Ω)
A	$7.3 \pm 0.7$	$43.4 \pm 3.3$	$19.5 \pm 0.9$	$0.86 \pm 0.03$	$3.15 \pm 1.52$	$170 \pm 29$
B	$11.3 \pm 0.8$	$54.5 \pm 2.7$	$20.6 \pm 0.1$	$1.01 \pm 0.03$	$29.81 \pm 23.37$	$139 \pm 22$
C	$13.3 \pm 2.2$	$64.2 \pm 7.7$	$21.0 \pm 0.4$	$0.98 \pm 0.04$	$57.93 \pm 30.35$	$68 \pm 6$
D	$12.8 \pm 0.5$	$61.0 \pm 1.4$	$21.2 \pm 0.3$	$0.99 \pm 0.02$	$12.96 \pm 3.47$	$90 \pm 5$
E	$10.0 \pm 0.3$	$51.5 \pm 1.5$	$19.0 \pm 0.1$	$1.02 \pm 0.01$	$9.10 \pm 1.43$	$80 \pm 1$

## 8.5 Laminated perovskite solar cells

With the optimized lamination process, stable laminated perovskite solar cells with remarkable PCEs are processed. For the lamination, optimized parameters: a temperature of 90°C, a hot-pressing duration of 5 min and a pressing pressure of ≈50 MPa are used.

Moreover, a thin PTAA buffer layer is incorporated to enhance electrical and mechanical contact between to perovskite and HTL interface.

The current density – voltage characteristics of the champion device is displayed in **Figure 8.10a**. Compared to previous work on laminated perovskite solar cells with comparable device architecture using  $\text{MAPbI}_3$ , the champion laminated perovskite solar cell is 38%<sub>rel</sub> (or 4%<sub>abs</sub>) higher in PCE and demonstrate a PCE of 14.6% [248]. The champion device exhibits a  $J_{\text{SC}}$  of  $20.0 \text{ mAcm}^{-2}$ , a  $V_{\text{OC}}$  of 1.04 V and an FF of 70% (see Figure 8.10a). The improvement in terms of PCE to the previous work mainly is related to the higher FF due to lower series  $R_{\text{S}}$  and higher shunt resistance  $R_{\text{SH}}$ . Nevertheless, the electrical parameters lack still behind record perovskite solar cells, with optimized architectures [167,168,209].

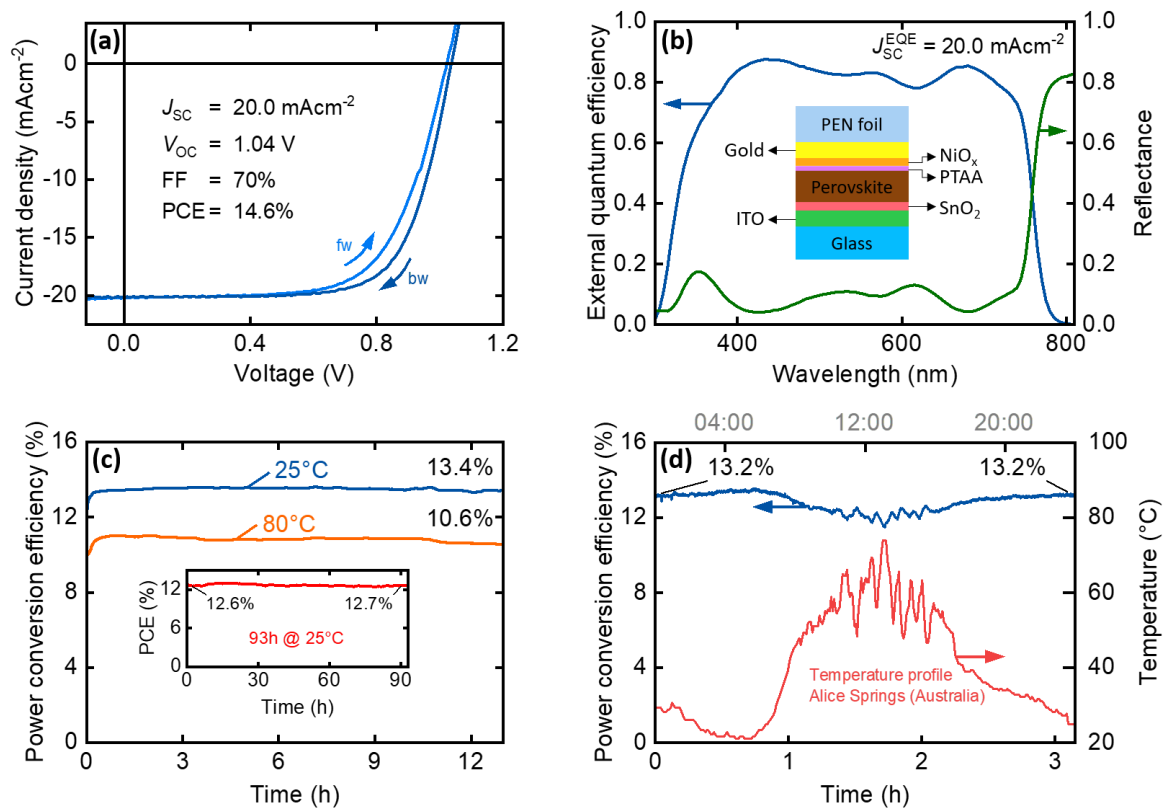


**Figure 8.10.** (a) Current density – voltage characteristics and (b) the EQE with the corresponding reflectance of the champion laminated perovskite solar cell. (c) Stabilized maximum power point (MPP) tracking for 25°C and 80°C. (d) MPP tracking with a measured outdoor temperature profile of a silicon module at the hottest day in Alice Springs (Australia) in 2014 (measured by the Desert Knowledge Australia Solar Center). Adapted with permission from ref. [218], © John Wiley & Sons.

In particular, the  $V_{\text{OC}}$  of only  $\approx 1.04 \text{ V}$  and the FF of 70% are not yet optimal and lack  $\approx 15\text{--}20\%$  behind the record perovskite solar cells processed by spin coating. Moreover, the comparably low  $J_{\text{SC}}$  – also lower than the previously reported value of  $22.3 \text{ mAcm}^{-2}$  – of our laminated perovskite solar cell might be attributed to reflectance losses (see Figure 8.10b) typical for planar all-thin-film layer stacks [15]. To address this, further

optimizations of the layer thicknesses and front ITO contact has to be performed. Moreover, to further increase the electrical parameters of the laminated perovskite solar cells, additional optimizations of the process parameters are needed.

In addition to the high PCE for laminated perovskite solar cells, for the first time, stable power outputs are reported. Stabilized power outputs are key for assessing realistic power outputs given the uncertainties that arise from hysteresis effects in perovskite PV [250]. In this regard, the power outputs are tracked for several minutes (>5 min) and the stabilized value at the end of the measurements are extracted. Moreover, the long-term (>1 h) measurements under continuous illumination are performed (see below) to test and verify the stability of the laminated perovskite solar cells [133].

At 25°C, the champion laminated perovskite solar cell shows a stabilized PCE over 13 h of 13.4% (see Figure 8.10c). Even after 93 h of MPP tracking, the laminated device exhibits a stable PCE.<sup>2</sup> In addition, the laminated perovskite solar cells demonstrate excellent thermal stability: after 13h of MPP tracking at 80°C, the PCE of the laminated perovskite solar cell remains constant. This stability against light and temperature stress is very remarkable and is founded in the use of inorganic CTLs and particularly the replacement of the organic charge transport layers like spiro-OMeTAD, which is known to degrade at elevated temperatures above 60°C [15,251–254].

Since not only constant temperatures, but also temperature variations are inevitable in outdoor operations, the laminated perovskite solar cells are stressed with measured temperature profiles of solar modules in Alice Springs (Australia) [133,255]. The stabilized PCE for temperatures ranging from 20°C to 75°C over the course of the day is displayed in Figure 8.10d. Here, the 24-h temperature profile of the hottest day in the dataset is reduced to 3 h to accelerate the temperature variations. The laminated perovskite solar cells confirm a high thermal stability for realistic temperature variations and recover its initial PCE after the temperature profile. This constant power output of the laminated perovskite solar cells is truly remarkable considering the reversible loss up to 10%<sub>rel</sub> in the first ≈100 h of triple cation perovskite solar cells in an *n-i-p* configuration [256,257]. In addition to that, the decrease in initial PCE of the laminated perovskite of ≈4%<sub>rel</sub> at elevated temperatures is comparable to carbon-based perovskite solar cells – known for their superior stabilities [258,259]. However, the laminated perovskite solar cells still have to compete with currently reported stabilities over 1000 h [258,260,261]. This high stability against light and temperature stress is hypothesized to stem from the replacement of the organic CTL like spiro-OMeTAD. In comparison to this, the two inorganic CTLs: SnO<sub>2</sub> and NiO<sub>x</sub> are known to provide good intrinsic chemical stability [15,224,227,228]. Moreover, the high melting point of the PTAA (>100°C) makes it perfect as buffer layer and ensures compliance with the IEC standard test conditions [262,263].

---

<sup>2</sup> Note this measurement was performed after putting the device to a lot of thermal and light stress by several temperature profiles. This explains the slightly smaller PCE of 12.6% compared to initial 13.4%.

To conclude, the demonstrated high PCE for laminated perovskite solar cells are encouraging for future research in this field. The approach offers new possibilities that might support optimizing the architecture or investigate new materials with regard to improved stability.

## 8.6 Flexible and semitransparent laminated devices

The laminated perovskite solar cells provide high PCE and a good thermal stability. Moreover, the lamination process provides new degrees of freedom for processing the perovskite solar cells. In this regard, also new material combinations and device architectures can be exploited. From a technological perspective, the lamination of the two separately processed half-stacks of the perovskite solar cell, enables direct encapsulation by the two substrates. This supports a new route to directly encapsulate the perovskite solar cells, which could provide potential barrier properties against oxygen and moisture [264]. This might be useful, since it can combine fabrication and encapsulation to a one-step self-encapsulation process without the need for an external adhesive. Moreover, the lamination enables further investigations on inverted architectures, avoiding TiO<sub>2</sub> as front CTL, to enhance robustness against ultraviolet (UV) light-induced degradation [265].

Another key perspective of perovskite solar cell is the combination in tandem PV as a top absorber. To demonstrate the versatility of the lamination process and ease of transfer towards tandem technologies, (a) semitransparent, (b) flexible opaque and (c) flexible semitransparent perovskite solar cells are laminated. In **Figure 8.11** the PCE of the three different configurations are displayed. The laminated semitransparent solar cell shows a PCE of 11.5% with a stabilized value of 11.4%. Here, the 80 nm gold electrode is replaced with a 150 nm thick ITO layer. For the two flexible configurations, a second flexible PEN foil replaces the rigid glass substrate at the front. The opaque flexible perovskite solar cell reaches a PCE of 11.3% with a stabilized value of 11.2%. The flexible and semitransparent device showed a PCE of 8.8%. The reduced PCE in the flexible devices is mainly linked to the reduced  $J_{SC}$ , which is reasoned in the lower transmittance of the PEN substrate compared to the glass substrate.

Further advances in device performance are expected in all three configurations by further optimizations in the lamination process. Nevertheless, the presented lamination method is encouraging for future research on laminated perovskite PV and in particular for tandem applications. In this regard, the lamination method can be useful to create self-encapsulated architectures or even multi-junction perovskite-based solar modules. In case of multi-junction PV, the half-stack with the perovskite absorber could be laminated directly on top of a bottom solar cell to construct a two-terminal tandem solar cell.

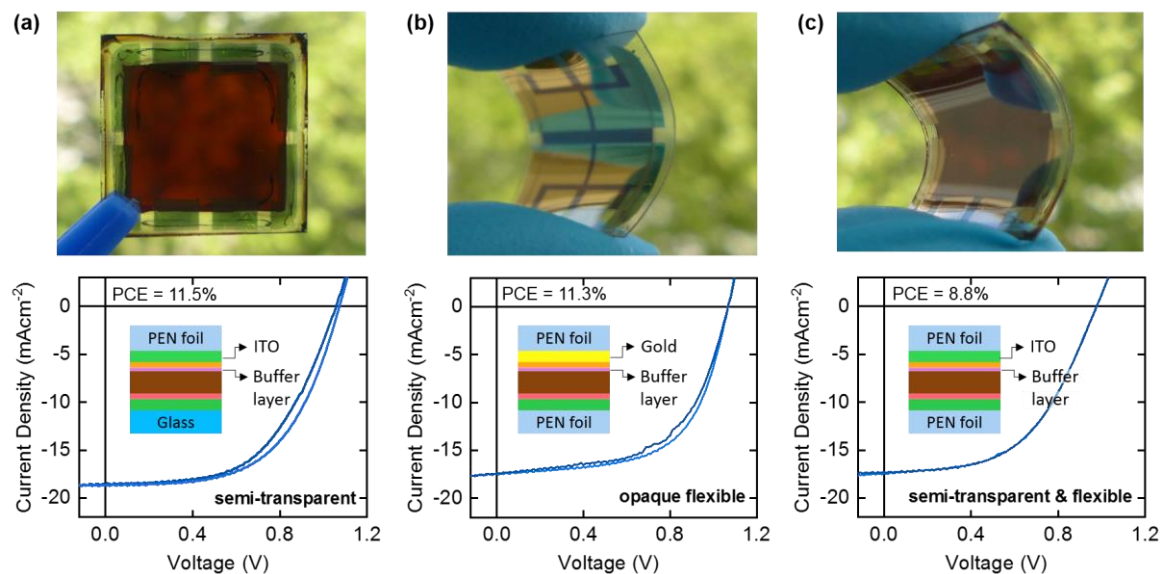


**Figure 8.11.** Current density – voltage characteristics and corresponding photographs of (a) a rigid semitransparent, (b) an opaque and flexible and (c) a semitransparent and flexible laminated perovskite solar cell. The laminated perovskite solar cells are made of the following architecture: substrate / ITO / SnO<sub>2</sub> / perovskite / buffer layer / NiO<sub>x</sub> / electrode / substrate. Adapted with permission from ref. [218], © John Wiley & Sons.

## 8.7 Summary

The preceding sections of this chapter describe the findings and results on laminated perovskite solar cells. The lamination of perovskite solar cells demonstrates an exciting possibility of a new concept. This paves the way for potential new manufacturing processes. The separate processing of two half-stacks of the perovskite solar cell offers an elegant solution to avoid layer incompatibilities in conventional layer depositions techniques. In this regard, the lamination route enables the access to novel device architectures and provides a new degree of freedom in the choice of electron and holes transport layers.

For the first time, the lamination of perovskite solar cells at the perovskite / hole transport interface is demonstrated and record power conversion efficiencies (PCE) of up to 14.6% are achieved. Moreover, the presented laminated perovskite solar cell with two inorganic charge transport layers, prove themselves through long-term and high-temperature stabilities. The champion device shows a stable power output of  $\approx 12.7\%$  after almost 100 hours of maximum power point (MPP) tracking and provides high-temperature stability for temperatures of up to 80°C. With regard to realistic temperature profiles, the examined laminated perovskite solar cell recovers to its initial PCE during MPP tracking, after tested with the measured temperature profile of the hottest day in Alice Springs (Australia) in 2014.

The measured constant power output of laminated perovskite solar cells in the first  $\approx 100$  h is truly remarkable when considering the reversible loss of up to  $10\%_{\text{rel}}$  of comparable triple-cation perovskite solar cells [256,257]. Moreover, the decrease in initial power conversion efficiency of the laminated perovskite solar cell of only  $\approx 4\%_{\text{rel}}$  at elevated temperatures is comparable to carbon-based perovskite solar cells - known for their superior stability [258,259]. Nevertheless, the laminated perovskite solar cells still need to compete with the currently reported stabilities over 1000 h [258,260,261].

In particular, the remaining issue of the laminated perovskite solar cells are a comparably low open-circuit voltage and only decent electrical fill factors. Both lack  $\approx 15 - 20\%$  behind the record perovskite solar cells processed by spin coating. Nevertheless, the implementation of the PTAA buffer layer was a big step towards substantially improved electrical properties. However, further increase of the electrical parameters of the laminated perovskite solar cells is needed by additional optimizations of the process parameters. Potential replacements of the thin PTAA layer might be one of the potential strategies. However, it must first be understood at which interface the most severe electrical losses currently occur.

Apart from the optimizations necessary to bring the lamination process to the level of record efficiency of current perovskite solar cells, the lamination also offers another exciting field of application: tandem photovoltaics. The first test on laminated flexible, semitransparent and the combination of both are demonstrated and proof their feasibility. Moreover, the semitransparent and flexible laminated perovskite solar cells show as well as their opaque competitors stable power outputs.

With regard to tandem applications, similar perovskite half-stack could be processed and laminated on top of a potential candidate bottom solar cell (e.g. c-Si). In this regard, the lamination method might be useful to create 2T tandem solar modules. Due to the superstrate of the perovskite cell being laminated on top, the perovskite/c-Si tandem solar cell could be directly encapsulated. Therefore, the presented lamination method is encouraging for future research on perovskite-based tandem photovoltaics and should be followed up.

## 9 Conclusion and Outlook

This thesis reports on advanced light management concepts for perovskite photovoltaics (PV). Distinct concepts are demonstrated to increase the power conversion efficiency (PCE) and moreover the annual energy yield (EY). In order to ascertain the annual EY, a simulation framework for EY modeling is developed and applied for the proposed concepts.

First, microtextures at the air/glass interface are investigated to improve the light-incoupling, which is important for any PV technology. The microtextures at the front of the solar module offer to eliminate the air/glass reflection almost completely for normal light incidence and reduce it by around 80%<sub>rel</sub> for oblique incidence angles (e.g. 80°). Applied on top of planar and textured crystalline silicon (c-Si) solar cells, this increases the PCE by 12%<sub>rel</sub> and 5%<sub>rel</sub>, respectively. The concept easily transfers to perovskite/c-Si tandem PV, where the PCE enhances by 6%<sub>rel</sub>. Due to the excellent angular stability of the microtextures, this improvement in the PCE is reflected in the EY as well, which is shown by the EY simulations, where the enhancements in the EY exceeds those of the PCE by around 2%<sub>rel</sub>.

Besides the front air/glass interface, the reflectance losses of the front semitransparent ITO electrodes are improved by nanotexturing the glass/ITO interface. The nanophotonic ITO electrodes effectively guide the light inside the top perovskite solar cell, and thus enhance the tandem PCE by 2%<sub>rel</sub>. Moreover, strong improvements of 22%<sub>rel</sub> in the transmittance of the semitransparent perovskite solar cells are observed in the nanophotonic devices. Furthermore, the nanotextured electrodes are angular stable and promise an increase in EY of 10%<sub>rel</sub> in simulations, which is higher than the simulated improvement in PCE of 9%<sub>rel</sub>.

Further nanophotonic modifications of the perovskite absorber layer itself improves the absorption near the band gap by coupling the incident light to quasi-guided modes. The coupling promises enhancements of up to 6%<sub>rel</sub> in the short-circuit current densities ( $J_{SC}$ ), and thus in the PCE. A thermal nanoimprint lithography process is developed to nanoimprint the perovskite layers, and first experimental results demonstrate improvements of 2%<sub>rel</sub> in the  $J_{SC}$ . In addition, the nanophotonic perovskite solar cells enable a facile way to mitigate the environmentally harmful lead content in perovskite

solar cells by about 30%<sub>rel</sub> while maintaining the same PCEs. In terms of angular stability, the nanophotonic perovskite solar cells are equally robust as the planar references and promise similar enhancements in EY as in PCE.

Finally, a novel manufacturing method for perovskite solar cells is presented, which enables a facile lamination of the perovskite solar cells. With this, the lamination of the perovskite solar cell offers flexibility and brings freedom in the choice of charge transport materials to the perovskite solar cell fabrication. First prototypes demonstrate already excellent long-term and thermal stability of the perovskite solar cells with PCEs above 14%. In addition, the presented concept of lamination paves the way for the direct lamination of perovskite solar cells onto the existing silicon technology, and thus has great potential for current perovskite-based tandem research.

Comparing the various light management concepts presented, they promise and demonstrate different potentials. Moreover, each concept finds itself at a different stage of development. Therefore, the current status, its potential and significance as well as further ideas are discussed in the following. Moreover, the energy yield modelling and the lamination, which are no light management concepts are discussed as well.

### **Energy yield modelling**

The energy yield (EY) modelling platform evolved to a robust tool for fast modelling of the annual EY for complex optical architectures. Realistic irradiance data are modelled and accurate electrical modelling is performed for the various interconnection schemes of perovskite-based tandem solar cells. Moreover, numerous one- and two-axis tracking algorithms as well as static tilts are implemented. Recently, bifacial tandems, self-shading and a rigorous treatment of three-terminal electrical interconnections have been added into the feature list.

In terms of potential, the EY modelling is a powerful tool providing fast insights into current research on existing or new concepts for single- and multi-junction photovoltaics. Although, the modelling has a high level of complexity, the implementation of the EY modelling is very fast (i5-8265u processor: <1 min). Moreover, due to the realistic irradiation data, the detailed electrical modelling and the high temporal resolution, realistic predictions are possible.

In this regard, the EY simulations will have a significant technological impact, since they can identify the potential of a multitude of researched architectures, most still in an early phase of development. Moreover, the EY modelling provides easy access to examine light management concepts under realistic operation conditions, as it was presented within this thesis.

Further work should be directed to triple-junction solar modules. Here, the three-junction perovskite/perovskite/c-Si will be a vital candidate. Moreover, with the evolving

field of perovskite photovoltaics and exploration of a broad range of band gaps, all-perovskite multi-junctions will grow in popularity. In addition, since first studies report on perovskite/c-Si tandem solar cells with non-conformal coverage of the perovskite thin-film stack on top of the textured c-Si bottom solar cell, further functionalities in the optics module might be necessary to implement. Finally, the EY framework might be relevant to forecast solar power generation by coupling solar parks to actual weather forecasts.

### **Microtextures**

In the field of microtextures various ideas have been presented within this thesis. The fabrication of artificial cones as well as the replication of the biomimetic partners, taken from leaves and petals, have proven themselves on different photovoltaic technologies, up to first perovskite/c-Si tandem minimodules (on 4 cm<sup>2</sup>). Moreover, a first proof of concept of micro-cones inside the front glass cover of solar modules has been demonstrated in a collaborative work.

In general, the light management concept based on the microtextures demonstrates to eliminate reflection of the first air/glass interface, every PV technology suffers from. Moreover, due to its broadband nature and the strong angular stability, the enhancement in the EY surpasses the improvements in PCE. However, the actual potential is strongly linked to the pristine reflection losses. Nevertheless, significant enhancements of the annual EY by around 7%<sub>rel</sub> are foreseen for the perovskite/c-Si tandem solar cells.

Since the microtextures can be applied to any (existing) photovoltaic technology having a glass or foil-like encapsulation, and in addition provide great improvement potentials, the cost-benefit ratio appears attractive. Nevertheless, upscaling of the technology first needs to prove this. Therefore, the next step is the development of an upscaling process to fabricate large areas of the presented microtextures with high aspect ratios (>0.5). The choice of texture might even fall on the biomimetic candidates, since due to their natural disorder they prevent glare effects.

### **Nanophotonic ITO electrodes**

In contrast to the microtextures, the development of nanophotonic ITO electrodes is still in its infancy. Although, first prototype 4T perovskite/c-Si tandem solar cells are fabricated, which demonstrate a significant enhancement in the PCE and EY, electrical losses (mainly in the open-circuit voltage) need to be tackled as well as the upscaling towards relevant module sizes.

Nevertheless, the optical advantages are huge, since the nanophotonic ITO front electrodes efficiently suppress reflection losses at the glass/ITO interface (roughly  $\approx 2\%$ <sub>abs</sub>). This boosts the current generation in the perovskite top solar cell and the transmittance into the bottom c-Si solar cell. Disregarding the electrical losses, the nanophotonic ITO

electrodes could enhance the PCE by  $\approx 9\%_{\text{rel}}$  for normal incidence. Moreover, due to the great angular stability, the enhancement in the EY totals to  $\approx 10\%_{\text{rel}}$ .

Therefore, the nanophotonic ITO electrodes, turn out as excellent and superior alternatives to single layer antireflection coatings between the glass and transparent front electrodes. Nevertheless, further optimization of the planar transparent ITO electrode as well as different electrode materials (e.g. IZO, IOH) in terms of optical and electrical performance needs to be followed up as well. However, simulations with improved optically transparent electrodes still promise potential improvements by the nanophotonic ITO electrodes.

Finally, the nanophotonic ITO electrodes might be interesting if inkjet printing of perovskite solar cells proves itself for the photovoltaic market. In this regard also the nanotextures could be inkjet printed on top of the glass superstrate.

### **Nanoimprinted perovskite solar cells**

The first prototypes of the nanoimprinted perovskite solar cells demonstrate an improved current generation and PCE. However, there is still a gap between the simulated improvements and the experimental realizations, which must be eliminated by further optimizations in the device fabrication. Especially the application of the hole transport layer seems to be the crux of the matter. Moreover, the concept is still limited to small lab-scale dimensions and needs to be developed for larger areas and higher throughput.

In total, the nanophotonic modification of the perovskite absorber by the thermal nanoimprint lithography promises enhancements in the current generation of up to  $6\%_{\text{rel}}$  and similar enhancements in the annual EY. However, this only holds true for single-junction perovskite solar cells and breaks down for perovskite/c-Si tandem solar cells, due to strong losses in the transmittance. Although the enhancements are significant, the significance for real applications remains to be shown. Further improvements in the device fabrication need to be achieved to reach simulated enhancements. Although, nanophotonic perovskite/c-Si tandem solar cells appear unfavorable, other tandem concepts might be more relevant. In this regard, the bottom solar cell in a perovskite/perovskite tandem might benefit from nano-patterning of its absorber.

Moreover, the optimized process of the thermal nanoimprint of the perovskite layers promise to be relevant for other fields of perovskite research as well: e.g. light emitting diodes or lasers.

### **Lamination of perovskite solar cells**

The work on laminated perovskite solar cells present a novel fabrication method for perovskite solar cell. The study, however, is still in an early phase of development. Therefore, the process needs to be further understood and optimized.

Nevertheless, the lamination is foreseen to have a huge potential. This is due to the fact that the lamination provides a potential way to process 2T perovskite/c-Si tandem solar cells and opens up a totally new fabrication route. This is a very promising since it brings – besides thermal evaporation and solution processing – a third processing method for the perovskite to be put onto the bottom c-Si solar cells. However, the different thermal expansion coefficients of currently used PEN foil and c-Si might be challenging and must be bypassed.

Moreover, further work should be directed to resolve the remaining interface problems and boost the electrical fill factors towards the levels of the current record perovskite solar cells. In this regard, optimization of the buffer layer will be most crucial part. Here, optimizing the currently used PTAA or testing other materials (e.g. PCBM, PMMA or BABr) as buffer layer should be the two strategies to be pursued.



# Appendix

## A Complex refractive index data

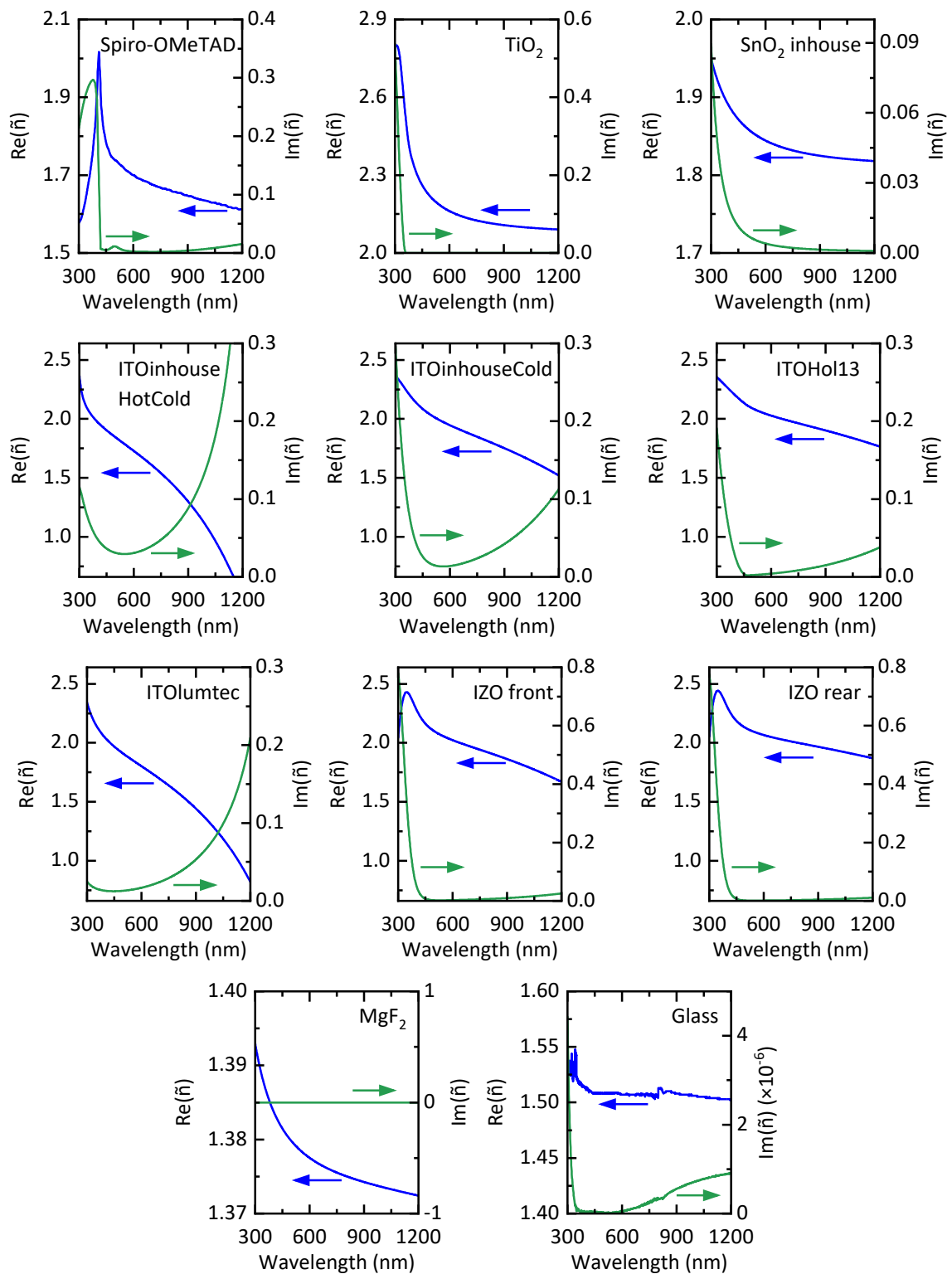


**Figure A.1.** Complex refractive index data used for the simulations in this thesis. The data of Spiro-OMeTAD and  $\text{TiO}_2$  is extracted from ref. [146]. The data for ITOHol13 is extracted from ref. [266]. The data for  $\text{MgF}_2$  is extracted from [267]. The other data is measured in-house.

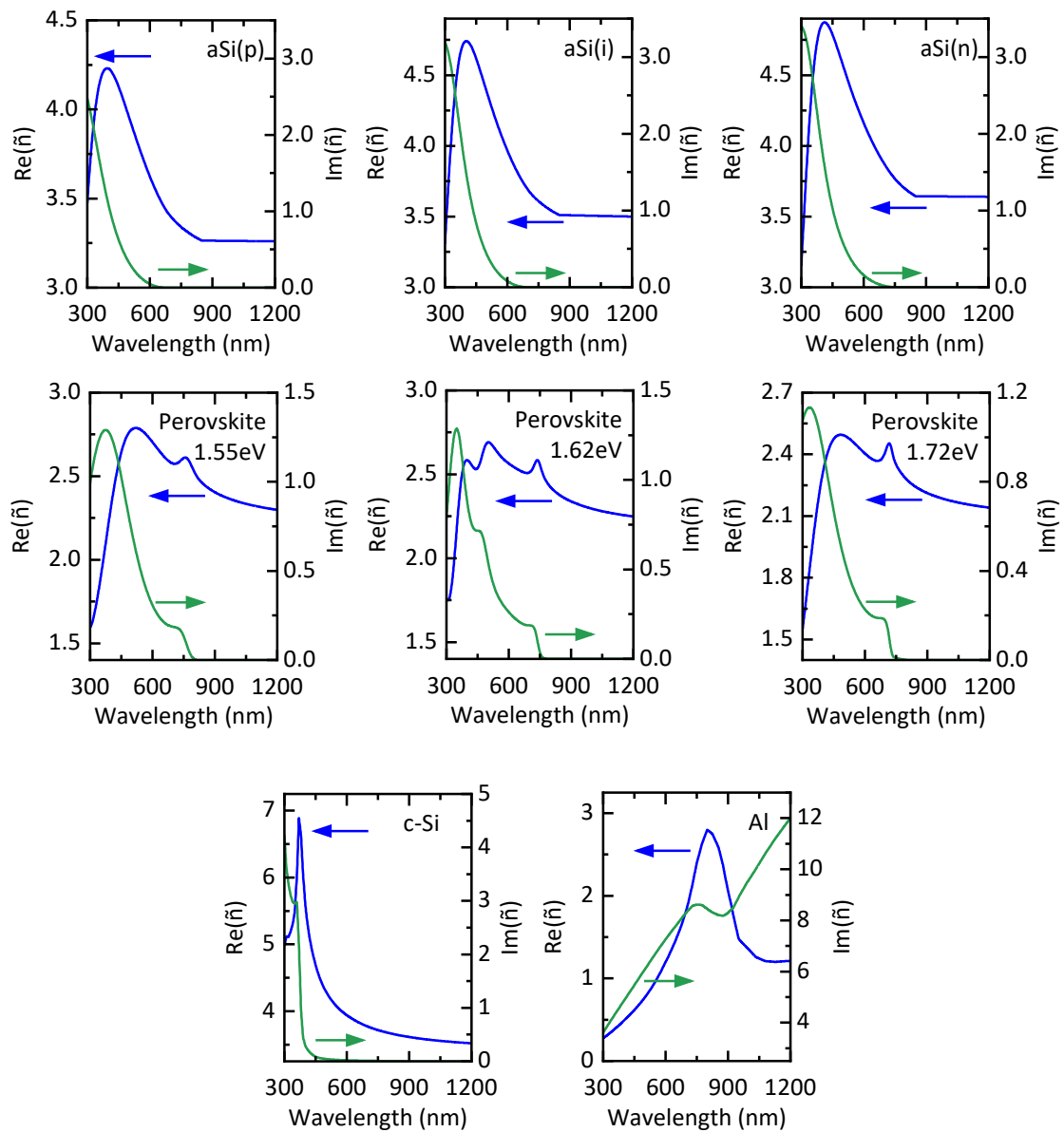


**Figure A.2.** Complex refractive index data used for the simulations in this thesis. The data for aSi(p), aSi(i), aSi(n) is extracted from [268]. The data for perovskite with band gap 1.55 eV is extracted from ref. [146]. The data for the perovskite with a band gap of 1.62 eV is extracted from ref. [166]. The data for the perovskite with a band gap of 1.72 eV is extracted from ref. [86]. The data for c-Si is extracted from ref. [269]. The data for the Al is extracted from ref. [270].

## B Indium zinc oxide as transparent electrode

Replacing the front ITO (here commercial ITO from Luminescence Technology), IZO is developed inhouse. Moreover, the IZO is tested at the rear of the semitransparent perovskite solar cell to replace the rear inhouse ITO. In **Figure B.1** the corresponding simulations and the optical characterization of first devices are shown. The simulation and experiments show a very good agreement. Replacing only the front ITO with IZO increases the overall transmittance by around 15%<sub>abs</sub>. Replacing only the rear ITO with IZO increase the transmittance by around 8%<sub>abs</sub>. Replacing both ITO layers with IZO demonstrates improvements up to 20%<sub>abs</sub>. The increase is due to the better match of the refractive indices within the layer stack (see below). Moreover, the low imaginary part of the complex refractive index in the longer wavelengths makes IZO suitable for tandem applications. However, the strong absorption in the UV might lead to reduced absorption in the perovskite layer and therefore the best choice is to replace the rear ITO by IZO.

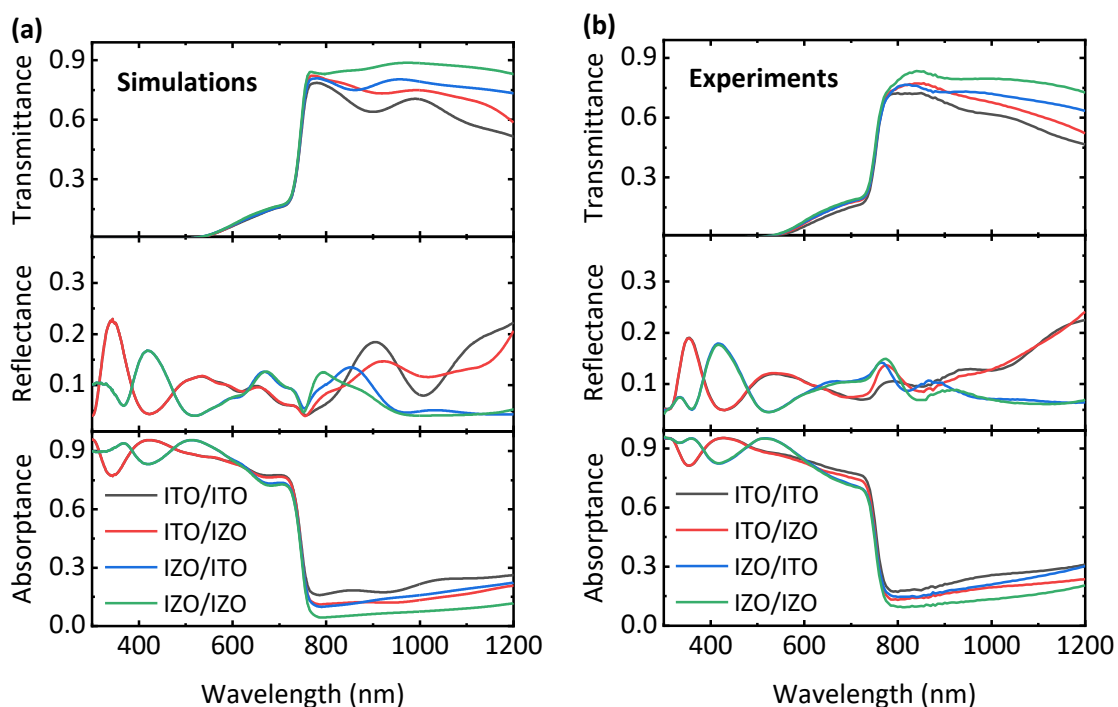


**Figure B.1.** Comparison between indium tin oxide (ITO) and indium zinc oxide (IZO) transparent electrodes within the perovskite stack. (a) Simulation and (b) experimental results of different ITO and IZO combinations. The simulated layer stacks are as follows: ITO/ITO: Glass / ITOLumtec (135 nm) / SnO<sub>2</sub> inhouse (10 nm) / perovskite 1.62eV (460 nm) / Spiro-OMeTAD (250 nm) / ITOinhouseCold (160 nm) / MgF<sub>2</sub> (155 nm) / Air; ITO/IZO: Glass / ITOLumtec (135 nm) / SnO<sub>2</sub> inhouse (10 nm) / perovskite 1.62eV (460 nm) / Spiro-OMeTAD (250 nm) / IZO rear (160 nm) / MgF<sub>2</sub> (155 nm) / Air; IZO/ITO: Glass / ITO front (165 nm) / SnO<sub>2</sub> inhouse (10 nm) / perovskite 1.62eV (460 nm) / Spiro-OMeTAD (250 nm) / ITOinhouseCold (160 nm) / MgF<sub>2</sub> (155 nm) / Air; IZO/IZO: Glass / ITO front (165 nm) / SnO<sub>2</sub> inhouse (10 nm) / perovskite 1.62eV (460 nm) / Spiro-OMeTAD (250 nm) / IZO rear (160 nm) / MgF<sub>2</sub> (155 nm) / Air.

## C.1 Disordered nanophotonic perovskite solar cells

The periodic nanophotonic perovskite solar cells demonstrated a strong coupling to quasi-guided modes close to the band gap of the perovskite solar cells. The enhanced  $J_{SC}$  is validated by experimentally fabricated nanoimprinted perovskite solar cells. Since the periodic gratings might be subject to angular instabilities, disordered photonic gratings are also evaluated for their feasibility for TNIL. Moreover, due to the disorder, the spectral range of coupling might increase.

A first proof of concept is displayed in in **Figure C.1**. Here, the AFM scan of a disordered imprinted perovskite layer is shown. For the TNIL, a disordered mold is fabricated with the phase separation method (see section 6.3). The holes inside the perovskite are  $\approx 80$  nm deep and the mean diameter is  $\approx 400$  nm, which is close to the optimum predicted by the simulations for the periodic gratings. The geometrical FF of the imprinted holes is comparably low. However, the completed devices (same architecture as in the previous chapter), demonstrate an improved  $J_{SC}$  of  $\approx 3\%$  (see Figure C.1b). The enhanced current is due to the shift in the absorption of the perovskite. Compared to the planar imprinted reference, the EQE improves around 700 nm for the nanoimprinted perovskite solar cell with the disorder texture. However, the PCE of the perovskite solar cells, both planar reference and nanoimprinted configuration, where rather low  $\approx 10\%$  and no stabilized PCE could be obtained.

Therefore, further work has to be directed to optimize the fabrication process for the disordered nano-gratings, since the initial results of the first prototypes look very promising.

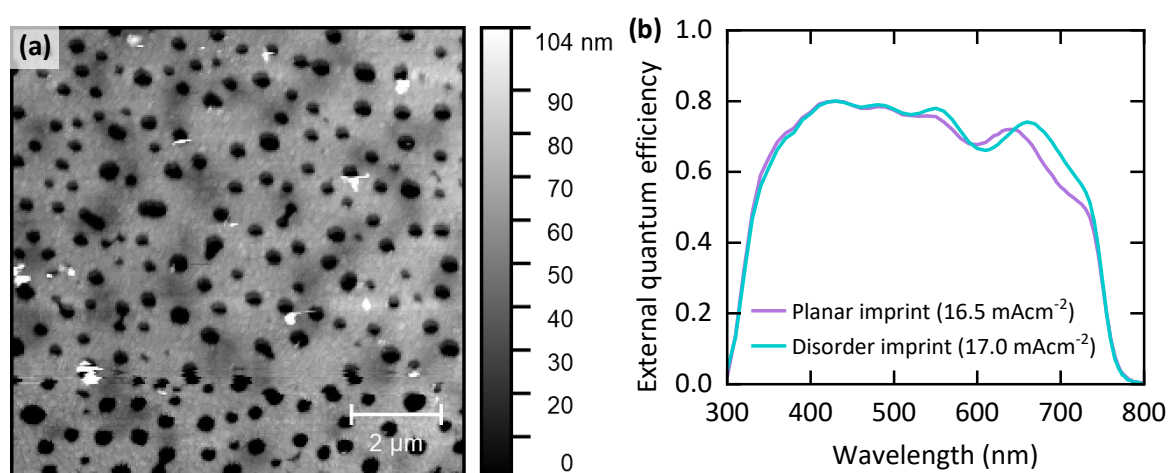


**Figure C.1.** (a) Atomic force microscopy (AFM) image of a perovskite layer with a disorder grating inside. The disorder grating was imprinted via TNIL. The disorder mold is fabricated with the phase separation method. (b) External quantum efficiency (EQE) of a disorder imprinted perovskite solar cell and a planar imprinted perovskite solar cell.

## C.2 Semitransparent nanophotonic perovskite solar cells

So far, it has been shown that the nanophotonic texture inside the perovskite absorber layer enhances the absorption and consequently the  $J_{SC}$  of the perovskite solar cells. In view on perovskite-based tandem PV, the enhancement in semitransparent nanophotonic perovskite solar cells is analyzed as well. For the semitransparent perovskite solar cells, a similar layer stack as shown in Figure 7.1 is used. In this regard, the perovskite layer in the planar reference is set to 370 nm. Moreover, an indentation depth of 180 nm is used for the periodic holes in the nanophotonic devices. Compared to the opaque perovskite solar cells, the rear gold electrode is replaced by a 150 nm thick semitransparent ITO electrode. The refractive index data is summarized in Appendix A.

For geometrical parameters similar to the optimized values of the opaque nanophotonic perovskite solar cell ( $P = 400$  nm,  $FF = 50\%$ ), strong gains of  $\approx 8\%_{rel}$  in the short-circuit current density in the nanophotonic semitransparent perovskite top solar cell are found (see **Figure C.2**). Compared to the planar reference (see Figure C.2a), the absorptance in the perovskite layer increases for the nanophotonic semitransparent solar cell. However, the transmittance is decreased in case of the nanophotonic modification of the perovskite absorber due to the coupling of the incident light to guided modes at longer wavelengths (see Figure C.2b). This coupling leads to strong parasitic absorption and therefore decreases the amount of transmitted light.

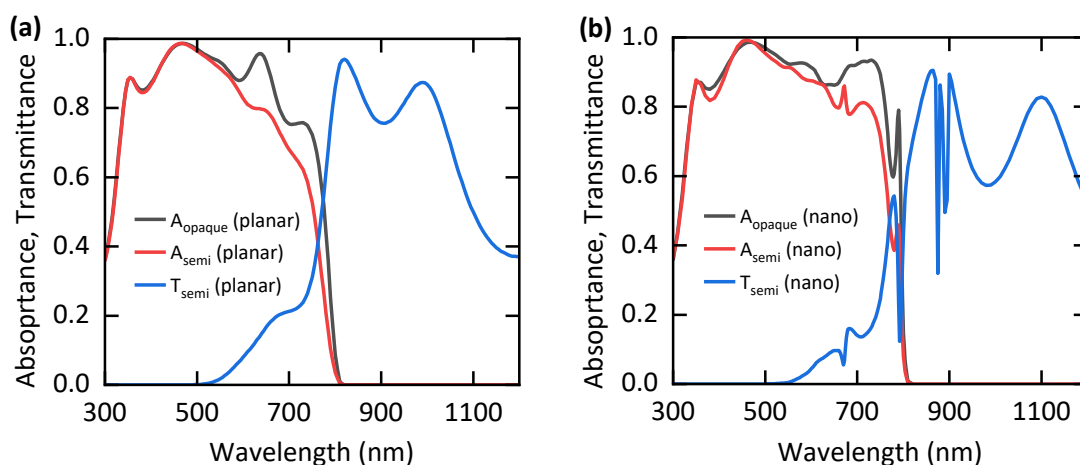


**Figure C.2.** Absorptance and transmittance of an opaque and semitransparent perovskite solar cell. (a) planar reference and (b) the nanophotonic (nano) configuration with a geometrical FF of 50%, a period of 400 nm and an indentation depth of 180 nm. The perovskite layer thickness of the planar reference is 370 nm.

For constant indentation depth of the nano-holes of 180 nm, the enhancement in  $J_{SC}$  is illustrated in Figure for an opaque nanophotonic perovskite solar cell (a) and a semitransparent nanophotonic perovskite solar cell (b) for different geometric fill factors (10 - 70%) and periods (50 - 500 nm). Compared to the opaque solar cell, the semitransparent nanophotonic perovskite solar cells show a broader optimum with similar enhancements in the  $J_{SC}$  of  $\approx 1.6$   $\text{mAcm}^{-2}$ . Assuming perfect absorption in the bottom solar

cell of the transmitted light, the equivalent transmitted short-circuit current  $J_{SC}^{Trans.}$  is calculated.

The change in  $J_{SC}^{Trans.}$  compared to the planar reference is positive only for small periods and small geometrical FF (see **Figure C.3c**). Here, the transmittance is enhanced by  $\approx 0.5 \text{ mAcm}^{-2}$ . The  $J_{SC}$  in the top perovskite solar cell is close to the planar reference ( $\Delta J_{SC} \approx 0$ ). For the maximum enhancement in the  $J_{SC}$  in the perovskite absorber, the decrease in transmitted light is  $\approx -2.0 \text{ mAcm}^{-2}$ .

In conclusion, it should be noted that semitransparent nanophotonic perovskite solar cells are possible, but the possible gain in the total 4T tandem efficiency will be mostly due to enhanced transmittance and not due to the coupling of incident light to (quasi-guided) modes in the perovskite absorber layer. For the strong coupling regime, a period of  $\approx 400 \text{ nm}$ , the loss in transmittance surpasses the absolute gain in  $J_{SC}$  of the top perovskite solar cell.

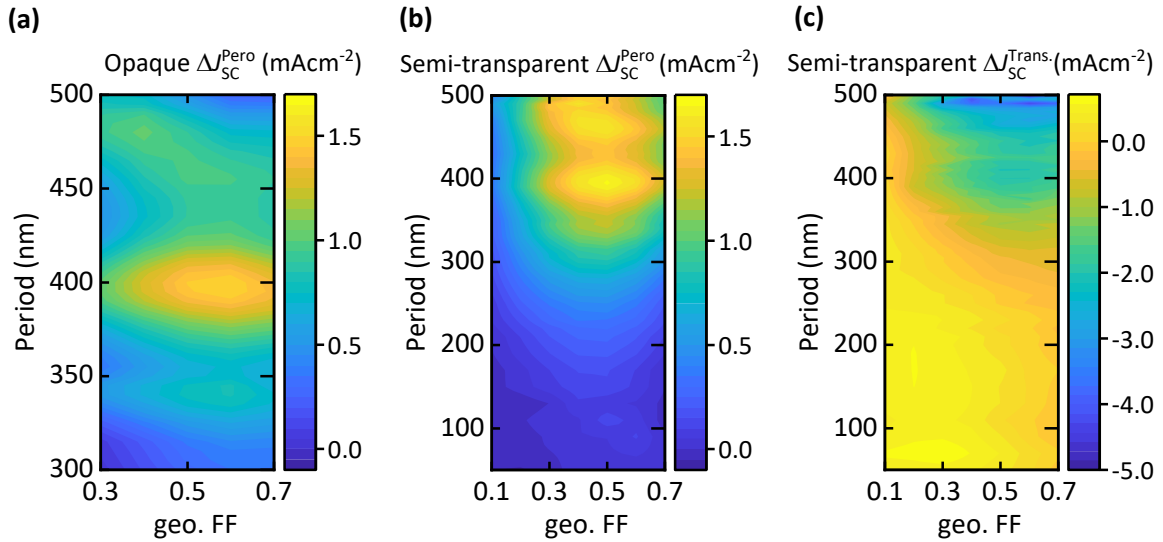


**Figure C.3.** Gain in the short-circuit current density  $J_{SC}$  for nanophotonic perovskite solar cells with an initial perovskite layer thickness of 370 nm and an indentation depth of 180 nm. The gain in  $J_{SC}$  is simulated for various geo. FF and periods. (a)  $\Delta J_{SC}$  for an opaque nanophotonic solar cell. (b)  $\Delta J_{SC}$  for semitransparent nanophotonic solar cell and (c) the equivalent  $\Delta J_{SC}$  of the transmitted light.

## D Change in energy yield due to optical coupling layer

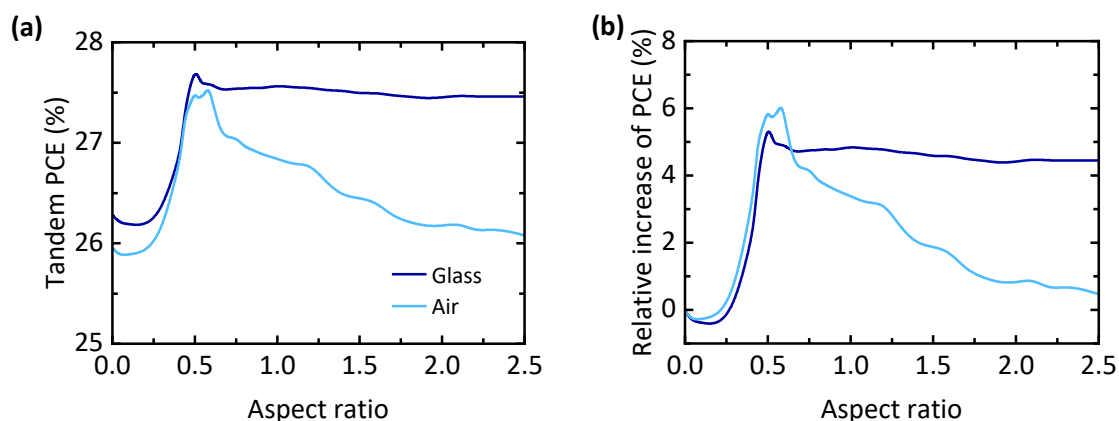


**Figure D.1.** (a) Tandem power conversion efficiency (PCE) and (b) relative increase in the tandem PCE of the simulated architecture in section 5.6. The tandem PCE increases for inverted pyramids on top of the perovskite/c-Si tandem solar cell above an aspect ratio (AR) of 0.3. A strong gain (5 - 6%) is visible for AR = 0.5. For glass as optical coupling layer, this gain remains almost constant for larger AR. For air between the two subcells, the tandem PCE decreases again.

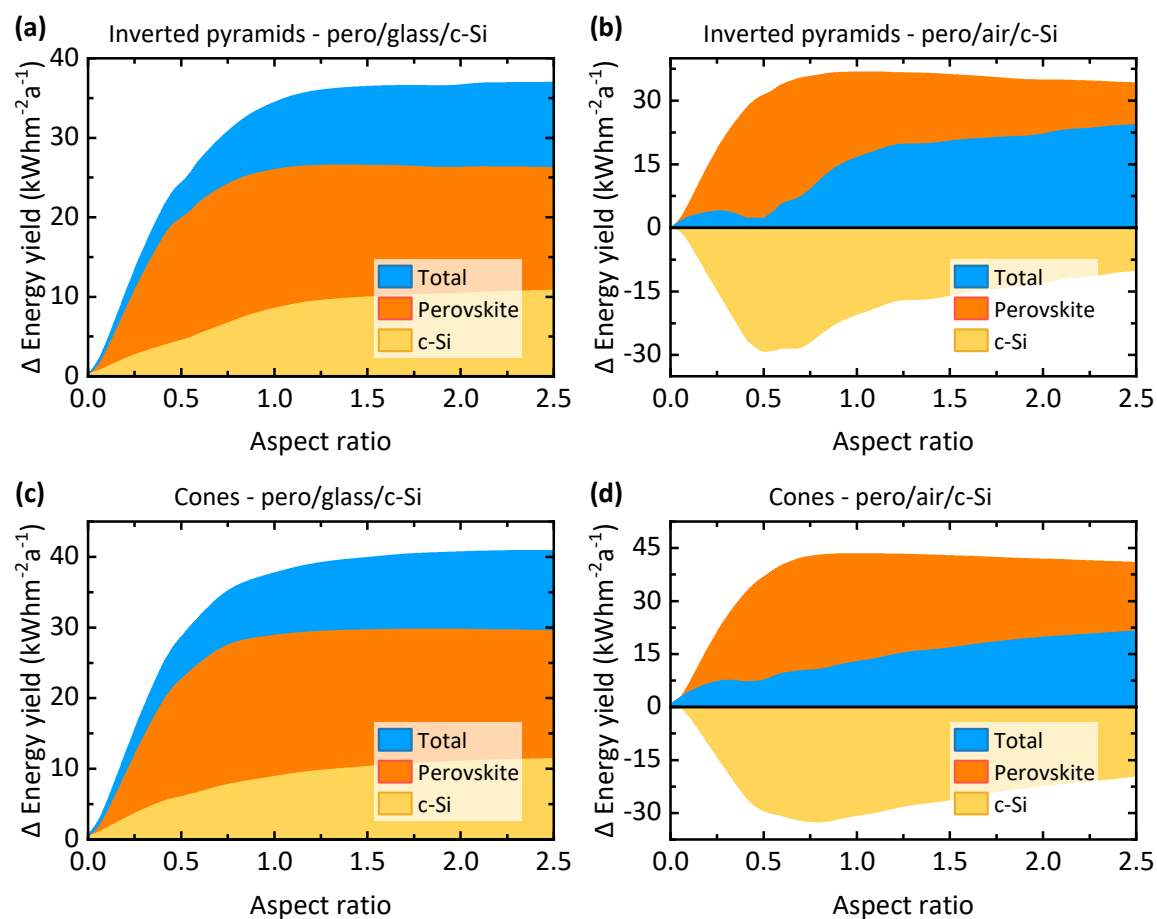


**Figure D.2.** Change in the annual energy yield (EY) for microtextures different aspect ratios (AR). The change in the EY is displayed for the top perovskite, bottom c-Si and the sum of both. The inverted pyramids on top of the perovskite solar cell with an intermedide (a) a glass layer and (b) air gap. (c) and (d) illustrate the change in the EY for cones on top of the perovskite solar cell.



## References

- [1] UNFCCC. Conference of the Parties (COP), Paris agreement 2015, 2015. doi:FC/CP/2015/L.9/Rev.1.
- [2] R.G. Newell *et al.*, Global Energy Outlook 2019: The Next Generation of Energy, 2019. [www.rff.org/geo](http://www.rff.org/geo).
- [3] W. van Sark *et al.*, Photovoltaic Solar Energy FROM FUNDAMENTALS TO APPLICATIONS, 2017. doi:10.4337/9781849806848.00017.
- [4] IEA, World Energy Outlook 2019, Paris, 2019. [www.iea.org/reports/world-energy-outlook-2019](http://www.iea.org/reports/world-energy-outlook-2019).
- [5] F.I. for S.E.S. ISE, Photovoltaics Report, 2019. [www.ise.fraunhofer.de](http://www.ise.fraunhofer.de).
- [6] U.S. Energy Information Administration, International Energy Outlook 2019 with projections to 2050, 2019. [www.eia.gov/outlooks/ieo/pdf/ieo2019.pdf](http://www.eia.gov/outlooks/ieo/pdf/ieo2019.pdf).
- [7] VDMA Photovoltaic Equipment, International Technology Roadmap for Photovoltaic (ITRPV) - 2018 Results, 2019. <http://www.itrpv.net/> (accessed March 9, 2020).
- [8] National Renewable Energy Laboratory (NREL), Efficiency Chart, (2020). [www.nrel.gov/pv/cell-efficiency.html](http://www.nrel.gov/pv/cell-efficiency.html) (accessed March 10, 2020).
- [9] M. Saliba *et al.*, Incorporation of rubidium cations into perovskite solar cells improves photovoltaic performance, *Science*. (2016). doi:10.1126/science.aah5557.
- [10] H. Tsai *et al.*, High-efficiency two-dimensional Ruddlesden-Popper perovskite solar cells, *Nature*. (2016). doi:10.1038/nature18306.
- [11] M. Saliba *et al.*, How to Make over 20% Efficient Perovskite Solar Cells in Regular (n-i-p) and Inverted (p-i-n) Architectures, *Chem. Mater.* (2018). doi:10.1021/acs.chemmater.8b00136.
- [12] E.H. Jung *et al.*, Efficient, stable and scalable perovskite solar cells using poly(3-hexylthiophene), *Nature*. (2019). doi:10.1038/s41586-019-1036-3.
- [13] J. Peng *et al.*, A Universal Double-Side Passivation for High Open-Circuit Voltage in Perovskite Solar Cells: Role of Carbonyl Groups in Poly(methyl methacrylate), *Adv. Energy Mater.* (2018). doi:10.1002/aenm.201801208.
- [14] S. Gharibzadeh *et al.*, Record Open-Circuit Voltage Wide-Bandgap Perovskite Solar Cells Utilizing 2D/3D Perovskite Heterostructure, *Adv. Energy Mater.* (2019). doi:10.1002/aenm.201803699.
- [15] T. Abzieher *et al.*, Electron-Beam-Evaporated Nickel Oxide Hole Transport Layers for Perovskite-Based Photovoltaics, *Adv. Energy Mater.* (2019). doi:10.1002/aenm.201802995.
- [16] Q. Jiang *et al.*, SnO<sub>2</sub>: A Wonderful Electron Transport Layer for Perovskite Solar Cells, *Small*. (2018). doi:10.1002/sml.201801154.
- [17] S.D. Stranks *et al.*, Electron-hole diffusion lengths exceeding 1 micrometer in an organometal trihalide perovskite absorber, *Science*. (2013). doi:10.1126/science.1243982.
- [18] L.M. Pazos-Outón *et al.*, Photon recycling in lead iodide perovskite solar cells, *Science*. (2016). doi:10.1126/science.aaf1168.
- [19] M. Saliba *et al.*, Perovskite Solar Cells: From the Atomic Level to Film Quality and Device Performance, *Angew. Chemie - Int. Ed.* (2018). doi:10.1002/anie.201703226.
- [20] P. Roy *et al.*, A review on perovskite solar cells: Evolution of architecture, fabrication techniques, commercialization issues and status, *Sol. Energy*. (2020). doi:10.1016/j.solener.2020.01.080.

- [21] I.A. Howard *et al.*, Coated and Printed Perovskites for Photovoltaic Applications, *Adv. Mater.* (2019). doi:10.1002/adma.201806702.
- [22] B.R. Sutherland, E.H. Sargent, Perovskite photonic sources, *Nat. Photonics.* (2016). doi:10.1038/nphoton.2016.62.
- [23] M.H. Futscher, B. Ehrler, Efficiency Limit of Perovskite/Si Tandem Solar Cells, *ACS Energy Lett.* (2016). doi:10.1021/acseenergylett.6b00405.
- [24] G.E. Eperon *et al.*, Metal halide perovskite tandem and multiple-junction photovoltaics, *Nat. Rev. Chem.* (2017). doi:10.1038/s41570-017-0095.
- [25] M.A. Green *et al.*, The emergence of perovskite solar cells, *Nat. Photonics.* (2014). doi:10.1038/nphoton.2014.134.
- [26] D.A. Jacobs *et al.*, Light Management: A Key Concept in High-Efficiency Perovskite/Silicon Tandem Photovoltaics, *J. Phys. Chem. Lett.* (2019). doi:10.1021/acs.jpcllett.8b03721.
- [27] A. Deinega *et al.*, Minimizing light reflection from dielectric textured surfaces, *J. Opt. Soc. Am. A.* (2011). doi:10.1364/josaa.28.000770.
- [28] M.J. Minot, Single-layer, gradient refractive index antireflection films effective from 0.35 to 2.5  $\mu\text{m}$ , *J Opt Soc Am.* (1976). doi:10.1364/josa.66.000515.
- [29] W.H. Southwell, Gradient-index antireflection coatings, *Opt. Lett.* (2008). doi:10.1364/ol.8.000584.
- [30] M. Langenhorst *et al.*, Liquid glass for photovoltaics: multi-functional front cover glass for solar modules, *ACS Appl. Mater. Interfaces.* (2019). doi:10.1021/acsaami.9b12896.
- [31] P. Campbell, M.A. Green, Light trapping properties of pyramidally textured surfaces, *J. Appl. Phys.* (1987). doi:10.1063/1.339189.
- [32] D. Redfield, Multiple-pass thin-film silicon solar cell, *Appl. Phys. Lett.* (1974). doi:10.1063/1.1655344.
- [33] S. V. Boriskina *et al.*, Roadmap on optical energy conversion, *J. Opt. (United Kingdom).* (2016). doi:10.1088/2040-8978/18/7/073004.
- [34] U. Rau *et al.*, Thermodynamics of light management in photovoltaic devices, *Phys. Rev. B - Condens. Matter Mater. Phys.* (2014). doi:10.1103/PhysRevB.90.035211.
- [35] M.F. Schumann *et al.*, All-Angle Invisibility Cloaking of Contact Fingers on Solar Cells by Refractive Free-Form Surfaces, *Adv. Opt. Mater.* (2017). doi:10.1002/adom.201700164.
- [36] S.J. Wilson, M.C. Hutley, The optical properties of 'moth eye' antireflection surfaces, *Opt. Acta (Lond).* (1982). doi:10.1080/713820946.
- [37] W.K. Kuo *et al.*, Moth-eye-inspired biophotonic surfaces with antireflective and hydrophobic characteristics, *ACS Appl. Mater. Interfaces.* (2016). doi:10.1021/acsaami.6b10960.
- [38] R. Dewan *et al.*, Studying nanostructured nipple arrays of moth eye facets helps to design better thin film solar cells, *Bioinspiration and Biomimetics.* (2012). doi:10.1088/1748-3182/7/1/016003.
- [39] R.H. Siddique *et al.*, The role of random nanostructures for the omnidirectional anti-reflection properties of the glasswing butterfly, *Nat. Commun.* (2015). doi:10.1038/ncomms7909.
- [40] C.-H. Hsu *et al.*, Fabrication and characteristics of black silicon for solar cell applications: An overview, *Mater. Sci. Semicond. Process.* (2014). doi:10.1016/j.mssp.2014.02.005.
- [41] P. Zhang *et al.*, An 18.9% efficient black silicon solar cell achieved through control of pretreatment of Ag/Cu MACE, *J. Mater. Sci. Mater. Electron.* (2019). doi:10.1007/s10854-019-01189-0.

- 
- [42] I.M. Thomas, Method for the preparation of porous silica antireflection coatings varying in refractive index from 122 to 144, *Appl. Opt.* (1992). doi:10.1364/AO.31.006145.
- [43] A. Papadopoulos *et al.*, Biomimetic Omnidirectional Antireflective Glass via Direct Ultrafast Laser Nanostructuring, *Adv. Mater.* (2019). doi:10.1002/adma.201901123.
- [44] H.A. Atwater, A. Polman, Plasmonics for improved photovoltaic devices, *Nat. Mater.* (2010). doi:10.1038/nmat2629.
- [45] S. Pillai *et al.*, Surface plasmon enhanced silicon solar cells, *J. Appl. Phys.* (2007). doi:10.1063/1.2734885.
- [46] S. Mokkaḡati, K.R. Catchpole, Nanophotonic light trapping in solar cells, *J. Appl. Phys.* (2012). doi:10.1063/1.4747795.
- [47] P. Bermel *et al.*, Improving thin-film crystalline silicon solar cell efficiencies with photonic crystals, *Opt. Express.* (2007). doi:10.1364/oe.15.016986.
- [48] D. Zhou, R. Biswas, Photonic crystal enhanced light-trapping in thin film solar cells, *J. Appl. Phys.* (2008). doi:10.1063/1.2908212.
- [49] R. Schmager *et al.*, Nanophotonic perovskite layers for enhanced current generation and mitigation of lead in perovskite solar cells, *Sol. Energy Mater. Sol. Cells.* (2019). doi:10.1016/j.solmat.2018.12.012.
- [50] R. Schmager *et al.*, Light coupling to quasi-guided modes in nanoimprinted perovskite solar cells, *Sol. Energy Mater. Sol. Cells.* (2019). doi:10.1016/j.solmat.2019.110080.
- [51] P. Sheng *et al.*, Wavelength-selective absorption enhancement in thin-film solar cells, *Appl. Phys. Lett.* (1983). doi:10.1063/1.94432.
- [52] R. Dewan, D. Knipp, Light trapping in thin-film silicon solar cells with integrated diffraction grating, *J. Appl. Phys.* (2009). doi:10.1063/1.3232236.
- [53] S.K. Ram *et al.*, Efficient light-trapping with quasi-periodic uniaxial nanowrinkles for thin-film silicon solar cells, *Nano Energy.* (2017). doi:10.1016/j.nanoen.2017.04.016.
- [54] S. Schauer *et al.*, Disordered diffraction gratings tailored by shape-memory based wrinkling and their application to photovoltaics, *Opt. Mater. Express.* (2018). doi:10.1364/ome.8.000184.
- [55] C. Rockstuhl *et al.*, Comparison and optimization of randomly textured surfaces in thin-film solar cells, *Opt. Express.* (2010). doi:10.1364/oe.18.00a335.
- [56] C. Battaglia *et al.*, Efficient light management scheme for thin film silicon solar cells via transparent random nanostructures fabricated by nanoimprinting, *Appl. Phys. Lett.* (2010). doi:10.1063/1.3432739.
- [57] E. Garnett, P. Yang, Light trapping in silicon nanowire solar cells, *Nano Lett.* (2010). doi:10.1021/nl100161z.
- [58] M.R. Khan *et al.*, Enhanced light trapping in solar cells with a meta-mirror following generalized Snell's law, *Opt. Express.* (2014). doi:10.1364/oe.22.00a973.
- [59] U. Schulz, Review of modern techniques to generate antireflective properties on thermoplastic polymers, *Appl. Opt.* (2006). doi:10.1364/AO.45.001608.
- [60] P. Wǖrfel, *Physics of Solar Cells: From Principles to New Concepts*, 2007. doi:10.1002/9783527618545.
- [61] A. Smets *et al.*, *Solar Energy - The Physics and Engineering of Photovoltaic Conversion Technologies*
-

- and Systems, 2016. doi:10.1016/B978-0-12-809597-3.00117-6.
- [62] W. Shockley, H.J. Queisser, Detailed balance limit of efficiency of p-n junction solar cells, *J. Appl. Phys.* (1961). doi:10.1063/1.1736034.
- [63] M. Chuang, Calculation and visualization tools for theoretical solar cell efficiencies based on the Shockley Queisser limit, (2019). [www.github.com/marcus-cmc/Shockley-Queisser-limit](http://www.github.com/marcus-cmc/Shockley-Queisser-limit) (accessed March 5, 2020).
- [64] A. De Vos, Detailed balance limit of the efficiency of tandem solar cells, *J. Phys. D. Appl. Phys.* (1980). doi:10.1088/0022-3727/13/5/018.
- [65] S. V. Boriskina, G. Chen, Exceeding the solar cell Shockley-Queisser limit via thermal up-conversion of low-energy photons, *Opt. Commun.* (2014). doi:10.1016/j.optcom.2013.10.042.
- [66] T. Trupke *et al.*, Improving solar cell efficiencies by down-conversion of high-energy photons, *J. Appl. Phys.* (2002). doi:10.1063/1.1492021.
- [67] M. Born *et al.*, Principles of Optics: Electromagnetic Theory of Propagation, Interference and Diffraction of Light, *Phys. Today*. (2000). doi:10.1063/1.1325200.
- [68] J. Schwinger *et al.*, Classical Electrodynamics, 2019. doi:10.1201/9780429503542.
- [69] James Clerk Maxwell, A dynamical theory of the electromagnetic field, *Philos. Trans. R. Soc. London.* (1865). doi:10.1098/rstl.1865.0008.
- [70] E. Yablonovitch, Statistical Ray Optics, *J. Opt. Soc. Am.* (1982). doi:10.1364/JOSA.72.000899.
- [71] and G.L.A. Miñano, J. C., A. Luque, Physical limitations to photovoltaic energy conversion, *Photovoltaics*. (1990). doi:10.1016/0379-6787(91)90099-b.
- [72] Z. Yu *et al.*, Fundamental limit of nanophotonic light trapping in solar cells, *Proc. Natl. Acad. Sci. U. S. A.* (2010). doi:10.1073/pnas.1008296107.
- [73] K.S. Yee, Numerical Solution of Initial Boundary Value Problems Involving Maxwell's Equations in Isotropic Media, *IEEE Trans. Antennas Propag.* (1966). doi:10.1109/TAP.1966.1138693.
- [74] W.K. Chen, The electrical engineering handbook, 2005. doi:10.5860/choice.38-0957.
- [75] A. Taflove *et al.*, Computational Electromagnetics: The Finite-Difference Time-Domain Method, in: *Electr. Eng. Handb.*, Elsevier, 2005: pp. 629–670. doi:10.1016/B978-012170960-0/50046-3.
- [76] J.-M. Jin, The finite element method in electromagnetics, John Wiley & Sons, Ltd, 2015.
- [77] C.C. Katsidis, D.I. Siapkas, General transfer-matrix method for optical multilayer systems with coherent, partially coherent, and incoherent interference, *Appl. Opt.* (2002). doi:10.1364/ao.41.003978.
- [78] S. Dottermusch *et al.*, Micro-cone textures for improved light in-coupling and retroreflection-inspired light trapping at the front surface of solar modules, *Prog. Photovoltaics Res. Appl.* (2019). doi:10.1002/ppp.3133.
- [79] M. Worgull, Hot Embossing: Theory and Technology of Microreplication, William Andrew, 2009. doi:10.1016/B978-0-8155-1579-1.50001-X.
- [80] I.M. Hossain *et al.*, Scalable Processing of Low-Temperature TiO<sub>2</sub> Nanoparticles for High-Efficiency Perovskite Solar Cells, *ACS Appl. Energy Mater.* (2018). doi:10.1021/acsaem.8b01567.
- [81] C.R. Blanchard, Atomic Force Microscopy, *Chem. Educ.* (1996). doi:10.1007/s00897960059a.
- [82] B. Voigtländer, Scanning Probe Microscopy: Atomic Force Microscopy and Scanning Tunneling

- Microscopy, *Nanosci. Technol.* (2015). doi:10.1007/978-3-662-45240-0.
- [83] L. Rakocevic *et al.*, Reliable Performance Comparison of Perovskite Solar Cells Using Optimized Maximum Power Point Tracking, *Sol. RRL.* (2019). doi:10.1002/solr.201800287.
- [84] R. Schmager *et al.*, Methodology of energy yield modelling of perovskite-based multi-junction photovoltaics, *Opt. Express.* (2019). doi:10.1364/oe.27.00a507.
- [85] J. Lehr *et al.*, Energy yield of bifacial textured perovskite/silicon tandem photovoltaic modules, *Sol. Energy Mater. Sol. Cells.* (2020). doi:10.1016/j.solmat.2019.110367.
- [86] J. Lehr *et al.*, Energy yield modelling of perovskite/silicon two-terminal tandem PV modules with flat and textured interfaces, *Sustain. Energy Fuels.* (2018). doi:10.1039/c8se00465j.
- [87] M. Langenhorst *et al.*, Performance of Silicon Solar Cells with Cloaked Contact Fingers under Realistic Conditions, in: *Opt. InfoBase Conf. Pap.*, 2017: p. PW2A.3. doi:10.1364/pv.2017.pw2a.3.
- [88] M. Langenhorst *et al.*, Energy yield of all thin-film perovskite/CIGS tandem solar modules, *Prog. Photovoltaics Res. Appl.* (2019). doi:10.1002/pip.3091.
- [89] Y. Hirata, T. Tani, Output variation of photovoltaic modules with environmental factors-I. The effect of spectral solar radiation on photovoltaic module output, *Sol. Energy.* (1995). doi:10.1016/0038-092X(95)00063-W.
- [90] R. Gottschalg *et al.*, The effect of spectral variations on the performance parameters of single and double junction amorphous silicon solar cells, *Sol. Energy Mater. Sol. Cells.* (2005). doi:10.1016/j.solmat.2004.05.011.
- [91] M. Alonso-Abella *et al.*, Analysis of spectral effects on the energy yield of different PV (photovoltaic) technologies: The case of four specific sites, *Energy.* (2014). doi:10.1016/j.energy.2014.01.024.
- [92] G.S. Kinsey, Spectrum sensitivity, energy yield, and revenue prediction of PV modules, *IEEE J. Photovoltaics.* (2015). doi:10.1109/JPHOTOV.2014.2370256.
- [93] S. Senthilarasu *et al.*, Effects of spectral coupling on perovskite solar cells under diverse climatic conditions, *Sol. Energy Mater. Sol. Cells.* (2015). doi:10.1016/j.solmat.2014.10.037.
- [94] O. Isabella *et al.*, Advanced modelling of E/UIPV systems from location to load, in: *2018 IEEE 7th World Conf. Photovolt. Energy Conversion, WCPEC 2018 - A Jt. Conf. 45th IEEE PVSC, 28th PVSEC 34th EU PVSEC, IEEE, 2018: pp. 2691–2696.* doi:10.1109/PVSC.2018.8548039.
- [95] A. Calcabrini *et al.*, A simplified skyline-based method for estimating the annual solar energy potential in urban environments, *Nat. Energy.* (2019). doi:10.1038/s41560-018-0318-6.
- [96] K. Araki, M. Yamaguchi, Influences of spectrum change to 3-junction concentrator cells, *Sol. Energy Mater. Sol. Cells.* (2003). doi:10.1016/S0927-0248(02)00140-X.
- [97] G.S. Kinsey, K.M. Edmondson, Spectral response and energy output of concentrator multijunction solar cells, *Prog. Photovoltaics Res. Appl.* (2009). doi:10.1002/pip.875.
- [98] S.P. Philipps *et al.*, Energy harvesting efficiency of III-V multi-junction concentrator solar cells under realistic spectral conditions, *AIP Conf. Proc.* (2010). doi:10.1063/1.3509215.
- [99] X. Wang, A. Barnett, The effect of spectrum variation on the energy production of triple-junction solar cells, *IEEE J. Photovoltaics.* (2012). doi:10.1109/JPHOTOV.2012.2199081.
- [100] N.L.A. Chan *et al.*, Validation of energy prediction method for a concentrator photovoltaic module in Toyohashi Japan, *Prog. Photovoltaics Res. Appl.* (2013). doi:10.1002/pip.2241.
- [101] A. Hoffmann *et al.*, Analysis of parasitic losses due to intermediate reflectors in silicon tandem solar

- cells, *Sol. Energy Mater. Sol. Cells*. (2017). doi:10.1016/j.solmat.2017.01.010.
- [102] H. Liu *et al.*, The realistic energy yield potential of GaAs-on-Si tandem solar cells: a theoretical case study, *Opt. Express*. (2015). doi:10.1364/oe.23.00a382.
- [103] H. Liu *et al.*, On the methodology of energy yield assessment for one-Sun tandem solar cells, *Sol. Energy*. (2016). doi:10.1016/j.solener.2016.06.028.
- [104] H. Liu *et al.*, Predicting the outdoor performance of flat-plate III–V/Si tandem solar cells, *Sol. Energy*. (2017). doi:10.1016/j.solener.2017.04.003.
- [105] H. Schulte-Huxel *et al.*, Energy Yield Analysis of Multiterminal Si-Based Tandem Solar Cells, *IEEE J. Photovoltaics*. (2018). doi:10.1109/JPHOTOV.2018.2846520.
- [106] M.H. Futscher, B. Ehrler, Modeling the Performance Limitations and Prospects of Perovskite/Si Tandem Solar Cells under Realistic Operating Conditions, *ACS Energy Lett.* (2017). doi:10.1021/acsenergylett.7b00596.
- [107] M.T. Hörantner, H.J. Snaith, Predicting and optimising the energy yield of perovskite-on-silicon tandem solar cells under real world conditions, *Energy Environ. Sci.* (2017). doi:10.1039/c7ee01232b.
- [108] O. Dupré *et al.*, Field Performance versus Standard Test Condition Efficiency of Tandem Solar Cells and the Singular Case of Perovskites/Silicon Devices, *J. Phys. Chem. Lett.* (2018). doi:10.1021/acs.jpcclett.7b02277.
- [109] M. Jošt *et al.*, Textured interfaces in monolithic perovskite/silicon tandem solar cells: Advanced light management for improved efficiency and energy yield, *Energy Environ. Sci.* (2018). doi:10.1039/c8ee02469c.
- [110] L. Ba *et al.*, Perovskite/c-Si Monolithic Tandem Solar Cells under Real Solar Spectra: Improving Energy Yield by Oblique Incident Optimization, *J. Phys. Chem. C*. (2019). doi:10.1021/acs.jpcc.9b10186.
- [111] M.T. Hörantner *et al.*, The Potential of Multijunction Perovskite Solar Cells, *ACS Energy Lett.* (2017). doi:10.1021/acsenergylett.7b00647.
- [112] A. Onno *et al.*, Predicted Power Output of Silicon-Based Bifacial Tandem Photovoltaic Systems, *Joule*. (2020). doi:10.1016/j.joule.2019.12.017.
- [113] C.A. Gueymard, Parameterized transmittance model for direct beam and circumsolar spectral irradiance, *Sol. Energy*. (2001). doi:10.1016/S0038-092X(01)00054-8.
- [114] S. Wilcox, W. Marion, *Users Manual for TMY3 Data Sets (Revised)*, Golden, CO, 2008. doi:10.2172/928611.
- [115] W. Köppen, Die Wärmezonen der Erde, nach der Dauer der heissen, gemässigten und kalten Zeit und nach der Wirkung der Wärme auf die organische Welt betrachtet., *Meteorol. Zeitschrift*. (1884). doi:10.1127/0941-2948/2011/105.
- [116] M. Kottek *et al.*, World map of the Köppen-Geiger climate classification updated, *Meteorol. Zeitschrift*. (2006). doi:10.1127/0941-2948/2006/0130.
- [117] E.P. Shettle, R.W. Fenn, Models for the Aerosols of the Lower Atmosphere and the Effects of Humidity Variations on their Optical Properties, (1979). <http://oai.dtic.mil/oai/oai?verb=getRecord&metadataPrefix=html&identifier=ADA085951> (accessed January 22, 2020).
- [118] J.S. Bartlett *et al.*, The spectral effects of clouds on solar irradiance, *J. Geophys. Res. Ocean*. (1998). doi:10.1029/1998jc900002.
- [119] C.R. Osterwald *et al.*, Photovoltaic module calibration value versus optical air mass: The air mass

- function, *Prog. Photovoltaics Res. Appl.* (2014). doi:10.1002/pip.2303.
- [120] H.H. Aumann *et al.*, Evaluation of Radiative Transfer Models With Clouds, *J. Geophys. Res. Atmos.* (2018). doi:10.1029/2017JD028063.
- [121] X. Liu *et al.*, Development of a fast and accurate PCRTM radiative transfer model in the solar spectral region, *Appl. Opt.* (2016). doi:10.1364/ao.55.008236.
- [122] J. Eisenlohr *et al.*, Matrix formalism for light propagation and absorption in thick textured optical sheets, *Opt. Express.* (2015). doi:10.1364/oe.23.00a502.
- [123] M. Langenhorst, Cloaked contact grids for perovskite-silicon tandem solar modules, 2020. doi:10.5445/IR/1000104384.
- [124] S.J. Byrnes, Multilayer optical calculations, (2016). <http://arxiv.org/abs/1603.02720> (accessed January 23, 2020).
- [125] S.C. Baker-Finch, K.R. McIntosh, Reflection of normally incident light from silicon solar cells with pyramidal texture, *Prog. Photovoltaics Res. Appl.* (2011). doi:10.1002/pip.1050.
- [126] K.R. McIntosh, S.C. Baker-Finch, OPAL 2: Rapid optical simulation of silicon solar cells, in: *Conf. Rec. IEEE Photovolt. Spec. Conf.*, 2012: pp. 265–271. doi:10.1109/PVSC.2012.6317616.
- [127] PVEDUCATION, OPAL 2, (2016). [www2.pvlighthouse.com.au/calculators/OPAL\\_2/OPAL\\_2.aspx](http://www2.pvlighthouse.com.au/calculators/OPAL_2/OPAL_2.aspx) (accessed January 23, 2020).
- [128] M.K. Fuentes, A Simplified Thermal Model for Flat-Plate Photovoltaic Arrays, *Sandia Rep.* (1987). <http://prod.sandia.gov/techlib/access-control.cgi/1985/850330.pdf> (accessed January 24, 2020).
- [129] T.W. Neises *et al.*, Development of a thermal model for photovoltaic modules and analysis of NOCT guidelines, *J. Sol. Energy Eng. Trans. ASME.* (2012). doi:10.1115/1.4005340.
- [130] R. Ross, M.I. Smokler, Flat-plate solar array project final report–volume VI: engineering sciences and reliability, *Jet Propuls. Lab. Publ.* (1986).
- [131] R.G. Ross, Flat-plate photovoltaic array design optimization, in: *Conf. Rec. IEEE Photovolt. Spec. Conf.*, 1980: pp. 1126–1132.
- [132] O. Dupré *et al.*, Physics of the temperature coefficients of solar cells, *Sol. Energy Mater. Sol. Cells.* (2015). doi:10.1016/j.solmat.2015.03.025.
- [133] J.A. Schwenzler *et al.*, Temperature Variation-Induced Performance Decline of Perovskite Solar Cells, *ACS Appl. Mater. Interfaces.* (2018). doi:10.1021/acsami.8b01033.
- [134] X. Gao *et al.*, Lambert W-function based exact representation for double diode model of solar cells: Comparison on fitness and parameter extraction, *Energy Convers. Manag.* (2016). doi:10.1016/j.enconman.2016.09.005.
- [135] A. Jain, A. Kapoor, Exact analytical solutions of the parameters of real solar cells using Lambert W-function, *Sol. Energy Mater. Sol. Cells.* (2004). doi:10.1016/j.solmat.2003.11.018.
- [136] F. Gota, Energy yield modelling of three-terminal perovskite/silicon tandem photovoltaics (in preparation), (2020).
- [137] E.E.L. Mitchell, A.E. Rogers, Quaternion Parameters in the Simulation of a Spinning Rigid Body, *Simulation.* (1965). doi:10.1177/003754976500400610.
- [138] A. Sucich *et al.*, Experimental design for remote laser evaporative molecular absorption spectroscopy sensor system concept, in: C.D. Norton, T.S. Pagano (Eds.), *CubeSats NanoSats Remote Sens. II*, SPIE, 2018: p. 24. doi:10.1117/12.2320879.

- [139] A.M. Baldridge *et al.*, The ASTER spectral library version 2.0, *Remote Sens. Environ.* (2009). doi:10.1016/j.rse.2008.11.007.
- [140] X. Sun *et al.*, Optimization and performance of bifacial solar modules: A global perspective, *Appl. Energy.* (2018). doi:10.1016/j.apenergy.2017.12.041.
- [141] H. Mousazadeh *et al.*, A review of principle and sun-tracking methods for maximizing solar systems output, *Renew. Sustain. Energy Rev.* (2009). doi:10.1016/j.rser.2009.01.022.
- [142] A.M. Humada *et al.*, Solar cell parameters extraction based on single and double-diode models: A review, *Renew. Sustain. Energy Rev.* (2016). doi:10.1016/j.rser.2015.11.051.
- [143] N.M.A. Alrahim Shannan *et al.*, Single-diode model and two-diode model of PV modules: A comparison, in: *Proc. - 2013 IEEE Int. Conf. Control Syst. Comput. Eng. ICCSCE 2013*, 2013: pp. 210–214. doi:10.1109/ICCSCE.2013.6719960.
- [144] M.A. De Blas *et al.*, Selecting a suitable model for characterizing photovoltaic devices, *Renew. Energy.* (2002). doi:10.1016/S0960-1481(01)00056-8.
- [145] R. Schmager *et al.*, Texture of the Viola Flower for Light Harvesting in Photovoltaics, *ACS Photonics.* (2017). doi:10.1021/acsp Photonics.7b01153.
- [146] M. van Eerden *et al.*, Optical Analysis of Planar Multicrystalline Perovskite Solar Cells, *Adv. Opt. Mater.* (2017). doi:10.1002/adom.201700151.
- [147] B. Fritz *et al.*, Assessing the influence of structural disorder on the plant epidermal cells' optical properties: A numerical analysis, *Bioinspiration and Biomimetics.* (2017). doi:10.1088/1748-3190/aa6c46.
- [148] J. Wohlgemuth *et al.*, Crystalline silicon photovoltaic modules with anti-reflective coated glass, in: *Conf. Rec. IEEE Photovolt. Spec. Conf., IEEE, 2005*: pp. 1015–1018. doi:10.1109/PVSC.2005.1488305.
- [149] A. Roslizar *et al.*, Self-cleaning performance of superhydrophobic hot-embossed fluoropolymer films for photovoltaic modules, *Sol. Energy Mater. Sol. Cells.* (2019). doi:10.1016/j.solmat.2018.09.017.
- [150] M. Jaysankar *et al.*, Perovskite-silicon tandem solar modules with optimised light harvesting, *Energy Environ. Sci.* (2018). doi:10.1039/c8ee00237a.
- [151] A.J. Schulte *et al.*, Biomimetic replicas: Transfer of complex architectures with different optical properties from plant surfaces onto technical materials, *Acta Biomater.* (2009). doi:10.1016/j.actbio.2009.01.028.
- [152] H.L. Gorton, T.C. Vogelmann, Effects of Epidermal Cell Shape and Pigmentation on Optical Properties of Antirrhinum Petals at Visible and Ultraviolet Wavelengths., *Plant Physiol.* (1996).
- [153] H.M. Whitney *et al.*, Floral iridescence, produced by diffractive optics, acts as a cue for animal pollinators, *Science.* (2009). doi:10.1126/science.1166256.
- [154] S. Vignolini *et al.*, The mirror crack'd: Both pigment and structure contribute to the glossy blue appearance of the mirror orchid, *Ophrys speculum*, *New Phytol.* (2012). doi:10.1111/j.1469-8137.2012.04356.x.
- [155] R. Hünig *et al.*, Flower Power: Exploiting Plants' Epidermal Structures for Enhanced Light Harvesting in Thin-Film Solar Cells, *Adv. Opt. Mater.* (2016). doi:10.1002/adom.201600046.
- [156] A. Roslizar *et al.*, Towards mass fabrication of hot embossed plant surface texture replicas as photovoltaic cover layers, in: A.E. Sakdinawat *et al.* (Eds.), *Nanoeng. Fabr. Prop. Opt. Devices XV*, SPIE, 2018: p. 17. doi:10.1117/12.2320555.
- [157] K. Goth, Design of nanophotonic ITO front electrodes for enhanced perovskite/c-Si tandem solar cells,

- Karlsruhe Institute of Technology, 2020.
- [158] I.M. Hossain *et al.*, Nanostructured front electrodes for perovskite/c-Si tandem photovoltaics, *Opt. Express*. (2020). doi:10.1364/OE.382253.
- [159] K.S. Han *et al.*, Enhanced transmittance of glass plates for solar cells using nano-imprint lithography, *Sol. Energy Mater. Sol. Cells*. (2010). doi:10.1016/j.solmat.2009.12.001.
- [160] M. Schultes *et al.*, Sputtered Transparent Electrodes (IO:H and IZO) with Low Parasitic Near-Infrared Absorption for Perovskite-Cu(In,Ga)Se<sub>2</sub> Tandem Solar Cells, *ACS Appl. Energy Mater.* (2019). doi:10.1021/acsaem.9b01224.
- [161] I. Khan *et al.*, Nanostructured as-deposited indium tin oxide thin films for broadband antireflection and light trapping, *Nanotechnology*. (2017). doi:10.1088/1361-6528/aa79df.
- [162] U.W. Paetzold *et al.*, Nanophotonic front electrodes for perovskite solar cells, *Appl. Phys. Lett.* (2015). doi:10.1063/1.4918751.
- [163] H.K. Park *et al.*, Fabrication and characterization of large-scale multifunctional transparent ITO nanorod films, *J. Mater. Chem. A*. (2013). doi:10.1039/c3ta10422b.
- [164] J.W. Leem, J.S. Yu, Indium tin oxide subwavelength nanostructures with surface antireflection and superhydrophilicity for high-efficiency Si-based thin film solar cells, *Opt. Express*. (2012). doi:10.1364/oe.20.00a431.
- [165] A. Kumar *et al.*, Enhancement of light extraction efficiency of organic light emitting diodes using nanostructured indium tin oxide, *Opt. Lett.* (2012). doi:10.1364/ol.37.000575.
- [166] S. Manzoor *et al.*, Optical modeling of wide-bandgap perovskite and perovskite/silicon tandem solar cells using complex refractive indices for arbitrary-bandgap perovskite absorbers, *Opt. Express*. (2018). doi:10.1364/oe.26.027441.
- [167] M. Saliba *et al.*, Cesium-containing triple cation perovskite solar cells: Improved stability, reproducibility and high efficiency, *Energy Environ. Sci.* (2016). doi:10.1039/c5ee03874j.
- [168] W. Zhou *et al.*, Constructing CsPbBr<sub>3</sub> Cluster Passivated-Triple Cation Perovskite for Highly Efficient and Operationally Stable Solar Cells, *Adv. Funct. Mater.* (2019). doi:10.1002/adfm.201809180.
- [169] A. Richter *et al.*, n-Type Si solar cells with passivating electron contact: Identifying sources for efficiency limitations by wafer thickness and resistivity variation, *Sol. Energy Mater. Sol. Cells*. (2017). doi:10.1016/j.solmat.2017.05.042.
- [170] R. Fu *et al.*, Ultrahigh open-circuit voltage for high performance mixed-cation perovskite solar cells using acetate anions, *J. Mater. Chem. A*. (2018). doi:10.1039/c8ta04453h.
- [171] D.L. Brundrett *et al.*, Homogeneous layer models for high-spatial-frequency dielectric surface-relief gratings: conical diffraction and antireflection designs, *Appl. Opt.* (1994). doi:10.1364/ao.33.002695.
- [172] F. Rebib *et al.*, Determination of optical properties of a-SiO<sub>x</sub>N<sub>y</sub> thin films by ellipsometric and UV-visible spectroscopies, *J. Phys. Conf. Ser.* (2008). doi:10.1088/1742-6596/100/8/082033.
- [173] C. Huang *et al.*, Polymer blend lithography: A versatile method to fabricate nanopatterned self-assembled monolayers, *Beilstein J. Nanotechnol.* (2012). doi:10.3762/bjnano.3.71.
- [174] X. Guo *et al.*, A New Strategy of Lithography Based on Phase Separation of Polymer Blends, *Sci. Rep.* (2015). doi:10.1038/srep15947.
- [175] Y.J. Donie *et al.*, Light trapping in thin film silicon solar cells: Via phase separated disordered nanopillars, *Nanoscale*. (2018). doi:10.1039/c8nr00455b.

- [176] R.H. Siddique *et al.*, Bioinspired phase-separated disordered nanostructures for thin photovoltaic absorbers, *Sci. Adv.* (2017). doi:10.1126/sciadv.1700232.
- [177] H. Shen *et al.*, Mechanically-stacked perovskite/CIGS tandem solar cells with efficiency of 23.9% and reduced oxygen sensitivity, *Energy Environ. Sci.* (2018). doi:10.1039/c7ee02627g.
- [178] A. Habermehl *et al.*, Roll-to-Roll Hot Embossing of 1D and 2D Photonic Nanostructures, *Adv. Eng. Mater.* (2019). doi:10.1002/adem.201900110.
- [179] Y.J. Donie, Towards Inkjet Printing of Phase-Separated Nanostructures for Light Extraction in Organic Light Emitting Diodes, in: *MRS Fall Meeting & Exhibit, Boston, Massachusetts, 2018*. <https://mrsfall2018.zerista.com/event/member/532683>.
- [180] F. Mathies *et al.*, Inkjet-Printed Triple Cation Perovskite Solar Cells, *ACS Appl. Energy Mater.* (2018). doi:10.1021/acsaem.8b00222.
- [181] H. Eggers *et al.*, Inkjet-Printed Micrometer-Thick Perovskite Solar Cells with Large Columnar Grains, *Adv. Energy Mater.* (2020). doi:10.1002/aenm.201903184.
- [182] I.A. Howard *et al.*, Coated and Printed Perovskites for Photovoltaic Applications, *Adv. Mater.* (2019). doi:10.1002/adma.201806702.
- [183] W.F. Wu, B.S. Chiou, Effect of annealing on electrical and optical properties of RF magnetron sputtered indium tin oxide films, *Appl. Surf. Sci.* (1993). doi:10.1016/0169-4332(93)90233-2.
- [184] N.M. Ahmed *et al.*, The effect of post annealing temperature on grain size of indium-tin-oxide for optical and electrical properties improvement, *Results Phys.* (2019). doi:10.1016/j.rinp.2019.102159.
- [185] E. Yousif, R. Haddad, Photodegradation and photostabilization of polymers, especially polystyrene: Review, *Springerplus.* (2013). doi:10.1186/2193-1801-2-398.
- [186] S. Ji *et al.*, Optimal moth eye nanostructure array on transparent glass towards broadband antireflection, *ACS Appl. Mater. Interfaces.* (2013). doi:10.1021/am402881x.
- [187] R. Schmager *et al.*, Towards nano-patterned perovskite layers for enhanced absorption in solar cells, in: *2018 IEEE 7th World Conf. Photovolt. Energy Convers., IEEE, 2018: pp. 15–17*. doi:10.1109/PVSC.2018.8548029.
- [188] D.J. Lee, Establishing of Hot Embossing Process for Imprinting Micro- and Nanostructures on Perovskites, Karlsruhe Institute of Technology, 2017.
- [189] A. Assadillayev, Nanoimprint lithography for perovskite optoelectronic devices, Karlsruhe Institute of Technology, 2017.
- [190] G.L. Whitworth *et al.*, Nanoimprinted distributed feedback lasers of solution processed hybrid perovskites, *Opt. Express.* (2016). doi:10.1364/oe.24.023677.
- [191] O. Bar-On *et al.*, Micro Lasers by Scalable Lithography of Metal-Halide Perovskites, *Adv. Mater. Technol.* (2018). doi:10.1002/admt.201800212.
- [192] M.S. Alias *et al.*, Enhanced Etching, Surface Damage Recovery, and Submicron Patterning of Hybrid Perovskites using a Chemically Gas-Assisted Focused-Ion Beam for Subwavelength Grating Photonic Applications, *J. Phys. Chem. Lett.* (2016). doi:10.1021/acs.jpcclett.5b02558.
- [193] J. Harwell *et al.*, Patterning Multicolor Hybrid Perovskite Films via Top-Down Lithography, *ACS Nano.* (2019). doi:10.1021/acsnano.8b09592.
- [194] S. Chen *et al.*, A Photonic Crystal Laser from Solution Based Organo-Lead Iodide Perovskite Thin Films, *ACS Nano.* (2016). doi:10.1021/acsnano.5b08153.

- 
- [195] S. Wang *et al.*, Lead Halide Perovskite Based Microdisk Lasers for On-Chip Integrated Photonic Circuits, *Adv. Opt. Mater.* (2018). doi:10.1002/adom.201701266.
- [196] C. Zhang *et al.*, Lead Halide Perovskite-Based Dynamic Metasurfaces, *Laser Photonics Rev.* (2019). doi:10.1002/lpor.201900079.
- [197] J. Mao *et al.*, Novel Direct Nanopatterning Approach to Fabricate Periodically Nanostructured Perovskite for Optoelectronic Applications, *Adv. Funct. Mater.* (2017). doi:10.1002/adfm.201606525.
- [198] S. Brittman *et al.*, Controlling crystallization to imprint nanophotonic structures into halide perovskites using soft lithography, *J. Mater. Chem. C.* (2017). doi:10.1039/c7tc02775c.
- [199] H. Wang *et al.*, Nanoimprinted Perovskite Nanograting Photodetector with Improved Efficiency, *ACS Nano.* (2016). doi:10.1021/acsnano.6b05535.
- [200] N. Pourdavoud *et al.*, Photonic Nanostructures Patterned by Thermal Nanoimprint Directly into Organo-Metal Halide Perovskites, *Adv. Mater.* (2017). doi:10.1002/adma.201605003.
- [201] N. Pourdavoud *et al.*, Distributed Feedback Lasers Based on MAPbBr<sub>3</sub>, *Adv. Mater. Technol.* (2018). doi:10.1002/admt.201700253.
- [202] A. Mayer *et al.*, Thermal nanoimprint to improve the morphology of MAPbX<sub>3</sub> (MA = methylammonium, X = I or Br), *J. Vac. Sci. Technol. B, Nanotechnol. Microelectron. Mater. Process. Meas. Phenom.* (2017). doi:10.1116/1.4991619.
- [203] W.W. Kim *et al.*, Oriented Grains with Preferred Low-Angle Grain Boundaries in Halide Perovskite Films by Pressure-Induced Crystallization, *Adv. Energy Mater.* (2018). doi:10.1002/aenm.201702369.
- [204] S.H. Ahn, L.J. Guo, High-Speed Roll-to-Roll Nanoimprint Lithography on Flexible Plastic Substrates, *Adv. Mater.* (2008). doi:10.1002/adma.200702650.
- [205] Y. Wang *et al.*, Diffraction-Grated Perovskite Induced Highly Efficient Solar Cells through Nanophotonic Light Trapping, *Adv. Energy Mater.* (2018). doi:10.1002/aenm.201702960.
- [206] K.R. Catchpole *et al.*, Plasmonics and nanophotonics for photovoltaics, *MRS Bull.* (2011). doi:10.1557/mrs.2011.132.
- [207] Q. Chen *et al.*, Controllable self-induced passivation of hybrid lead iodide perovskites toward high performance solar cells, *Nano Lett.* (2014). doi:10.1021/nl501838y.
- [208] P.P. Mondal *et al.*, Performance Analysis of Perovskite Solar Cells with Different Structures, in: 2nd Int. Conf. Electr. Comput. Commun. Eng. ECCE 2019, Institute of Electrical and Electronics Engineers Inc., 2019. doi:10.1109/ECACE.2019.8679329.
- [209] H.B. Lee *et al.*, Boosting the Efficiency of SnO<sub>2</sub>-Triple Cation Perovskite System Beyond 20% Using Nonhalogenated Antisolvent, *Adv. Funct. Mater.* (2019). doi:10.1002/adfm.201903213.
- [210] A. Akbari *et al.*, First principles modelling of perovskite solar cells based on TiO<sub>2</sub> and Al<sub>2</sub>O<sub>3</sub>: stability and interfacial electronic structure, *J. Mater. Chem. A.* (2017). doi:10.1039/c6ta08874k.
- [211] H. Hu *et al.*, Low-toxic metal halide perovskites: opportunities and future challenges, *J. Mater. Chem. A.* (2017). doi:10.1039/c7ta00269f.
- [212] Q. Tai *et al.*, Recent advances toward efficient and stable tin-based perovskite solar cells, *EcoMat.* (2019). doi:10.1002/eom2.12004.
- [213] W.F. Yang *et al.*, Tin Halide Perovskites: Progress and Challenges, *Adv. Energy Mater.* (2019). doi:10.1002/aenm.201902584.
-

- 
- [214] G. Volonakis *et al.*, Lead-Free Halide Double Perovskites via Heterovalent Substitution of Noble Metals, *J. Phys. Chem. Lett.* (2016). doi:10.1021/acs.jpcllett.6b00376.
- [215] R. Wang *et al.*, Opportunities and Challenges of Lead-Free Perovskite Optoelectronic Devices, *Trends Chem.* (2019). doi:10.1016/j.trechm.2019.04.004.
- [216] J. Xiao *et al.*, Pressure-assisted CH<sub>3</sub>NH<sub>3</sub>PbI<sub>3</sub> morphology reconstruction to improve the high performance of perovskite solar cells, *J. Mater. Chem. A.* (2015). doi:10.1039/c4ta06700b.
- [217] F. Isabelli *et al.*, Solvent Systems for Industrial-Scale Processing of Spiro-OMeTAD Hole Transport Layer in Perovskite Solar Sells, *ACS Appl. Energy Mater.* (2018). doi:10.1021/acsaem.8b01122.
- [218] R. Schmager *et al.*, Laminated Perovskite Photovoltaics: Enabling Novel Layer Combinations and Device Architectures, *Adv. Funct. Mater.* (2020). doi:10.1002/adfm.201907481.
- [219] J. Roger, Optimierung des Laminierverfahrens für effiziente und stabile Perowskit Solarzellen, Karlsruhe Institute of Technology, 2019.
- [220] N. Rai, Hot Embossing Process Optimization For Lamination Of Perovskite Solar Cells, Indian Institute of Technology & Karlsruhe Institute Of Technology, 2018.
- [221] Z. Song *et al.*, Pathways toward high-performance perovskite solar cells: review of recent advances in organo-metal halide perovskites for photovoltaic applications, *J. Photonics Energy.* (2016). doi:10.1117/1.JPE.6.022001.
- [222] N. Torabi *et al.*, Progress and challenges in perovskite photovoltaics from single- to multi-junction cells, *Mater. Today Energy.* (2019). doi:10.1016/j.mtener.2018.12.009.
- [223] T. Abzieher *et al.*, Towards Inexpensive and Stable All-Evaporated Perovskite Solar Cells for Industrial Large-Scale Fabrication, in: 2018 IEEE 7th World Conf. Photovolt. Energy Convers., IEEE, 2018: pp. 2803–2807. doi:10.1109/PVSC.2018.8547364.
- [224] S. Sajid *et al.*, Breakthroughs in NiO<sub>x</sub> -HTMs towards stable, low-cost and efficient perovskite solar cells, *Nano Energy.* (2018). doi:10.1016/j.nanoen.2018.06.082.
- [225] N. Arora *et al.*, Perovskite solar cells with CuSCN hole extraction layers yield stabilized efficiencies greater than 20%, *Science.* (2017). doi:10.1126/science.aam5655.
- [226] Y.-F. Li, First-Principles Prediction of the ZnO Morphology in the Perovskite Solar Cell, *J. Phys. Chem. C.* (2019). doi:10.1021/acs.jpcc.9b01008.
- [227] E.H. Anaraki *et al.*, Highly efficient and stable planar perovskite solar cells by solution-processed tin oxide, *Energy Environ. Sci.* (2016). doi:10.1039/c6ee02390h.
- [228] Q. Dong *et al.*, Improved SnO<sub>2</sub> Electron Transport Layers Solution-Deposited at Near Room Temperature for Rigid or Flexible Perovskite Solar Cells with High Efficiencies, *Adv. Energy Mater.* (2019). doi:10.1002/aenm.201900834.
- [229] J.Y. Seo *et al.*, Boosting the Efficiency of Perovskite Solar Cells with CsBr-Modified Mesoporous TiO<sub>2</sub> Beads as Electron-Selective Contact, *Adv. Funct. Mater.* (2018). doi:10.1002/adfm.201705763.
- [230] I.M. Hossain *et al.*, Scalable processing of low-temperature TiO<sub>2</sub> nanoparticles for high-efficiency perovskite solar cells, *ACS Appl. Energy Mater.* (2019). doi:10.1021/acsaem.8b01567.
- [231] T. Li *et al.*, Melt Processing of Hybrid Organic–Inorganic Lead Iodide Layered Perovskites, *Chem. Mater.* (2017). doi:10.1021/acs.chemmater.7b02363.
- [232] B. Abdollahi Nejad *et al.*, New Physical Deposition Approach for Low Cost Inorganic Hole Transport Layer in Normal Architecture of Durable Perovskite Solar Cells, *ACS Appl. Mater. Interfaces.* (2015). doi:10.1021/acsaem.5b05477.
-

- [233] K.A. Bush *et al.*, 23.6%-Efficient Monolithic Perovskite/Silicon Tandem Solar Cells With Improved Stability, *Nat. Energy*. (2017). doi:10.1038/nenergy.2017.9.
- [234] E. Nouri *et al.*, Introduction of Graphene Oxide as Buffer Layer in Perovskite Solar Cells and the Promotion of Soluble n-Butyl-substituted Copper Phthalocyanine as Efficient Hole Transporting Material, *Electrochim. Acta*. (2017). doi:10.1016/j.electacta.2017.03.027.
- [235] S. Guarnera *et al.*, Improving the Long-Term Stability of Perovskite Solar Cells with a Porous Al<sub>2</sub>O<sub>3</sub> Buffer Layer, *J. Phys. Chem. Lett.* (2015). doi:10.1021/jz502703p.
- [236] F. Sahli *et al.*, Fully textured monolithic perovskite/silicon tandem solar cells with 25.2% power conversion efficiency, *Nat. Mater.* (2018). doi:10.1038/s41563-018-0115-4.
- [237] Z. Li *et al.*, Laminated carbon nanotube networks for metal electrode-free efficient perovskite solar cells, *ACS Nano*. (2014). doi:10.1021/nn501096h.
- [238] P. You *et al.*, Efficient Semitransparent Perovskite Solar Cells with Graphene Electrodes, *Adv. Mater.* (2015). doi:10.1002/adma.201501145.
- [239] J.H. Heo *et al.*, Efficient Organic-Inorganic Hybrid Flexible Perovskite Solar Cells Prepared by Lamination of Polytriarylamine/CH<sub>3</sub>NH<sub>3</sub>PbI<sub>3</sub> /Anodized Ti Metal Substrate and Graphene/PDMS Transparent Electrode Substrate, *ACS Appl. Mater. Interfaces*. (2018). doi:10.1021/acsami.8b11411.
- [240] M. Makha *et al.*, A transparent, solvent-free laminated top electrode for perovskite solar cells, *Sci. Technol. Adv. Mater.* (2016). doi:10.1080/14686996.2016.1176512.
- [241] J.H. Heo, S.H. Im, CH<sub>3</sub>NH<sub>3</sub>PbBr<sub>3</sub>-CH<sub>3</sub>NH<sub>3</sub>PbI<sub>3</sub> Perovskite-Perovskite Tandem Solar Cells with Exceeding 2.2 V Open Circuit Voltage, *Adv. Mater.* (2016). doi:10.1002/adma.201501629.
- [242] C.O. Ramírez Quiroz *et al.*, Interface Molecular Engineering for Laminated Monolithic Perovskite/Silicon Tandem Solar Cells with 80.4% Fill Factor, *Adv. Funct. Mater.* (2019). doi:10.1002/adfm.201901476.
- [243] C.W. Jang *et al.*, Lamination-produced semi-transparent/flexible perovskite solar cells with doped-graphene anode and cathode, *J. Alloys Compd.* (2019). doi:10.1016/j.jallcom.2018.10.190.
- [244] H. Zhang *et al.*, Vacuum-free fabrication of high-performance semitransparent perovskite solar cells via e-glue assisted lamination process, *Sci. China Chem.* (2019). doi:10.1007/s11426-019-9481-3.
- [245] Y. Shao *et al.*, Insight into the Interfacial Elastic Contact in Stacking Perovskite Solar Cells, *Adv. Mater. Interfaces*. (2019). doi:10.1002/admi.201900157.
- [246] W.A. Dunlap-Shohl *et al.*, Interfacial Effects during Rapid Lamination within MAPbI<sub>3</sub> Thin Films and Solar Cells, *ACS Appl. Energy Mater.* (2019). doi:10.1021/acsaem.9b00747.
- [247] F. Jiang *et al.*, Metal electrode-free perovskite solar cells with transfer-laminated conducting polymer electrode, *Opt. Express*. (2015). doi:10.1364/OE.23.000A83.
- [248] S.P. Dunfield *et al.*, Curtailing perovskite processing limitations via lamination at the perovskite/perovskite interface, *ACS Energy Lett.* (2018). doi:10.1021/acsenerylett.8b00548.
- [249] I. Deretzis *et al.*, Stability and Degradation in Hybrid Perovskites: Is the Glass Half-Empty or Half-Full?, *J. Phys. Chem. Lett.* (2018). doi:10.1021/acs.jpcclett.8b00120.
- [250] A.K. Jena, T. Miyasaka, Hysteresis characteristics and device stability, in: *Org. Halide Perovskite Photovoltaics From Fundam. to Device Archit.*, Springer International Publishing, 2016: pp. 255–284. doi:10.1007/978-3-319-35114-8\_10.
- [251] J. Cao *et al.*, Low-temperature solution-processed NiO<sub>x</sub> films for air-stable perovskite solar cells, *J. Mater. Chem. A*. (2017). doi:10.1039/c7ta02228j.

- [252] T. Malinauskas *et al.*, Enhancing Thermal Stability and Lifetime of Solid-State Dye-Sensitized Solar Cells via Molecular Engineering of the Hole-Transporting Material Spiro-OMeTAD, *ACS Appl. Mater. Interfaces*. (2015). doi:10.1021/am5090385.
- [253] K. Domanski *et al.*, Systematic investigation of the impact of operation conditions on the degradation behaviour of perovskite solar cells, *Nat. Energy*. (2018). doi:10.1038/s41560-017-0060-5.
- [254] A.K. Jena *et al.*, Role of spiro-OMeTAD in performance deterioration of perovskite solar cells at high temperature and reuse of the perovskite films to avoid Pb-waste, *J. Mater. Chem. A*. (2018). doi:10.1039/c7ta07674f.
- [255] T. Abzieher *et al.*, Efficient All-Evaporated pin -Perovskite Solar Cells: A Promising Approach Toward Industrial Large-Scale Fabrication, *IEEE J. Photovoltaics*. (2019). doi:10.1109/JPHOTOV.2019.2920727.
- [256] K. Domanski *et al.*, Migration of cations induces reversible performance losses over day/night cycling in perovskite solar cells, *Energy Environ. Sci*. (2017). doi:10.1039/c6ee03352k.
- [257] M. Saliba *et al.*, Measuring Aging Stability of Perovskite Solar Cells, *Joule*. (2018). doi:10.1016/j.joule.2018.05.005.
- [258] C. Zhang *et al.*, Efficient stable graphene-based perovskite solar cells with high flexibility in device assembling via modular architecture design, *Energy Environ. Sci*. (2019). doi:10.1039/C9EE02391G.
- [259] N. Arora *et al.*, Low-Cost and Highly Efficient Carbon-Based Perovskite Solar Cells Exhibiting Excellent Long-Term Operational and UV Stability, *Small*. (2019). doi:10.1002/sml.201904746.
- [260] S.H. Turren-Cruz *et al.*, Methylammonium-free, high-performance, and stable perovskite solar cells on a planar architecture, *Science*. (2018). doi:10.1126/science.aat3583.
- [261] E.A. Alharbi *et al.*, Atomic-level passivation mechanism of ammonium salts enabling highly efficient perovskite solar cells, *Nat. Commun*. (2019). doi:10.1038/s41467-019-10985-5.
- [262] S. Barard *et al.*, Separate charge transport pathways determined by the time of flight method in bimodal polytriarylamine, *J. Appl. Phys*. (2009). doi:10.1063/1.3054180.
- [263] International Electrotechnical Commission, Thin film terrestrial photovoltaic (PV) modules—design qualification and type approval., IEC Int. Stand. Geneva, Switzerland, Tech. Rep. (2008). doi:10.3403/30138584.
- [264] R. Cheacharoen *et al.*, Encapsulating perovskite solar cells to withstand damp heat and thermal cycling, *Sustain. Energy Fuels*. (2018). doi:10.1039/c8se00250a.
- [265] A. Farooq *et al.*, Spectral Dependence of Degradation under Ultraviolet Light in Perovskite Solar Cells, *ACS Appl. Mater. Interfaces*. (2018). doi:10.1021/acsami.8b03024.
- [266] Z.C. Holman *et al.*, Infrared light management in high-efficiency silicon heterojunction and rear-passivated solar cells, *J. Appl. Phys*. (2013). doi:10.1063/1.4772975.
- [267] M.J. Dodge, Refractive properties of magnesium fluoride, *Appl. Opt*. (1984). doi:10.1364/ao.23.001980.
- [268] Z.C. Holman *et al.*, Current losses at the front of silicon heterojunction solar cells, *IEEE J. Photovoltaics*. (2012). doi:10.1109/JPHOTOV.2011.2174967.
- [269] C. Schinke *et al.*, Uncertainty analysis for the coefficient of band-to-band absorption of crystalline silicon, *AIP Adv*. (2015). doi:10.1063/1.4923379.
- [270] E.D. Palik, Handbook of optical constants of solids, 2012. doi:10.1016/C2009-0-20920-2.

# List of publications and contributions to conferences

## Peer-reviewed publications (first author)

**R. Schmager, J. Roger**, J. A. Schwenzler, F. Schackmar, T. Abzieher, M. Malekshahi Byranvand, B. Abdollahi Nejand, M. Worgull, B. S. Richards U. W. Paetzold, *Laminated perovskite photovoltaics: Enabling novel layer combinations and device architectures*, Adv. Funct. Mater. (2020) doi:10.1002/adfm.201907481.

**R. Schmager**, I. M. Hossain, F. Schackmar, B. S. Richards, G. Gomard, U. W. Paetzold, *Light coupling to quasi-guided modes in nanoimprinted perovskite solar cells*, Sol. Energy Mater. Sol. Cells. (2019). doi:10.1016/j.solmat.2019.110080.

**R. Schmager, M. Langenhorst**, J. Lehr, U. Lemmer, B.S. Richards, U.W. Paetzold, *Methodology of energy yield modelling of perovskite-based multi-junction photovoltaics*, Opt. Express. 27 (2019) A507. doi:10.1364/oe.27.00a507.

**R. Schmager**, G. Gomard, B.S. Richards, U.W. Paetzold, *Nanophotonic perovskite layers for enhanced current generation and mitigation of lead in perovskite solar cells*, Sol. Energy Mater. Sol. Cells. 192 (2019) 65–71. doi:10.1016/j.solmat.2018.12.012.

**S. Schauer, R. Schmager**, R. Hünig, K. Ding, U.W. Paetzold, U. Lemmer, M. Worgull, H. Hölscher, G. Gomard, *Disordered diffraction gratings tailored by shape-memory based wrinkling and their application to photovoltaics*, Opt. Mater. Express. 8 (2018). doi:10.1364/ome.8.000184.

**R. Schmager**, B. Fritz, R. Hünig, K. Ding, U. Lemmer, B.S. Richards, G. Gomard, U.W. Paetzold, *Texture of the Viola Flower for Light Harvesting in Photovoltaics*, ACS Photonics. 4 (2017). doi:10.1021/acsp Photonics.7b01153.

## Peer-reviewed publications (co-author)

**A. Roslizar**, S. Dottermusch, **R. Schmager**, M. Guttman, G. Gomard, H. Hölscher, B. S. Richards, U. W. Paetzold, *Hot-embossed microcone-textured fluoropolymer as self-cleaning and anti-reflective photovoltaic module covers*, Sol. Energy Mater. Sol. Cells (2020). doi:10.1016/j.solmat.2020.110582.

**I. M. Hossain, Y. J. Donie, R. Schmager**, M. S. Abdelkhalik, M. Rienäcker, T. F. Wietler, R. Peibst, A. Karabanov, J. A. Schwenzler, S. Moghadamzadeh, U. Lemmer, B. Richards, G. Gomard, U. W. Paetzold, *Nanostructured Front Electrodes for Perovskite/c-Si Tandem Photovoltaics*, Opt. Express. (2020). doi:10.1364/OE.382253.

**J. Lehr**, M. Langenhorst, **R. Schmager**, F. Gota, S. Kirner, U. Lemmer, B. S. Richards, C. Case, U. W. Paetzold, *Energy yield of bifacial textured perovskite/silicon tandem photovoltaic modules*, Sol. Energy Mater. Sol. Cells. (2020). doi:10.1016/j.solmat.2019.110367.

**M. Langenhorst**, D. Ritzer, F. Kotz, P. Risch, S. Dottermusch, A. Roslizar, **R. Schmager**, B. S. Richards, B. E. Rapp, U. W. Paetzold, *Liquid glass for photovoltaics: multi-functional front cover glass for solar modules*, ACS Appl. Mater. Interfaces. (2019). doi:10.1021/acsaami.9b12896.

**S. Nanz, R. Schmager**, M. G. Abebe, C. Willig, A. Wickberg, A. Abass, G. Gomard, M. Wegener, U. W. Paetzold, C. Rockstuhl, *Photon recycling in nanopatterned perovskite thin-films for photovoltaic applications*, APL Photonics. (2019). doi:10.1063/1.5094579.

**S. Dottermusch, R. Schmager**, E. Klampaftis, S. Paetel, O. Kiowski, K. Ding, B. S. Richards, U. W. Paetzold, *Micro-cone textures for improved light in-coupling and retroreflection-inspired light trapping at the front surface of solar modules*, Prog. Photovoltaics Res. Appl. (2019). doi:10.1002/pip.3133.

**S. Gharibzadeh**, B. Abdollahi Nejad, M. Jakoby, T. Abzieher, D. Hauschild, S. Moghadamzadeh, J.A. Schwenzer, P. Brenner, R. Schmager, A. A. Haghighirad, L. Weinhardt, U. Lemmer, B.S. Richards, I.A. Howard, U.W. Paetzold, *Record Open-Circuit Voltage Wide-Band gap Perovskite Solar Cells Utilizing 2D/3D Perovskite Heterostructure*, Adv. Energy Mater. (2019) 1803699. doi:10.1002/aenm.201803699.

**M. Langenhorst**, B. Sautter, R. Schmager, J. Lehr, E. Ahlswede, M. Powalla, U. Lemmer, B.S. Richards, U.W. Paetzold, *Energy yield of all thin-film perovskite/CIGS tandem solar modules*, Prog. Photovoltaics Res. Appl. 27 (2019) 290–298. doi:10.1002/pip.3091.

**T. Abzieher**, S. Moghadamzadeh, F. Schackmar, H. Eggers, F. Sutterlütli, A. Farooq, D. Kojda, K. Habicht, R. Schmager, A. Mertens, R. Azmi, L. Klohr, J.A. Schwenzer, M. Hetterich, U. Lemmer, B.S. Richards, M. Powalla, U.W. Paetzold, *Electron-Beam-Evaporated Nickel Oxide Hole Transport Layers for Perovskite-Based Photovoltaics*, Adv. Energy Mater. 9 (2019) 1802995. doi:10.1002/aenm.201802995.

**M. Langenhorst**, J. Lehr, B. Sautter, R. Schmager, U. Lemmer, B. Richards, U.W. Paetzold, B. Richards, U.W. Paetzold, U.W. Paetzold, *Energy yield Modelling of Wide Band gap Perovskite-Based Tandem Solar Modules*, in: Light. Energy Environ. 2018 (E2, FTS, HISE, SOLAR, SSL), OSA, Washington, D.C., 2018: p. OW5C.3. doi:10.1364/OSE.2018.OW5C.3.

**M. Langenhorst**, M.F. Schumann, S. Paetel, R. Schmager, U. Lemmer, B.S. Richards, M. Wegener, U.W. Paetzold, *Freeform surface invisibility cloaking of interconnection lines in thin-film photovoltaic modules*, Sol. Energy Mater. Sol. Cells. (2018). doi:10.1016/j.solmat.2018.03.034.

**J. Lehr**, **M. Langenhorst**, R. Schmager, S. Kirner, U. Lemmer, B.S. Richards, C. Case, U.W. Paetzold, *Energy yield modelling of perovskite/silicon two-terminal tandem PV modules with flat and textured interfaces*, Sustain. Energy Fuels. (2018). doi:10.1039/c8se00465j.

**M. Jaysankar**, M. Filipič, B. Zielinski, R. Schmager, W. Song, W. Qiu, U.W. Paetzold, T. Aernouts, M. Debucquoy, R. Gehlhaar, J. Poortmans, *Perovskite-silicon tandem solar modules with optimised light harvesting*, Energy Environ. Sci. 11 (2018). doi:10.1039/c8ee00237a.

**B. Fritz**, R. Hünig, R. Schmager, M. Hetterich, U. Lemmer, G. Gomard, *Assessing the influence of structural disorder on the plant epidermal cells' optical properties: A numerical analysis*, Bioinspiration and Biomimetics. 12 (2017). doi:10.1088/1748-3190/aa6c46.

## Conference proceedings:

R. Schmager, I. M. Hossain, Y. J. Donie, F. Schackmar, G. Gomard, B. S. Richards, U. W. Paetzold, *Nanophotonic perovskite thin-film solar cells by thermal nanoimprint lithography*, OSA Advanced Photonics Congress (AP), 2019. doi.org/10.1364/PVLED.2019.PM4C.3

**S. Gharibzadeh**, B. Abdollahi Nejad, M. Jakoby, T. Abzieher, S. Moghadamzadeh, J. A. Schwenzer, P. Brenner, R. Schmager, A. A. Haghighirad, U. Lemmer, B. S. Richards, I. A. Howard, U. W. Paetzold, *High Open-Circuit Voltage in Wide-Band gap Perovskite Photovoltaics with Passivation Layers Based on Large Cations*, IEEE 46th Photovoltaic Specialists Conference, 2019. 10.1109/PVSC40753.2019.8981234

**M. Langenhorst**, D. Ritzer, F. Kotz, P. Risch, I. Hossain, S. Dottermusch, A. Roslizar, R. Schmager, B. S. Richards, B. E. Rapp, U. W. Paetzold, *Advanced optical microstructures embedded in transparent encapsulation glass for photovoltaics*, International Society for Optics and Photonics, 2019. doi.org/10.1117/12.2509748

**S. Nanz**, R. Schmager, A. Abass, M. G. Abebe, G. Gomard, U. W. Paetzold, C. Rockstuhl, *Rigorous Wave-Optical Simulation of Photon Recycling in Nanostructured Perovskite Solar Cells*, Optical Society of America, 2018. 10.1364/OSE.2018.OT5C.2

**M. Langenhorst**, J. Lehr, B. Sautter, R. Schmager, U. Lemmer, B. S. Richards, U. W. Paetzold, Energy Yield Modelling of Wide Band gap Perovskite-Based Tandem Solar Modules, Optical Society of America, 2018. 10.1364/OSE.2018.OW5C.3

R. Schmager, T. Abzieher, P. Brenner, A. Assadillayev, D.J. Lee, S. Moghadamzadeh, I.M. Hossain, U. Lemmer, B.S. Richards, U.W. Paetzold, *Towards nano-patterned perovskite layers for enhanced absorption in solar cells*, IEEE 7th World Conf. Photovolt. Energy Conversion, WCPEC 2018 - A Jt. Conf. of 45th IEEE PVSC, 28th PVSEC & 34th EU PVSEC, 2018. doi:10.1109/PVSC.2018.8548029.

**M. Langenhorst**, M.F. Schumann, R. Schmager, J. Lehr, U. Lemmer, M. Wegener, B. Richards, U.W. Paetzold, *Performance of Silicon Solar Cells with Cloaked Contact Fingers under Realistic Conditions*, Optical Society of America, 2017. doi:10.1364/pv.2017.pw2a.3.

## Contributions to conferences

R. Schmager, I. M. Hossain, R. Hünig, K. Ding, B. Fritz, U. Lemmer, B. S. Richards, G. Gomard, U. W. Paetzold, *Biomimetic Surfaces Increase Performance of Prototype Solar Cells (Talk)*, EMRS, Strasbourg, 2017.

R. Schmager, U. Lemmer, B. S. Richards, G. Gomard, U. W. Paetzold, *Nanophotonics for perovskite / silicon multijunction solar cells (Poster)*, KDOP, Karlsruhe, 2017.

R. Schmager, T. Abzieher, P. Brenner, A. Assadillayev, D. J. Lee, S. Moghadamzadeh, I. M. Hossain, U. Lemmer, B. S. Richards, U. W. Paetzold, *Towards nano-patterned perovskite layers for enhanced absorption in solar cells (Talk)*, WCPEC-7, Waikoloa, 2018.

R. Schmager, B. S. Richards, G. Gomard, U. W. Paetzold, *Nanophotonic Perovskite Solar Cells (Talk)*, KSOP Technical Module, Strasbourg, 2018.

R. Schmager, P. Brenner, A. Assadillayev, D. J. Lee, T. Abzieher, S. Moghadamzadeh, I. M. Hossain, U. Lemmer, B. S. Richards, U. W. Paetzold, *Nanophotonic Perovskites for Enhanced Absorption in Solar Cells (Talk)*, SPIE Photonics Europe, Strasbourg, 2018.

R. Schmager, I. M. Hossain, R. Hünig, K. Ding, B. Fritz, U. Lemmer, B. S. Richards, G. Gomard, U. W. Paetzold, *Increasing the Performance of Solar Cells by Biomimetic Surfaces (Talk)*, SPIE Photonics Europe, Strasbourg, 2018.

R. Schmager, T. Abzieher, P. Brenner, A. Assadillayev, D. J. Lee, S. Moghadamzadeh, A. Farooq, I. M. Hossain, U. Lemmer, B. S. Richards, U. W. Paetzold, *Nanophotonic Perovskite Layers for Enhanced Absorption in Perovskite Thin-Film Solar Cells (Poster)*, SPIE, San Diego, 2018.

R. Schmager, I. M. Hossain, Y. J. Donie, F. Schackmar, G. Gomard, B. S. Richards, U. W. Paetzold, *Nanophotonic perovskite thin-film solar cells by thermal nanoimprint lithography (Talk)*, OSA, San Francisco, 2019.

R. Schmager, J. Roger, J. A. Schwenzler, F. Schackmar, T. Abzieher, M. Malekshahi Byranvand, B. Abdollahi Nejand, M. Worgull, B. S. Richards, Ulrich W. Paetzold, *Laminated Perovskite Photovoltaics Enabling novel layer combinations and device architectures (Talk)*, PSCO, Lausanne, 2019.



## Acknowledgements

First of all, I would like to take the opportunity to thank all those who have supported me on my way to my PhD. Above all, special thanks go to Dr. Ulrich W. Paetzold for giving me the opportunity to pursue my PhD as one of the first students in his research group “Advanced Optics for Photovoltaics”. I would like to express my sincere gratitude for his guidance, motivation and enthusiasm, his investment of countless hours of proofreading as well as his open door for profound scientific and personal discussions. Moreover, I would like to offer my special thanks to Prof. Dr. Bryce S. Richards and Prof. Dr. Uli Lemmer for their continuous support during my time at the Institute of Microstructure Technology and the Light Technology Institute at KIT. Furthermore, I would like to thank Prof. Dr. Carsten Rockstuhl for the co-supervision of two of my students and especially for agreeing to act as second referee.

A special thanks goes to my colleges Dr. Malte Langenhorst and Ihtez M. Hossain, with whom I have had the pleasure to start my PhD. On our journey, we shared many successful joint projects, had endless scientific and non-scientific discussions and truly an exciting time.

I am particularly grateful to Dr. Guillaume Gomard and Benjamin Fritz for the numerous fruitful discussions, the pleasant office atmosphere and especially the unforgettable conference trip to San Diego.

In additionally, I am very grateful to all my colleges during my thesis. Special thanks go to Dr. Tobias Abzieher, Jonas Schwenzer, Fabian Schackmar, Dr. Stephan Dottermusch, Dr. Paul Faßl, Saba Gharibzadeh, Jonathan Lehr, Yidenekachew J. Donie, Dominik Theobald, Henning Mescher, Dr. Philipp Brenner, Dr. Adrian Mertens, Amjad Farooq, Somayeh Moghadamzadeh, Aiman Roslizar, Tobias Berger, Dmitry Busko, Helge Eggers, Dr. Bahram Abdollahi Nejand, and Dr. Mahdi Malekshahi Byranvand. And indeed, all other former and current group members as well. It really were enjoyable years with many scientific discussions and other fun joint activities.

Moreover, special thanks go to all the external collaboration partners, namely Dr. Aimi Abass and Dr. Stefan Nanz (Institute for Theoretical Solid-State Physics at KIT), Dr. Manoj Jaysankar (IMEC), and The Duong (Australian National University).

I also want to thank the Karlsruhe School of Optics and Photonics (KSOP) for providing a graduate program and for the great organization of many social events.

Moreover, a very special thanks is directed to all my students: Dong Jae Lee, Artyom Assadillayev, Emilio Gutiérrez-Partida, Koen Bertens, Nitish Rai, Simon Geisert, Julie Roger, and Katharina Goth for their great work, which has significantly contributed to the success of this work and many other projects.

*Besonders bedanken möchte ich mich natürlich auch bei meinen Eltern Claus und Raymonde für ihre jahrelange Unterstützung. Ohne sie wäre mein Studium so nicht möglich gewesen. Meiner Schwester Isabelle möchte ich für die vielen kritischen Fragen und konstruktiven Anmerkungen danken und ihrem Mann Niklas für so manche handwerkliche Ablenkung. Meiner Freundin Silvia danke ich für ihre großartige Unterstützung. Auch in schwierigen Zeiten nahm sie mir jeden Selbstzweifel und hat mich stets motiviert.*